Mechano-Electrochemistry for Advanced Energy Storage and Harvesting Devices

By

Nitin Muralidharan

Dissertation

Submitted to the Faculty of the

Graduate School of Vanderbilt University

in partial fulfillment of the requirements

for the degree of

DOCTOR OF PHILOSOPHY

in

Interdisciplinary Materials Science

June 30, 2018

Nashville, Tennessee

Approved:

Cary Pint, Ph.D.

Douglas Adams, Ph.D.

Greg Walker, Ph.D.

Rizia Bardhan, Ph.D.

Leon Bellan, Ph.D.

Piran Kidambi, Ph.D.

This dissertation is dedicated to my loving grandparents: K. N. Rajappan Nair and Sarasamma; T. R. Gopalakrishnan and Sathiamma, a source of courage and unconditional love

Acknowledgements

First and foremost, I would like to sincerely thank my advisor Dr. Cary Pint who through his constant and patient efforts have made me the researcher I am now. Your passion for exciting new research frontiers and your constant drive towards achieving the goals you set out to do are the key things that inspires me to give my best in what I do. I thank you for leading by example and showing me the path towards excellence. Further, I would like to thank my dissertation committee: Dr. Douglas Adams, Dr. Greg Walker, Dr. Rizia bardhan, Dr. Leon Bellan and Dr. Piran Kidambi who have given their valuable insights, suggestions and ideas at various point of my research over the past four years.

I would like to thank our group members who have not only been a valuable source of knowledge and support but have been my good friends over these years. I specifically like to thank Dr. Landon Oakes for your remarkable patience for putting up with all the research and life related questions during my early years of grad school, Dr. Andrew Westover for helping me navigate through the early days of grad school and also working with me on several interesting projects, Dr. Rachel Carter who has always been there as a friend and a source of constructive feedback, Dr. Adam Cohn for being a good friend and for the wonderful discussions over new thought provoking research ideas, Dr. Keith Share for his effective and crisp feedback, Anna Douglas for working with me on the transient project and being a wonderful friend, Mengya Li for being my gym mate and friend whom I enjoyed working with in the energy harvester project, Kate Moyer for your help with the structural battery project and Janna Eaves for the insights and feedback. Further I would like to thank Deanna Schauben, the first Masters' student I mentored, my undergraduate students; Chuanzhe Meng for being a good friend and for all your hard work and dedication on the structural battery project, Jeremiah Afloabi, Nick Galioto, Thomas Metke and Siyuan Jiang for their sincere efforts. I also thank my friend Malavarayan for all the support and friendship.

Further I would like to thank the Dr. Rizia Bardhan and her research group for their valuable support and graciously sharing their lab space with us, Dr. Leon Bellan and his research group for the gracious use of lab space and facilities, Dr. Greg Walker and Casey Brock for working with me on the strain engineering project, Dr. Karl Zelik and Emily Matijevich for working with me on the energy harvester project and Dr. Douglas Adams and Liudmyla Prozorovska for working with me on the cure monitoring project. I extend my thanks to Sarah Satterwhite, Dr. Dmitry Koktysh, Dr. Anthony Hmelo, Dr. Alice Leach and all the VINSE staff for all their help. I would especially thank Robin Midgett for being such a wonderful source of knowledge and your help with all the machining and mechanical testing challenges.

I also want to express my sincere thanks to my parents, Rekha Murali and R. Muralidharan for being there for me in every aspect of my life. I wouldn't have been able to do any of this if it wasn't for your prayers, support and unconditional love. I also thank my dear uncle Ashok for his prayers, support and pragmatism which inspires me to keep a level-headed approach to things. I also thank my sister Neetu for all the pleasant distractions and friendship.

I deeply and sincerely thank my best friend for life, my pillar of strength, my dearest wife, Vidya Kishore for making me the person I am today. Ever since you came into my life, you have tirelessly worked towards making me realize what I am capable of. Your foresight and unwavering pursuit of wanting the best for me is what keeps me going. Your constant prayers, care, love and support keeps me sane and happy through the ups and downs of life. Thank you for introducing me to your wonderful family and I sincerely feel that I am blessed, and forever grateful to have you in my life.

Finally, I thank God for this wonderful life, for the wonderful family, for good health and helping me write this acknowledgement to all the important people in my life.

TABLE OF CONTENTS

Page

LIST OF FIGURES

Figure Page

Chapter I

Chapter II

Chapter V

Chapter VII

Chapter IX

LIST OF TABLES

Table Page

Chapter III

Chapter IV

Chapter V

Chapter VIII

Chapter IX

LIST OF PUBLICATIONS

Portions of this dissertation have been drawn from the following publications:

(1) **N. Muralidharan**, A. Douglas, R. E. Carter, K. Share, C. L. Pint, "Ultrafast triggered transient energy storage by atomic layer deposition into porous silicon for integrated transient electronics," Nanoscale 8, 7384-7390 (2016).

(2) **N. Muralidharan**, R. E. Carter, L. Oakes, A. P. Cohn, C. L. Pint, "Strain Engineering to Modify the Electrochemistry of Energy Storage Electrodes," Scientific Reports 6, 27542 (2016).

(3) **N. Muralidharan**, A. S. Westover, H. Sun, N. Galioto, R. E. Carter, A. P. Cohn, L. Oakes, C. L. Pint, "From the Junkyard to the Power Grid: Ambient Processing of Scrap Metals into Nanostructured Electrodes for Ultrafast Rechargeable Batteries," ACS Energy Letters 1, 1034-1041 (2016).

(4) **N. Muralidharan**, C. Brock, A. P. Cohn, D. Schauben, R. E. Carter, L. Oakes, D. G. Walker, C. L. Pint, "Tunable MechanoChemistry of Lithium Battery Electrodes," ACS Nano, 11, 6243–6251 (2017).

(5) **N. Muralidharan**, M. Li, R. E. Carter, N. Galioto, C. L. Pint, "Ultralow Frequency Electrochemical–Mechanical Strain Energy Harvester using 2D Black Phosphorus Nanosheets," ACS Energy Letters 2, 1797-1803 (2017).

(6) **N. Muralidharan**, J. Afloabi, K. Share, M. Li, C. L. Pint, "A Fully Transient Mechanical Energy Harvester," just accepted (05/2018) at Advanced Material Technologies.

(7) **N. Muralidharan**, A. P. Cohn, K. Share, E. Matijevich, L. Branscombe, M. Li, K. E. Moyer, T. Metke, K. E. Zelik, C. L. Pint, "Extreme Volume Change Sodium Co-Intercalation Electrodes for Harvesting Ambient Mechanical Energy During Human Motion" in preparation.

(8) **N. Muralidharan**, R. E. Carter, A. S. Westover, A. P. Cohn, B. Schmidt, H. Sun, C. L. Pint, "Systematic hierarchical micro/nanostrutcuring to improve faradaic energy storage" in preparation.

(9) **N. Muralidharan**, E. Teblum, A. S. Westover, D. Schauben, A. Titzhak, M. Muallem, G. D. Nessim, C. L. Pint, "Carbon nanotube reinforced structural composite supercapacitor" in resubmission.

(10) **N. Muralidharan**, C. Meng, T. Eti, K. E. Moyer, G. D. Nessim, C. L. Pint, "A multifunctional structural 'ultra-battery' composite" in preparation.

Chapter I

1 Introduction

1.1 Motivation

Energy generation and utilization has been the primary driving force the led to the present-day modern civilization. Using millions of years old energy from dead plants and animals, aptly named 'fossil fuels', we have not only shaped our modern society but have also gained the ability to change the environment of our planet completely. Never has been a time in human history where we have experienced the high standard of living we enjoy today. However, the latter half of the 20th century came as a reality check to this model through the stark realization that fossil fuels are not infinite and by using them unsustainably, large amounts of greenhouse gases and byproducts have started to alter the climate of our planet in an adverse manner. As a result, not only further development but also sustaining today's modern society will soon become an existential challenge. Thus, the quest for harnessing alternate sources of energy such as renewables and ambient energy from the environment have garnered great interest in recent years.

1.2 Need for electrochemical energy storage

1.2.1 Renewables and the 'duck curve'

Addition of renewable technologies to our existing electrical grids designed to handle fossil/nuclear/hydroelectric based energy generation technologies results in a unique challenge. This challenge can be visualized by the 'duck curve' (figure 1.1). For example, solar cell technologies for energy generation have been widely implemented in California in recent years to meet the ever-growing energy demands. The issue however has been that integrating the solar

cell systems directly to the existing grid creates load leveling issues. The peak energy consumption in a 24-hour day cycle occurs during the evenings when the solar cell systems become inoperable as a result of receding daylight. To compensate, existing fossil fuel-based power plants have to be run beyond capacity (ramping) to meet the demand. Additionally, passing cloud cover over the solar cell installation site creates fluctuations in energy generations even during daytime. These issues significantly highlight the need for energy storage technologies to offset the load imbalances by load leveling and prevent load fluctuations.

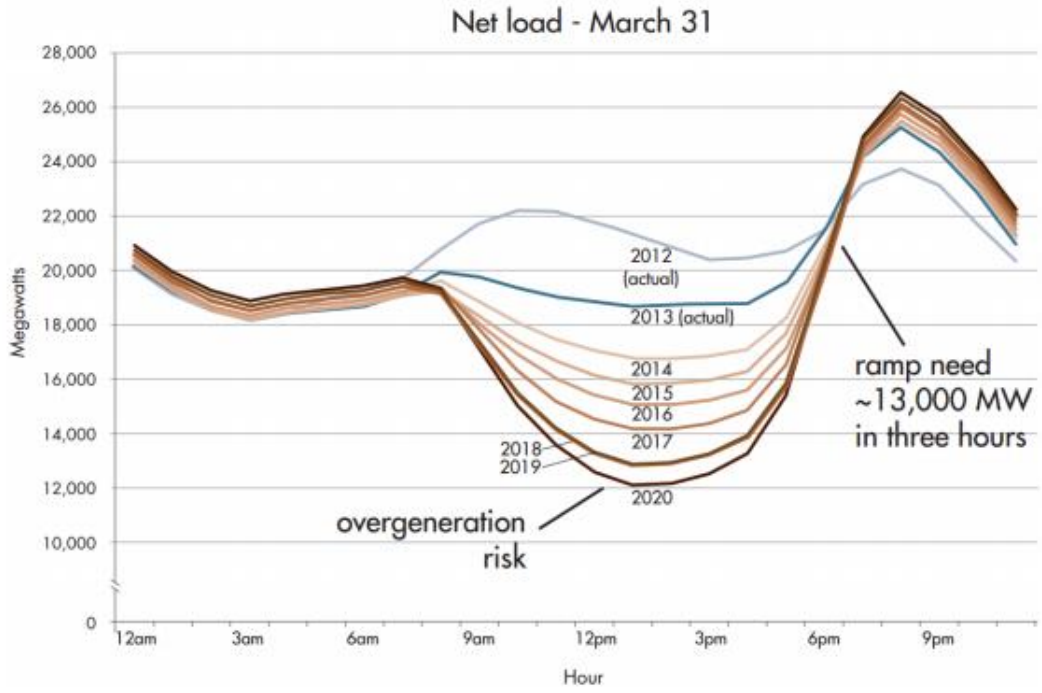

Figure 1.1. The duck chart highlighting the load-leveling requirement. (Figure reproduced from source: First published in CASIO 2013)[1, 2]

1.2.2 Advent of electric vehicles and wearable technologies

With the advent of electric vehicles, need for on-board, light-weight, cost-effective energy storage systems have emerged. Coupled with this, the mass influx of new wearable technologies into the consumer markets has accelerated this requirement even further. This requirement has

rejuvenated research efforts into on-demand and on-board energy storage architectures. Most research efforts are focused on developing next generation batteries and supercapacitors that fit this need. As shown in figure 1.2, the differences in performance for batteries and supercapacitors can be highlighted using the Ragone plot. The energy density is provided on the 'y-axis' and power density is provided on the 'x-axis'. Capacitors including supercapacitors have high power densities but low energy densities but batteries such as Li-ion, Na-ion, sulfur as well as air batteries have high energy densities but comparatively low power densities.

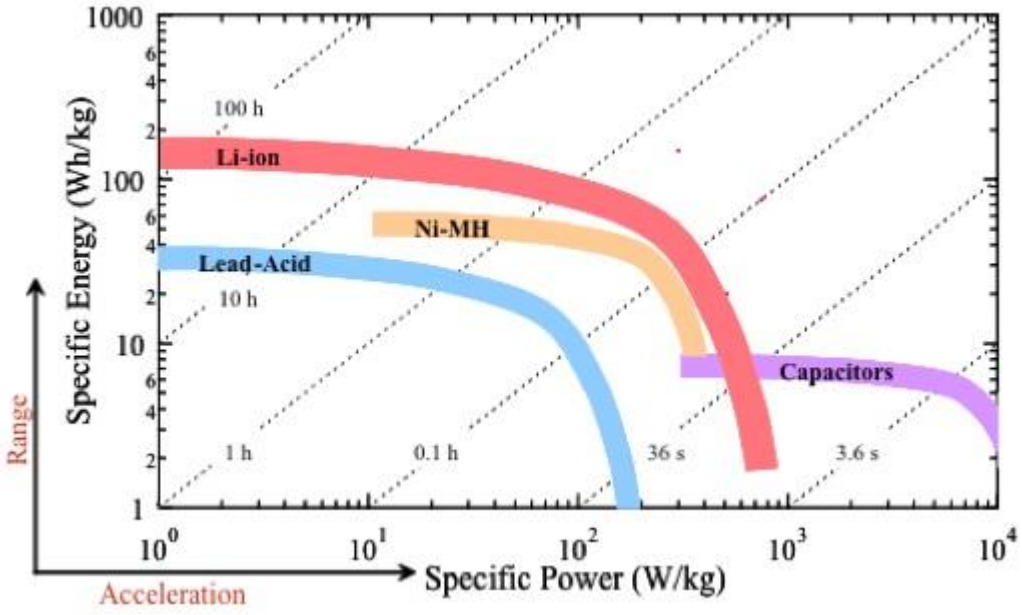

Figure 1.2. Ragone plot showing the performance metrics of energy storage systems and their relevance to electric vehicle technologies. (Courtesy: Venkat Srinivasan[3])

1.2.3 Ambient mechanical energy – an on-demand energy source

Ambient mechanical energy is present abundantly in our everyday working environment. In general, this ambient mechanical energy is typically wasted. If there were some means to harness this otherwise wasted energy, it would be ideal for decentralized energy production

operation to power portable electronic devices. This on-demand energy source coupled with on-board energy storage has the potential to meet the wearable technology energy demand of the future. Though there are numerous energy harvesters based on piezoelectric, electro kinetic and piezoelectric effects, they are severely limited in harvesting extremely low frequency mechanical energy (<5 Hz) in the regime of every day human activity such as running and walking or once a day activity such as sleeping. As conventional piezoelectric systems operate effectively at their resonant frequencies (>10Hz), they cannot effectively harvest such low frequency mechanical inputs. In order to harness such low-frequency ambient mechanical energy, a harvesting process with matched frequencies owing to a slower operational phenomenon when comparted to the operational mechanism of piezoelectric and triboelectric systems is necessary.

1.2.4 The rise of multifunctional devices

Keeping up with the drive towards efficient energy storage technologies for electric vehicles and wearables, an intriguing and promising approach has risen to the forefront over the recent years. This approach constitutes the field of multifunctional energy storage systems. Multifunctionality is the property of adding additional capabilities to an existing technology to perform functions more than just the primary function of the system. Especially in recent years two topics of research have garnered great interest: (i) transient energy storage devices and (ii) load-bearing energy storage devices. Transient energy storage systems can perform their energy storage function until they are triggered to undergo complete dissolution or disappearance. Such systems can be integrated with other transient electronic devices for application where security and data sensitivity are of primary concern. Load-bearing energy storage systems are those that can simultaneously handle massive amounts of mechanical load at the same time perform their energy storage function effectively. Such systems can be potentially made into polymer or

ceramic composites which can be used as structural materials in construction of future homes or as structural materials that are used in chassis, doors and panels of future electric vehicles and drone technologies.

These factors have contributed to a variety of research efforts focused on achieving these objectives to meet the burgeoning demands to make renewable technology as well as electric vehicles and wearable technologies of the future a sustainable and accessible reality. Maintaining a balance between energy requirement of our society and energy generation cannot be achieved without efficient energy storage systems.

1.3 The path forward – towards better energy storage and harvesting systems

Today's energy storage research is motivated along these lines where an emphasis on the balance between energy demand and consumption is given categorical importance from decentralized to centralized energy distribution and storage systems. This approach has proven fruitful with the advent of new generation electrochemical energy storage devices which include supercapacitors and batteries. From the view point of innovation in the sectors of present day electrochemical energy storage devices, formulation of new advanced material compositions constitutes the bulk of the academic research. With the rapid increase in hand held electronic devices fueled by the concept of miniaturization in the semi-conductor industry is presently exerting an enormous drain on current state of the art battery technologies. Energy storage devices boasting high storage capacity and faster power delivery have become an urgent necessity. Even though, lithium-sulfur and lithium-air battery technologies prove to be promising, migration from existing battery manufacturing technologies to these systems requires a complete overhaul of existing manufacturing infrastructures. If we examine the reason for the

rate of growth of the semi-conductor industry which has so far been able to keep up with Moore's Law, we find answers in the unique field of strain engineering.[4, 5]

1.3.1 Strain engineering and mechano-electrochemical coupling

Strain engineering refers to the systematic tuning of mechanical strains in materials to achieve unprecedented properties. The six dimensions of the strain tensor offers a wide range of tunable parameters which can be individually or collectively adjusted to achieve material properties otherwise inaccessible.[6] The foundations of this field of strain engineering can be explained using the universal binding energy relationship. The bond strength between two atoms similar or dissimilar in any material can be adjusted by tuning the distance between the two, bring them closer and. they tend to repel each other and vice versa.[7] This alters the properties of the material under consideration fundamentally. Strain engineering can be applied both to modify both bulk material properties as well as properties in the length scales of individual crystals (Fig. 1.3).

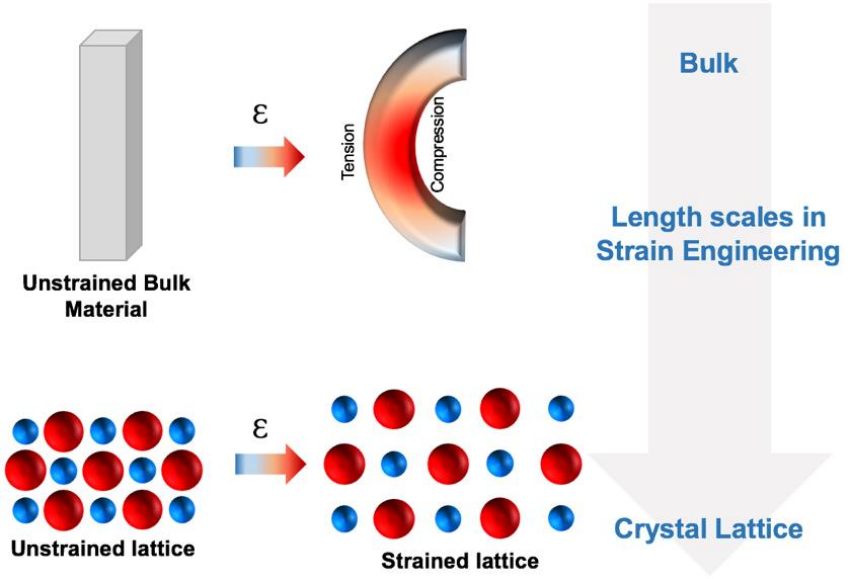

Figure 1.3. Schematic representation of the operational length scales where mechanical strains can be engineered into materials

Mechanical strains imposed on materials produce elastic deformations (recoverable) initially followed by plastic deformations (not-recoverable). To observe unprecedented property modifications using strain engineering, it is essential to operate in the elastic regime. Elastic strains do not produce permanent deformations but create various metastable conditions. However, owing to the recoverable nature of these elastic deformations these metastable states of materials are difficult to explore. If elastic strains could be controllably 'locked-in' materials without letting them regain initial state, we could exploit these metastable conditions to observe properties which are otherwise inaccessible thus creating the fundamental principle of the field of elastic strain engineering.[4] Traditional methods of elastic strain engineering involve epitaxial strains[8], strains through doping[9], thermal strains[10] and substrate assisted strain.[11] These techniques have been widely implemented to modify a variety of properties in the field of semi-conductor electronics[12], catalysis and improving ion diffusion in fuel cells.[13]

Traditional viewpoint in the field of electrochemical energy storage considers these systems (batteries and supercapacitors) as purely electrochemical systems. On the contrary, they are dynamic mechano-electrochemical systems where the mechanical component cannot be ignored. Most researchers emphasize discovery of new material formulations and battery systems while considering the associated mechanical processes as an unavoidable byproduct. In some cases, mechanical strains are considered an adverse effect attributed to the failure mechanisms of both cathode (phase transformations)[14] and anode (volume expansion).[15] This has led to various research efforts on mitigating strain in both anodes and cathodes in battery systems.[16-18] The coupling between mechanics and electrochemistry is called 'mechano-electrochemical coupling'. This coupling remains a relatively unexplored area of research in the field of electrochemical energy storage. Though there have been a limited number of reports using theoretical simulations illustrating the benefits of input mechanical strains, there exists a very low number of experimental works in this area.[19, 20] A beneficial product of the mechano-electrochemical coupling in battery systems is that this phenomenon can be used to design low-frequency energy harvesters that can effectively harness ambient mechanical energy. Moreover, with the recent rapid emergence multifunctional devices, understanding this fundamental relationship and utilizing this to the fullest beneficial extent remains an unexplored domain of research. This dissertation is therefore aimed at creating a paradigm shift towards understanding, isolating and thereby controlling mechanical process occurring in energy storage systems.

In this work, I begin by exploring the fundamental relationship between micro/nanostructures and electrochemical behavior using surface oxides on NiTi shapememory alloy. Leveraging this unique property of this versatile alloy and using principles of elastic strain engineering, I explore the modulation of electrochemical parameters governing energy storage

systems by imposing ‘locked-in’ elastic strains on them. Building off these principles, I explore the development of electrochemical-mechanical energy harvesters for harnessing ambient mechanical energy at very low frequencies. Energy harvesting capabilities of sodiated black phosphorus and sodium co-intercalated multilayered graphene at a broad range of low frequencies provide insights and understanding into the mechano-electrochemical coupling in these systems. Additionally, to further illustrate the relationship between mechanical and electrochemical properties, we developed multifunctional energy storage and harvesting devices including transient energy storage/harvesting devices and structural supercapacitor and ultra-battery composites for use in load-bearing applications. Overall, these approaches provide paradigm shifting fundamental insights as well as create a framework for developing such multifunctional energy storage/harvesting architectures for a multitude of applications.

1.4 Dissertation organization

This dissertation is organized as follows:

Chapter II presents the development of energy storage micro/nano architectures on a multifunctional superelastic and shapememory NiTi alloy (Nitinol). This chapter deals with the effect of micro/nano structuring on electrochemical energy storage behavior of this versatile alloy.

Chapter III utilizes the unique shapememory property of the NiTi alloy to strain engineer surface oxides grown on it. The effect of applied and ‘locked-in’ mechanical strain on the electrochemical energy storage behavior of the surface oxide is discussed in this chapter.

Chapter IV builds upon the findings of in chapter III to develop a detailed understanding of mechano-electrochemical coupling in lithium battery electrodes such as vanadium pentoxide.

The effect of ‘locked-in’ mechanical strain using NiTi alloy substrate on the electrochemical parameters of lithium intercalation reaction in vanadium pentoxide is discussed in this chapter.

Chapter V utilizes the understanding of mechano-electrochemical coupling battery materials discussed in chapter III and IV to develop electrochemical-mechanical strain energy harvesters to harvest the otherwise wasted ambient mechanical energy in everyday human interactions. Owing to the diffusion-controlled processes of sodium ion alloying reaction with high capacity 2D black phosphorus electrodes, effective harvesting of low-frequency ambient mechanical energy can be achieved.

Chapter VI builds upon the findings of the earlier chapters and utilizes a fast sodium co-intercalation reaction with multilayered graphene electrodes to achieve ambient energy harvesting during human walking scenarios.

Chapter VII presents a multifunctional energy storage system utilizing atomic layer deposited vanadium oxide coatings in porous silicon architectures for transient energy storage applications.

Chapter VIII presents an electrochemical-mechanical transient energy harvester which utilizes a lithium-aluminum system to effectively harvest ambient low-frequency mechanical energy as a potential on-demand energy source for a transient energy storage system.

Chapter IX presents a multifunctional energy storage system utilizing carbon nanotubes grown on stainless steel decorated with electrochemically deposited nickel and iron oxides/hydroxides. The developed Ni-Fe ‘ultra-battery’ composite can be potentially integrated into load-bearing architectures.

Chapter X summarizes this work and discusses future opportunities

Chapter II

2 Systematic Hierarchical Micro/Nanostructuring to Improve Faradaic Energy Storage

2.1 Introduction

With the advent of the fourth industrial revolution, smart technological systems with extensive and fast computing capabilities in decentralized stand-alone architectures are an inevitable future. A key ingredient for the successful implementation of such technologies, efficient on-board energy storage systems have emerged as a primary requirement. However, present typical energy storage systems such as most batteries have long charging/discharging times. Though, supercapacitors were once envisioned to fulfil this need, their low energy density has often been a drawback. To keep pace with the envisioned scenario, high energy as well as high speed charge/discharge is of categorical importance. Therefore, faradaic energy storage systems capable of storing more energy than traditional supercapacitors, must be developed with these capabilities operating at significantly higher rates (100 to 1000 times faster) than conventional battery electrodes.[21-27] Despite a significant body of literature on these systems, some key fundamental challenges remain and warrants more investigation. For example; in the well explored area of pseudocapacitors (surface faradaic energy storage) as well as the recently developed MXene[28-30] based systems, the challenge of improving the inherently low ionic/electronic conductivities of the constituent materials is still present. Oxides/hydroxides of nickel and titanium, in particular hydroxides of nickel (high theoretical capacitance of about 2000 F/g)[22, 31] are considered promising in the field of high rate faradaic energy storage. In any case, the challenge still remains owing to the fact that nickel hydroxide ($Ni(OH)_2$ is inherently

resistive. Most strategies to overcome these challenges involve addition of carbon based additives and conductive binders during electrode fabrication.[22, 24, 32-37] In the contrary, direct binder free simple fabrication techniques are considered as a viable alternative to not only mitigate the performance challenges associated with these inherently resistive materials but also to improve the feasibility in direct manufacturing of these high rate energy storage devices. In this regard, nitinol (Niti Alloy) is widely considered a potential candidate for multifunctional energy storage[38-42] applications offering a versatile platform owing to its shape memory and superelastic properties along with its bio-compatibility.[43-46] The elements (Nickel and Titanium) that make up the composition of this alloy can be converted to their respective oxides/hydroxides by surface treatments.

In the case of NiTi alloys, the direct fabrication techniques to generate the nickel oxides/hydroxides involve dealloying,[47-49] anodizing,[50-55] oxidizing[25, 56] and annealing processes.[25, 55] However, the performance attributes of $Ni(OH)_2$ pseudocapacitor developed through these techniques which include rate capability, high charge storage and good cycling are still limited. A strategy to address the challenges posed by $Ni(OH)_2$ is by systematically tailoring the NiTi alloy surface using simple surface treatment techniques to develop hierarchical micro/nanostructures. Hierarchical nanostructures with well-organized distribution of redox active metal hydroxides enable faster electron conduction and ion transport minimizing the internal resistance of traditional $Ni(OH)_2$ pseudocapacitors.[25, 57, 58] Fabrication of hierarchical micro/nanosturctures on superelastic NiTi alloy has so far been limited due to the processing challenges involved.[46, 47, 52] Techniques such as dealloying, anodization and oxidation of NiTi surface pose unique challenges as both nickel and titanium are non-valve metals. A systematic

approach to selectively combine one or more of these surface treatment techniques to improve energy storage capability at high rates of charge and discharge is required.

In this work, we propose a systematic approach to implement structural hierarchy to $Ni(OH)_2$ pseudocapacitor developed to the surface of NiTi alloy by selective combination of dealloying, anodizing and oxidation techniques. We developed hierarchical micro/nanostructures comprising of electrochemically active $Ni(OH)_2$ on the surface of superelastic NiTi alloys. The ability to control and engineer the pseudocapacitive response of $Ni(OH)_2$ by altering the surface of NiTi alloy is demonstrated in this study. Hierarchical micro/nanostructures with nanopores on two different length scales provide electron and ion conduction pathways significantly increasing the charge storage and rate capabilities. This work provides a binder free method for controlled fabrication of hierarchical micro/nanostructures and selectively modulating the pseudocapacitive response of nickel hydroxide developed on the surface of NiTi alloy.

2.2 Experimental section

2.2.1 Preparation of Nanoporous NiTi surface

As drawn, mechanically polished NiTi superelastic alloy (oxide free, thickness ~1.34 mm) obtained from Nitinol Devices and Components, Inc was cut into squares of dimensions ~ 1 cm X 1 cm. The cut sheets were ultrasonically cleaned in acetone (Fischer), ethanol (Fischer) and nanopure water for 10 min respectively. To create Nanoporous surface structures on the alloy, sheets were subjected to ultrasonic treatment in H_2O_2 (Aldrich 30%) for 90 min at room temperature.

2.2.2 Imparting first level of hierarchy to the NiTi surface

To impart the first level of hierarchy to the NiTi surface, the ultrasonically cleaned cut sheets were subjected to dealloying proess by soaking in 20 mL concentrated HCl (Fischer 37%) for

varying time periods (1hr to 24 hr). Following the dealloying treatment, the NiTi sheets were ultrasonically treated in peroxide to create the nanoporous surface structure on the surface structures imparted by the dealloying process (Hierarchical 1).

2.2.3 Imparting two levels of hierarchy to the NiTi surface

The super hierarchical micro/nanostructure (Hierarchical 2) was obtained by introducing an anodization step in-between the dealloying and peroxide ultra-sonic treatment steps. The dealloyed NiTi sheets were potentiostatically anodized at 30 V for 300 seconds using a LabView-operated Keithley 2602A Sourcemeter. Anodization was performed using a dealloyed NiTi sheet as the anode and a platinum foil (Alfa Aesar) 10mm X 10mm as the cathode in a solution of ethylene glycol (Aldrich) containing 0.25 wt% NH_4F (Aldrich) and 1.5 wt% nanopure water. The dealloyed and anodized sheets were then subjected to sonication in peroxide for 90 min to obtain the Hierarchical 2 micro/nanostructure.

2.2.4 Material Characterization

Micro/nanostructural characterization was performed using scanning electron microscopy (SEM) (Raith eLine). Surface oxide analysis was performed using Raman spectroscopy (Reinshaw) with a 532 nm laser with exposure times upto 1800 seconds, X-Ray photoelectron spectroscopy (XPS PHI 5000 Versaprobe) using Al Kα 1486.6 eV 100 μm spot size and X-Ray diffraction (Scintag XGEN 4000) using Cu Kα 1.542 A^o.

2.2.5 Electrochemical Characterization

The NiTi sheets with different levels of hierarchy, a platinum foil (1cm X 1cm, Alfa Aesar) and a saturated calomel electrode (SCE) (Koslow) were the working, the counter and the reference electrodes respectively. The electrodes were immersed in a 2M solution of NaOH (Aldrich) in a 3-electrode configuration. Electrochemical tests including cyclic voltammetry (CV),

galvanostatic charge-discharge (CD) and electrochemical impedance spectroscopy (EIS) were performed using a Metrohm Autolab multichannel testing unit. CV scans at various scan rates from 5 mV/s to 500 mV/s, CD scans with various constant currents of 0.1 mA/cm^2 to 5 mA/cm^2 and potentiostatic EIS scans of perturbation amplitude of 0.25 V in the frequency range of 0.01 Hz to 100 kHz were performed on the working electrodes.

2.3 Results and discussion

2.3.1 Schematic representation of the process

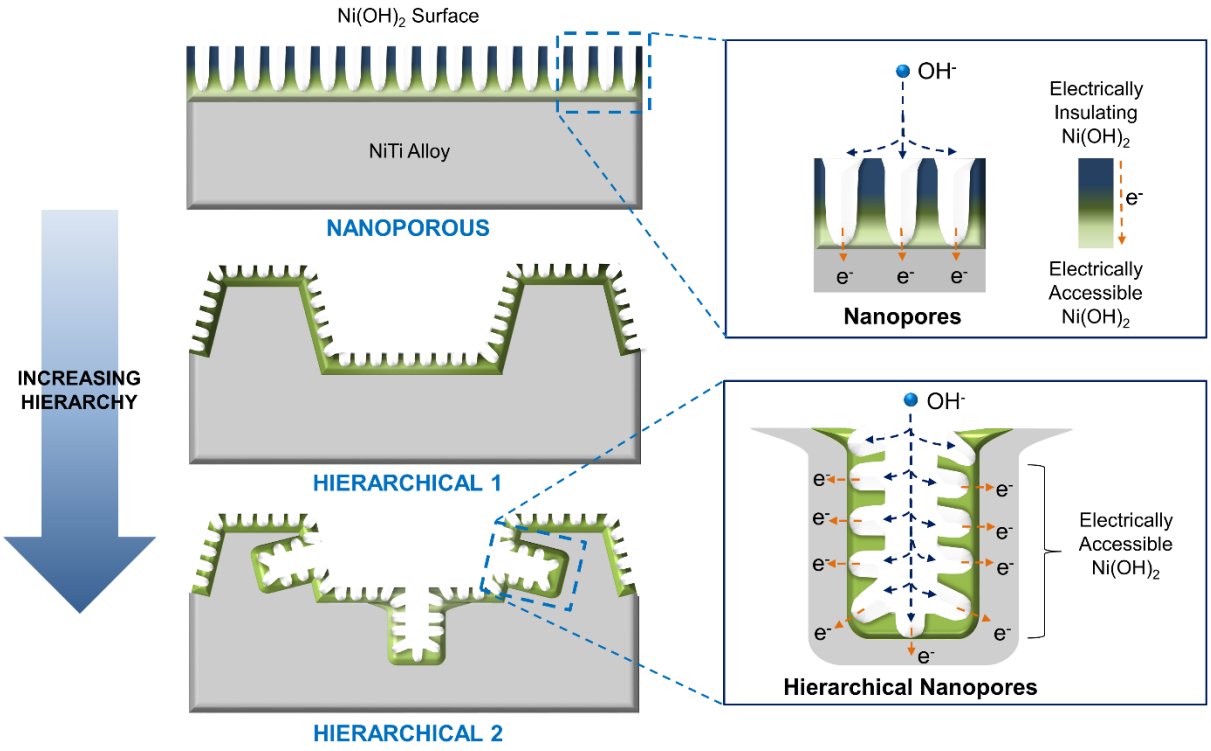

Figure 2.1. Schematic representation of the advantages of the micro/nanostructures developed in the order of increasing hierarchy

The schematic representation for the development of hierarchical structures on NiTi is shown in Figure 2.1. A nanoporous surface on NiTi alloy can be generated using simple ultrasonic treatments. Using the oxidizing nature of peroxide combined with the ultrasonic effect, we

produced a nanoporous surface architecture on the alloy (Nanoporous).[56, 59] As the superelastic NiTi alloy, was cold rolled (~20% thickness reduction) and was not subjected to subsequent aging and thermal treatments, residual stresses in the alloy are expected. Dealloying this state using strong mineral acids results in the formation of stress relief martensitic planes on the surface.[60-62] Soaking the alloy in a fixed volume of concentrated HCl (Appendix, Figure 2.6) dealloys the NiTi surface through free corrosion process. Creation of the nanoporous surface feature to the dealloyed NiTi surface is achieved through peroxide sonication. This combination generates the first level of hierarchy (Hierarchical 1) comprising of the obtained nanoporous structure superimposed on a dealloyed macrostructure. Using the principles of two-step anodization technique, a second level of hierarchy (Hierarchical 2) can be achieved by introducing an additional anodization step after the dealloying process and prior to peroxide sonication. Anodization of dealloyed NiTi results in the formation of Ni-Ti-O nanotubes on the surface of the stress-relief martensitic planes. A subsequent peroxide sonication process removes these tubes leaving behind nano patterns which through the action of peroxide can be developed into a hierarchical nanoporous surface structure with hierarchical nanopores on two different length scales.

2.3.2 Microstructural characterization

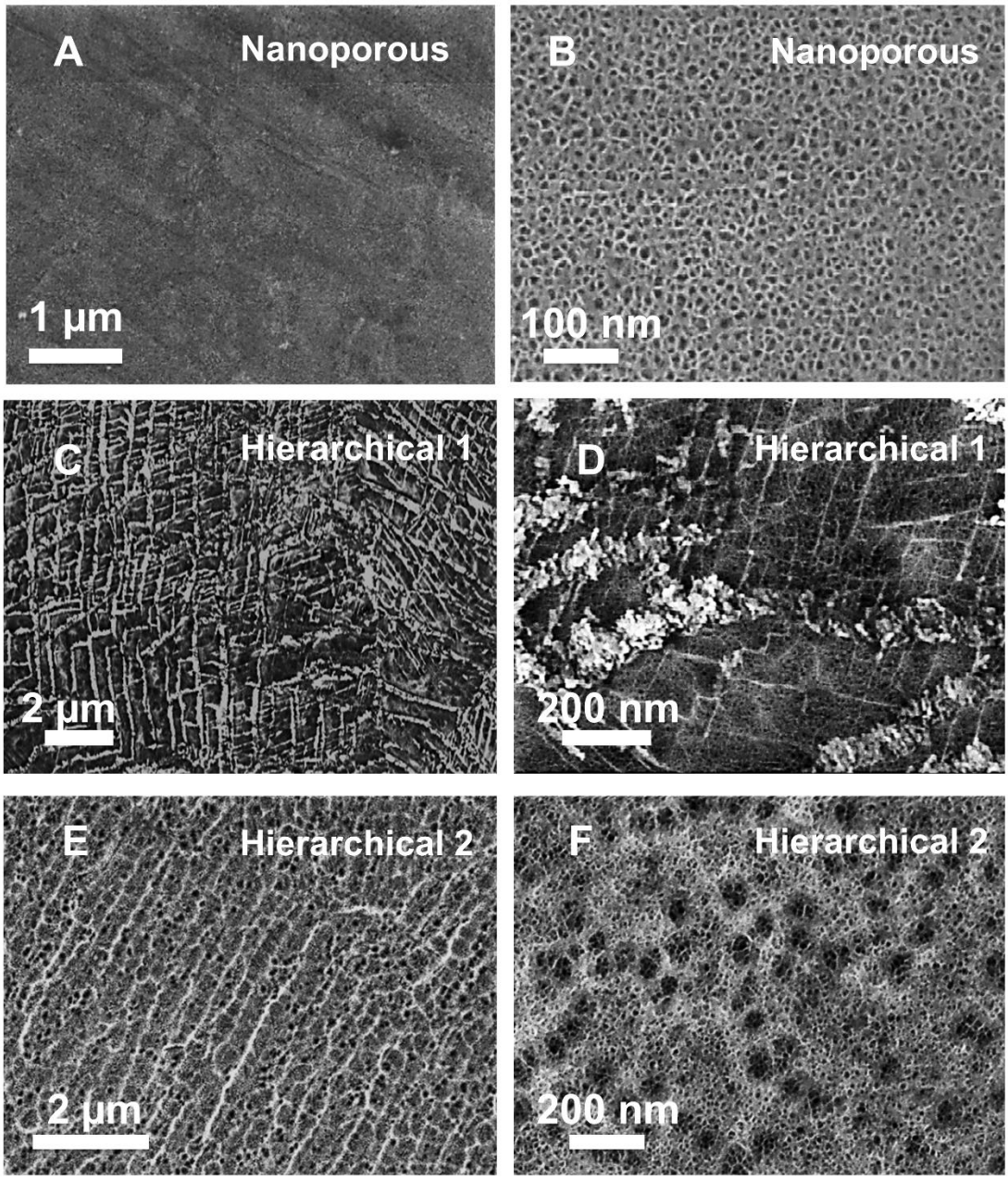

Figure 2.2. SEM micrographs of **(A)** Nanoporous alloy surface. **(B)** Nanoporous structure Nanoporous NiTi alloy. **(C)** Martensitic planes on Hierarchical 1. **(D)** Nanostructure of Hierarchical 1. **(E)** Hierarchical 2. **(F)** Hierarchical nanostructures of Hierarchical 2

To verify the presence of these micro/nanostructures on the NiTi surface, Scanning Electron Microscopy (SEM) was performed. Using image analysis techniques, the average pore diameter of the surface pores on nanoporus NiTi (Figure 2.2A and 2.2B) surface was estimated to be ~10 nm. Electron micrographs of Hierarchical 1 (Figure 2.2C and 2.2D) indicates the superimposition of nanopores (averaging ~10 nm diameter) on a dealloyed NiTi surface showing stress-relief planes. Hierarchical 2 (Figure 2.2E and 2.2F) is the result of introducing an anodization step in-between dealloying and peroxide sonication processes. We used a standard anodization process to obtain Ni-Ti-O nanotubes of average diameters of about 100 nm (Appendix, Figure 2.7. A-D).[52, 55, 56, 63, 64] To introduce smaller nanopores on the surface of the bigger nanopores, ultrasonication process using peroxide was performed on the dealloyed and anodized NiTi surface. The resulting micro/nanostructure (Hierarchical 2) comprises of a dealloyed macro structure with hierarchical nanopores.

2.3.3 Raman spectroscopy and X-ray photoelectron spectroscopy (XPS) analysis

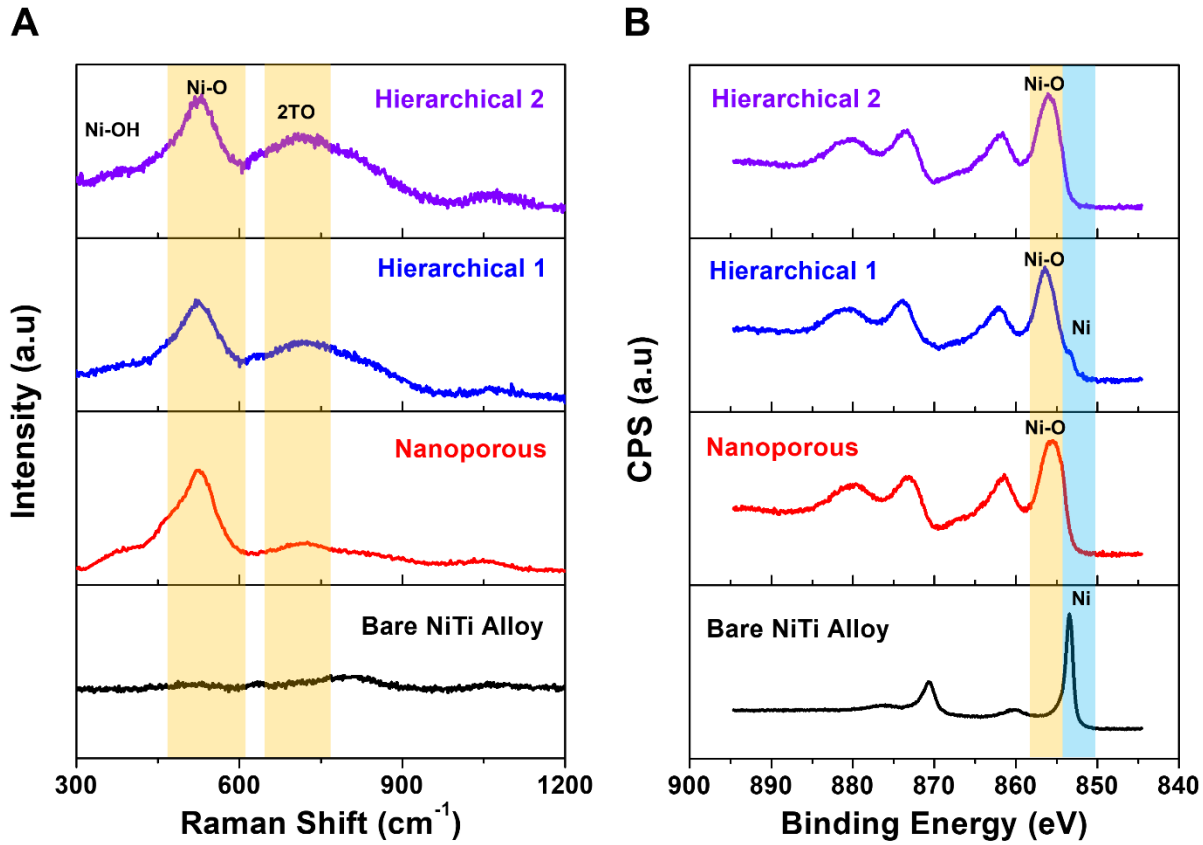

Figure 2.3. (A) Raman spectra of bare NiTi alloy, Nanoporous, Hierarchical 1 and Hierarchical 2. **(B)** XPS spectra of Ni 2p for bare NiTi, Nanoporous, Hierarchical 1 and Hierarchical 2 micro/nanostructures.

To qualitatively assess the composition, we performed Raman spectroscopy (Figure 2.3A) on the different hierarchical and nanoporous surfaces. Two broad peaks corresponding to the Ni-OH[22, 65, 66] and Ni-O[22, 65, 66] stretching modes can be observed in the spectra of all treated surfaces at around 400 cm^{-1} and 500 cm^{-1} respectively. Additional broad peaks around 700 cm^{-1} correspond to the 2 phonon 2TO stretch modes (Ni-O)[67] structure resulting from the presence of defects. As the process of dealloying results in etching of the superelastic NiTi surface leading to the formation of martensitic stress relief planes, it is essential to understand the crystallographic

features imparted in this process. X-Ray diffractograms (Appendix, Figure 2.8) indicates the presence of these stress relief martensites generated through the dealloying process.

To further examine the surface composition, we performed XPS analysis (Figure 2.3B) of these different surfaces (Appendix, Figure 2.9 for survey spectra). Analysis of the Ni $2p_{3/2}$ and Ni $2p_{1/2}$ peaks present around ~856 eV and ~873 eV confirms the presence of $Ni(OH)_2$ on the surface of the nanoporous alloy, Hierarchical 1 and Hierarchical 2. These peak positions and the separation (17.6 eV) between them correspond to the $Ni(OH)_2$ structure based on previous reports.[68-70] In the case of the Hierarchical 1 micro/nanostructure, apart from peaks corresponding to $Ni(OH)_2$, we observe the presence of Ni peak (Ni $2p_{3/2}$ and Ni $2p_{1/2}$ at 853.4 eV and 870.6 eV respectively) with a peak separation of 17.1 eV. This can be attributed to the induced martensitic relief planes on Hierarchical 1 as observed in SEM micrographs (Figure 2.2C and 2.2D). Presence of metallic Ni peaks in Hierarchical 1 when compared to nanoporous and Hierarchical 2 micro/nanostructures can be due the fact that multiple surface features on the Hierarchical 1 alloy are averaged to obtain the XPS spectra where the size of the X-Ray spot around 100 µm could include some of the exposed planes. Overall, Raman and XPS spectra indicate the presence of nickel hydroxide on the surface of these processed alloys which is in accordance with previous reports.[52, 57]

2.3.4 Electrochemical characterization

To assess the benefits of hierarchy on energy storage capability of the redox active $Ni(OH)_2$, electrochemical characterization of the three micro/nanostructures was performed. Cyclic voltammograms (Figure 2.4A) indicates the differences in electrochemical response of the three micro/nanostructures.

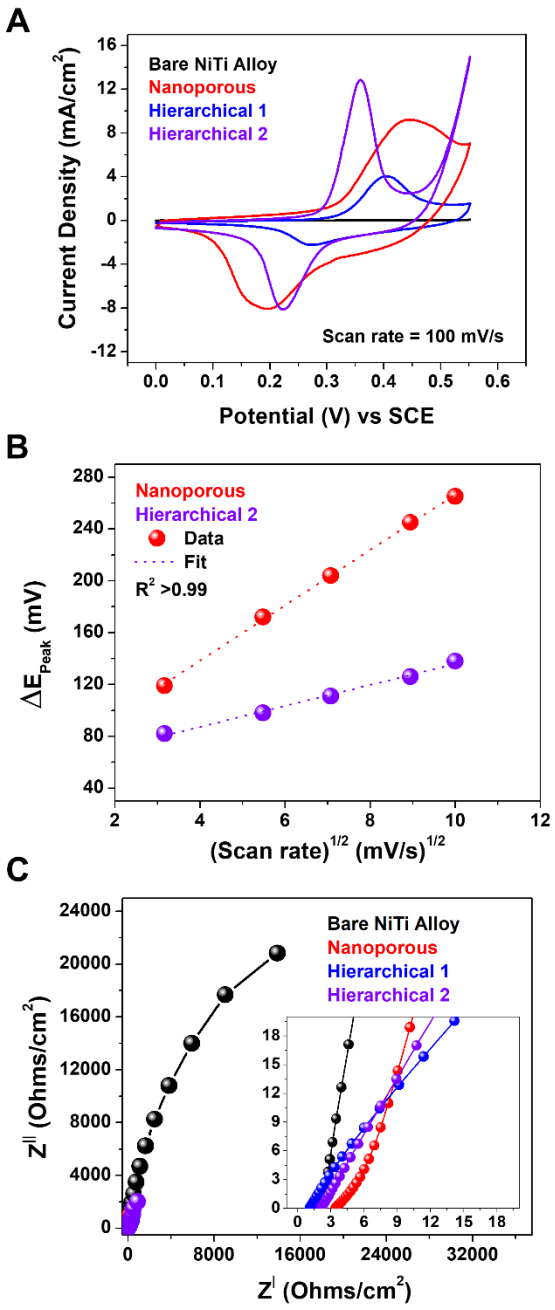

Figure 2.4. (A) Cyclic voltammetry at scan rate of 100 mV/s for Bare, Nanoporous, Hierarchical 1 and Hierarchical 2 micro/nanostructures, **(B)** ΔEPeak (anodic and cathodic peak potential difference) variation with the square root of scan rate for the nanoporous and the hierarchical 2 micro/nanostructures **(C)** EIS-Nyquist plots for Bare, Nanoporous, Hierarchical 1 and Hierarchical 2 micro/nanostructures and inset showing the ESR variation

The electrochemically active $Ni(OH)_2$ undergoes the following quasi-reversible redox reaction.[22, 71, 72]

$$Ni(OH)_2 + OH^- \leftrightarrow NiOOH + H_2O + e^- \qquad 1$$

Structural effects and their contribution to electrochemical redox energy storage reactions of $Ni(OH)_2$ are apparent through the voltammograms. The peak split (Figure 2.4B) between the anodic (reduction) and cathodic (oxidation) reactions ($\Delta E_{peak} = E_{cathodic} - E_{anodic}$) at various scan rates (Appendix, Figure 2.10 A-B) gives a good indication of the internal resistance of these different electrodes. Redox peaks of the nanoporous alloy has anodic and cathodic peak potentials at 0.2 V and 0.45 V respectively with a peak split of 250 mV at a scan rate of 100 mV/s. Compared to the nanoporous alloy, we observed a significantly lower peak split (ΔE_{peak} ~ 130 mV) for the Hierarchical 1 and Hierarchical 2 micro/nanostructures. This reduction in peak split corresponds to a lower overpotential for these redox reactions to occur resulting from lowering of the internal resistance of $Ni(OH)_2$. A lower overpotential signifies enhanced reversibility of the quasi reversible redox electrochemical reaction of $Ni(OH)_2$. The CV curve of Hierarchical 2 indicates an increased charge storage when compared to the nanoporous and Hierarchical 1. Superfast electron and ion conduction pathways offered by the hierarchical micro/nano structures to the surface $Ni(OH)_2$ results in an increased accessibility of redox active sites thus improving charge storage.

Determination of specific capacitance would give an assessment of the charge storage capability of these different micro/nanostructures owing to the faradaic $Ni(OH)_2$ reactions. Specific capacitance (mF/cm^2), normalized to the total immersed area of the electrode in the

electrolyte, was calculated from the area under the cathodic branch of the CV curve using the following equation,

$$C = \frac{1}{Av(V_2 - V_1)} \int_{V_1}^{V_2} I(V)dV \qquad 2$$

where A is the total immersed area of the electrode (cm^2), V_2 and V_1 represent the voltage window (V), ν is the scan rate (mV/s) and I is the anodic current (mA). At a scan rate of 5 mV/s, the specific capacitance of nanoporous, Hierarchical 1 and Hierarchical 2 micro/nanostructures were about 35 mF/cm^2, 11 mF/cm^2 and 45 mF/cm^2 respectively. Although the nanoporous state had good specific capacitance, a greater internal electrode resistance (ΔE_{peak} ~ 250 mV) when compared to Hierarchical 1 and 2 limits the performance of the nanoporous electrode at higher rates which is an essential feature of a pseudocapacitor. The low specific capacitance of Hierarchical 1 when compared to Hierarchical 2 could result from less active $Ni(OH)_2$ on the electrode surface.

To further examine the differences in internal resistances of the electrodes offered by the three micro/nanostructures, potentiostatic EIS measurements were performed. A simple Randle's circuit (Appendix, 2.10 C) can be used to determine the equivalent series resistance (ESR). As these measurements were performed in a 3-electrode setup, the ESR corresponds well to the internal resistance of the working electrode. EIS-Nyquist plot (Figure 2.4C and inset) indicate a relatively greater equivalent series resistance (ESR) of about 3.5 $Ohms/cm^2$ for the nanoporous state when compared to Hierarchical 2 (ESR of 2.1 $Ohms/cm^2$). The hierarchal 2 micro/nano structure has lower resistance than the nanoporous structure as well as increased charge storage due to the presence of superfast electron conduction pathways offered by the surface hierarchy. The increase in ESR of Hierarchical 2 when compared to Hierarchical 1 can be attributed to the

result of increased active material on the surface of the alloy. As the resistive nature of electrochemically active $Ni(OH)_2$ is a limiting factor in the development of high rate pseudocapacitors, minimizing internal resistance is essential. However, a tradeoff between active material loading and organization of active material on the surface of a current collector is essential to simultaneously increase energy storage capability as well as rate capability.

2.3.5 Performance assessment of NiTi alloy with developed hierarchical micro/nanostructure

Based on the CV curves and EIS analysis, Hierarchical 2 micro/nanostructure Hierarchical 2 showed increased reversibility (low internal resistance) and increased charge storage capability due to the enhanced utilization of the active $Ni(OH)_2$ on the surface. To further examine the performance of Hierarchical 2 micro/nanostructure, we performed CV scans at various scan rates from 5 mV/s to 500 mV/s (Figure 2.5A). The shape and symmetric nature of the CV curves show no appreciable change even at higher scan rates indicating improved mass transport and good electron conduction provided by the hierarchical structure. The peak split of about 0.25 V at a scan rate of 500 mV/s is still indicative of low internal resistance of the Hierarchical 2 structure and extremely fast kinetics of the $Ni(OH)_2$ redox reaction. Hierarchical 2 surface with nanopores of two different length scales enhances active material-electrolyte contact and shortening the OH^- ion diffusion paths.[32, 48, 57, 73-75]

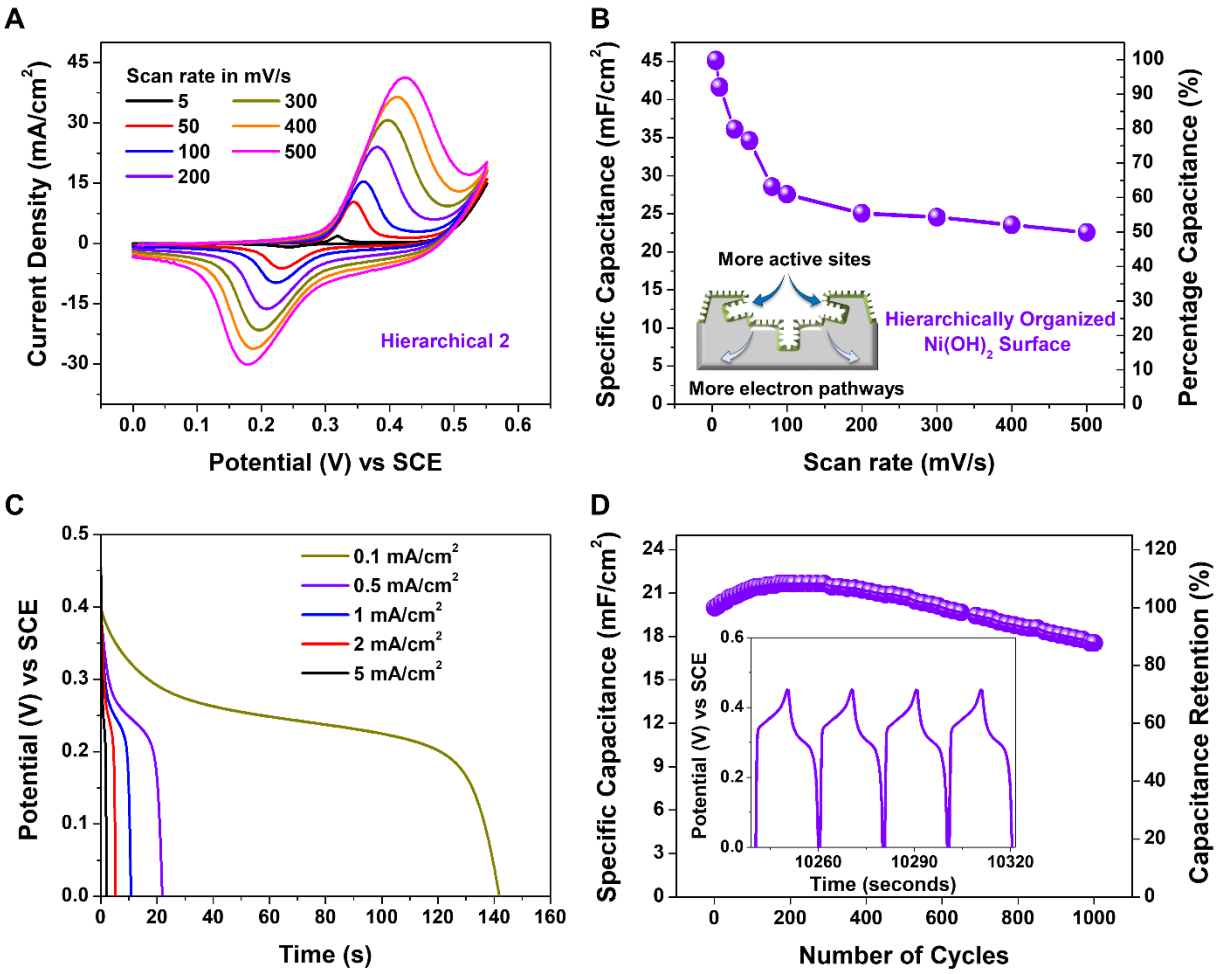

Figure 2.5. (A) Cyclic voltammograms of Hierarchical 2 micro/nanostructure at various scan rates. **(B)** Capacitance variation with scan rate and percentage capacitance at each scan rate tested for Hierarchical 2 micro/nanostructure. **(C)** Galvanostatic charge discharge curves at various current densities for Hierarchical 2 micro/nanostructure. **(D)** Cycling performance and capacitance retention for 1000 cycles of galvanostatic charge discharge at 1 mA/cm^2 for Hierarchical 2 micro/nanostructure, inset- galvanostatic charge discharge of a few cycles during cycling performance test.

We assessed the rate capability of the Hierarchical 2 electrode was by determining the specific capacitance at the different scan rates from the voltammograms (Figure 2.5A). Figure

2.5B shows the variation of specific capacitance with scan rates from 5 mV/s to 500 mV/s. The Hierarchical 2 structure has high rate capability maintaining about 50% (23 mF/cm^2) capacitance at 500 mV/s compared to 45 mF/cm^2 at 5 mV/s. The greater number of accessible active sites and the hierarchical micro/nanostructure enables the electrode to have good ionic as well as electronic transport properties thus improving rate capability.[55] At a scan rate of 500 mV/s, specific capacitance of Hierarchical 2 was about 10 times higher than anodized NiO/TiO_2 nanotube arrays[52, 55] and significantly higher than the capacitance from other similar reports on NiTi alloy based pseudocapacitors.[47] For comparison an anodized NiTi alloy developed similar to previous reports[52, 55, 76-80] was compared to that of Hierarchical 2 (Appendix, Figure 2.11) which showed that the Hierarchical 2 micro/nanostructure has significantly better charge storage capability. Further examination of the rate capability was performed through galvanostatic charge discharge (CD) tests on Hierarchical 2. Discharge curves of the Hierarchical 2 micro/nanostructure (Figure 2.5C) at various current densities ranging from 0.1 mA/cm^2 to 5 mA/cm^2 indicate a nonlinear discharge curve representative of pseudocapacitive behavior. Specific capacitance (mF/cm^2) was also determined from the discharge curves using the equation,

$$C = \frac{Idt}{A(V_2 - V_1)} \qquad 3$$

where, V_2 and V_1 represent the voltage window (V), I is the constant discharge current (mA), dt is the discharge time (seconds) and A is the total immersed area of the electrode in the electrolyte. Hierarchical 2 maintains about 60% capacitance (22 mF/cm^2) at a current density of 5 mA/cm^2 similar to that observed in CV analysis (Appendix, Figure 2.12). To determine cycling stability, the Hierarchical 2 electrode was subjected to a 1000 charge/discharge cycles at 0.5

mA/cm^2. Figure 2.5D shows a capacitance increase from the initial value to about 108% and gradually declines to about 90%. A minimal capacitance reduction of about 10% is observed after 1000 CD cycles. A major issue in hindering cycling performance of $Ni(OH)_2$ is expansion and contraction of the active surface during the redox process which may cause dislodging of the active material from surface.[22] Structural hierarchy in micro/nanoscale mitigates the dislodging of active material from the surface during charging and discharging resulting in good capacitance retention for Hierarchical 2 micro/nanostructures. Overall, the hierarchical architecture developed on NiTi alloy offers enhanced faradaic energy storage capability with a high specific capacitance of 45 mF/cm^2 (scan rate of 5 mV/s) and enhanced rate capability. The ability to improve and modulate electrochemical redox energy storage parameters through the systematic tailoring of micro/nanostructures of high rate energy storage materials using combinations of simple solution techniques offers significant value for developing next generation energy storage devices.

2.4 Conclusion

We report here, the ability to modulate redox electrochemistry of $Ni(OH)_2$ through systematic tailoring of structural hierarchy. Higher rate capability, lower internal resistance and high specific capacitance of $Ni(OH)_2$ observed as a function of different levels of hierarchy imparted on the NiTi surface gives insight to the relationship between micro/nanostructures and electrochemistry. Electrodes with hierarchically tailored surface delivered high specific capacitance of 45 mF/cm^2 maintaining about 50% of this capacitance at 100 times higher scan rates. Reduction in internal resistance of the electrodes with hierarchical micro/nanostructures was observed leading to high rate capability with low overpotential of 130 mV at fast scan rates of 100 mV/s. We also observed a good cycling behavior retaining ~90% of the capacitance after

1000 charge discharge cycles. Our work broadly illustrates the feasibility and advantages of developing hierarchical micro/nano structures for optimizing electrochemical parameters of high rate faradaic energy storage systems.

Acknowledgements

We thank Landon Oakes, Anna Douglas, Keith Share, Mengya Li and Thomas Metke for useful discussions regarding the results of this work. We also thank Dr. Rizia Bardhan for the generous use of Raman microscope and lab facilities provided to us. We also thank VINSE for their support in performing the necessary material characterizations.

2.5 Appendix

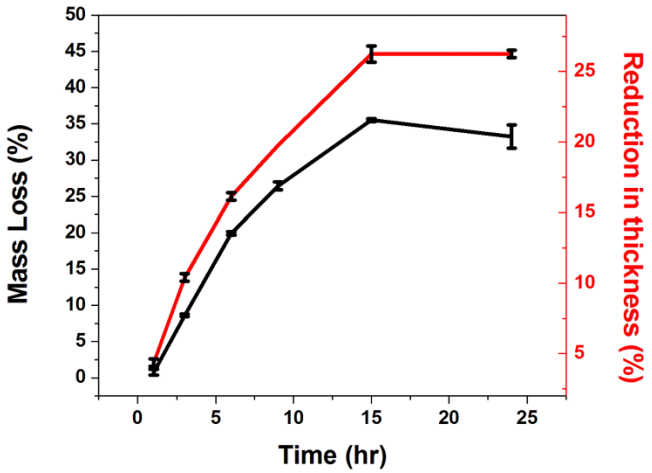

Figure 2.6. Mass loss and reduction in thickness of the NiTi alloy after different soaking periods in concentrated HCl (37%)

As both Nickel and Titanium are non-valve metals, we used a concentrated mineral acid to dealloy NiTi alloy. Both Nickel and Titanium are converted to their respective chlorides through the corrosive attack of the acid. All samples were pre-cleaned as per mentioned procedures and were soaked in HCl at room temperature. Error bars represent variations between 10 samples subjected to the dealloying process. Samples soaked for 24 hours were chosen for further

processing as the curves representing mass loss and thickness reduction show that the concentration gradient required for dealloying process has gradually reduced and almost absent for 24-hour soaking. After dealloying the samples were once again cleaned by sonicating in DI water and dried in a stream of compressed air.

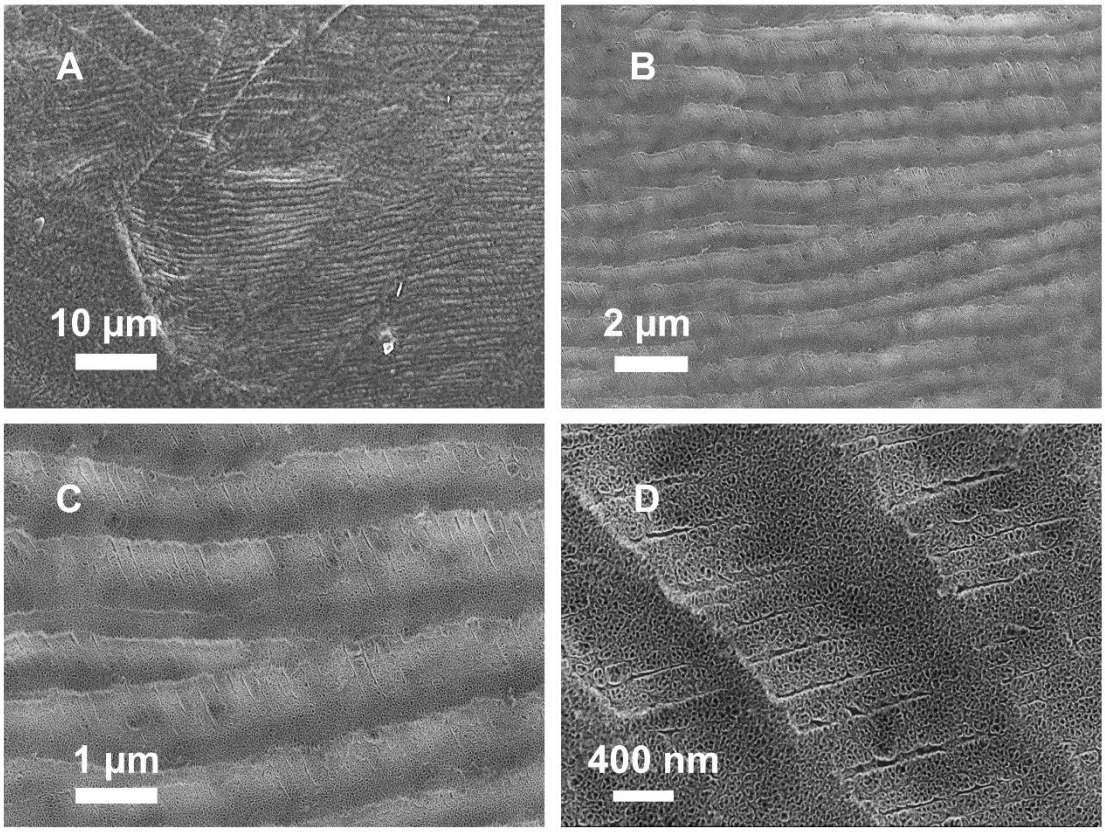

Figure 2.7. (A-D) SEM micrographs of nickel titanium oxide nanotubes after anodization process at various magnifications.

Anodization of a dealloyed NiTi surface results in the formation of Ni-Ti-O nanotubes on the surface of the stress released martensitic planes. These SEM micrographs show the presence of nickel titanium nanotubes similar to previous reports but on martensitic planes of the dealloyed NiTi samples. These nanotubes unlike the nanoporous structure which is obtained as a result of sonicating the alloy in peroxide, appear to be uniformly distributed on the surface of the

martensitic planes. Subsequent peroxide sonication of these nickel titanium nanotubes should generate nanopores on these structures.

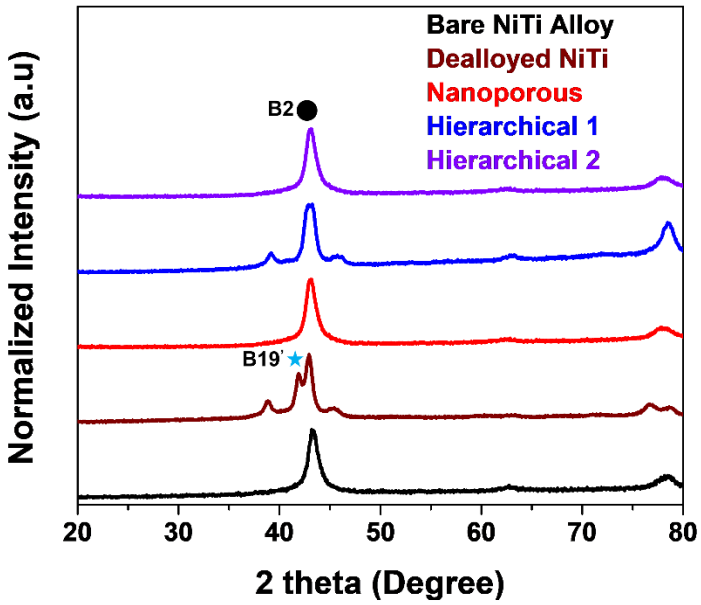

Figure 2.8. X-Ray diffractograms of the bare, nanoporous, Hierarchical 1 and Hierarchical 2 states of the surface treated alloy.

Crystallographic examination of the martensitic relief planes generated during dealloying was performed using X-Ray diffractograms is given in the supporting information. The diffractograms confirm the presence of B19' martensitic phase in dealloyed cold rolled NiTi alloy. The strongest peaks around 43° in all the diffractograms correspond to the (110) plane of the austenitic B2 NiTi phase. The two additional peaks at 62° and 78° are from the (200) and (211) planes of the B2 phase (JCPDS no. 18-0899). Diffractogram of dealloyed NiTi alloy confirms the existence of B19' martensitic phase observed in the SEM micrographs. Peaks at around 39° and 42° are from the B19' phase. According to previous reports which employ similar processing techniques on nickel and its alloys, report the presence of oxides and hydroxides on the surface of the alloys. XRD however, does not give sufficient information regarding surface

oxides if the oxide layer is very thin or if the intensity of the major peaks of NiTi alloy is very high when compared to the strongest peaks from $NiO/Ni(OH)_2$.

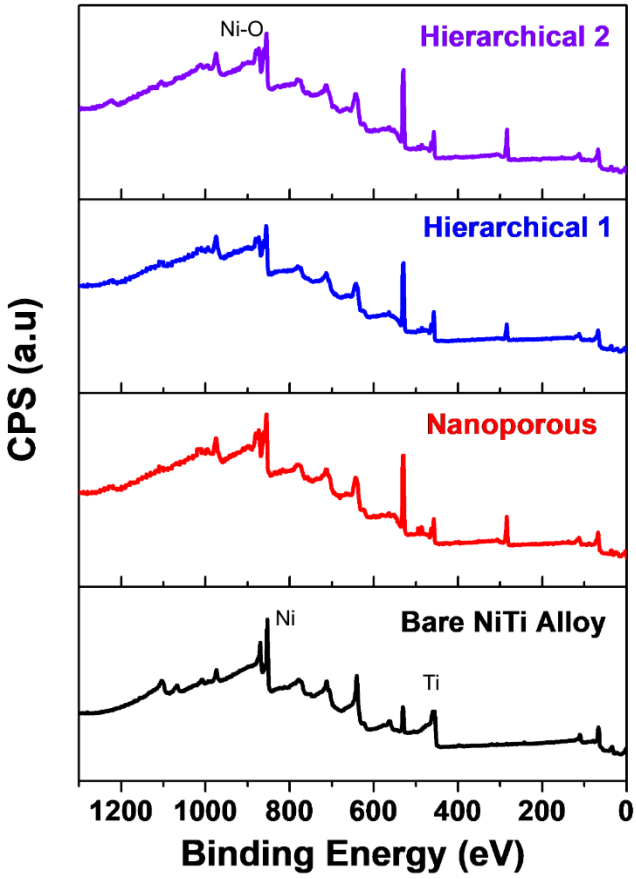

Figure 2.9. X-Ray photoelectron survey spectra of the bare, nanoporous, Hierarchical 1 and Hierarchical 2 states of the surface treated alloy.

The survey spectra were normalized to the peak positions of carbon as a reference. The spectra indicate the presence of nickel and titanium along with their respective oxides.

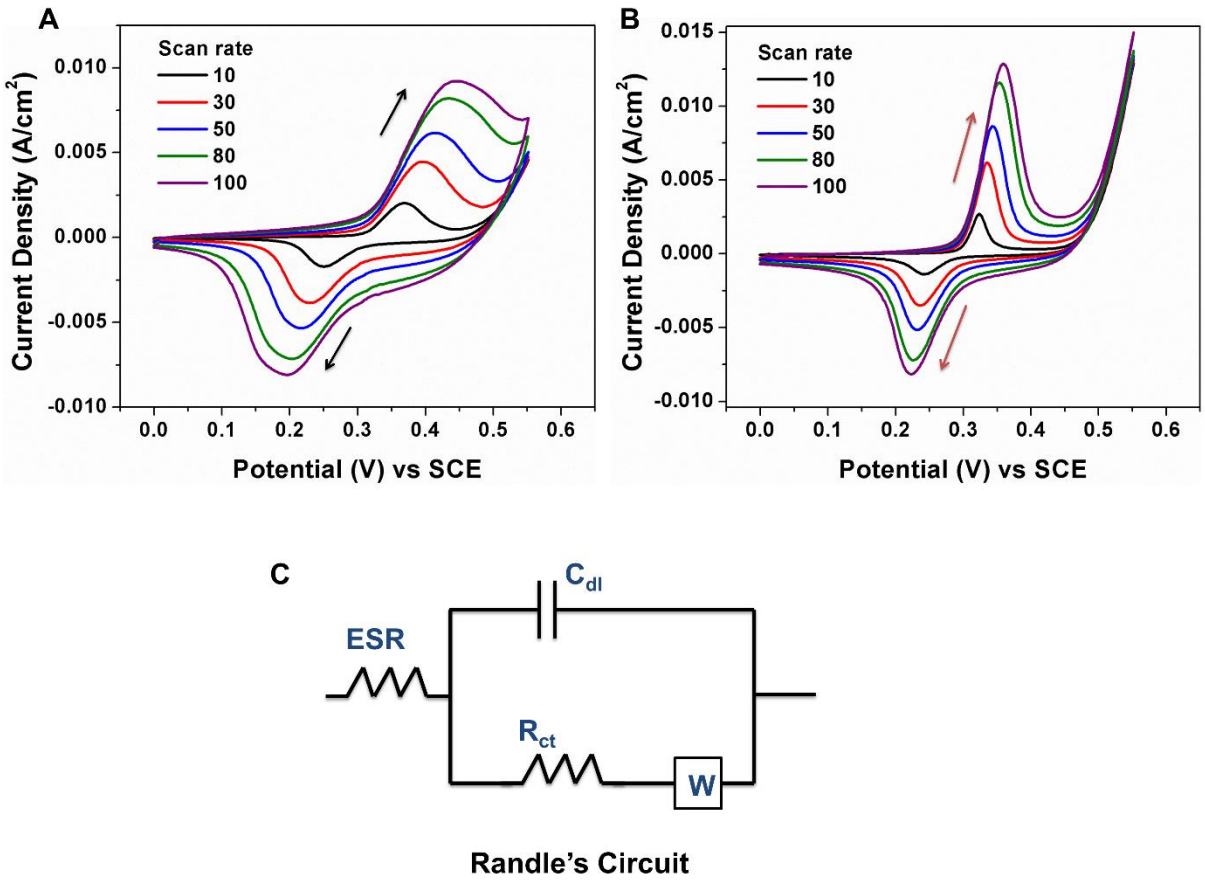

Figure 2.10. (A) Cyclic voltammograms of the nanoporous alloy at scan rates of (10-100 mV/s). **(B)** Cyclic voltammorgams of the Hierarchical 2 micro/nanostructure at scan rates of (10-100 mV/s). **(D)** Randle's circuit model for the EIS Nyquist plots.

As the measurements were performed in a three-electrode system, the potential measurements were accurately measured with the use of a reference electrode. To illustrate the difference between Nanoporous (Figure 2.10 A) and Hierarchical surfaces (Figure 2.10 B), cyclic voltammograms at different scan rates from 10-100 mV/s were obtained for both the Nanoporous and Hierarchical 2 micro/nano structures. The internal resistance of the electrode is a parameter coupled into the equivalent series resistance of measured during EIS measurements. A simple Randle's circuit (Figure 2.10 C) can be considered to explain the EIS Nyquist spectra observed. The ESR values of the Hierarchical 1 and Hierarchical 2 are 0.9 and 2.1 Ohms/cm^2 respectively.

This difference can be accounted for the fact that an additional treatment in the form of anodization was performed to develop the Hierarchical 2 micro/nanostructure. This results in increased active material on the surface of the electrode resulting in increased charge storage at the same time low over potential corresponding to decreased internal electrode resistance. The ESR values for the Bare and Nanoporous alloy were 2 and 3.5 Ohms/cm^2 respectively.

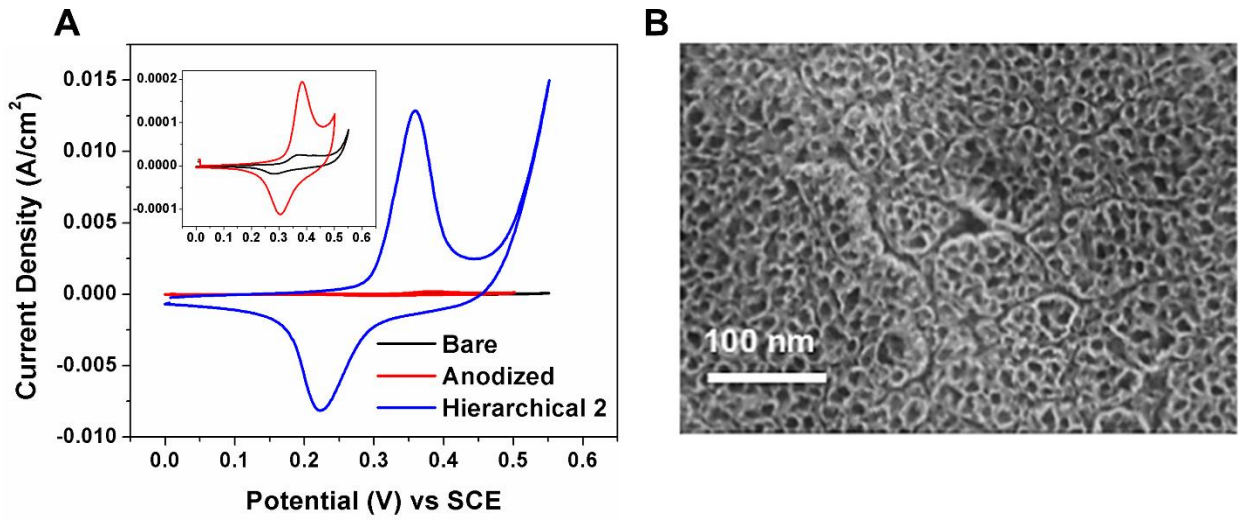

Figure 2.11. (A) CV curves comparing the electrochemical response of bare, anodized and Hierarchical 2 structures, inset- Comparison between anodized and bare NiTi alloy. **(B)** Nickel titanium oxide nanotubes on the surface of NiTi alloy.

From the voltammograms, even though the anodized alloy has good charge storage as indicated the area under the CV curve, the Hierarchical 2 micro/nanostructure has a better performance.

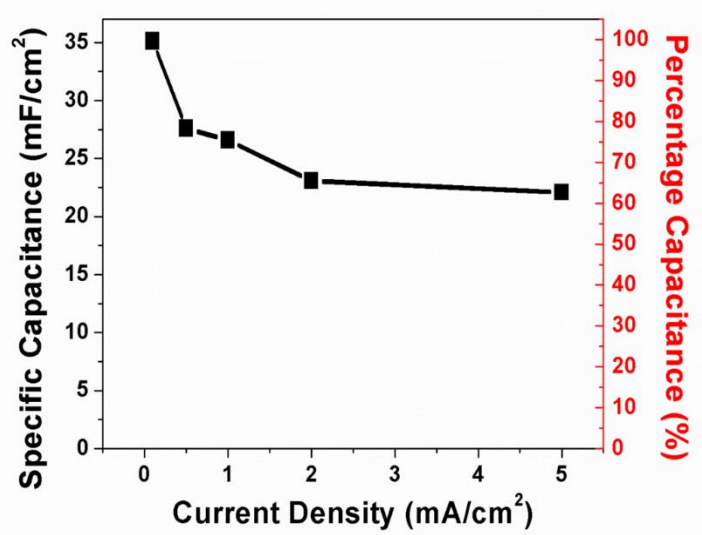

Figure 2.12. Specific capacitance and percentage capacitance determined from galvanostatic charge/discharge tests at various current densities.

The current densities are normalized to total immersed area of the electrode. Hierarchical 2 micro/nanostructure has about 60% capacitance maintenance at 5 mA/cm^2 when compared to the capacitance at 0.1 mA/cm^2.

Chapter III

3 Strain Engineering to Modify the Electrochemistry of Energy Storage Electrodes

3.1 Introduction

Traditional routes to design materials for electrochemical applications require modification of material chemical composition to control reduction-oxidation energetics when coupled with an electrolyte.[81, 82] This causes the search for improved nanomaterials in electrochemical applications to be driven by discovery-focused nanomaterial synthesis and fabrication. Due to the complex cooperative nature of energy storage device performance based on the pairing of electrodes and electrolytes, such routes rarely lead to new materials with characteristics, such as operating voltage, that outperform existing materials. Further, whereas computational guidance has brought about a new paradigm to predict targeted material compounds that can improve advanced energy storage systems,[83, 84] experimentalists often remain challenged by the synthesis process of such compounds, many of which are not naturally occurring. This presents a fundamental bottleneck in the conventional approach in which electrochemistry-oriented material research and development occurs that limits the rate of industry innovation in energy storage (and conversion) systems.

Strain engineering, a concept widely implemented in semiconductor electronics,[85, 86] opens new opportunities to engineer materials for electrochemical systems. The six-dimensional parameter space of the strain tensor[87] enables a nanostructure with a fixed chemical composition to have electronic and physical properties finely modulated in a manner that is virtually

impossible to replicate by varying chemical composition. Unlike bulk materials, many nanostructures exhibit sizes where strain can homogenously propagate throughout the whole material, instead of only on a surface or an interface.[86, 88-94] In this spirit, recent efforts have demonstrated the capability of strain in nanostructures to modify the energy landscape of catalytic and electro-catalytic surface-bound reactions[95-99] and modify oxygen diffusion in fuel cell technology.[100-102] The direct controlled correlation between mechanical strain as an input parameter and electrochemical processes in nanostructures for energy harvesting applications has only very recently been reported.[103]

In the specific case of energy storage electrodes such as pseudocapacitors and batteries,[81, 104] Faradaic reactions especially in metal oxides induce a change to the oxidation state of the active material often regulated by the physical characteristics of the lattice structure to enable insertion or alloying of an ion species. Focus of current research so far has been on the adverse effects of strain arising from the changes to the host lattice structures during electrochemical cycling of energy storage electrodes.[105-107] In this regard, mechanical strain imposed onto a nanostructure leading to both physical and electronic changes that can synergistically influence energy storage redox reactions has not yet been reported despite significant advances in the ability to produce, image, and understand strain effects in materials,[95, 108] especially those related to semiconductor electronics. Moreover, at present pre-straining the lattice of metal oxides using elastic strain engineering is being considered as a possible method to improve their energy storage capability using theoretical simulations.[109] However, so far experimental methods to develop pre-strained metal oxide architecture has remained a challenge.

Here we demonstrate a study where nanostructured metal oxide materials are synthesized directly on the surface of a superelastic/shapememory NiTi wire. Under the application of strain

applied to the NiTi and transferred to the surface-bound oxides, we observe consistent shifts in the anodic and cathodic potentials. By recovering this imposed strain, we observe consistent recovery of the electrochemical potentials, clearly demonstrating that strain is modulating the shifts in electrochemical potentials and can be a viable tool for the design of energy storage materials.

3.2 Experimental Methods

3.2.1 Aging of NiTi superelastic wire

NiTi superelastic wires (0.5 mm diameter, 55% Ni from Nitinol Devices & Components, Inc.) were repeatedly sonicated for 10 min in Acetone (Aldrich) followed by Ethanol (Aldrich) and then nanopure water (Millipore water purifier). The wires were dried in air and were subjected to aging process by heating them to about 600 ^{o}C for 1 hour under vacuum with a small controlled flow of air. This led to the formation of a ~200nm mixed oxide layer on the surface of the wires. The aging process was used to perform two functions; the activation of the superelastic/shapememory capability of the NiTi wire and to grow a thin oxide layer on the surface of the wire.

3.2.2 Strain setting the surface oxide

The NiTi superelastic wires were subjected to tensile deformation up to 10% and 15% strains at a rate of 2 mm/min using an Instron 5944 mechanical testing system. The unstrained (0%) and the tensile deformed (10% and 15%) wires were subjected to sonication treatment for 30 min in 30% peroxide solution to impart nanotexturing on the oxide surface and to electrochemically activate the surface oxide layer. The treated wires were rinsed in nanopure water followed by drying in air.

3.2.3 Differential Scanning Calorimetry

Differential Scanning Calorimetry (DSC, TA Instruments) was performed on the unstrained and strained wires to understand the strain recovery property of the alloy. The unstrained and strained wires were heated from room temperature to 100 ^{o}C in the first heating cycle followed by cooling to -100 ^{o}C in the cooling cycle and equilibrating at these respective temperatures for 5 min in aluminum pans. The subsequent heating cycle was from -100 ^{o}C to 100 ^{o}C followed by cooling. After two heating and cooling cycles the wires were equilibrated at room temperature.

3.2.4 SEM characterization and EDS analysis

Characterization of the microstructure and Energy Dispersive Spectroscopy analysis was performed using a Zeiss Merlin SEM at various magnifications using 5 KV beam voltage for imaging and 20 KV beam voltage for EDS elemental analysis.

3.2.5 TEM characterization and STEM EDS analysis

Characterization of the nanostructure of the surface oxide was performed using FEI Tecnai Osiris TEM using a 200 kV S/TEM system. STEM EDS maps were obtained on an oxide flake scrapped off from the surface of the NiTi wire to further characterize the composition of the surface oxide.

3.2.6 Raman and XRD characterization

Raman spectroscopy measurements were carried out using a Reinshaw Raman microscope using 532 nm Laser excitations. Maps comprising of 800-1000 spots across the surface of the wire was obtained with 60s exposure time at 10% laser power to yield a statistical strain distribution of the strained surface oxide layer. Mean peak shift corresponding to various Raman active modes of the surface oxide was obtained by using Lorrentzian fits on the obtained spectra. XRD

measurements were carried out using a Scintag XGEN 4000 using Cu Kα 1.542 A^{o}. To yield good X-Ray counts, 40 sec exposure times per 0.2 degree increments were maintained throughout the measurement.

3.2.7 Electrochemical Measurements

Electrochemical measurements were performed using a 3 electrode configuration in a beaker type cell with the NiTi alloy with surface oxide as the working electrode, a platinum foil (Alfa Aesar 1cm X 1cm) as the counter electrode and a Saturated Calomel Electrode (SCE) as the reference electrode. The electrolyte used was a 2M NaOH solution. Cyclic voltammograms were obtained for all the unstrained and strained states of the surface oxides at a scan rate of 100 mV/s in the voltage range of 0V to 0.5V. All the samples were cycled for a 100 cycles at 100 mV/s to get reproducible voltammograms. All electrochemical data was normalized to the immersed area of the wire electrodes.

3.2.8 Strain Recovery and Analysis

The strain recovery was performed by heating the strained wires with strained surface oxides to 60 ^{o}C in a Quartz CVD tube furnace under vacuum for 1min. Due to the recovery process the strain imposed on the wire and the oxide was recovered. The change in the wire length after the recovery process was used to estimate the strain recovery by the NiTi alloy. Raman and XRD measurements were performed on the strain recovered to study the recovered strain state of the surface oxide followed by electrochemical testing using the same conditions as the unstrained and strained wires.

3.3 Results and discussion

3.3.1 Metal-oxide nanostructures on superelastic NiTi

A Ni-Ti-O based oxide was grown on NiTi superelastic wires at 600 ^{o}C comprising of a mixed NiO-TiO_2 layer formed on top of a titanate layer on the surface of the NiTi material.[110, 111] EDS maps (Appendix) obtained from the surface of the wire indicated a mixed Ni-Ti-O based surface oxide. Scanning electron microscopy (SEM) (Figure 3.1A) was performed on the nanostructured surface oxides formed on the wire. To study strain-related modifications to energy storage processes, NiTi wires were tensile deformed to 10% and 15% strain at room temperature using an Instron mechanical testing system, with a corresponding small percentage of this input strain (less than 1%) transferred to the surface-bound oxide nanomaterial. The strained and unstrained wires with the mixed oxide layers were sonicated in peroxide at room temperature to impart nanotexturing to the oxide. This leads to a material architecture where nanostructured petals of NiO-TiO_2-based metal oxides are conformally coated on the surface of a NiTi wire in a seamless manner (Figure 3.1B). The Ni-Ti-O surface metal oxide was further examined through Transmission electron microscopy (TEM) (Appendix, Figure 3.8) indicating the crystalline nanostructure of the surface oxide. The presence of the constituent elements of the nanostructured oxide (Nickel, Titanium and Oxygen) was further verified using STEM EDS maps. This architecture is ideally suited to correlate strain as an input parameter to the NiTi to assess its effect on the surface-bound redox active Ni-Ti-O material for energy storage applications.

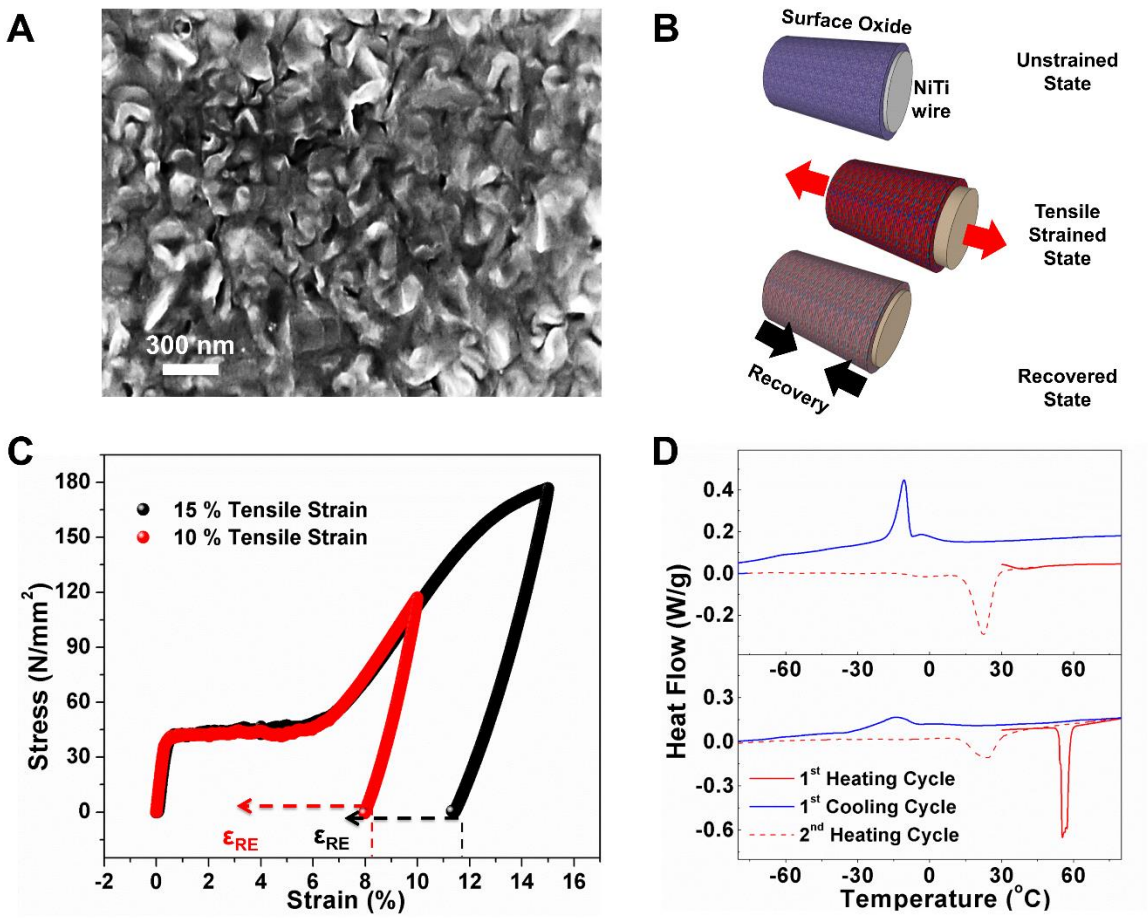

Figure 3.1. (A) SEM image of the active NiO-TiO_2 based metal oxide formed on the surface of the NiTi alloy. **(B)** Schematic illustration of experimental system, including the application of strain and strain recovery on a NiTi wire with surface-bound active material. **(C)** Stress-strain behavior of the NiTi superelastic alloy deformed up to 10% and 15% tensile strain. The dashed lines and ε_{RE} indicates the heat assisted transformation process and the recovered strain respectively. **(D)** DSC thermograms of the unstrained (0%) and the tensile strained (15%) states. Red (line and dots) represents the heating cycle and blue line represents the cooling cycles.

The stress-strain response of the alloy is shown in Figure 3.1C. The deformation behavior of the wire is described by elastic deformation of the austenite followed by the stress induced martensitic transformation below and up to 5% strain. Beyond 5% strain, oriented martensites

begin to deform leading to plastic deformation of oriented martensites above 15% strain. These stress induced martensites can be transformed back to austenite by heating strained wires beyond their austenitic finish (A_f) temperatures. The final mechanical strain input onto the NiTi alloy is ~ 8% and 11% for tensile deformations of 10% and 15% respectively, due to the intrinsic mechanical recovery of the alloy.[112] Strain recovery (10% R, 15% R) in the alloy was also measured to be ~ 3.5% and 4.5% respectively.

Differential scanning calorimetry (DSC) thermograms on 15% deformed and 0% deformed wires (Figure 3.1D) demonstrates the transformation from stress induced martensite to parent austenite during the first heating cycle is present for the 15% tensile deformed wire in the temperature range of 50 ^oC to 60 ^oC whereas the unstrained (0%) wire showed no such transformations in this temperature range. This transformation during the first heating cycle is complete at a temperature of 60 ^oC which is the austenitic finish temperature (A_f). Based on the DSC results, the 15% and 10% tensile deformed alloy was heated to 60 ^oC in vacuum to complete the reverse transformation from stress induced martensitic state to parent austenite state. The transformation temperature around 60 ^oC is ideal in the case of metal oxides to avoid annealing effects which are prevalent at higher temperatures.

3.3.2 Spectroscopic strain analysis

To characterize the transfer of strain applied to the superelastic/shapememory NiTi to the metal oxide nanostructured active material on the surface, Raman spectroscopy was carried out with 532 nm excitations. (Figure 3.2)

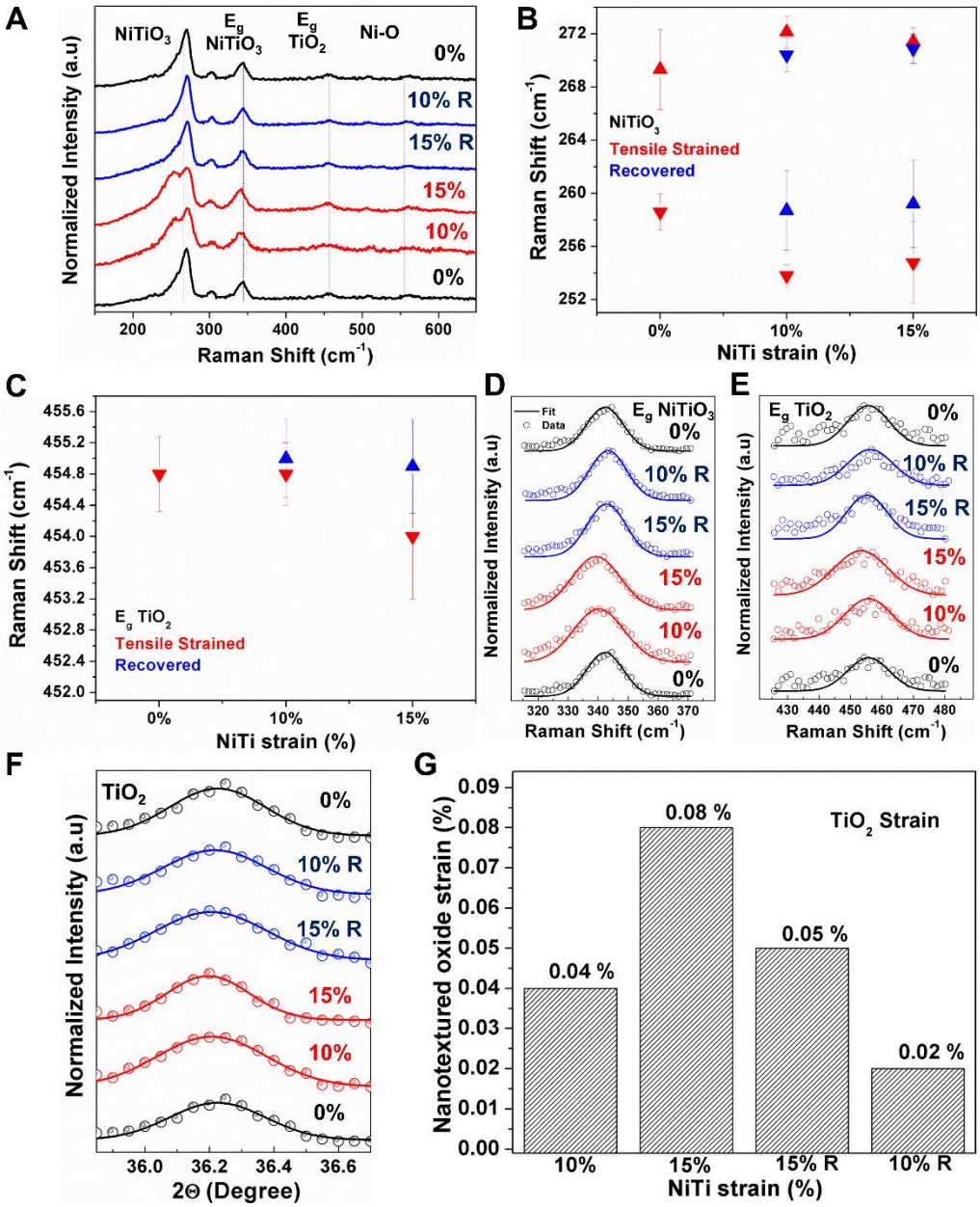

Figure 3.2. (A) Raman spectra of the strained (10% and 15%), unstrained (0%) and recovered (10% R and 15% R) states. **(B-C)** Raman maps based on 800-1000 individual scans showing average strain effect on titanate-$NiTiO_3$ **(B)** and TiO_2 **(C)** active materials. **(D-E)** Selected spectra and the fitted curves of **(D)** E_g mode of $NiTiO_3$ and **(E)** E_g mode of TiO_2 at various strained and recovered states. **(F)** Selected X-Ray diffraction spectra and Gaussian fits of the peak corresponding to (012) plane of TiO_2 (brookite) at various strained and recovered states.

(G) Percent strain corresponding to **(F)** based on both strained and recovered states. Note classifications of 10% and 15% strain correspond to strain applied to NiTi only.

The coupling of strain into a material will modify local stretch modes, hence enabling Raman spectroscopy as a sensitive tool for identifying strain in materials with distinct Raman modes. Similar to previous reports on heat treated NiTi alloys[113] we find the Raman spectra of the nanostructured surface oxide to exhibit a strong peak near 269 cm^{-1} attributed to the titanate mode which are the Raman active modes of $NiTiO_3$,[114-117] peaks centered on 300 cm^{-1} and 342 cm^{-1} attributed to the E_g modes of $NiTiO_3$,[118-121] and a peak near 454 cm^{-1} attributed to the E_g mode of rutile phase TiO_2.[122, 123] Whereas shifts and mode-splitting can be observed in these peaks as a function of applied strain, statistical Raman maps over large areas of the surface (800-1000 total Raman scans in each map) were performed to quantify strain-related shifts observed in the active materials, specifically for the modes identified in Fig. 3.2A. Lorentzian fits were applied to these Raman modes (Figures 3.2B, 3.2C) and statistically validated strain effects can be isolated. Importantly, upon strain recovery, these Raman modes revert back near or toward the unstrained peak positions, indicating the correlation between the measured Raman response and strain applied on the petaled nanostructured oxide surface. Furthermore, the E_g mode of $NiTiO_3$ (Figure 3.2D) and TiO_2 (Figure 3.2E) are observed to exhibit similar recoverable shifts in the Raman modes that can be correlated with strain and straightforwardly identified. The low intensities of the observed Ni-O stretch modes[67, 124, 125] near 508 cm^{-1} and 571 cm^{-1} prohibited quantitative analysis on these modes.

Despite the clear signature of strain deduced through Raman spectroscopy, X-ray diffraction (XRD) provides further quantitative insight. XRD measurements indicate the same trend as Raman spectroscopy, where shifts toward lower angles are observed upon strain

application, with recovery leading to the opposite shift. This is specifically shown for the (012) plane of TiO_2 (Brookite) in Figures 3.2F and 3.2G. Using a standard analytical procedure to correlate strain to the *d*-spacing of the strained and unstrained states (Appendix), the application of 10% and 15% strain to the NiTi alloy is observed to transfer ~ 0.04% and ~ 0.08% strain to the surface oxide, which can also be recovered as described in Figure 2.1C. Full XRD analysis of the material is discussed in the supporting information. Strain transfer using NiTi superelastic/shapememory alloys have so far been limited to metals[97] and alloys deposited on the surface with a maximum strain transfer of 2.18% achieved for an Fe-Pt metal alloy.[126, 127] The surface oxide on the NiTi alloy, being a brittle ceramic is not as ductile as metals and metal alloys, therefore experiences cracking in less than 1% strain applied to it.[128] Overall, strain measured at < 0.1% is expected due to the stress relief through cracking of the surface oxide and strain transfer across a nanostructured-bulk interface. Though cracking is a method of releasing the stress applied to the surface oxide, the cracked oxide forms islands on the surface of the NiTi alloy and increasing the applied strain results in saturation of the crack density on the surface. This in turn results in locked up elastic strains on the surface oxide.[129] However, XRD and Raman spectroscopy provide a combined toolset that can together identify the signature of elastic strains locked in a metal or metal oxide crystal structure to impact electrochemical behavior.[97] Combined with the versatility of superelastic/shape memory NiTi materials, this provides the ideal platform for assessing and understanding the mechano-electrochemical response of the surface oxide.

3.3.3 Strain engineered electrochemistry

To characterize the effect of quantifiable strain on electrochemical performance, we build on the principle that Ni-Ti-O based oxide is active for the redox reaction with OH^- ions in

alkaline electrolyte solutions.[113, 130, 131] Due to the ability to strain set conductive NiTi alloys, this provides an excellent platform for characterizing the role of strain transferred to the active Ni-Ti-O containing surface oxide layer on the observed redox couple in alkaline electrolytes. Cyclic Voltammetry (CV) was carried out using 2M NaOH electrolyte in a 3-electrode configuration with a Saturated Calomel Electrode (SCE) reference and a platinum counter electrode at scan rates of 100 mV/s. As SCE electrode is a commonly used reference electrode for studying the electrochemical response of NiO, $Ni(OH)_2$ and Ni-Ti-O based metal oxides in alkaline solutions, it was chosen as the reference electrode for the electrochemical tests.[22, 36, 130, 132] (Figure 3.3)

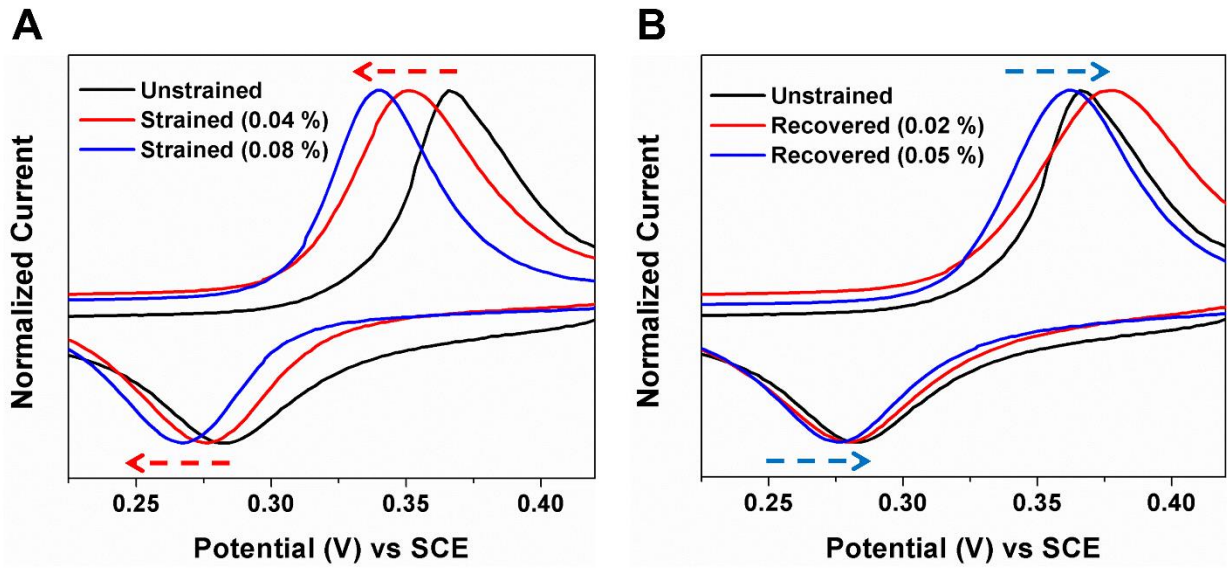

Figure 3.3. (A) Cyclic voltammograms with normalized current densities of the unstrained and the tensile strained (0.04 %) and (0.08 %) states based on surface oxides at a voltage window of 0.2 to 0.45 V. **(B)** Cyclic voltammograms with normalized current densities of the unstrained and recovered (0.02 %) and (0.05 %) states based on surface oxides at a voltage window of 0.2 to 0.45 V at scan rate of 100 mV/s.

For purposes of comparison, the current densities were normalized to analyze the potential shifts in the anodic and cathodic branches. To accurately measure the redox peak potentials and to exclude other possible sources of errors, 100 CV sweeps at a scan rate of 100 mV/s within the operating voltage window were performed to obtain reproducible voltammograms. To ensure accuracy, Gaussian fits were applied to the anodic and cathodic peaks to measure the peak potentials. CV curves comparing redox performance for both (1) different amounts of total strain applied to the surface-bound NiO-TiO_2 materials (Figure 3.3A) and (2) the same materials except with the strain recovered in a manner consistent with Figure 2.1C (Figure 3.3B) elucidate the principle that strain has an evident and reversible effect on the voltage of the redox couple. In the first case, the shift of both the anodic and cathodic peaks toward lower potentials indicates that the observed effect is not explained by resistance or activation polarization in the electrode. The strain-induced modification to the redox energetics is further highlighted by experiments where the strain on the NiO-TiO_2 based active material can be partially recovered, leading to a shift of both the anodic and cathodic peaks toward the native potential of the redox couple measured in the unstrained material. These results suggest for the first time that mechanical strain as an input parameter can modify or control electrochemical reduction potentials relevant to metal oxide-based energy storage materials. Whereas previous recent reports have indicated the effect of strain on catalysis,[96, 97, 133-135] our results are both consistent with these reports, but with key differences. Similar to a catalytic system where charge-transfer reactions are confined to a surface, reduction and oxidation reactions contributing to the pseudocapacitance of NiO-TiO_2 involves surface reaction with OH^- ion from the electrolyte. Previous studies have indicated that doping effects can modify the oxidation state changes of Ni-based metal oxides[136-138] where redox potential shifts can be attributed to structural distortions from doping.[136] In

particular, the shift in equilibrium redox potential E_{eq} or E_o can be observed through doping redox active metal oxides. This can be attributed to the change in the crystal field energies of such redox active metal oxides. In our study, we demonstrate mechanical strain as an input parameter, verified by XRD and Raman spectroscopy, where the local distortions of the surface oxide facilitate insertion of the OH^- ion into the surface oxide layer. This is further corroborated by taking advantage of the shapememory response of NiTi alloy to recover the structural distortions imposed by the applied tensile strain on the surface oxides, which in turn recovers the electrochemical response.

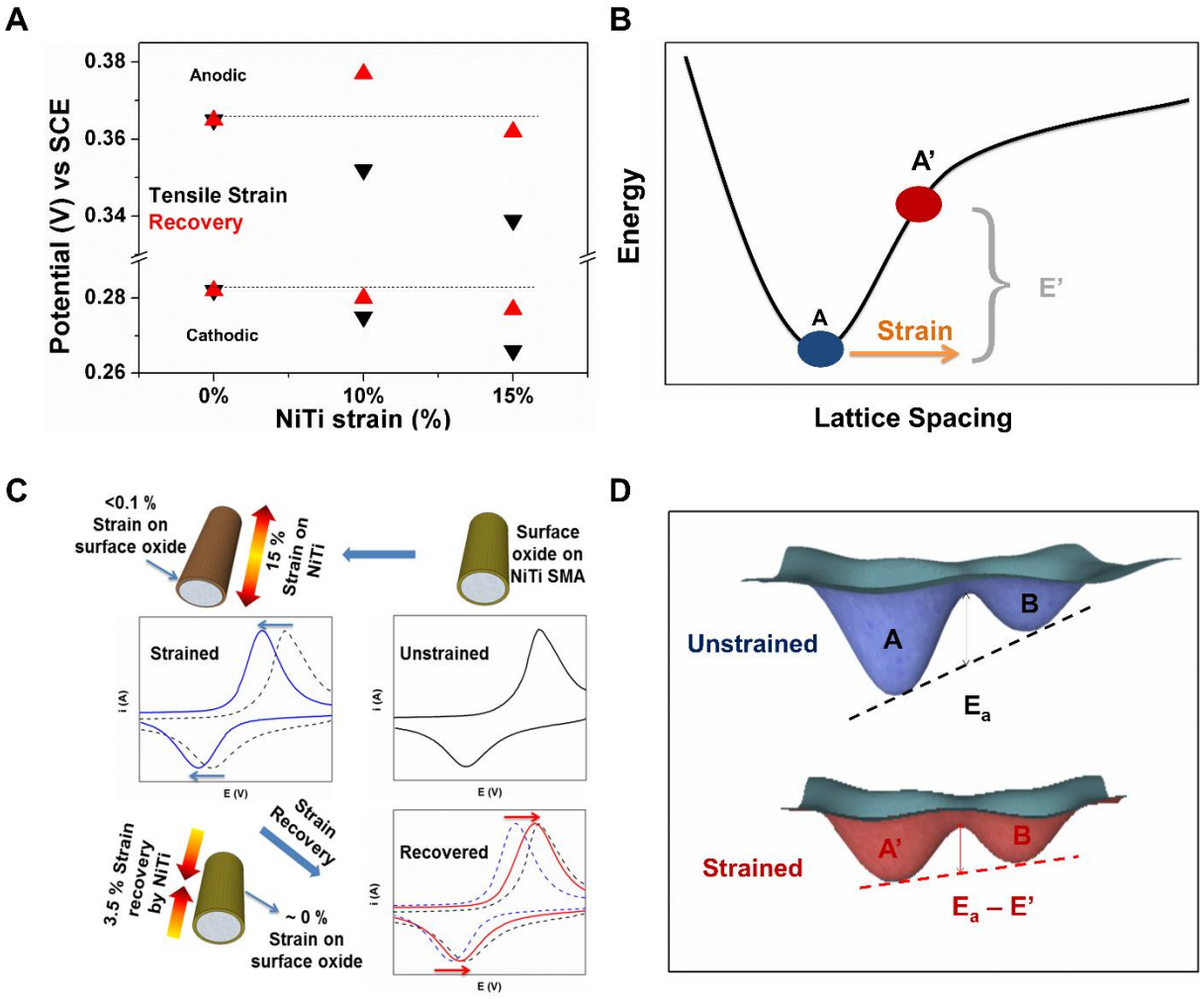

Figure 3.4. (A) Anodic and cathodic peak potentials plotted versus SCE at various unstrained, strained, and recovered states of the NiTi alloy. **(B)** General plot of the total cohesive energy as a function of lattice spacing with energy difference E' in tensile strained state that facilitates anion insertion. **(C)** Scheme representing the unstrained, strained, and recovered states of the NiTi alloy and the transferred strains on the surface oxide resulting in redox potential shifts. **(D)** Potential well representation of the transition between these states for electrochemical processes with E' for the strained state schematically illustrated in panel B.

In all cases, we observe that tensile strain lowers the equilibrium redox potential associated with the physical insertion of anions to store energy in the NiO-TiO_2-based material in a manner that correlates with the total amount of applied strain. (Figure 3.4A and Appendix Figure 3.11) This change in reduction potential can be reversed by recovering the strain imposed in the material. As only elastic strains have the ability to simultaneously affect Raman modes, lattice spacing, and electrochemical behavior, the NiTi platform provides a versatile substrate for locking such strains in metal oxides deposited on the surface.

Based on these observations, we propose a simple concept to describe this effect that is illustrated in Figure 3.4B. By applying tensile strain to the nanostructured material, the total free energy of the crystal is above its equilibrium value as described through relationships between the total cohesive energy of the crystal and the lattice parameter, such as the universal binding energy relationship (UBER). As only <0.1% strain is transferred to the surface oxide even though the alloy undergoes 15% tensile strain, the reversible effects observed in electrochemical measurements (Figure 3.4C) are most likely from the changes in the energy landscape of the surface oxide. Since the process requires the insertion of an anionic species into the host lattice, accompanied by an oxidation state change in the metal oxide, this increase in free energy facilitates a smaller energy barrier between the strained metal oxide (A') and the inserted state (B) in comparison to the unstrained metal oxide (A) and the inserted state (B). This is visually represented through a potential well diagram shown in Figure 3.4D. This process is distinguished from that described in electrocatalytic reactions, since effects in such systems are likely to be minimal until the imposed strain is of a significant magnitude to modify the electronic band structure of the catalytic material. Even in the case of applied strain at <0.1%, our results indicate a marked effect of strain on electrochemical redox reactions relevant to

redox-based energy storage systems that could be a critical tool in the future vision of engineered materials for advanced energy storage systems. Moreover, the strain can be applied to the surface oxide and be reversed to varying degrees based on the extent of preloading, thickness of the surface oxide and anchoring to the NiTi surface which leads to isolation of mechano-electrochemical effects of energy storage redox active materials owing to the fact that the only parameter capable of reversing redox potential shifts based on this system are the mechanical strains present in the surface oxides. Also, transformational structural distortions that accompany ion insertion into metal oxide lattices during electrochemical reactions in pseudocapacitors and batteries can be studied using the NiTi platform. This would offer a control knob that can directly tailor energy landscape of existing energy storage materials.

3.4 Conclusion

In summary, we demonstrate the ability to leverage strain engineering to modify the electrochemical potential of Ni-based metal oxide nanostructures fabricated on the surface of superelastic/shape memory NiTi materials during OH^- insertion and extraction. With less than 0.1% strain, we observe shifts in the electrochemical potential up to ~ 30 mV. Notably, this effect is uniquely correlated with strain as the reversal of strain in the material (a feature enabled by the superelastic NiTi) leads to a subsequent recovery of the electrochemical potential shifts. This elucidates the strain tensor as a six-dimensional framework to modify the electrochemical response of materials, opens a new area where foundational principles of electrochemistry (such as the Nernst potential) can intersect mechanical properties of materials, and provides a practical framework for improving the function of energy storage materials. As pairing of anodic and cathodic potentials dictate the total energy density of a battery, strain could potentially open a route to improve energy storage performance of batteries building from already existing

materials, instead of engaging new synthesis driven routes toward new materials. Unlike semiconductor manufacturing routes that leverage strain engineering to modulate electronic properties of materials, we propose electrochemistry to be more amenable to strain engineering since both the electronic properties of a material *and* the physical insertion and storage of ions in a material are attributes that can be controlled with strain, as we discuss in this work.

Acknowledgements

We thank Bradly Baer for assistance in strain measurements, Dr. Leon Bellan for generous use of facilities in his laboratory for strain setting, Dr. Rizia Bardhan for use of the Raman microscope for strain analysis, Timothy Boire for his guidance during DSC measurements, and Alice Leach for assistance with XRD. We also thank Andrew Westover, Anna Douglas, Keith Share, and Mengya Li for useful discussions. This work was supported by an NSF graduate research fellowship (A.P.C.) number 1445197 and Vanderbilt University start-up funds.

3.5 Appendix

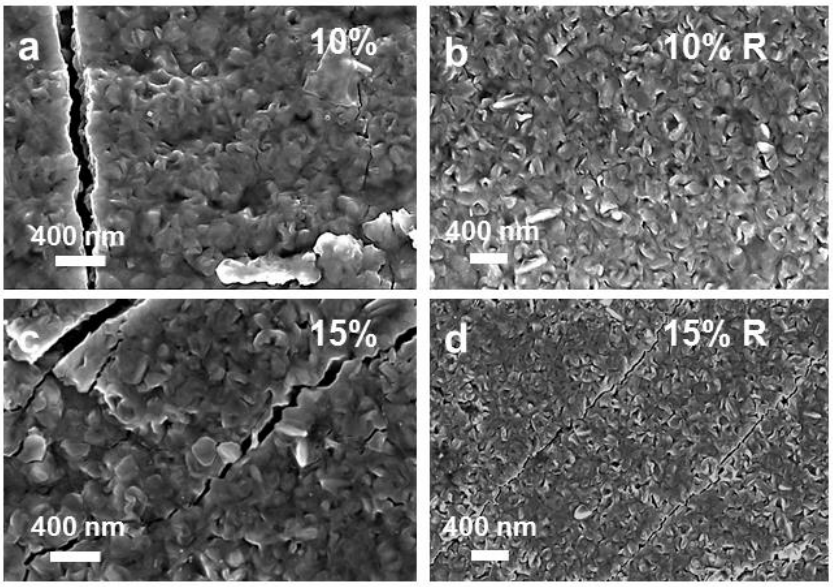

Figure 3.5. SEM micrographs of the nanotextured surface oxides at a) 10% tensile strained, b) 10% strain recovered, c) 15% tensile strained and d) 15% strain recovered

Figure 3.5 (a-d) show the scanning electron micrographs of the strained and strain recovered wires representing the strained 10%, 15% and recovered 10% R and 15% R. The nanotextured oxide undergoes cracking during the straining process which represents areas of strain release which lowers the overall strain transfer from the alloy to the surface oxide even if the intimate contact of the as grown oxide on the wire is strong. The NiTi alloy is superelastic whereas the ceramic based NiO-TiO_2 oxide is brittle; cracking of the surface oxide is possible at very low strains of about 1% according to previous reports.[139-141] Upon recovery, the cracked oxide appears to almost revert back to the unstrained state in the case of 10% R whereas cracking is still observed in 15% R which indicates a better strain recovery in the case of 10% R which is consistent with the observations from mechanical tests.

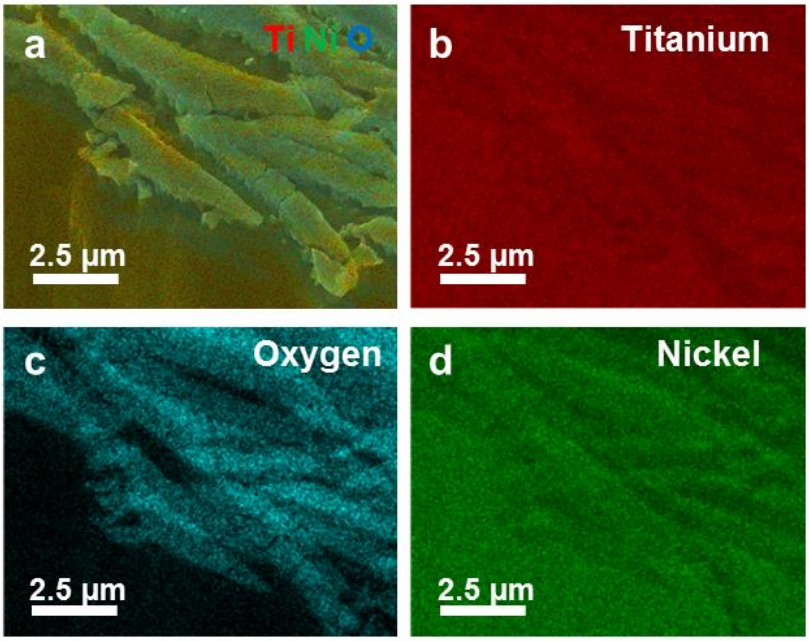

Figure 3.6. EDS maps of cross-section of the wire with the strained surface oxide; a) Full EDS map showing Ni, Ti and O distribution, b) EDS map showing Titanium distribution, c) EDS map showing Oxygen distribution and d) EDS map showing Nickel distribution

Figure 3.6 (a-d) shows the EDS maps of the cross-section of the NiTi wire representing Titanium, Oxygen and Nickel elemental distributions. The cracks on the surface oxide are partly due to the strain imposed on the wire and partly due to the mechanical cutting process of the wire. EDS maps suggest the surface oxide is composed of a mixed Ni-Ti-O based surface oxide. Cross-sectional image analysis show the thickness of the surface oxide is about 200nm. Figure S2 C shows the EDS map of Oxygen distribution indicating low oxygen concentration in the bulk alloy and in-between the cracks of the surface oxide.

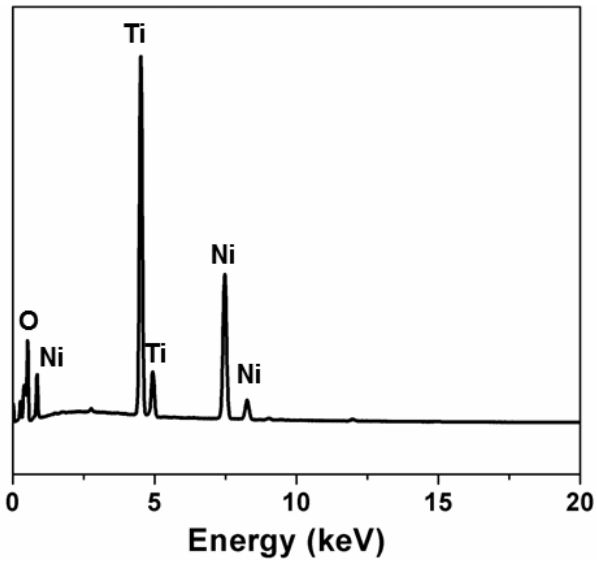

Figure 3.7. EDS Spectra of cross-section of the wire with surface oxide

EDS spectra shown in Figrue S3 indicates the presence of a Ni-Ti-O based surface oxide which comprises of a mixed oxide phase consisting NiO, TiO_2 and $NiTiO_3$ layers based on Raman and XRD analysis.

Element	Line Type	Apparent Concentration	k Ratio	Wt%
O	K series	7.31	0.02461	18.68
Ti	K series	30.06	0.30062	37.42
Ni	K series	34.50	0.34504	43.90
Total:				100.00

Table 3.1. Compositional analysis based on EDS spectra of the cross section of the NiTi wire with surface oxide.

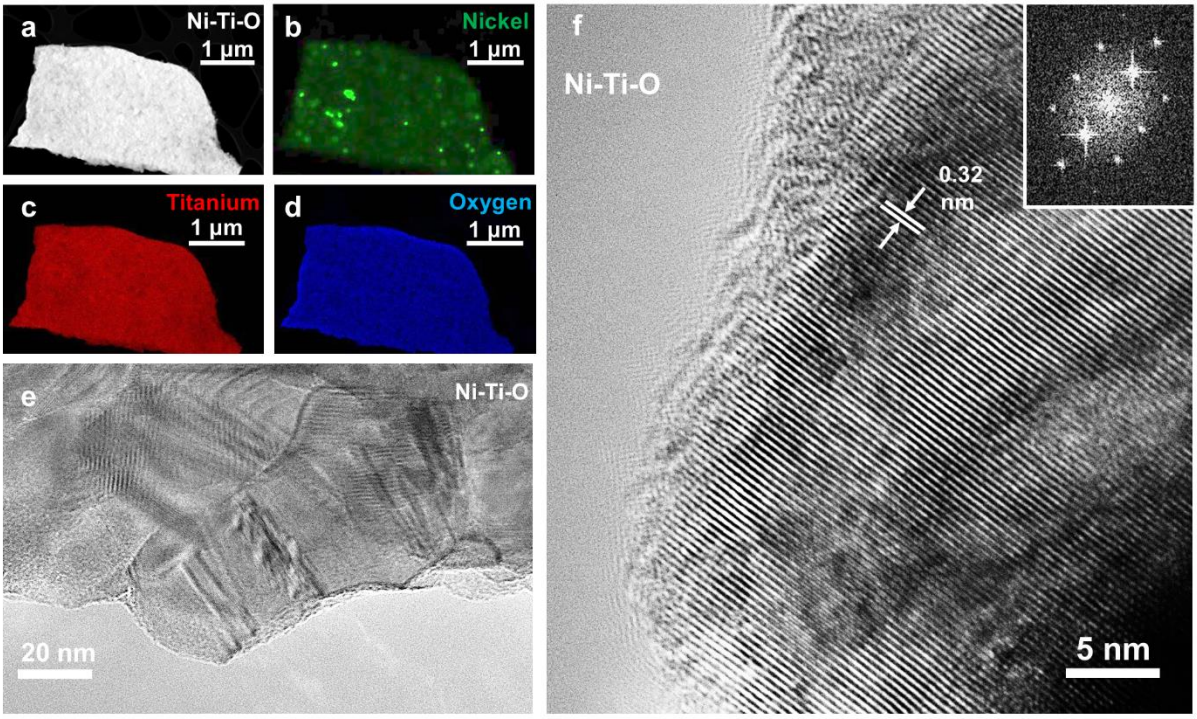

Figure 3.8. a) HAADF image of a Ni-Ti-O surface oxide flake, (b-d) STEM EDS maps of the surface oxide showing elemental composition of Nickel, Titanium and Oxygen, c) HRTEM image of the nanostructured surface oxide showing a polycrystalline surface oxide and d) HRTEM image of the surface oxide showing well defined crystal lattice, inset: diffraction pattern of the crystal lattice after performing FFT analysis.

TEM analysis was performed on the surface oxide by scrapping off the oxide from the wire surface on to a copper grid. As the oxide is adhered to the surface of the wire, scrapping the surface results in further fragmentation of the oxide. The elemental composition of the surface oxide was observed using HAADF and STEM EDS maps (Figure S5. a-d). The presence of a polycrystalline surface oxide feature was observed through HRTEM micrograph (Figure S5. e). At higher magnifications, clear distinguished crystal lattice of the surface metal oxide was

observed (Figure S5. f). FFT analysis was performed on the crystal lattice to determine a spacing of 0.32 nm between the observed atomic planes.

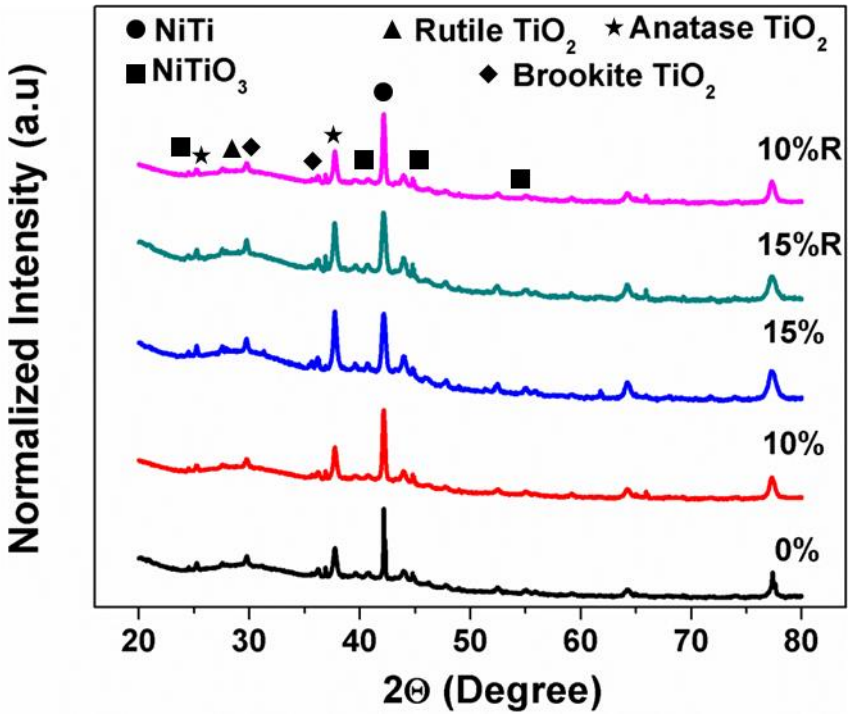

Figure 3.9. XRD full spectra of the surface oxides on NiTi alloy

X-Ray Diffractograms of the unstrained (0%), strained (10% and 15%) and recovered (10% R and 15% R) states of the wires and surface oxides were obtained using -Ray diffraction (Scintag XGEN 4000) using Cu Kα 1.542 A^{o}. As the thickness of the wire was 0.5 mm, signal acquisition was performed between 2θ values of 20^{o} and 80^{o} with 40 sec per 0.2^{o} exposure time. Due to the geometry of the wire, tensile strain along the axis of the wire is accompanied by a reduction in thickness along the radial directions of the wire and on recovery this is reversed causing a possibility for biaxial effects of strain on the surface oxide. The peak positions were indexed using JCPDF cards 29-1360, 21-1272, 21-1276, 33-0960 and 18-0899. As only elastic strains on the oxide could result in such peak shifts, the % of elastic strain on the oxide on the different planes of the surface oxides were determined using the equation below:

$$\% \text{ elastic strain} = \left(\frac{d_{T\ or\ R} - d_{0\%}}{d_{0\%}}\right) \times 100\ \% \qquad 4$$

where d_T, d_R and $d_{0\%}$ represent the d-spacing of the tensile strained states, the recovered states and the unstrained (0%) strained states respectively. In all cases, only a small percentage of strain is transferred to the surface oxides even though the strain applied and recovered on the NiTi alloy is large. As the ceramic oxide layer on the surface is brittle, this is an expected result.

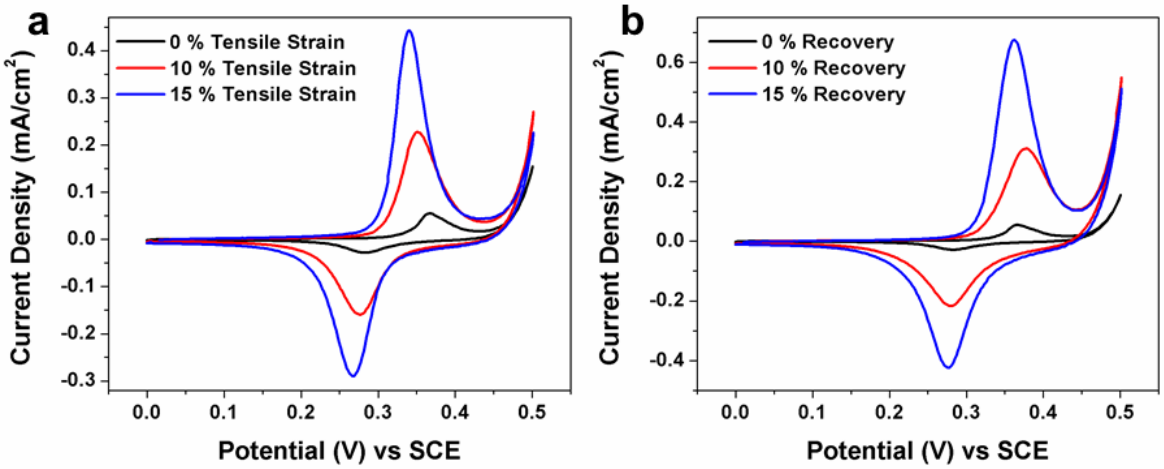

Figure 3.10. a) Cyclic voltammograms of the tensile strained states compared to the unstrained state and b) Cyclic voltammograms of the strain recovered states compared to the unstrained state.

Figure 3.10 (a and b) show the cyclic voltammograms of the unstrained, strained, and strain recovered surface oxides. Based on the EDS spectra, it is evident that the surface oxide is composed of Nickel and Titanium oxides. Based on the XRD strain analysis and Raman spectra, there is evidence of strain on the surface oxides which show patterns with the behavior of the NiTi alloy. The cumulative effect of these imposed and recovered surface oxide strains on the electrochemical performance of the NiO-TiO_2 based surface oxide was examined using Cyclic Voltammetry using 2M NaOH electrolyte in a 3-electrode configuration with a Platinum foil

(1cm X 1cm, Alfa Aesar) and a Saturated Calomel Electrode (SCE) as the counter and the reference electrodes. The potential is measured against an SCE electrode in a 3-electrode configuration which enables accurate characterization of the redox potentials. The NiTi wires with different strain states with nanotextured surface oxide were CV cycled 100 times at a scan rate of 100 mV/s to obtain reproducible voltammograms. Based on the redox potentials vs SCE, and redox peak potentials based on previous reports,[142, 143] the surface redox process is attributed to a near surface reaction corresponding to the insertion and extraction of OH^- ions from the alkaline electrolyte, leading to a modification of the oxidation state of the active Ni-Ti-O material. Prior to all measurements, peroxide sonication step was employed to impart nanotexturing to the surface oxide and to electrochemically activate the surface for both strained and unstrained states of the alloy.

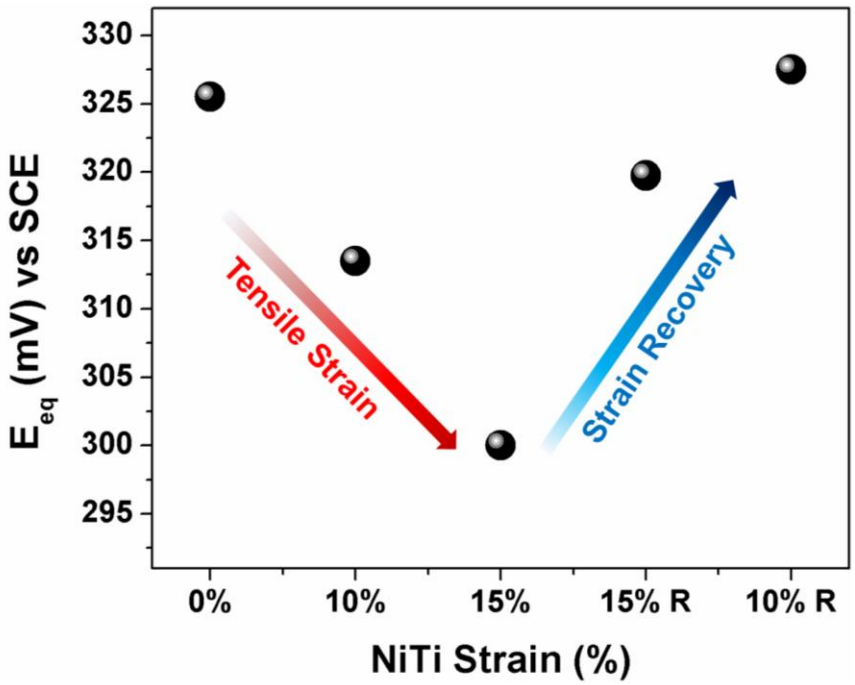

Figure 3.11. Variation of equilibrium redox potential with applied and recovered strain conditions.

The equilibrium redox potential E_{eq} or E_o is given by the equation,

$$E_{eq} = \frac{E_{anodic} + E_{cathodic}}{2} \qquad 5$$

where, E_{anodic} and $E_{cathodic}$ are the anodic and cathodic peak potentials shift corresponding to the unstrained, strained and recovered states. The shift in the E_{eq} or E_o with applied strain and recovered strain conditions is a consequence of the changes occurring to the crystal lattice of the redox active metal oxide. This effect is otherwise observed in doped metal oxides where slight distortions (strains ~ <1%) through doping alters the energy landscape of the redox active species. As the process of electrochemical insertion and extraction of ions during the redox reaction is accompanied by oxidation state changes to the redox active species, structural distortions are often a negative consequence. However, through the effect of metal ion doping in to metal oxide lattices, these distortions can be minimized resulting in easier insertion and extraction of electrolyte ions which leads to changing equilibrium redox potentials. In our study, we use small lattice strains (< 1%) to effect the same type of shifts in the equilibrium redox potentials and reversing the shifts through the strain recovery process.

Chapter IV

4 Tunable MechanoChemistry of Lithium Battery Electrodes

4.1 Introduction

During an intercalation reaction, the local displacement of atoms in the host battery material accommodates the volume of a stored metal ion. In other words, at an atomic scale this means that mechanical *work* is intrinsically tied to the mechanistic principles of battery operation, even though energy storage processes remain centrally described by the associated charge transfer electrochemistry. In this spirit, recent efforts have been made to better understand the fundamental mechano-electrochemical coupling between alkali metal ion electrode (alloying/intercalation) parameters and mechanics as a result of energy storing reactions through theoretical and experimental approaches.[144-147] Predominantly these mechanical changes (stresses and strains) are regarded to have an adverse effect on the performance of both anodes (large volume expansion[148]) and cathodes (irreversible structural distortions[149]) in these devices.[150-154] Advanced research strategies have been focused on developing electrode materials that can mitigate these issues through the addition of dopants,[149, 155-158] application of nanostructuring techniques[159-164] or development of nanoscale architectures.[165-170] However, in most cases, stresses and strains arising from intercalation processes are viewed as an adverse by-product of the electrochemical reaction, with no expectation that mechanics could in turn control the electrochemistry.

In this regard, there has been a considerable interest in recent years outside of battery materials focused on utilizing mechanical stress and strain effects to engineer and improve energetics and kinetics of some electrochemical[171, 172] and electrocatalytic systems.[173, 174] This

approach, which is drawn from the principles of elastic strain engineering readily applied in the semiconductor industry, is aimed at achieving otherwise unexpected material property enhancements by placing materials under pre-applied elastic strains. In a pre-strained state, novel material properties can be observed as a result of modification to the energy landscape when compared to the unstrained natural state.[8, 173, 174] Applying these principles to a dynamic system, such as an alkali metal ion battery electrode, opens up possibilities for understanding and enhancing parameters that govern their functionality, such as voltage, cycling rate, and durability. However, understanding of how strain can be used to tune energy storage properties remains devoid of experimental support.[171, 175-177] Whereas atomistic simulations provide a framework for understanding the positives involved in using input mechanical stresses and strains to modulate electrochemical performance, the experimental challenges are quite significant to realize this. Conventional processing requirements of most anode and cathode materials limit the feasibility of fabricating pre-strained electrodes. Commonly employed strain engineering techniques to develop pre-strained architectures include epitaxial lattice mismatch,[178, 179] thermal strain development through thermal expansion coefficient (CTE, α_{CTE}) mismatch[175, 180] and strain transfer through coupling with a substrate such as Nitinol.[126, 171, 172, 174]

In this report, we provide the results of the first study aimed to probe how programmed mechanical strain transferred to V_2O_5 insertion cathodes can modulate the electrochemical potential and insertion kinetics of battery reactions. In this case, V_2O_5 is a well-studied battery cathode material[168, 178, 181] and can be controllably deposited onto superelastic shape memory NiTi using ALD. This enables us to use the NiTi material dually as a conductive current collector and as a means to transfer strain to the active V_2O_5. Our findings, which are supported by atomistic simulations using density functional theory (DFT), demonstrates the capability to

modulate the electrochemical potential by 40 mV, and increase metal ion diffusion coefficients by up to 2.5 times with less than 2% applied strain to the V2O5. This highlights the versatile mechanochemistry of batteries, emphasizing that mechanics can be a tool to modulate the chemistry in the same way that chemistry is more often used to control the mechanical response of electrodes.

4.2 Experimental Methods

4.2.1 Activation of NiTi shapememory superelastic alloy and pretreatments

NiTi superelastic wires (0.5 mm diameter, 55% Ni from Nitinol Devices & Components, Inc.) were subjected to aging process at 600 ^{o}C for 1 hour under vacuum in a Lindberg Blue 1" Quartz CVD tube furnace. The aged wires were mechanically polished using 600 grit silicon carbide papers to remove the native surface oxide. The mechanically polished wires were repeatedly sonicated for 10 min in Acetone (Aldrich) followed by Ethanol (Aldrich) and nanopure water (Millipore water purifier). The wires were then air dried prior to further processing. This aging process was used to activate the superelastic/shapememory property of the NiTi alloy.

4.2.2 Atomic layer deposition of vanadium oxide films and annealing treatments

Vanadium oxide coatings were deposited on the aged, mechanically polished NiTi wires using a GemStar 6" ALD system. The precursor, (98+%) Vanadium(V)tri-i-propoxy oxide (VTIP) with a chemical formula, $VO(OC_3H_7)_3$ (Strem Chemicals) was preheated to 55 ^{o}C. The oxidizer used in this process was nanopure water (Millipore water purifier). Heating the precursor and oxidizer manifolds to 115 ^{o}C ensured that no condensation of the reagents occurred inside the manifolds. The carrier gas used was ultra-high pure Argon and a reaction temperature of 200 ^{o}C was maintained throughout the process to ensure uniform deposition on the surface of the NiTi wire. VTIP and water pulses of 2 seconds each and long residence times of 20 seconds for both

reactants in the reaction chamber was employed to achieve complete saturation of the precursors in the reaction chamber, similar to previous reports.[39, 182] The wires were subjected to repeated ALD cycles to achieve a thin conformal coating of vanadium oxide on the surface. The deposited oxide films were annealed at 450 ^{o}C for 30 min in a Lindberg Blue 1" Quartz CVD tube furnace open to air to achieve crystalline coatings of vanadium pentoxide (V_2O_5) on the surface of the alloy.

4.2.3 Surface ellipsometry analysis and mass estimations

To determine the thickness and mass of the oxide deposited per cycle, a silicon wafer (Diameter: 100 mm) was used along with the NiTi wires during the ALD process. Surface ellipsometry analysis was performed on these silicon wafers after annealing treatments using a JA Woollam M2000VI Spectroscopic Ellipsometer. The mass of the wafer before and after the ALD process post annealing treatments gives an estimation of the mass of oxide deposited per cycle. This provides a comparable estimate of thickness and mass of the thin vanadium pentoxide films deposited on NiTi wires.

4.2.4 Straining the surface coating

The NiTi wires with the surface V_2O_5 coatings were subjected to axial tensile deformation up to 5% and 10% strains at a rate of 2 mm/min using an Instron 5944 mechanical testing system. Tensile deformations beyond 10% were not performed to avoid delamination of the coating from the wire surface.

4.2.5 Electron Imaging

Microstructural characterization and Energy Dispersive Spectroscopy (EDS) analysis was carried out using a Zeiss Merlin SEM using a 5 kV acceleration voltage for imaging and 20 kV beam voltage for EDS elemental analysis and mapping.

4.2.6 Raman spectroscopy and X-Ray diffraction

Analysis of the 'locked-in' elastic strains on the surface V_2O_5 coatings was performed using X-Ray Diffraction (XRD) and Raman spectroscopy. Raman spectroscopy was carried out using a Renishaw Raman microscope using 532 nm laser excitations. Statistical analysis of the strained surface coating was obtained through maps comprising of >500 spots across the surface of the wire. The laser exposure time was 60s at power of 10% to avoid thermal effects. Lorentzian fits were applied to the individual stretch modes to obtain peak positions. Crystallographic analysis to quantify the strain on the surface V_2O_5 coating was performed by obtaining X-Ray diffractograms using a Scintag XGEN 4000 using Cu Kα 1.542 A°. To maximize the X-Ray counts, a 40 sec exposure time per 0.02 degree increment was maintained throughout the measurement.

4.2.7 Electrochemical measurements

Electrochemical measurements and analysis were performed in a 3-electrode configuration using a beaker type cell. The V_2O_5 coating on NiTi wire was used as the working electrode with a platinum foil (Alfa Aesar 1cm x 1cm) as the counter electrode and a Saturated Calomel Electrode (SCE) as the reference electrode. The electrolyte used in this study was freshly prepared 1 molar lithium perchlorate ($LiClO_4$) (Aldrich) dissolved in propylene carbonate (PC) solvent (Aldrich). The electrochemical data were normalized to the immersed wire electrode area in the electrolyte. Cyclic voltammograms and galvanostatic charge discharge curves were

obtained for the unstrained and strained states of the surface V_2O_5 coating at various scan rates (10 mV/s to 100 mV/s) in the potential range of 0 V to 0.6 V using a Metrohm Autolab Multichannel Analyzer.

4.2.8 Density functional theory simulations

We used density functional theory (DFT) calculations to computationally model the effect of strain on intercalation energies in V_2O_5. The intercalation energy comes from comparing changes in total energy between lithiated and non-lithiated structures, and changes in this energy can be modeled by straining the structure computationally. This model corresponds to the experimental process of pre-straining the lattice before intercalation of lithium. We apply in-plane strain by manually increasing or decreasing the 'a' and 'b' lattice parameters while allowing the 'c' lattice parameter and all ionic positions to relax to the minimum energy state. The energy of intercalation per lithium atom is estimated as

$$E_I = 2E\,[Li_{0.5}V_2O_5] - (E[Li] + 2E\,[V_2O_5]) \qquad 6$$

where $E[V_2O_5]$ and $E[Li_{0.5}V_2O_5]$ are the total energy given by DFT, and E[Li] is the constant total energy of BCC Li also given by DFT calculations. The DFT parameters and further details on the calculations are provided in the supplemental information. The lattice constants 'a' and 'b' are passed as parameters to the DFT calculations so that the energy E=E(a, b). 'a_0' and 'b_0' are the lattice parameters where $E[V_2O_5]$ is minimum. Note that the values of 'a' and 'b' where $E[Li_{0.5}V_2O_5]$ is minimized are smaller than a_0 and b_0 respectively because the layer spacing expansion during lithiation tends to compress the in-plane directions. In this work, we always vary 'b' by the same percentage as we vary 'a', meaning 'a' alone can specify the applied strain, therefore E=E(a). Note that we are assuming here and throughout this work that 'a' and 'b' are

fixed during the intercalation process, allowing us to get the intercalation energy by calculating E[V] and E[Li] at the same 'a' and 'b' (see supporting information), thus $E_I=E_I(a)$. Additionally, we calculated E_I at several values of 'a' and plotted vs applied in-plane strain on 'a', defined as $a_{Strain}=(a-a_0)/a_0$. These data are fit with a third order polynomial. Note that E_I is negative because the total energy of the system decreases when a lithium ion moves from BCC Li to the V_2O_5 lattice. This decrease in energy makes lithiation energetically favorable, with larger decreases in energy being more energetically favorable than smaller decreases in energy.

4.3 Results and discussion

4.3.1 Interface strained V_2O_5

Ultrathin coatings of vanadium oxide were deposited using ALD onto NiTi wires (see experimental methods). The as deposited coatings were initially composed of poorly crystalline VO_x where highly crystalline V_2O_5 was achieved with post-deposition annealing (see experimental methods and Appendix, Figure 4.6).[39, 183, 184] By varying the number of deposition cycles, ALD offers the possibility to control the thickness of these films, which was estimated using a surface ellipsometry technique (see experimental methods and Appendix, Figure 4.7). In the case of thin films deposited on substrates with dissimilar coefficients of thermal expansions (CTE) significant interface strains can be generated using thermal treatments.

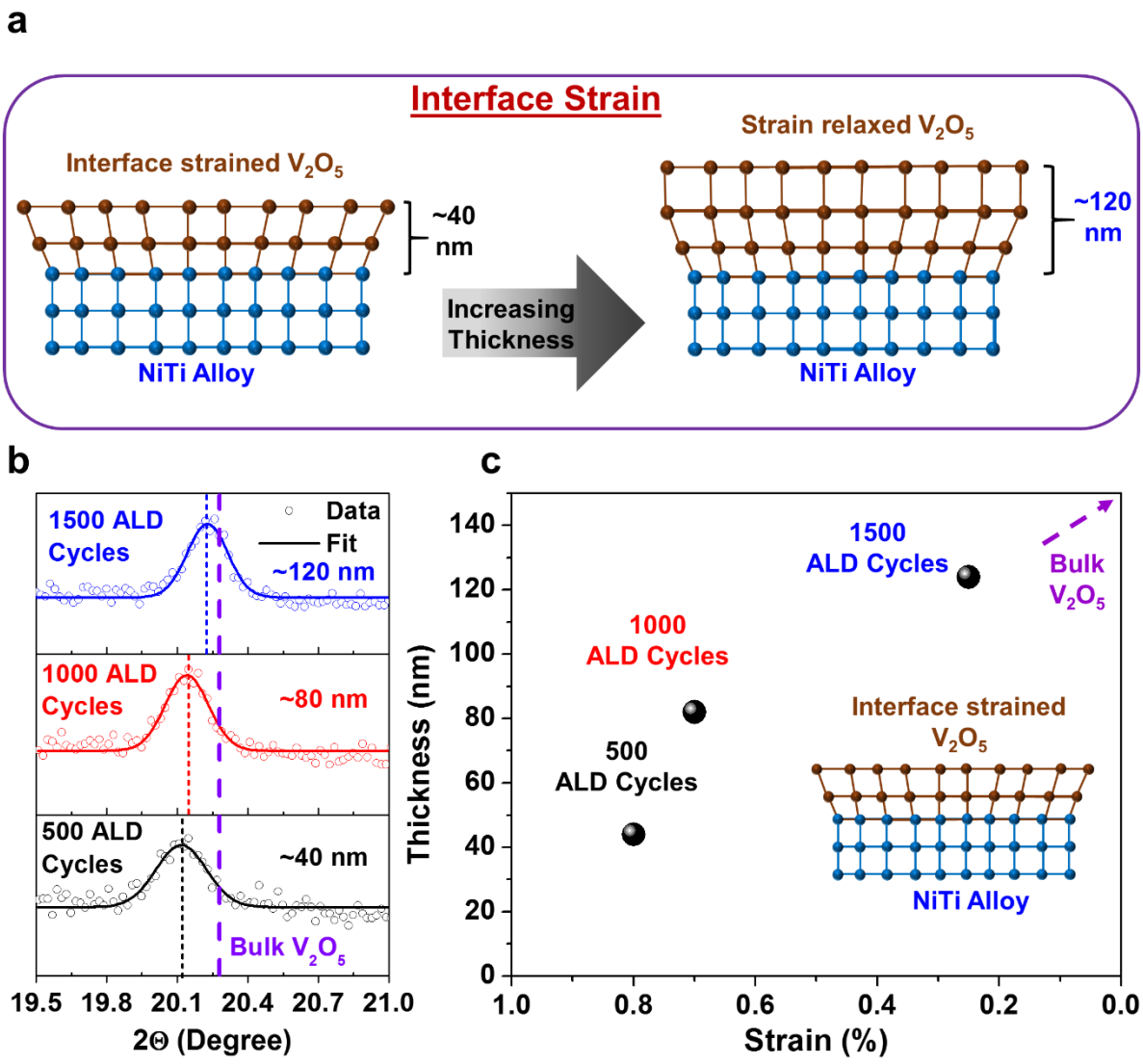

Figure 4.1. **(a)** Schematic representation of the process of placing the surface V2O5 film under 'locked-in' mechanical strains by straining the NiTi substrate axially **(b)** X-Ray diffraction peak corresponding to the (001) plane of the surface V2O5 film with different substrate strain states of NiTi along with the bulk V_2O_5 X-Ray diffraction (001) peak position from JCPDF 41-1426 file **(c)** Strain % on the surface V_2O_5 film based on the X-Ray peak shifts observed for the (001) plane and the corresponding in-plane expansion caused owing to the Poisson ratio (v = 0.3)."

The CTE of the V_2O_5 film is considerably lower than the CTE of the metallic substrate (Nitinol) ($\alpha_{substrate} >> \alpha_{film}$) and upon cooling after the annealing treatment an intrinsic thermal strain is imposed on the film (see Appendix). This interface strain can be varied by controlling the thickness of the deposited coatings as a result of strain relaxations which are dominant at greater thicknesses (Figure 4.1a). Here, thicker coatings will lead to greater average strain relaxation in the deposited V_2O_5 layer since the strain originates from the V_2O_5/NiTi.[185-187] Through crystallographic analysis of the deposited films using XRD (see experimental methods), we observe the presence of a crystalline α-phase of V_2O_5 with preferential (001) orientation similar to such films reported elsewhere (see Appendix, Figure 4.8).[168, 182] The obtained diffractograms were compared to the diffractogram of unstrained bulk V_2O_5 obtained from JCPDF: 41-1426. As XRD is a global probe which samples the entire coating, this yields an average value of strain and therefore a higher strain percentage measured for thin coatings. Analyzing the 'c' directional (001) diffraction peak in Figure 4.1b, compared to bulk V_2O_5, a higher 2 theta value for the (001) peak is observed and attributed to the thickness dependence of strain in V_2O_5 coatings, as shown in Figure 4.1c.

4.3.2 Strain engineering V_2O_5

To mechanically lock-in elastic strains onto the deposited V_2O_5 coating, the NiTi wire was subjected to axial tensile strains of 0% to 10% (see experimental methods and Appendix, Figure 4.9). Owing to the unique shapememory property of the NiTi alloy, the applied strains (5% and 10%) were maintained after unloading, placing the surface V_2O_5 film under varying mechanical strains. Axial tensile strains on the substrate cause the deposited V_2O_5 film to experience an average compressive strain along the 'c' direction (001) as shown in the schematic Figure 4.2a.

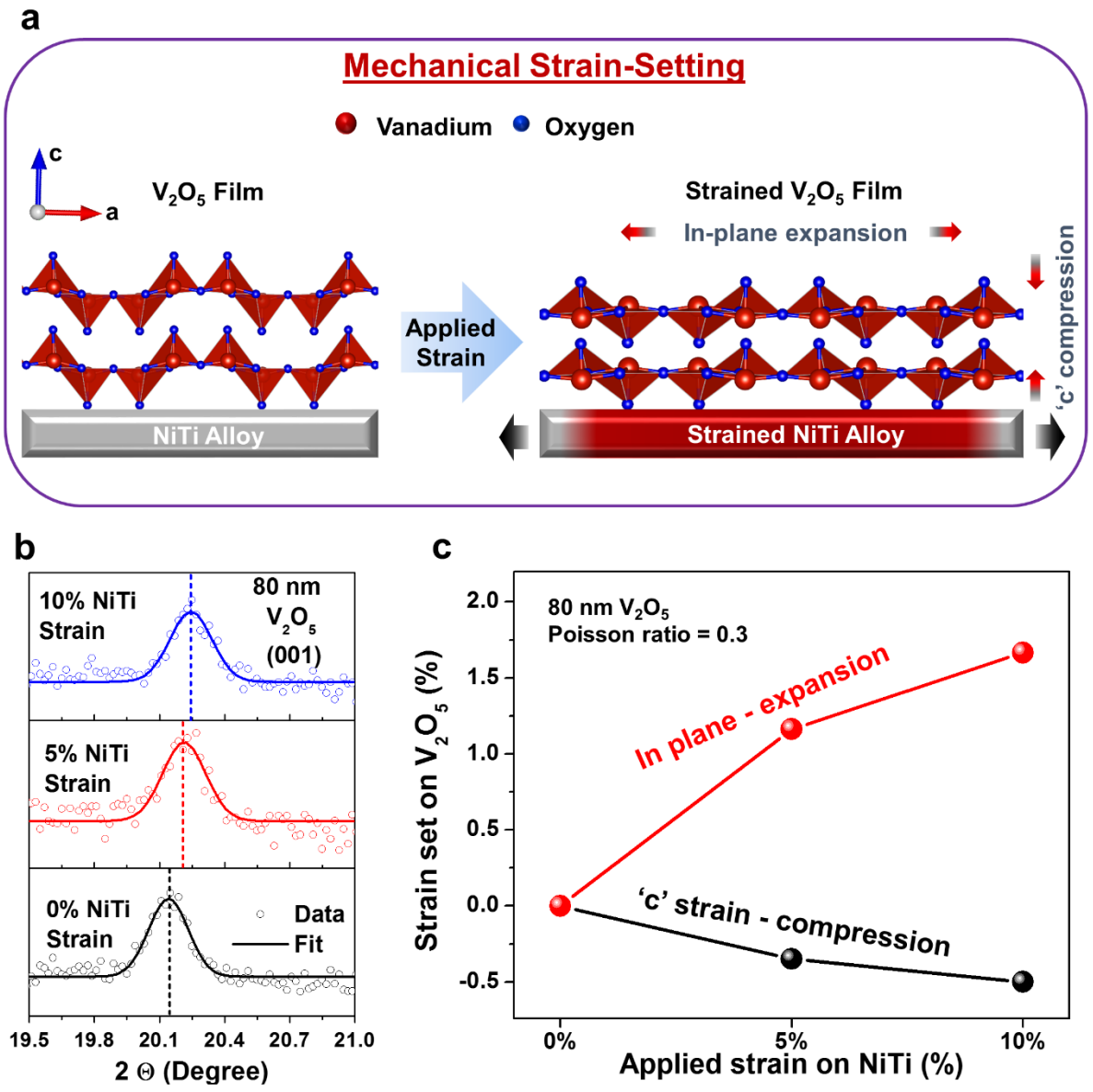

Figure 4.2. (a) Schematic representation of the process of placing the surface V_2O_5 film under 'locked-in' mechanical strains by straining the NiTi substrate axially **(b)** X-Ray diffraction peak corresponding to the (001) plane of the surface V_2O_5 film with different substrate strain states of NiTi **(c)** Strain % on the surface V_2O_5 film based on the X-Ray peak shifts observed for the (001) plane and the corresponding in-plane expansion caused owing to the Poisson ratio (v = 0.3).

Through XRD analysis, we observe that the (001) peak shifts to higher angles indicating that an out of plane ('c' directional) compressive strain (<1%) is imposed on the metal oxide films (Figure 4.2b). As a result of elastic of strains imposed to the alloy, the applied strain % on NiTi in each case was higher than the critical strains required for cracking these films for a given thickness (see Appendix, Figure 4.10 for electron micrographs).[129, 171] We chose substrate strains of 5% and 10%, which would sufficiently exceed the saturation crack density as reported for similar films deposited using ALD.[129] As most oxides have a Poisson coefficient,'ν' between 0 and 0.5, a net positive volume change should occur due to compression in 'c' direction.[176, 188, 189] We assumed a Poisson coefficient ν = 0.3 (typical for metal oxides) to estimate the in-plane strain imposed on the film as shown in Figure 2c. We estimated an in-plane tensile strain of 1.6% for an out of plane 'c' directional compressive strain of 0.5%. XRD analysis corresponding to the ~40 nm V_2O_5 film is given in the supporting information (see Appendix, Figure 4.11).

4.3.3 Raman spectroscopic analysis of strain on V_2O_5 coatings

As XRD provides an estimate of the average 'locked-in' elastic strain on the V_2O_5 coating, a local probe such as Raman spectroscopy (see experimental methods) can provide information regarding the elastic strain effect on the local bonding environment in the coating.

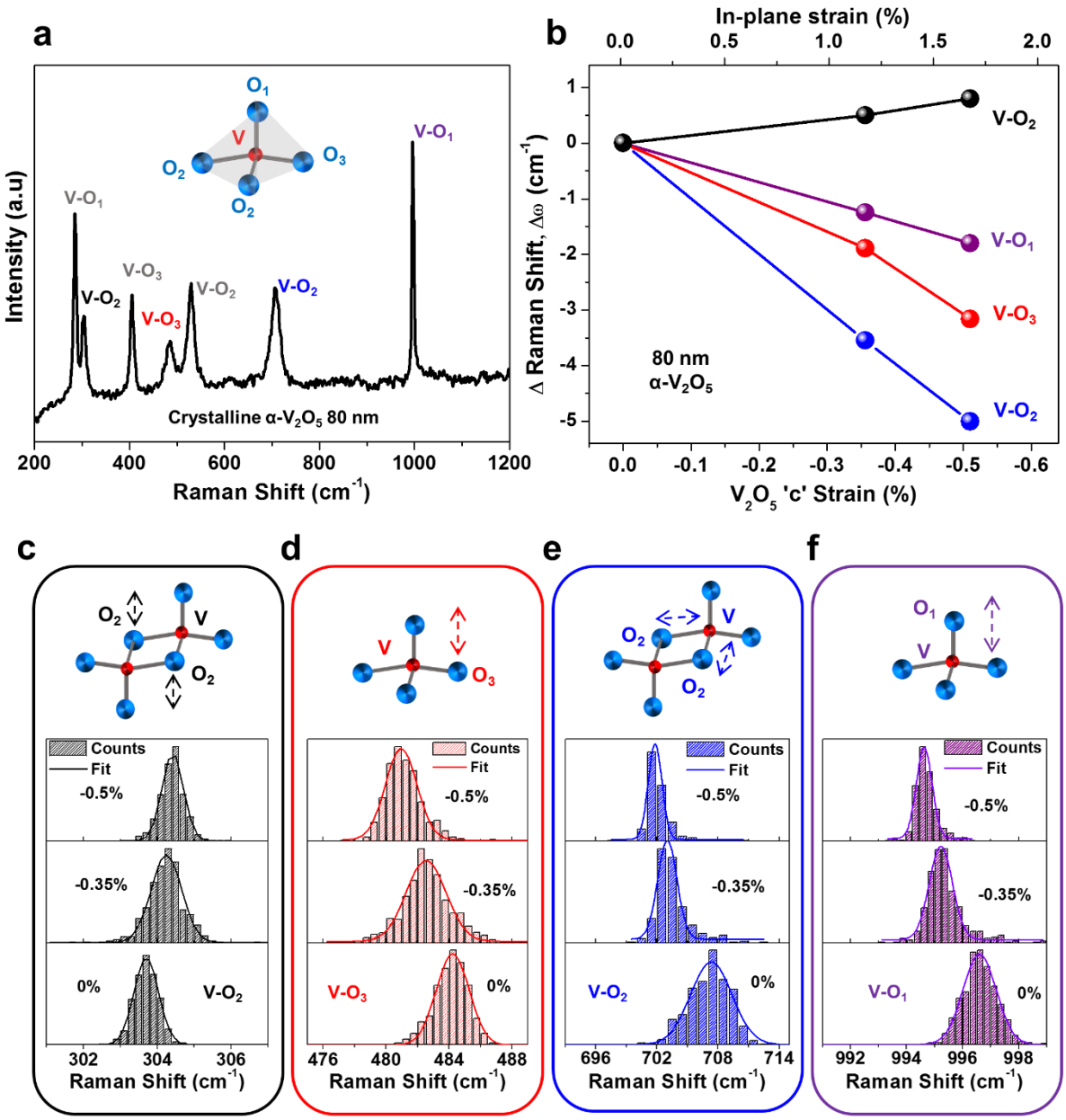

Figure 4.3. (a) Raman spectra of ~80 nm α-V_2O_5 coating (1000 ALD cycles) on NiTi showing the various Raman modes **(b)** Mean peak positional Raman shifts caused by strain, Δω ($\omega_{Strained} - \omega_{Unstrained}$) cm^{-1} of the individual Raman modes analyzed. **(c-f)** Histograms of the most strain sensitive modes from Raman maps (>500 individual Raman spectra) of the strained and unstrained states of V_2O_5 (based on (001) plane).

Raman spectra in Figure 4.3a show the vibrational modes corresponding to V-O_1 (~997 cm^{-1} and ~282 cm^{-1}), V-O_2-V (~708 cm^{-1}), V-O_2 (~528 cm^{-1} and ~ 303 cm^{-1}) and V-O_3-V (~483 cm^{-1} and ~407 cm^{-1}).[190, 191] The Raman spectra of the strained films (see Appendix, Figure 4.12) do not indicate additional modes occurring due to imposed strains on the film. To address potential concerns of strain homogeneity we acquired over 500 individual Raman spectra obtained across a large area on the surface was performed to yield a statistical assessment of the imposed strain effect. The obtained Raman stretch modes from these surface maps were fitted to Lorentzian curves to obtain a statistical distribution of peak positions. Mean shifts in peak positions, $\Delta\omega$ ($\omega_{Strained} - \omega_{Unstrained}$) cm^{-1} of strain sensitive Raman modes are given in Figure 4.3b. We observed a mean redshift of ~2 cm^{-1} for V-O_1 (~997 cm^{-1}), ~3.5 cm^{-1} for V-O_3-V (~483 cm^{-1}) and ~5 cm^{-1} for V-O_2 (~708 cm^{-1}) and a mean blue shift of 1 cm^{-1} for V-O_2 (~ 303 cm^{-1}) when the V_2O_5 film is pre-strained. We speculate that owing to a 'c' direction compression and a resulting in-plane expansion when straining these films, certain Raman modes experience a mean redshift when certain modes undergo a mean blue shift. The corresponding histograms of these vibrational modes showing mean redshifts and blue shifts are given in Figure 4.3 (c-f). Using XRD and Raman analysis, we show for the first time that the α-V_2O_5 film is controllably strained to varying degrees using the shape memory property of the NiTi alloy.

4.3.4 Electrochemical measurements of strained V_2O_5 coatings

Electrochemical measurements were performed on the strained and unstrained V_2O_5 films to assess the effect of imposed mechanical strains. The V_2O_5 (α phase) can intercalate lithium ions in the interlayer spacing along the 'c' direction according to the equation;

$$V_2O_5 + xLi^+ + xe^- \leftrightarrow Li_xV_2O_5 \qquad 7$$

V_2O_5 undergoes a series of electrochemically and structurally reversible transformations from the α phase to the ε phase and the δ phase during intercalation and deintercalation of Li^+ ions (x=1).[155] Intercalation beyond the δ-V_2O_5 phase (when x>1), results in structurally irreversible phase transformations (γ and ω phases) which were avoided in our work.[155, 181] These phase transformations occurring during the Li^+ ion intercalation process are accompanied by structural changes (strains) to the layered V_2O_5 crystal structure. Therefore, we expect that, pre-straining V_2O_5 can contribute to changes in the energetics of the intercalation reaction. Figure 4.4a shows the cyclic voltammograms of the unstrained (0%) and strained (0.35%, 0.5% based on 'c' direction) at a scan rate of 30 mV/s normalized to the maximum peak current. The anodic and cathodic peaks corresponding to the reversible transformations α ↔ ε and ε ↔ δ were observed to shift to lower voltages (also see Appendix, Figure 4.13). We attribute the shift in intercalation potentials to the property changes caused by the elastic strains on the film (also see Appendix, Figure 4.14 and 4.15). The effect of these stored elastic strains on the redox potentials during galvanostatic charge discharge testing and repeated cyclic voltammetry cycling are provided in the appendix (Figures 4.16 and 4.17). The average equilibrium potential ($\Delta E_{eq(avg)}$) can be determined from the mid-point of the anodic and cathodic peak potentials from the voltammograms at various scan rates (see Appendix, Figure 4.18). Figure 4.4b shows the variation of the $\Delta E_{eq(avg)}$ with imposed strains with potential shifts of ~40 mV. For both ~80nm and ~40nm (see Appendix, Figure 4.19) V_2O_5 films, similar shifts in values of $\Delta E_{eq(avg)}$ were observed (see Appendix, Figure 4.20) owing to the similar % 'locked in' elastic strains.

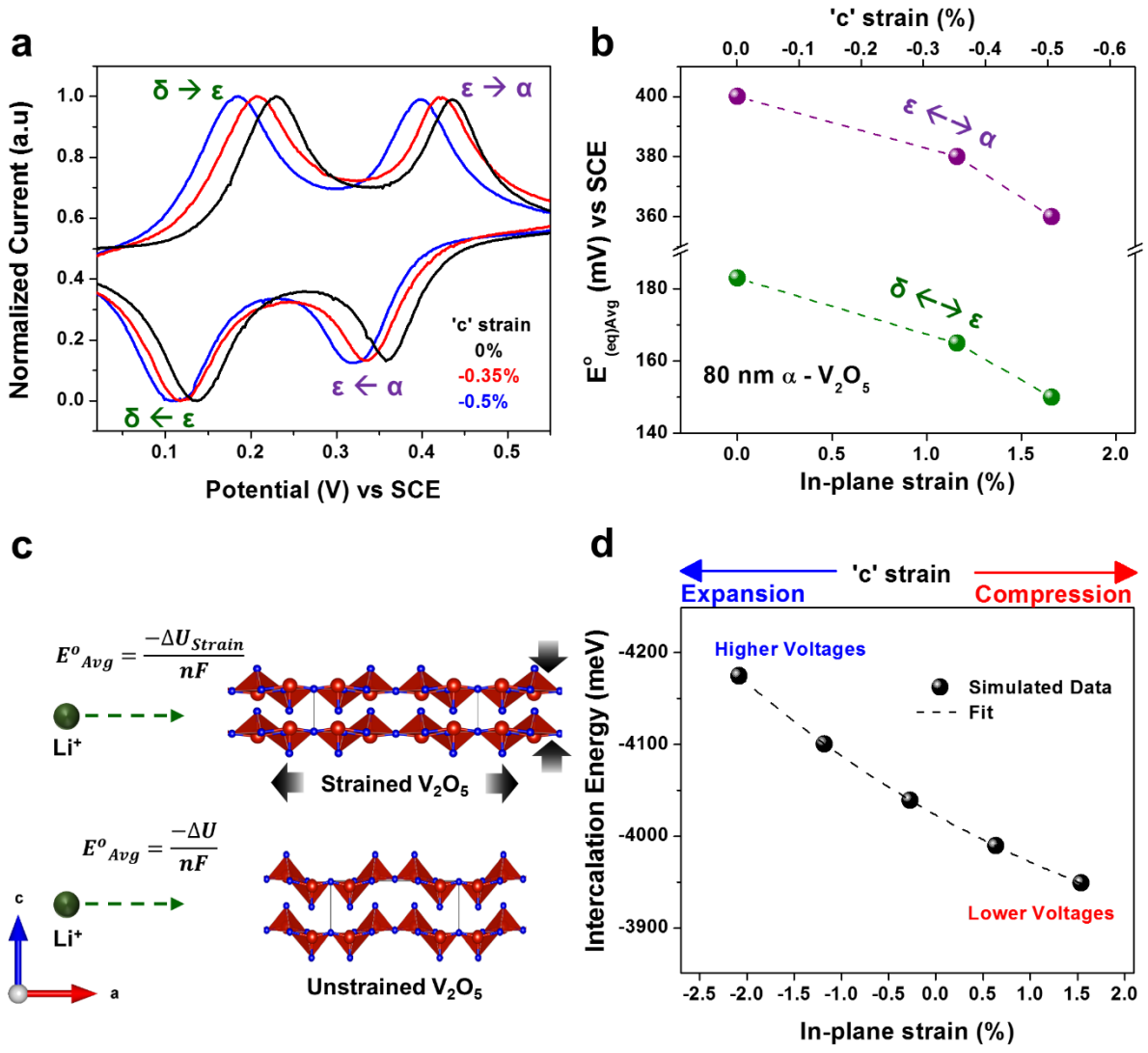

Figure 4.4. (a) Normalized cyclic voltammograms of the unstrained and strained states of the surface V_2O_5 film at a scan rate of 30 mV/s **(b)** Average equilibrium potential variation with imposed strain on the surface film. **(c)** Schematic representation of the energetics governing the electrochemistry of strained and unstrained states of V_2O_5 **(d)** Intercalation energy of the Li^+ ion intercalation process arising from in-plane pre-straining the V_2O_5 lattice to ±2% determined using DFT simulations

$\Delta E_{eq(avg)}$ shift with strain (see Appendix) can be related to the change in free energy ($\Delta G_{Strained}$) and in turn related to the change internal energy ($\Delta U_{Strained}$) of the metal oxide film based on the following equation,[192, 193]

$$\Delta E_{eq(Strained)} = -\frac{\Delta G_{Strained}}{nF} = -\frac{\Delta U_{Strained}}{nF} \qquad 8$$

where n is the number of electrons transferred and F is the Faraday constant (Figure 4.4c). Simultaneous modulation of XRD peaks, Raman shifts, and electrochemical potentials are a result of changes to the total internal energy of the metal oxide films. In particular, only stored elastic strain in our system can alter the internal energy landscape of the V_2O_5 film.[8, 174] Ab initio simulations using density functional theory (DFT) were performed to determine the change in intercalation energy, E_I, between a pre-strained state of V_2O_5 undergoing lithiation compared to an unstrained state (see Appendix, Figure 4.21). This intercalation energy is a measure of the change in total energy of the system when a single lithium atom is removed from BCC lithium metal and placed inside the V_2O_5 lattice. We can model applied strain by changing lattice parameters and assessing how this affects E_I. A change in intercalation energy of ~75 meV (~75 mV) was calculated with an applied in-plane strain of +1.5% on the V_2O_5 lattice (Figure 4.4d), comparable to the measured change in potential of ~40 mV at about ~1.66% in-plane pre-strain in Figure 4.4b. These data corroborate the fact that elastic strains can be an input control parameter to alter the energetics of Li^+ ion intercalation electrodes. Additionally, this model can be used to predict changes in intercalation potentials over a wide range of applied in-plane strains.

4.3.5 Effect of imposed strain on the diffusion coefficient

An important parameter in the study of intercalation electrodes such as V_2O_5 is diffusion of the ions through the crystal lattice. By determining potential dependent 'b' values (see Appendix, Table 4.1) from the relationship, $i=av^b$, where '*i*' is the peak current, '*v*' is the scan rate, '*a*' and '*b*' are adjustable parameters, we observe a combination of diffusion controlled and intercalation pseudocapacitive processes at these peak voltages[163, 169, 194] Based on Randle Sevcik analysis (see Appendix, Figure 4.22) the diffusion coefficient of Li^+ ions (see Appendix, Table 4.2) during the different phase transformations was determined.[17, 155] Owing to the sub-100 nanometer thickness of these strained V_2O_5 films on NiTi alloy, diffusion coefficients in the order of 10^{-9} to 10^{-10} cm^2s^{-1} were observed for all the phase transformations studied in this work.[195-198] The diffusion coefficient ratio between the strained and unstrained states of the V_2O_5 films is given in Figure 4.5a. Due to Poisson's ratio (assuming ~0.3 in our case), a net positive volume change is expected in the film. An out of plane compressive strain results in in-plane tensile strains, which effectively increase the total volume of the crystal (Figure 4.5b). In accordance with this, the diffusion coefficient in the strained state is observed to increase to about 2.5 times when compared to the unstrained state. It can also be noted that as Li^+ ion intercalation in V_2O_5 is accompanied by phase transformations, elastic pre-strains can have an effect on the transformational strain[149] produced due to diffusion of Li^+ ions resulting in significant variation between the diffusion coefficient ratios. Based on previous reports using simulated studies of intercalation cathodes, it can be implied that in our system, the increase in diffusion coefficient could be due to the reduction of ion migration barriers which can be achieved through imposed mechanical strains.[176, 177]

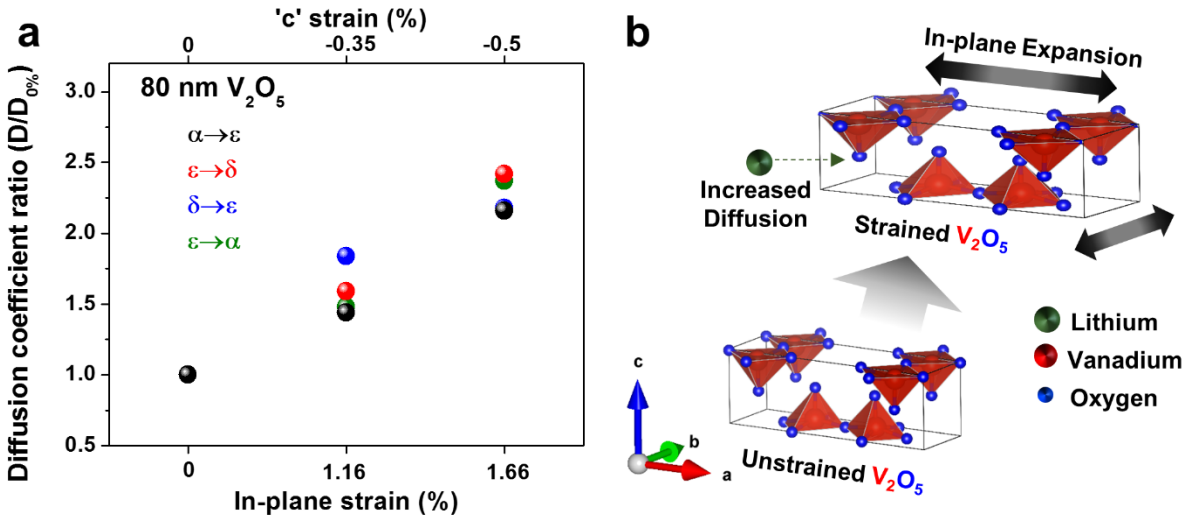

Figure 4.5. (a) Diffusion coefficient ratio $D_{Strained}/D_{Unstrained}$ variation with both 'c' strain and corresponding in-plane strain owing to Poisson ratio, $\nu = 0.3$ **(b)** Schematic representation of the enhancement in diffusion coefficient arising due to a pre-strained V_2O_5 electrode.

The results presented here highlight the principle that tunable mechanochemistry can be a tool to modulate the energetics and kinetics during ion intercalation reactions in energy storage electrode materials. Going forward with this approach where V_2O_5 is only one of many host electrode options, strain engineering can be further applied to emerging research areas focused on storage using alternative ions (Na^+ and K^+)[158, 166, 199] and multivalent ions (Mg^{2+} and Ca^{2+})[200, 201]. The ion size of these alternative materials remains a challenge, but mechanical strains could offset the insertion barriers for these systems and be an important tool for moving beyond lithium. In addition, because strain engineering is a widely-applied principle in solid-state semiconductor electronics, it could be integrated with solid-state battery architectures developed on thin film substrates as well as next generation microbatteries. In any case where cutting-edge battery research efforts have focused efforts on analyzing mechanical strains as a byproduct of intercalation chemistry, our work provides a new picture highlighting the tunable interplay

between mechanics and chemistry of battery electrodes toward development of efficient energy storage devices.

4.4 Conclusion

In summary, we provide insight into the mechanochemistry of battery electrodes, or more generally the ability to modulate battery electrochemistry using tunable mechanical strains. We leverage ALD to deposit nanoscale coatings of V_2O_5 cathodes onto superelastic shape memory NiTi current collectors that are "locked in" at various strain states for electrochemical testing. Our findings indicate modulation of the intercalation potentials by ~40 mV and improving the diffusion coefficient of lithium ions in V_2O_5 by around 2.5 times for applied strains <2%. Further, DFT simulations provide corroboration to experimental results that indicate mechanical strain can be used as a tool to engineer the electrochemistry of batteries. Overall, our work provides insights into the interplay between tunable mechanics and chemistry of battery materials utilizing the principles of strain engineering as a precise engineering tool to improve electrochemical properties of battery materials.

Acknowledgements

We sincerely thank Dr. Rizia Bardhan for the generous use of Raman spectrometer critical for the statistical strain measurements, and Dr. Leon Bellan for use of Instron testing system for tests in this work. We also thank Robin Midget, Bradley Baer, and Alice Leach for useful inputs regarding mechanical tests and XRD measurements. We also thank Andrew Westover, Keith Share, Anna Douglas and Mengya Li for useful technical discussions. This work was supported in part by NSF grants CMMI 1400424 and CBET 1403456, the Vanderbilt University discovery grant program, and R.C. was supported by a VINSE graduate fellowship.

4.5 Appendix

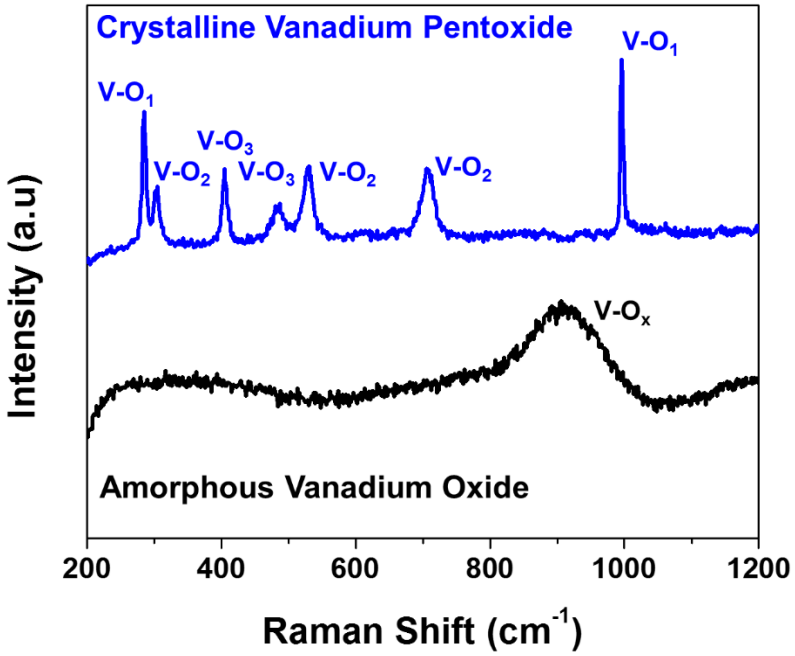

Figure 4.6. Raman spectra of the ALD deposited coating before and after annealing process

The as deposited amorphous VO_x on the NiTi alloy was converted to crystalline V_2O_5 by annealing the coatings in air at 450 ^oC for 30 min. Figure 4.6 shows the Raman spectra of the deposited coatings before and after annealing treatments. The amorphous VO_x coating shows a broad peak in the range of 800 cm^{-1} to 1000 cm^{-1} indicative of lack of long-range order in the coatings. The Raman spectrum of the annealed coating however shows distinct Raman modes corresponding to the various V-O stretch modes of vanadium pentoxide, which indicates the presence of long range order in the V_2O_5 coatings.

4.5.1 Development of thermal interface strain on the V_2O_5 coatings

The deposited vanadium oxide coating using atomic layer deposition technique is amorphous in nature as evidenced by the Raman spectroscopy measurements. Crystallization of the amorphous coating into vanadium pentoxide is achieved through the annealing treatment at 450 ^oC. This

process of high temperature crystallization results in thermal strain development in the coatings during cooling. The thermal strain is developed because of differences in thermal expansion coefficients (CTE or α) between the substrate (NiTi alloy) and the metal oxide coating (V_2O_5) formed during the annealing process. This process is dependent on the temperature and the strain that can be developed in the coatings in such scenarios is called the temperature dependent strain (S_m) given by the following equation,[10, 202]

$$S_m = S_m(T_g) + S_{therm}(T) \qquad 9$$

Where S_m (T_g) is the temperature dependent lattice strain at the growth temperature T_g. Assuming this value to be negligible for simplification, an estimate of the temperature dependent strain can be obtained by determining the thermal strain $S_{therm.}$

$$S_{therm}(T) = (\alpha_s - \alpha_f)(\Delta T) \qquad 10$$

α_s and α_f are the coefficients of thermal expansions of the substrate (NiTi alloy) and the metal oxide film (V_2O_5) respectively. The thermal expansion coefficient of the NiTi alloy from reported literature values[203, 204] is α_{NiTi} = 10.4 x 10^{-6} / ^oC and typical values for CTE of metal oxide films is around 10^{-7} / ^oC. As ($\alpha_s >> \alpha_f$) and using the temperature gradient (ΔT) of around 425 ^oC, we estimate an interface strain of about 0.5% developed between the V_2O_5 film and the NiTi substrate during cooling. Measured strain values from XRD measurements on the film indicated a 'c' directional strain of ~0.8% for thin ALD coatings after 500 ALD cycles when compared to bulk V_2O_5 powders (JCPDF 41-1426). As XRD technique measures an average strain on the surface film, increasing the ALD cycles showed a decrease in the 'c' directional strain owing to strain relaxation effects in thicker coatings.

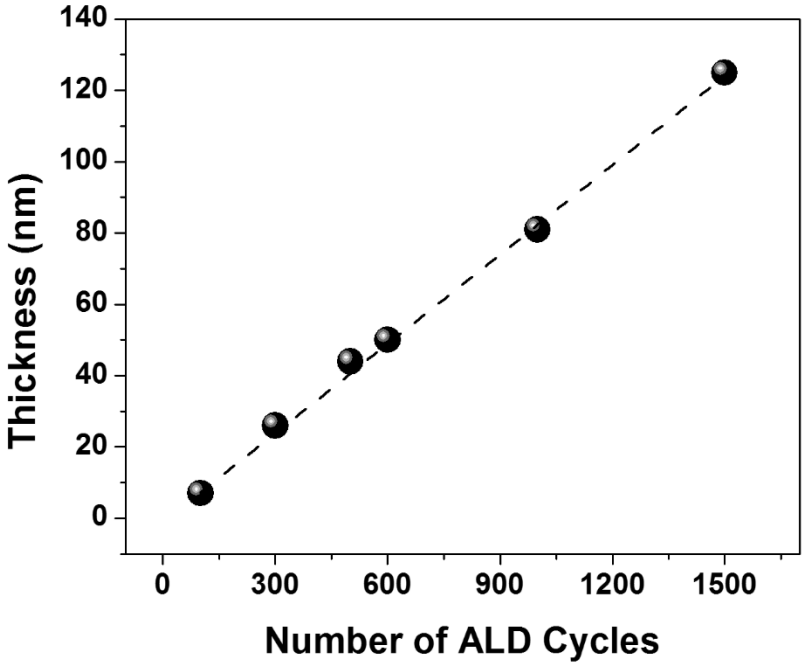

Figure 4.7. Thickness of the crystalline V_2O_5 coatings based on silicon control

Assessment of the thickness of the deposited V_2O_5 surface coatings was performed using surface ellipsometry measurements on a silicon wafer control similar to previous works.[205] Measurements using a silicon control give an estimate of the thickness of the surface coating on NiTi alloy. The actual thickness of the coating on NiTi surface may vary owing to the difference between the nature of seeding layers on NiTi and silicon for vanadium oxide during the ALD process.

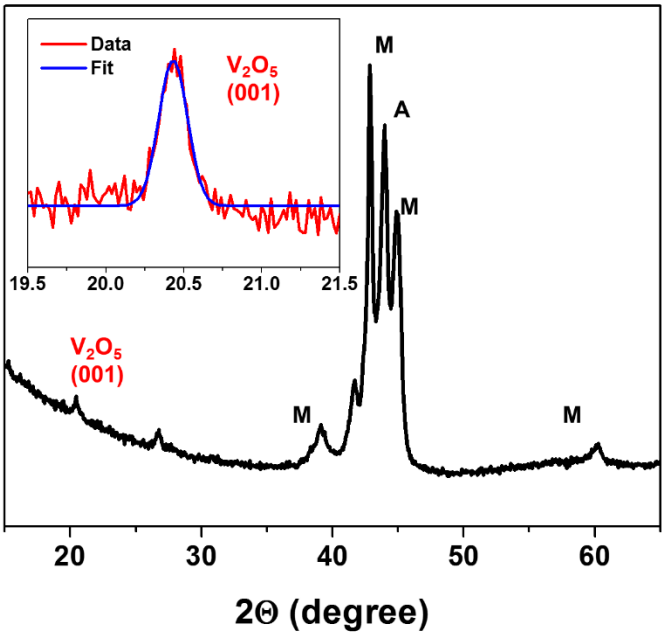

Figure 4.8. X-Ray Diffractogram of the crystalline V_2O_5 coating on NiTi substrate

X-Ray diffraction technique was employed to determine the percent strain on the surface V_2O_5 coatings. Similar to previous reports, we observe a comparatively strong (001) peak indicating the α phase of V_2O_5 (JCPDF 41-1426) with preferred 'c' directional orientation perpendicular to the surface of the NiTi alloy. Owing to the thickness of the V_2O_5 coatings in the nanometer scale, the intensity of the peaks corresponding to the substrate (NiTi austenitic and martensitic phases, JCPDF 18-0899 and JCPDF 27-0344) dominates the diffractogram. Utilizing the observed (001) peak for the V_2O_5 coating and comparing different strain conditions on the NiTi alloy, we determined the percent elastic strain that was 'locked-in' the V_2O_5 coating due to the shape memory effect of the NiTi alloy using the following equation.

$$\% \, Elastic \, Strain = \left(\frac{d_{Strained} - d_{Unstrained}}{d_{Unstrained}}\right) \times 100 \, \% \qquad 11$$

where $d_{Strained}$ and $d_{Unstrained}$ corresponds to the 'd' spacing in the 'c' direction obtained using Bragg's law from the (001) peak positional shifts. To accurately determine the shifts in the (001) peak position based on various strain conditions, Gaussian fits were applied to the peaks.

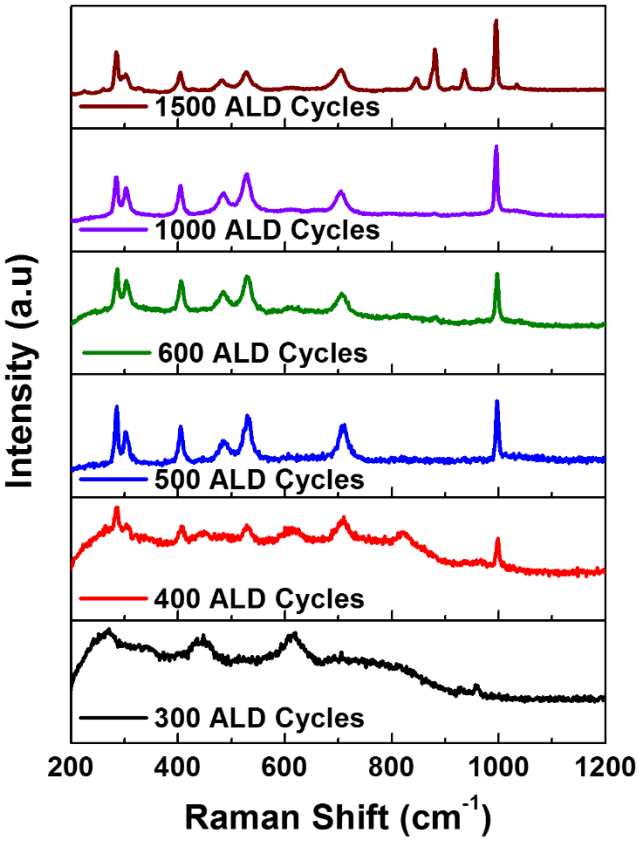

Figure 4.9. Raman spectra of crystalline V_2O_5 coatings at varying thicknesses

Raman spectra of V_2O_5 films of different thicknesses deposited by varying the ALD cycle numbers is given in figure S4. Raman spectra of the crystalline films obtained with fewer than 500 cycles show the lack of a homogenous phase corresponding to α-V_2O_5. The Raman spectra corresponding to 1500 ALD cycles show additional peaks indicative of the presence of V^{4+} oxides along with α-V_2O_5. This gives a usable range of 500 to 1000 ALD cycles and in this study, we chose the ALD cycles of 500 and 1000 as a comparison.

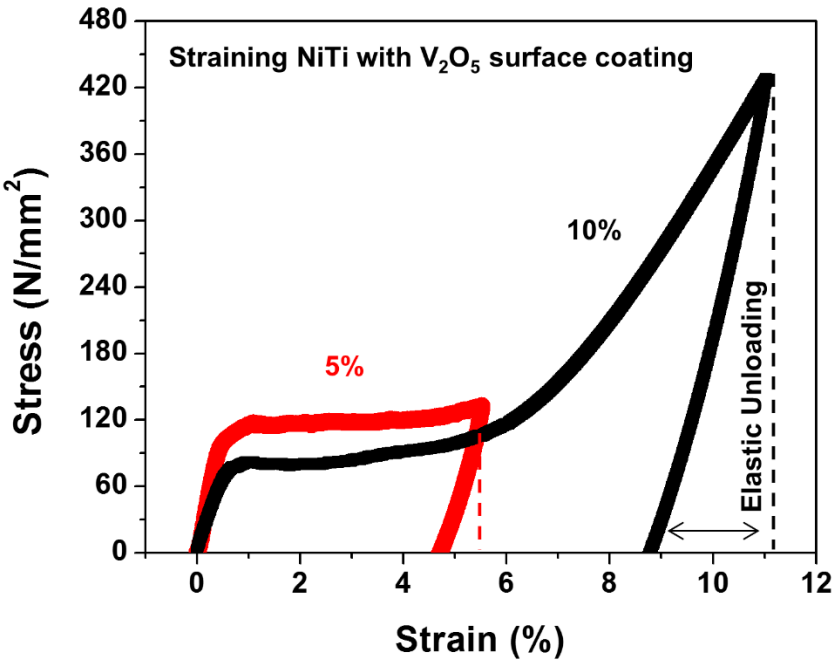

Figure 4.10. Stress-strain response of the NiTi alloy with the V_2O_5 surface coating

The stress-strain response of the alloy indicates an elastic deformation of the austenitic phase of NiTi alloy followed by transformation of austenite to martensite with increasing strains up to 5%. Beyond 5% strain, the transformed martensitic phases in the alloy undergo plastic deformation beyond 10% up to 15% strain. The deformed alloy can be unloaded under different strain conditions after a small elastic unloading retaining most of the applied deformation. Owing to the shape memory property of the NiTi alloy, the applied strains of 5% and 10% can be fixed, which enables the surface V_2O_5 coating to be placed under 'locked-in' elastic strains. The metallic NiTi alloy in our case performs the dual function of strain setting as well as the function of a current collector during electrochemical measurements.

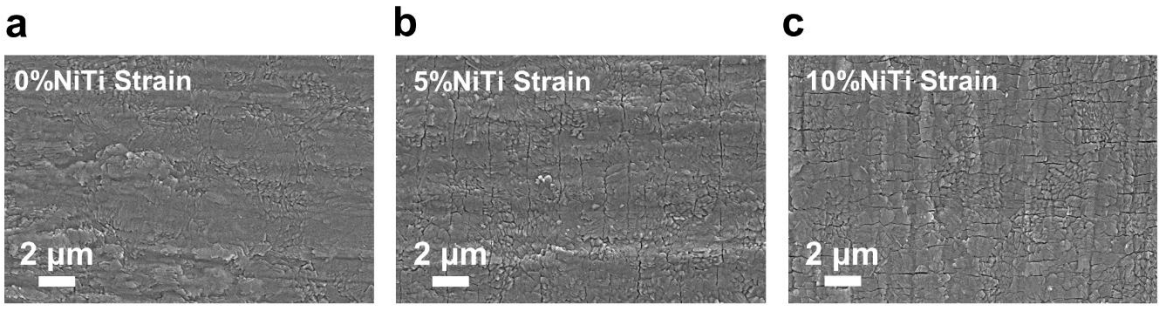

Figure 4.11. (a) Scanning electron micrograph of the surface coating at 0% NiTi strain state. **(b)** Scanning electron micrograph of the surface coating at 5% NiTi strain state. **(c)** Scanning electron micrograph of the surface coating at 10% NiTi strain state

Scanning electron micrographs of the V_2O_5 coatings under different strain states of NiTi indicates the formation of cracks on the surface. As the surface oxide is a brittle ceramic when compared to the ductile NiTi alloy, most of the deformation experienced by the alloy is not transferred to the surface oxide, which limits the strain transfer (<1%).

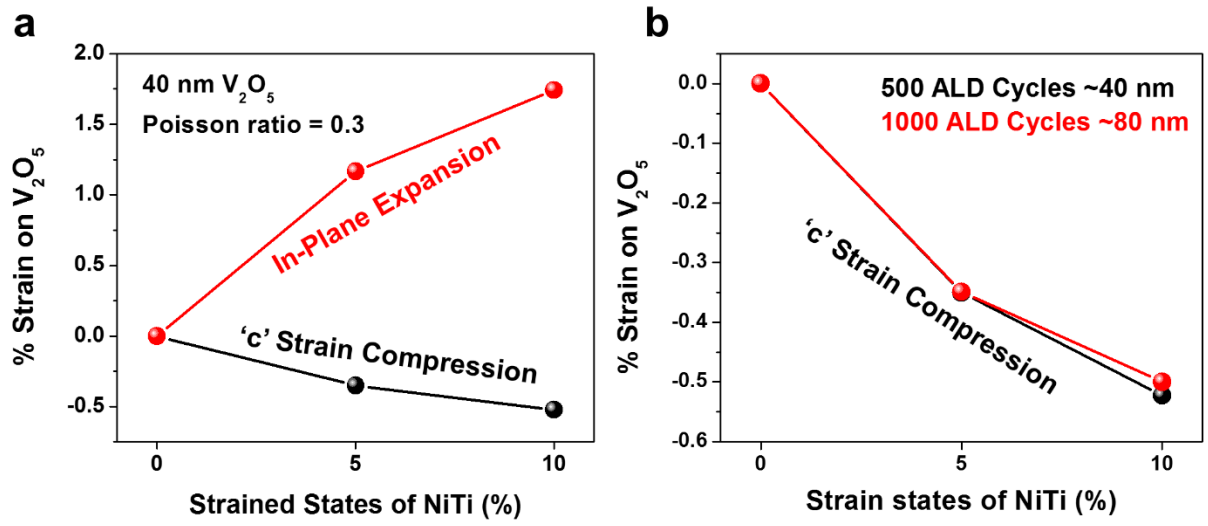

Figure 4.12. (a) percent strain on the ~40 nm V_2O_5 coating at various strain states of NiTi. **(b)** Comparison of locked-in strains between the ~40 nm and ~80 nm V_2O_5 coating at various strained states of NiTI alloy

To understand the feasibility of shape memory alloy assisted strain setting technique in metal oxide coatings such as V_2O_5, we compared two different thicknesses for the oxide film. 500 and 1000 ALD cycles resulted in V_2O_5 films of 40 and 80 nm respectively. 'c' strain values obtained from X-Ray diffractograms for the two thicknesses at the various NiTi strain states indicate a similar strain transfer profile. Comparing both thicknesses, we observe that at 10% strain states for NiTi, a 'c' directional compressive strain of 0.5% and 0.53% for the 80 nm and 40 nm coatings respectively.

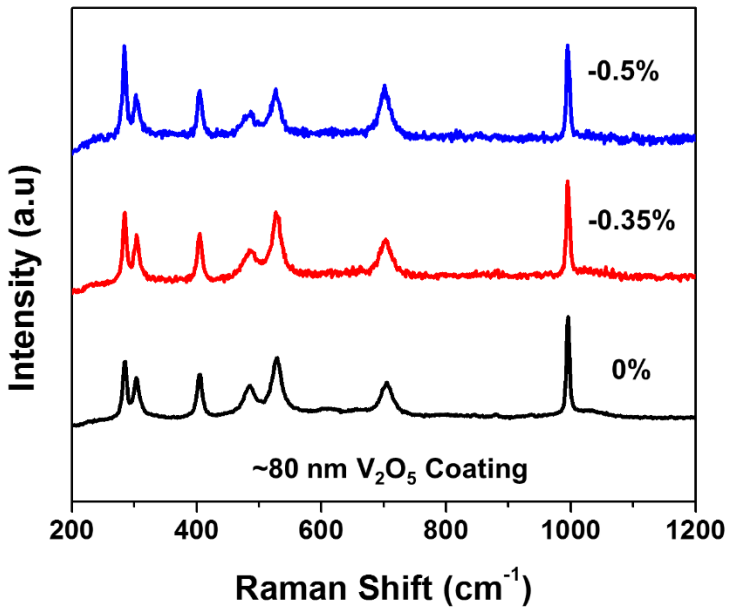

Figure 4.13. Raman spectra of the strained ~80 nm V_2O_5 surface coating

Raman spectra of the ~80 nm V_2O_5 coatings under different applied strains show the presence of all the distinct Raman modes corresponding to the α phase of vanadium pentoxide. This indicates that the strained films maintain their crystallinity. To assess the effect of the applied elastic strains on Raman modes, peak positional analysis was performed by obtaining Raman maps across the surface of these coatings. Each Raman map contained over 500 individual Raman spectra. Lorentzian fits were applied to the individual Raman modes to obtain a statistical analysis of the mean positional redshifts/blueshifts indicating a strained surface film. Histograms of the peak positions indicate a mean shift in the Raman modes of V_2O_5, which varies with the applied strain.

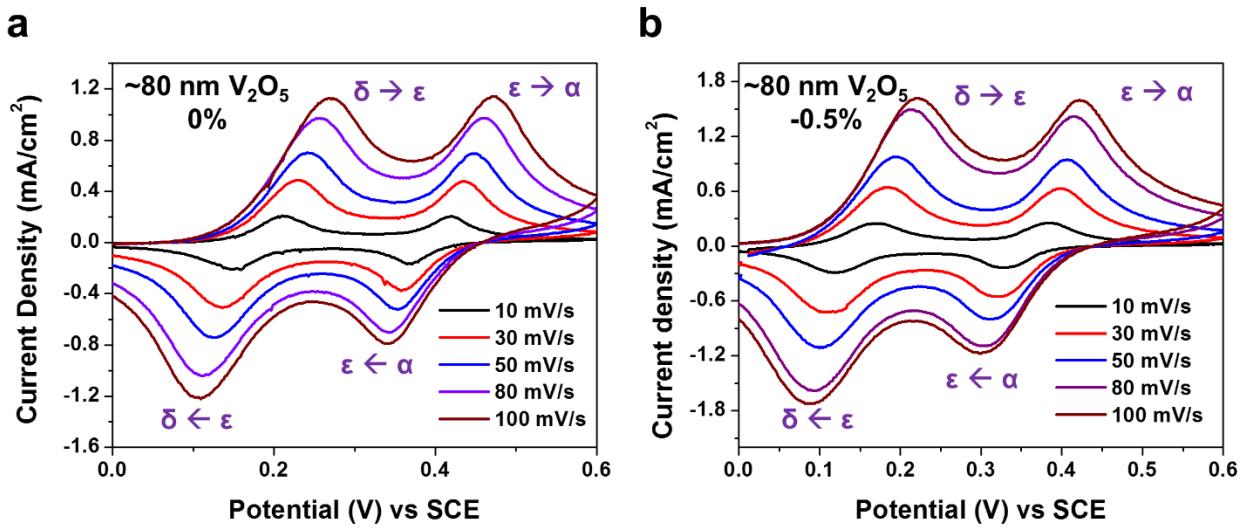

Figure 4.14. (a) Cyclic voltammograms at various scan rates for the unstrained, ~80 nm V_2O_5 coating **(b)** Cyclic voltammograms at various scan rates for the strained (-0.5% 'c' strain), ~80 nm V_2O_5 coating

Cyclic voltammograms of the unstrained and strained ~80 nm V_2O_5 coatings at different scan rates (10 mV/s to 100 mV/s) show stable redox behavior during the intercalation and deintercalation of Li^+ ions. The electrodes were cycled between 0V to 0.6V ensuring both electrochemical and structural reversibility when V_2O_5 undergoes phase transformations (α ←→ ε ←→ δ). The structurally irreversible phases of γ and ω were avoided in this study.

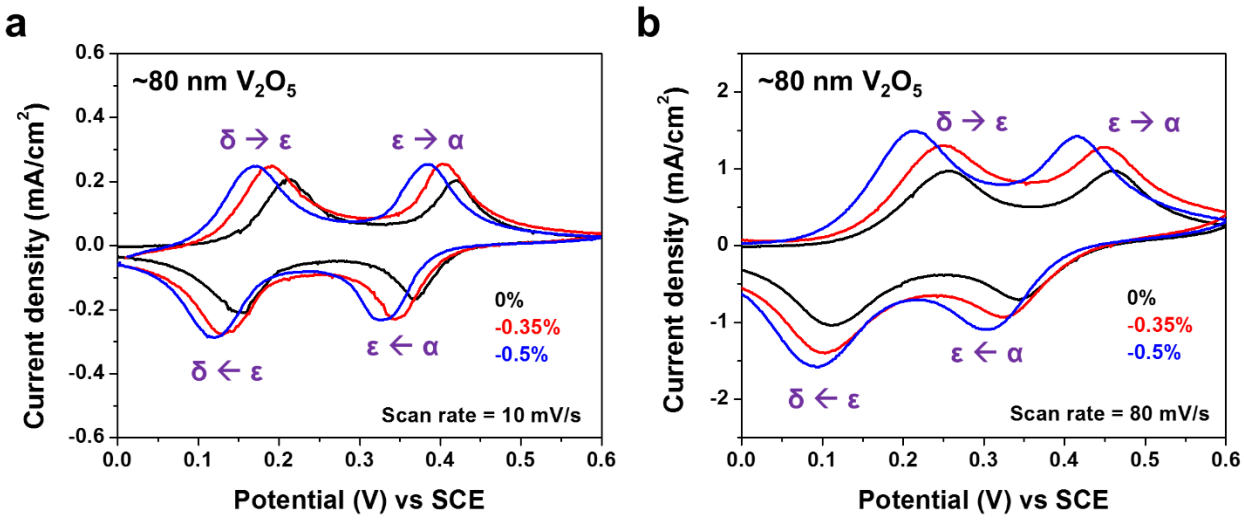

Figure 4.15. (a) Cyclic voltammograms at 10 mV/s for the ~80 nm V_2O_5 coating at different 'c' strain conditions **(b)** Cyclic voltammograms at 80 mV/s for the ~80 nm V_2O_5 coating at different 'c' strain conditions

Cyclic voltammograms of the ~80nm coating at different 'c' directional strain conditions (0-0.5%) indicate a comparative shift in both anodic and cathodic reaction potentials for the two phase transformations of V_2O_5. The shift in peak potentials can be observed in the case of the various scan rates used in measurement as shown in the figure. As these strained metal oxide films undergo surface fissuring, the increase in current density from the unstrained to the strained states can be attributed to an increase in the redox active sites for the intercalation processes.[172]

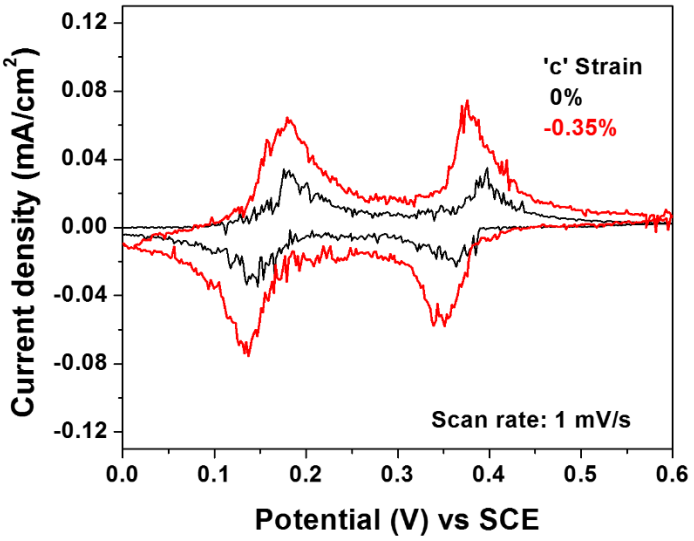

Figure 4.16. Cyclic voltammograms at 1 mV/s for the ~80 nm V_2O_5 coating at different 'c' strain conditions

The coatings were tested at a low scan rate of 1 mV/s to observe shifts to the redox peak potentials. However, owing to the ultrathin coating of V_2O_5 on the surface of a ~0.5mm thin NiTi wire resulted in considerable noise in the current response as a result of the low current detected.

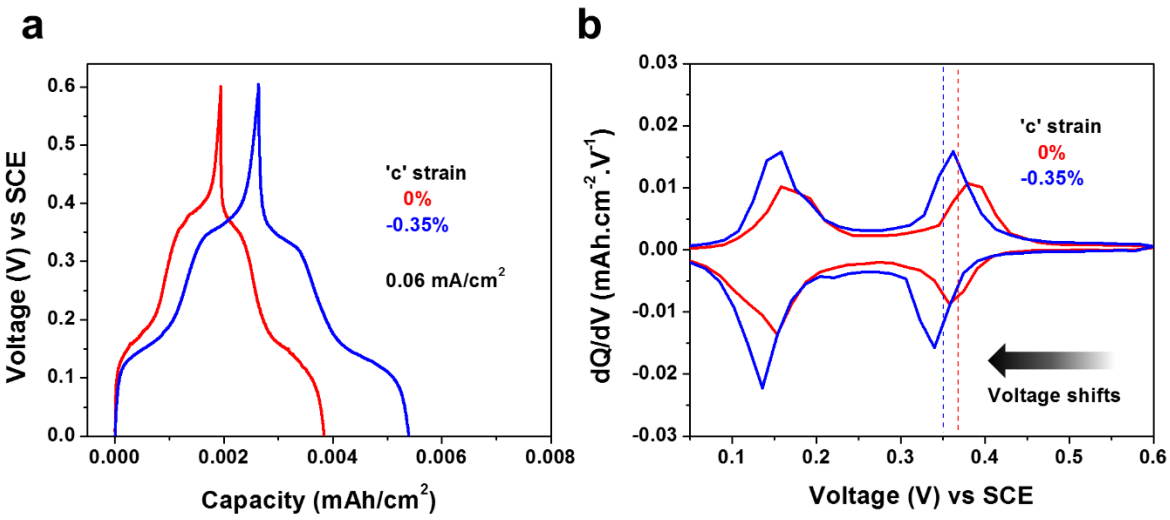

Figure 4.17. (a) Galvanostatic charge discharge curves of the unstrained and strained V_2O_5 coatings at a current density of 0.06 mA/cm^2. **(b)** The corresponding dQ/dV curves for the unstrained and strained V_2O_5 coatings showing voltage shifts.

The galvanostatic charge discharge data for the unstrained and the strained states of the V_2O_5 coatings and the corresponding dQ/dV curves show similar voltage shifts observed in cyclic voltammetric responses. The applied current was normalized to the total immersed area of the electrode.

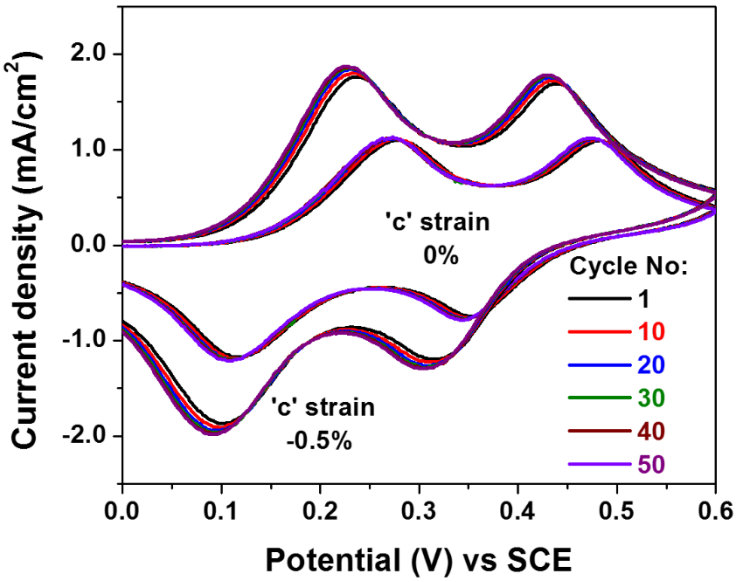

Figure 4.18. Cyclic voltammograms showing cycling of the 80 nm V_2O_5 films at different strain conditions at a scan rate of 100 mV/s.

Cyclic voltammograms of the unstrained and strained V_2O_5 films during cycling is given in figure 4.18. We compared the unstrained 0% to the 'c' strained -0.5% in the cycling tests after an initial 20 conditioning cycles to obtain reproducible voltammograms. During the cycling tests, repeated reversible structural transformations accompany the intercalation process of Li^+ ions into V_2O_5 resulting in a small potential change overtime which is considerably lower than the shifts observed as a result of elastic pre-strains 'locked-in' using the substrate (NiTi alloy).

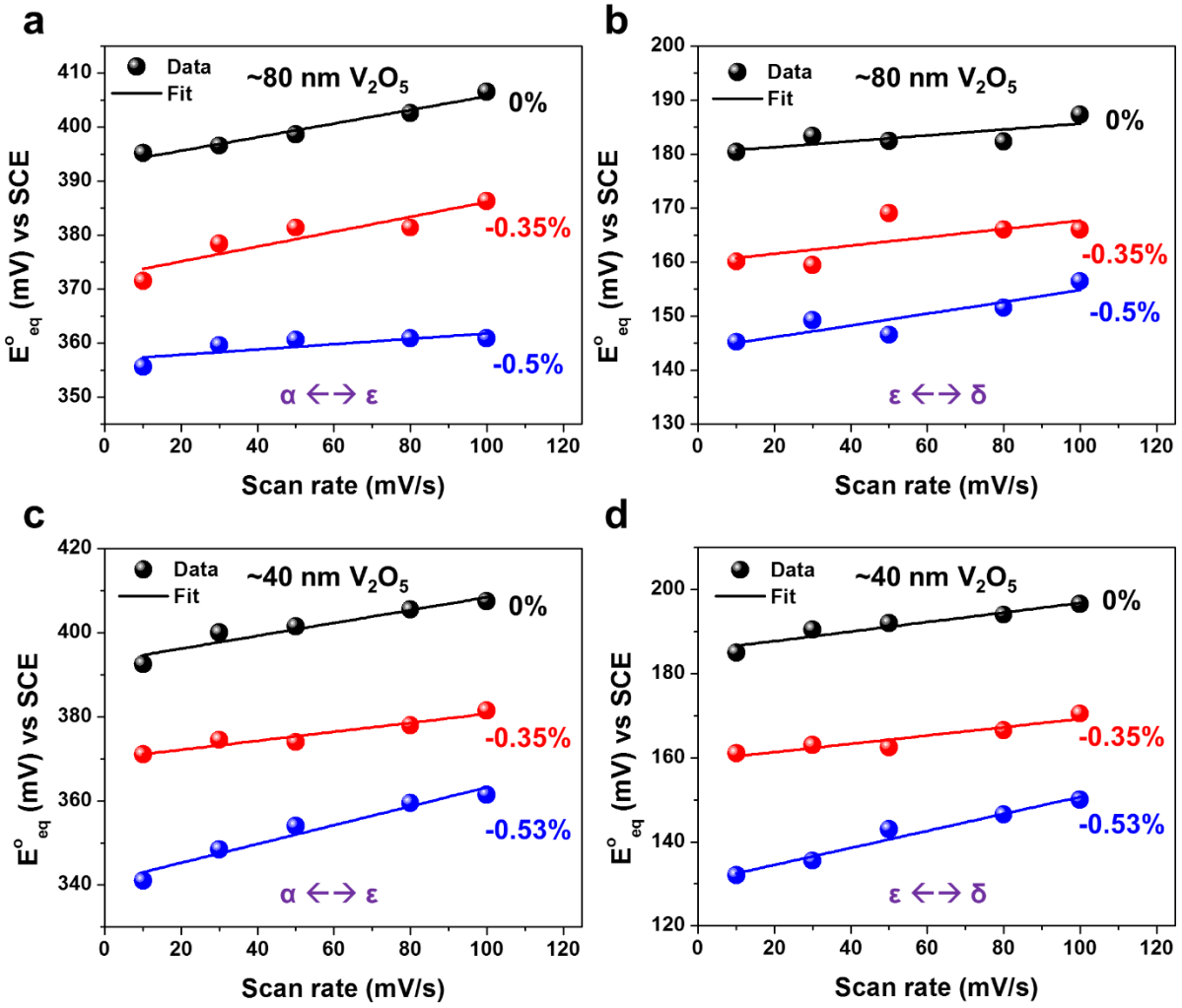

Figure 4.19. (a) E^{o}_{eq} at various scan rates for the ~80 nm V_2O_5 coating at different 'c' strain conditions for the α ←→ ε redox reaction. **(b)** E^{o}_{eq} at various scan rates for the ~80 nm V_2O_5 coating at different 'c' strain conditions for the ε ←→ δ redox reaction. **(c)** E^{o}_{eq} at various scan rates for the ~40 nm V_2O_5 coating at different 'c' strain conditions for the α ←→ ε redox reaction. **(d)** E^{o}_{eq} at various scan rates for the ~40 nm V_2O_5 coating at different 'c' strain conditions for the ε ←→ δ redox reaction.

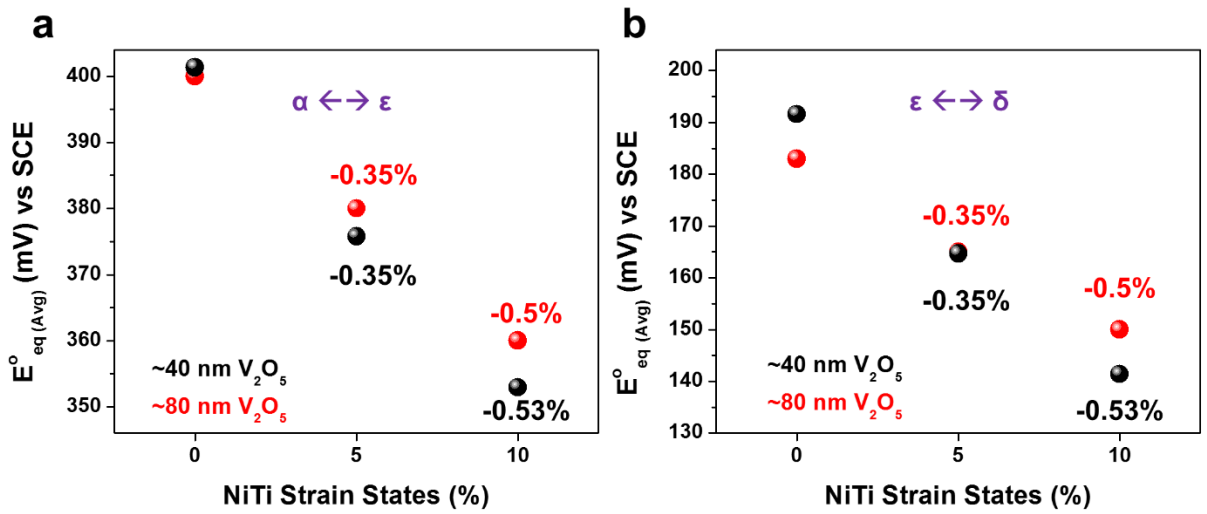

Figure 4.20. (a) Comparison of $E^{o}_{eq(Avg)}$ at various scan rates for the ~40 nm and ~80 nm V_2O_5 coatings at different 'c' strain conditions for the α ←→ ε redox reaction. **(b)** Comparison of $E^{o}_{eq(Avg)}$ at various scan rates for the ~40 nm and ~80 nm V_2O_5 coatings at different 'c' strain conditions for the ε ←→ δ redox reaction.

The E^{o}_{eq} values obtained from the cyclic voltammograms at the different scan rates can be averaged to obtain the value of $E^{o}_{eq(Avg)}$ for two thickness of V_2O_5 coatings at various 'locked-in' strains. As only elastic strains can simultaneously alter XRD peaks, Raman modes and electrochemistry of the surface coating, the 'locked-in' strain can be considered as 'locked-in' elastic strain energy. Shifts in $E^{o}_{eq(Avg)}$ can occur due to various reasons that can be strain induced which include modifications of the energetics of the Li^{+} intercalation reactions, changes to the oxidation state of vanadium in the oxide coating and strain induced variations to the SEI owing to changes to surface reactivity of the electrode all of which require detailed future investigations. However, the shifts observed in our case can be attributed to a strain induced effect as the only input parameter that was varied is the applied strain to the coating.

4.5.2 Energetics of the strained V_2O_5 electrode

Li^+ ion intercalates into vanadium pentoxide undergoing a series of phase transformations. The overall reaction is given by

$$V_2O_5 + xLi^+ + e^- \leftrightarrow Li_xV_2O_5 \qquad 12$$

According to the Nernst equation, the average intercalation voltage can be considered as[206]

$$V_{Avg} \approx \frac{-\Delta G}{F} \qquad 13$$

where ΔG is the Gibbs free energy and F is the Faraday constant. Neglecting entropic contributions, the Gibbs free energy can be replaced with the change in internal energy ΔU.

$$V_{Avg} \approx \frac{-\Delta U}{F} \qquad 14$$

The total internal energy of the reaction can be expressed as,

$$\Delta U = U_{Total}[LiV_2O_5] - U_{Total}[V_2O_5] - U_{Total}[Li] \qquad 15$$

where $U_{Total}[LiV_2O_5]$ and $U_{Total}[V_2O_5]$ represents the total energies per formula unit of LiV_2O_5 and V_2O_5 respectively and $U_{Total}[Li]$ corresponds to the total energy of lithium metal.

To deduce the effect of strain in modifying Li^+ ion intercalation energetics, the change in internal energy can be rewritten as ΔU_{Strain}.

$$\Delta U_{Strain} = U_{Total}[LiV_2O_5]_{Strain} - U_{Total}[V_2O_5]_{Strain} - U_{Total}[Li] \qquad 16$$

where $U_{Total}[LiV_2O_5]_{Strain}$ and $U_{Total}[V_2O_5]_{Strain}$ represents the total energies per formula unit of the intercalated LiV_2O_5 (including pre-strain) and pre-strained V_2O_5 respectively. The changes brought about by the applied pre-strains on the Li^+ intercalation energetics can be obtained using

the energy differences between ΔU_{Strain} and ΔU. To deduce the changes to internal energies occurring in the strained and unstrained cases of V_2O_5, we performed DFT analysis.

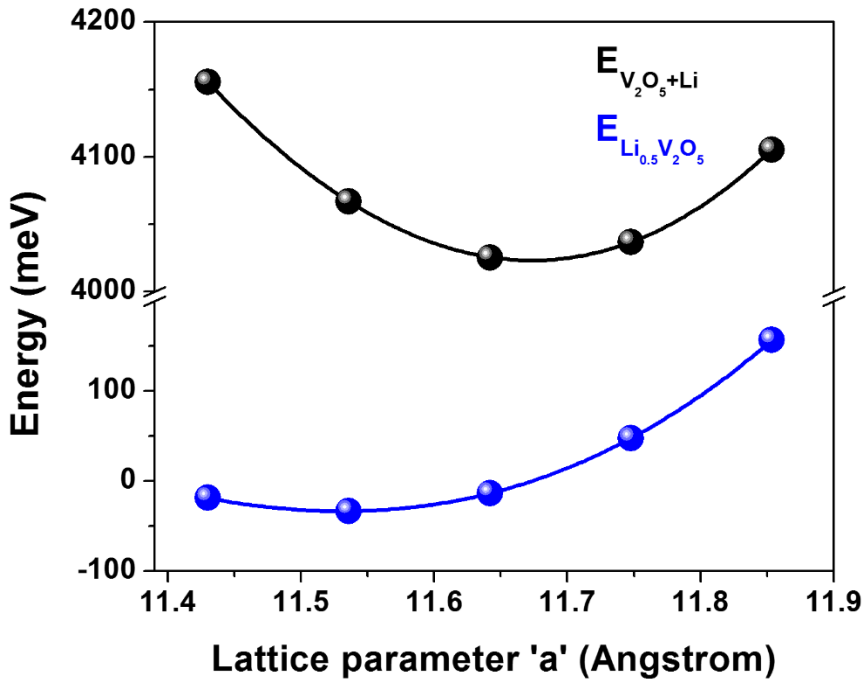

Figure 4.21. Energy curves of the lithiated (blue) and non-lithiated (black) V_2O_5 under applied in-plane strains

The plane-wave DFT calculations were performed in the Abinit code[207, 208] using the LDA XC functional[209] and projector augmented wave datasets[210] generated by Jollet et al.[211] using the AtomPAW code.[212] Total energy differences were converged within 1 meV using a plane wave cutoff of 800 eV and a 2x4x4 Monkhorst Pack k-point grid. Full structure relaxations of the lattice parameters and ionic positions were performed using the Broyden-Fletcher-Goldfarb-Shanno minimization with a force tolerance of $5x10^{-6}$ Ha/Bohr. We relaxed the structure of V_2O_5 starting with an initial structure for V_2O_5 from Laubach et al.[213] The relaxation gave lattice parameters of a=11.53 Angstrom, b=3.56 Angstrom, and c=4.03 Angstrom. The layer spacing (c) was under-predicted compared to experiment, likely because LDA does not correctly capture the

interlayer Van der Waals interaction. We can predict the structure of lithiated V_2O_5, $Li_{0.5}V_2O_5$, by starting with our relaxed nonlithiated V_2O_5 structure and adding one lithium atom to the unit cell which contains two formula units of V_2O_5. We probed 3 sites for potential favorable lithium sites. These initial sites were taken from Braithwaite et al.[214] We fully relaxed the structure for each initial site and chose the one with the lowest final energy. Our final favorable site for the lithium ion in reduced coordinates was (0.5003, -.0008, 0.7495). We used the lithiated structure as a starting point for subsequent total energy calculations for $Li_{0.5}V_2O_5$. For intercalation energy calculations, we also needed the total energy of BCC lithium, which we calculated after relaxing the lattice constant. We can estimate E_I using total energy calculations: $2E[Li_{0.5}V_2O_5]-(E[Li]+2E[V_2O_5])$, where E_I is the approximate voltage of intercalation, $E[Li_{0.5}V_2O_5]$ is the total energy of $Li_{0.5}V_2O_5$ per unit cell, $E[V_2O_5]$ is the total energy of V_2O_5 per unit cell, and E[Li] is the total energy of BCC lithium per atom.[206, 215, 216] $(E[Li]+E[V_2O_5])$ and $E[Li_{0.5}V_2O_5]$ plotted with respect to a lattice parameter are shown in Figure S13. The change in intercalation energy (the difference between the two curves) with applied strain can be obtained by stretching or compressing the unit cell resulting in energy changes. Starting with the relaxed ionic positions above, we calculate $E[Li_{0.5}V_2O_5]$ and $E[V_2O_5]$ at a=(21.6, 21.8, 22.0, 22.2, 22.4). The c lattice parameter and ionic positions are relaxed at each value of applied strain. As noted in the Methods section, we are assuming throughout this work that a and b are fixed during the intercalation process, allowing us to obtain the intercalation energy by calculating $E[V_2O_5]$ and $E[LiV_2O_5]$ at the same a and b. We justify this assumption because physically the a and b directions are held approximately fixed by the substrate, while the layer spacing direction, c, is free to expand or contract. We then fit this data with a 3rd order polynomial for an analytical model of total energy with applied strain.

'c' strain	In-plane strain	α ←→ ε Cathodic	ε ←→ δ Cathodic	ε ←→ δ Anodic	α ←→ ε Anodic
0%	0%	0.67	0.76	0.73	0.74
-0.35%	1.16%	0.64	0.76	0.75	0.72
-0.5%	1.66%	0.71	0.79	0.83	0.80

Table 4.1. Potential dependent 'b' values from the plot of log(i) against log(ν) for the α ←→ ε and the ε ←→ δ redox reactions for the ~80 nm V_2O_5 coating at different c strain and the corresponding in-plane strain conditions.

Using the relationship, $i=av^b$ where 'i' is the current, 'ν' is the scan rate, 'a' and 'b' are adjustable parameters, we obtain the potential dependent 'b' value for the different phase transformations observed in our system from the plot of log(i) vs log(ν). If these 'b' values are close to 0.5 then the current obtained is due to diffusion controlled processes however if it is close to 1 then the current is predominantly due to capacitive processes such as intercalation pseudocapacitance. We see that the 'b' values at these potential dependent phase transformations for the scan rates used in our study was around ~0.6-0.8. Owing to the <100 nanometer thickness of the films used in our study the 'b' values indicate a combination of both diffusion controlled and intercalation pseudocapacitive processes similar to other works in literature.[163, 169, 194]

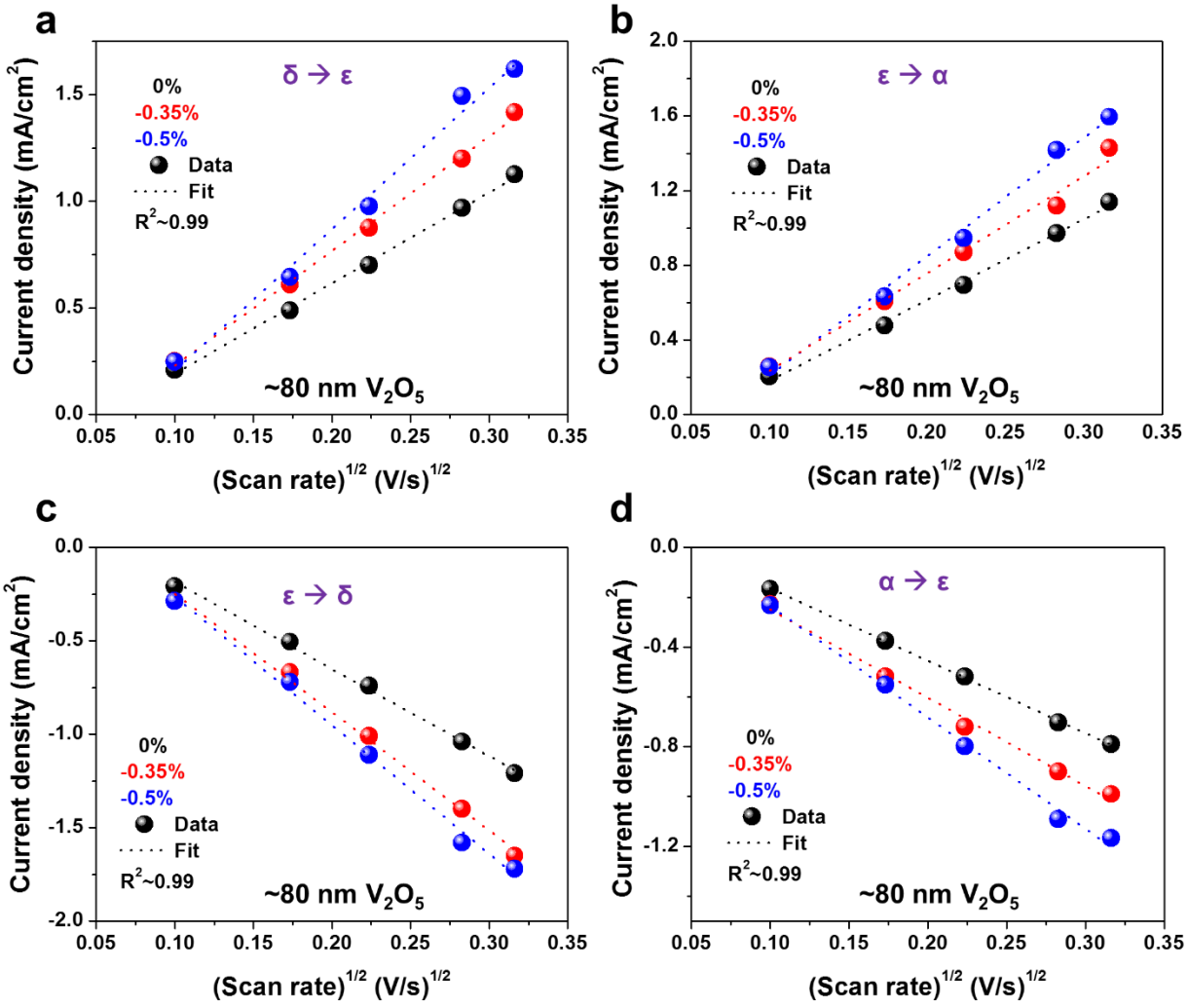

Figure 4.22. (a) Current response with square root of scan rates for the ~80 nm V_2O_5 coating at different 'c' strain conditions for the δ → ε anodic reaction. **(b)** Current response with square root of scan rates for the ~80 nm V_2O_5 coating at different c strain conditions for the ε → α anodic reaction. **(c)** Current response with square root of scan rates for the ~80 nm V_2O_5 coating at different c strain conditions for the ε → δ cathodic reaction. **(d)** Current response with square root of scan rates for the ~80 nm V_2O_5 coating at different 'c' strain conditions for the ε → α cathodic reaction.

Diffusion coefficients for the Li^+ intercalation and de-intercalation into the V_2O_5 lattice through the different phase transformations were determined using the Randle-Sevcik equation.[153]

$$i_{peak} = 268600\, n^{3/2}\, A\, D^{1/2}\, C\, \vartheta^{1/2} \qquad 17$$

where i_{peak} represents the peak current in $A.cm^{-2}$ during the various redox events, 'n' is the charge transfer number, D is the diffusion coefficient in $cm^2.s^{-1}$, A is the area of the electrode surface in cm^2, 'C' is the concentration of Li^+ ions in $mol.cm^{-3}$ and 'ν' represents the scan rate in $V.s^{-1}$. From the plot of peak current and √ν, we observe a linear relationship with typical R^2 values of 0.99. From the slope of the current response, the following diffusion coefficient values were obtained for the ~80 nm V_2O_5 coating at the different strain conditions.

'c' Strain (%)	In-plane Strain (%)	ε-α Anodic (cm^2/s)	α-ε Cathodic (cm^2/s)	δ-ε Anodic (cm^2/s)	ε-δ Cathodic (cm^2/s)
0	0	2.07E-09	9.27E-10	1.99E-09	2.39E-09
-0.35	1.16	2.99E-09	1.38E-09	3.17E-09	4.41E-09
-0.5	1.66	4.47E-09	2.20E-09	4.83E-09	5.22E-09

Table 4.2. Diffusion coefficients determined using Randle-Secvik analysis for the α ←→ ε and the ε ←→ δ redox reactions for the ~80 nm V_2O_5 coating at different c strain and the corresponding in-plane strain conditions.

As per the Poisson's ratio, a c directional compressive strain should result in an in-plane expansion in the crystalline V_2O_5 film. The net volume in such cases increases which could result in reduction in Li^+ migration barriers into the V_2O_5 lattice. It should be noted that the nature of strain applied to the metal oxide film can also be modulated by the geometry of the substrate.

Chapter V

5 Ultralow Frequency Electrochemical – Mechanical Strain Energy Harvester using 2D Black Phosphorus Nanosheets

5.1 Introduction

An ambient mechanical energy harvester converts input mechanical energy into electrical energy, which can be transferred and utilized in other systems.[217, 218] Conventional methods of ambient mechanical energy harvesting commonly utilize a variety of piezoelectric and triboelectric materials.[219-221] Although these materials are capable of effective energy harvesting at high frequencies (>10 Hz), their performance drastically drops when these devices are operated under low frequency (<1-5 Hz) and static loading conditions corresponding to ambient human mechanical interactions.[217, 221, 222] Consequently, human gait is distributed at frequencies below 5 Hz, leaving high frequency harvesters that inherently operate at low conversion efficiencies to harvest energy in only a small window of a normal human motion.[223, 224] To overcome this, new device platforms need to be developed with the simultaneous capability to operate at high mechanical conversion efficiencies and harvest energy through full duration of low-frequency human motions. This requires the development of harvesting methodologies beyond existing materials and systems.

In this regard, researchers have recently started to investigate the mechanical – electrochemical coupling in conventional Faradaic energy storage materials and batteries.[41, 175, 217, 225-228] Observations by Kim *et al.* demonstrated a small potential difference that emerges in a silicon – lithium system that is instigated by mechanical stresses, which can be leveraged for strain energy harvesting.[229] Similarly, other recent efforts have demonstrated stress-induced shifts to

equilibrium potentials in electrochemical energy storage materials by using strain as a controlled input parameter, which reveals the origin of this electrochemical-mechanical coupling.[41] These early studies leverage mechanical stresses, which are otherwise considered an adverse side-product of an ion-storing electrochemical system,[144, 230] to modulate the energetics of ion insertion that can be leveraged for strain energy harvesting. This allows the high energy density storage through Faradaic reactions occurring in battery materials to be tapped in systems designed to use mechanical energy inputs to drive or control these reactions. Since battery materials natively undergo charge-discharge processes at low frequencies, this means that harvesters built on the working principles of battery materials will natively exhibit a frequency range of operation that is better matched to low-frequency human motions < 5 Hz.[217, 225]

Whereas early studies discussing and leveraging the mechano-chemical response of batteries have so far focused on thick bulk-like materials, two-dimensional (2-D) materials present an exciting alternative for strain harvesting. Strain coupling into 2-D materials can be highly efficient unlike the case for bulk materials, and many 2D materials exhibit strain responses deviating from their bulk material counterparts that can be exploited in such devices.[41, 231] An excellent example of this is 2-D black phosphorus, or phosphorene, which exhibits a negative Poisson's ratio in a single-layer configuration and remains an exciting material to study due to its anisotropic optical/electronic response.[232-234] Additionally, phosphorene has also been demonstrated to exhibit the highest known capacity for sodium ion storage (2596 $mAhg^{-1}$) and unlike bulk silicon,[230] boasts a 2D material structure that enables robust stability over cycling durations at slow rates.[165, 235, 236] Until now, the concept of electrochemical-mechanical coupling in 2-D materials remains unexplored, and materials such as phosphorene remain at the forefront as ideal candidates for such systems.[237]

This motivates our current study, which is to exfoliate, assemble, and sodiate 2-D black phosphorus nanosheets to produce a low-frequency energy harvester device. By combining equipotential Na_xP electrodes in a sandwich configuration, we demonstrate stress-induced migration of sodium ions resulting from ambient mechanical inputs such as bending and pressing at frequencies otherwise inaccessible by conventional piezoelectric materials (0.1 – 0.01 Hz). This prototype device configuration generates peak power of 42 nW/cm^2 and energy of 0.203 $\mu J/cm^2$ in bending mode (0.1 Hz) and peak power of 9.1 nW/cm^2 and energy of 0.792 $\mu J/cm^2$ in pressing mode (0.01 Hz). These results emphasize the promise of 2-D material platforms for high performance human motion harvesters.

5.2 Experimental methods

5.2.1 BP exfoliation, deposition and electrode assembly

Bulk BP (Smart Elements) was added to NMP (99.5%, Aldirch) solution with an initial concentration of 0.625 mg/mL. BP exfoliation was assisted by a tapered-tip on a probe sonicator (Sonics, VCX750, 40% amplitude) with a 3s on and a 3s off pulse in ice bath for 5 hrs. Exfoliated solution was left overnight for further use. Few layered graphene was grown on Cu foil (Strem Chemicals) using chemical vapor deposition technique (CVD) using C_2H_2 (0.3 sccm) as the precursor gas in an Ar (500 sccm) and H_2 (2 sccm) atmosphere at 1000 ^oC. Cu foil with the CVD grown graphene was selected as the substrate for the deposition of black phosphorus. Electrophoretic deposition (EPD) was performed using a Keithley 2400 Sourcemeter integrated with LabView data acquisition software at a constant voltage. Graphene on Cu foil with dimension of ~1.5 cm x 3 cm was used as positive electrode, 316 stainless steel with same dimensions was used as counter electrode. The separation between the two electrodes was ~1

cm. A constant voltage of 10 V was applied for 2 hrs and the resulting electrode was placed in a vacuum oven to dry overnight before further characterization and device assembly.

5.2.2 Electrode characterization

The morphology of exfoliated BP was characterized using a FEI Osiris TEM transmission electron microscope (TEM). Zeta potential and particle size measurements were determined using a Malvern Zetasizer Nano ZS instrument. The morphology of the BP deposited graphene/Cu electrodes were characterized using a Zeiss Merlin scanning electron microscope (SEM). Raman spectroscopy was carried out using a Renishaw inVia MicroRaman system with a 532 nm laser. For electrochemical characterization, the electrode was cut into ~0.7 cm x 0.6 cm pieces, and then directly assembled into a CR2032 type coin cell inside an Argon-filled glovebox. Sodium metal (Aldrich) was used as counter electrode. 1 M $NaClO_4$ (≥98.0%, Aldrich) in ethylene carbonate (EC)/diethyl carbonate (DEC) (99%/>99%, Aldrich) with 1:1 volume ratio was used as the electrolyte with an additional 10 vol% 4-Fluoro-1,3-dioxolan-2-one (FEC, 98%, Alfa Aesar) as an additive. A Whatman grade GF/F glass fiber microfiber filter (Aldrich) was used as separator. Galvanostatic discharge was performed at a current density of 0.01 mA/cm^2 from open circuit voltage (V_{OC}) to 0.02 V.

5.2.3 Fabrication of the energy harvester and testing

The BP deposited graphene/Cu electrodes were connected in short circuit mode against pure sodium metal (Aldrich) using the same electrolyte as mentioned to sodiate the black phosphorus for 4 hours. The sodiated electrode was then cut into two identical halves which form the two electrodes of the energy harvester. The two electrodes were then assembled in a sandwich configuration with an electrolyte soaked polypropylene separator (Celgard 2500) was used as the separation between the two electrodes. Kapton tapes (Ted Pella) were used to encase the device

thereby sealing the system from external environments as well as creating an air tight configuration. The device was then connected in short circuit mode using an external wire for 2 hours to homogenize the composition of both electrodes of the harvester. Small compositional inhomogeneity between the two electrodes of the harvester would result in unsteady background currents during the initial bending and unbending cycles. Reproducible current responses can be obtained after a few initial bending, holding and unbending conditioning cycles. Bending and pressing tests were conducted manually using hand bending around pipes of various diameters and pressing load determined using a weighing balance during testing. Short circuit currents and open circuit voltages were determined during repeated bending and pressing tests using a portable Autolab PGSTAT 101 testing system.

5.3 Results and discussion

5.3.1 Materials development and characterization

To form electrodes to test as mechano-chemical strain energy harvesters, nanosheets were exfoliated from black phosphorus (BP) in 1-methyl-2-pyrrolidone (NMP) solutions by using probe sonication (Figure 5.1a). Transmission electron microscope (TEM) images of the exfoliated 2D BP (Figure 5.1b and 5.1c) show thin BP nanosheets generally between 3-20 atomic layers with a measured interlayer spacing of 3.80 Å. Dynamic light scattering (DLS) was also used to characterize the exfoliated materials (Figure 5.6, Appendix) and demonstrates effective exfoliation of nanosheets into NMP.

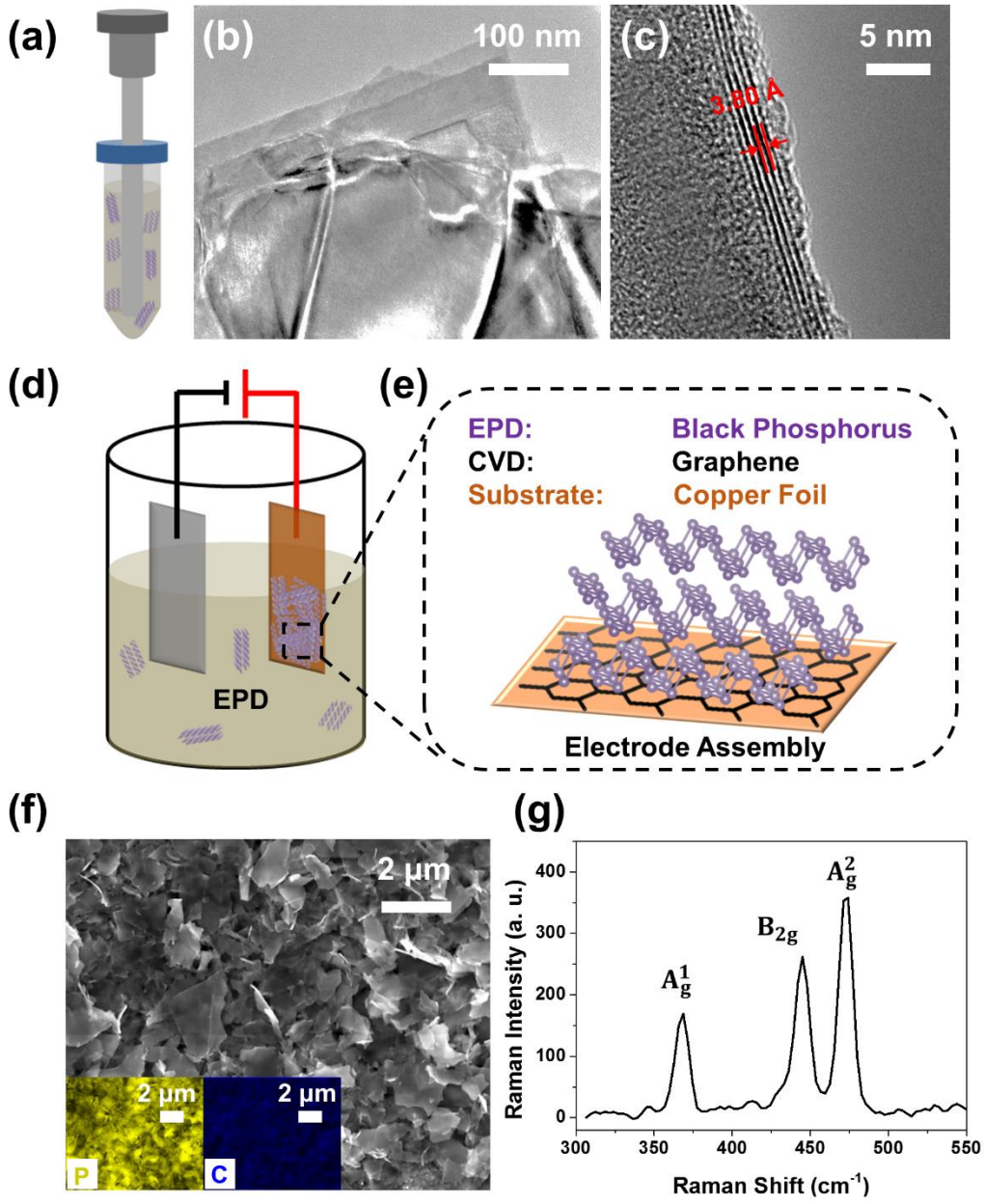

Figure 5.1. (a) Schematic illustration of BP exfoliation in NMP solution through tip sonication. **(b)** Low and **(c)** High-magnification TEM images of exfoliated BP nanosheets. **(d)** Scheme of EPD set-up. **(e)** Zoom-in view of the electrode configuration. **(f)** SEM image of top-down view of deposited BP on graphene on Cu (with insets indicating SEM EDS elemental mappings of phosphorus and carbon). **(g)** Raman spectroscopy of the deposited BP.

To produce strain harvester electrodes from these 2D building blocks, electrophoretic deposition (EPD)[238, 239] was used (see experimental methods). To produce a bendable and electrically conducting interface for BP nanosheet coatings, graphene was grown on thin copper foils using chemical vapor deposition, which was found to be the best interface for the harvester active material. The zeta potential for the exfoliated BP solution was measured as -56.7 mV, which dictates a negative surface charge of the exfoliated BP nanosheets. EPD was performed by applying a constant voltage on the positive electrode (graphene/Cu) and counter electrode (stainless steel) that was immersed in exfoliated BP suspended in NMP (schematically represented in Figure 5.1d). Due to the negative surface charge of the BP nanosheets, the dispersed exfoliated BP preferably deposit onto the positive electrode (graphene/Cu) under an applied electric field. The corresponding deposition I-t curve is provided in the Figure 5.7 (Appendix). Figure 5.1e gives a schematic representation of the assembled BP nanosheets on the graphene/Cu substrate. Scanning electron microscopy (SEM) and corresponding elemental maps obtained from energy dispersive X-ray spectroscopy (Figure 5.1f) show effective assembly of exfoliated BP nanosheets on the graphene/Cu substrate. The mass of exfoliated BP deposited onto the positive electrode was measured as 0.95 mg/cm^2 for a 2 hour deposition at a bias voltage of 10 V. Raman spectroscopy of the deposited BP on graphene/Cu (Figure 5.1g) shows the A_g^1, B_{2g}, and A_g^2 modes of BP (~ 367 cm^{-1}, 445 cm^{-1}, and 473 cm^{-1}, respectively).[165] The complete Raman spectrum of the BP-graphene electrode is provided in Figure 5.8 (Appendix).

5.3.2 *Fabrication of the strain energy harvester*

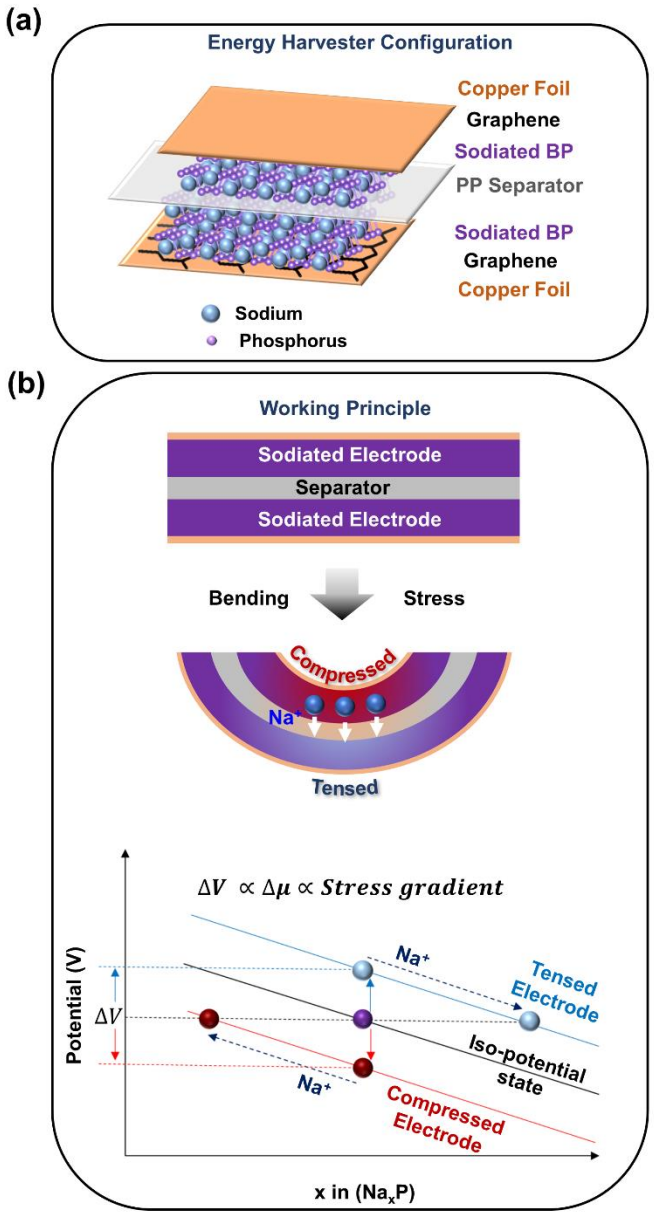

Figure 5.2. (a) Schematic representation of the configuration of the black phosphorus mechanical energy harvester. **(b)** Schematic representation of the working principle of the energy harvester.

To produce an electrochemical-mechanical strain harvester, a BP nanosheet coated electrode was shorted against sodium metal for 4 hours, cut into two identical pieces, and then combined into the configuration illustrated in Figure 5.2a with a polypropylene separator. The entire assembly was left connected in short circuit using an external wire for 2 hours to reach an isopotential state between the two electrodes (see methods and schematic illustration of the sodiation process in Figure 5.9, Appendix). As illustrated in Figure 5.2b, the device operates on the principle that bending or pressing induces a stress gradient between the two electrodes. Considering the scenario when the device is bent, the Na_xP electrode becomes compressed on one side whereas the other electrode becomes tensed. These stresses are hence directly transmitted to the 2D building blocks making up the harvester. This generates a potential difference that originates from the different mechano-chemical response of electrochemical systems under compressive or tensile stress.[41, 175, 228] This mechanism generally holds true for pressing as well since the indentation in the material generated by pressing will lead to a strain gradient, albeit with smaller magnitude than bending motions. To reach an equilibrium potential on the electrodes, Na^+ ions travel from the compressed region to the tensed region across the separator which is accompanied by the flow of electrons in the external circuit resulting in measured current flow. Here, the compressed electrode becomes the cathode and the tensed electrode becomes the anode.

5.3.3 Electrochemical response of the energy harvester

The current output of the device can be monitored using short circuit current measurements from the device during the application of bending and pressing stresses (Figure 5.3 a-b). A sharp increase in current signal is observed in both cases followed by gradual decay of current when the device is held under bending/pressing condition (Figure 5.3a). The decay

occurs due to the relaxation of the stress gradient through alloying induced stress of the migrating Na^+ ion resulting in gradual neutralization of the chemical potential gradient. The duration of ion migration matches the duration of the stress gradient imposed, and upon unbending or releasing the load on the device, the stress gradient vanishes leading to a cessation of ion flow, and hence current generation. Full width at half maximum values for the current response was ~ 10 seconds for both bending and pressing tests which was considerably higher than traditional piezoelectric materials (~ 100 milliseconds).[229, 240-243] Thus, our device can be utilized in harvesting ambient mechanical energy in the ultra-low frequency regime (0.1 Hz to 0.01 Hz). Notably, whereas this device exhibits performance that builds upon battery operation, the device is not inhibited by the same safety concerns as traditional battery systems. Since the harvester operates from an isopotential state, shorting the device will simply deactivate the harvesting capability of the device and not generate thermal runaway that leads to electrolyte ignition and battery fires. Safety considerations of this electrochemical harvester are discussed at length in the appendix.

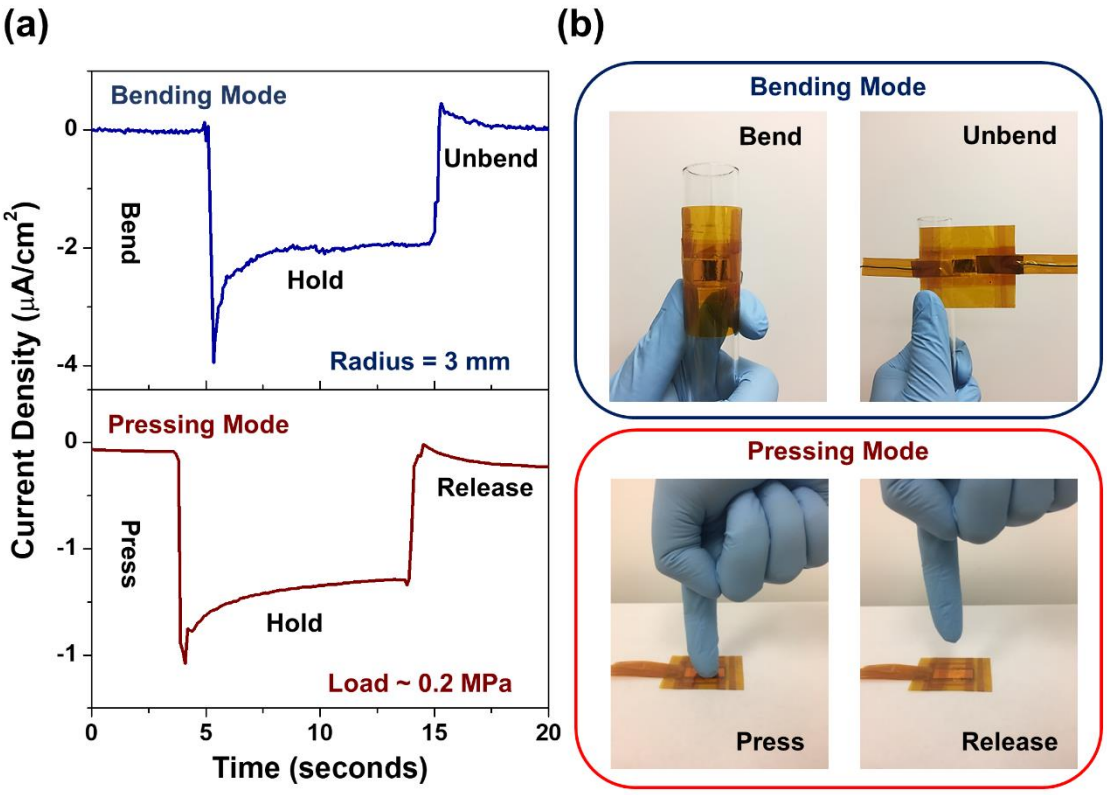

Figure 5.3. (a) Short circuit current response of the energy harvester during bending and pressing mode. **(b)** Representative images of bending and pressing tests performed on the developed energy harvester.

5.3.4 Open circuit and short circuit responses of the harvester

Repeated bending-unbending and pressing-releasing tests were performed on the device to assess repeatability of the electrical responses (Figure 5.4). Open circuit voltage measurements (V_{OC}) provide the maximum possible voltage outputs for a given stress condition in the absence of any current flow. Figure 5.4a shows the V_{OC} response of the device bent at a radius of curvature of 3 mm at a frequency of 0.1 Hz. When the bending stress is applied, the V_{OC} increases to reach a maximum value that is maintained as long as the stress is applied. Upon unbending the device, the V_{OC} recovers to its initial isopotential state. Notably, the nature of

measuring V_{OC} that does not explicitly involve Na^+ ion migration to neutralize the mechanically induced stress gradient causes a gradual decrease of background potential as one electrode of the harvester is repeatedly placed under tension and the other is repeatedly under compression. The device was tested at different bending radii (Figure 4.10, see Appendix) which shows an inverse dependence of the V_{OC} on the bending radii as expected (Figure 4.11, see Appendix). Figure 5.4b shows the short circuit current measurements during repeated bending-unbending tests at a frequency of 0.1 Hz. Large bending radii result in lower applied stress/strain leading to lower chemical potential gradient and lower current flow. Figure 5.4c and 5.4d show the V_{OC} and short circuit current responses during repeated pressing and releasing tests at frequencies of 0.1 Hz. Similar to the bending response, pressing the electrodes sets up chemical potential gradients correlated to the open circuit and short circuit current response from the device. Pressing tests were performed by the application of static loads (~ 0.2 MPa) held for various time periods (10 and 100 seconds). Repeated pressing tests were performed at very-low frequencies of 0.01 Hz corresponding to a 100 second hold time (see Figure 5.12, Appendix). During pressing tests, the response time of these devices can be varied from 10 seconds to 100 seconds depending upon the hold time providing a framework for harvesting electrical energy from static load conditions. To demonstrate the stability of the device response over long cycling duration, we carried out repetitive bending experiments with 50 cycles shown in Figure 5.4e at 0.1 Hz frequency and bending radius of 3 mm. Over the course of long-term cycling experiments, we observed no significant degradation in the mechano-chemical response associated with the strain harvester operation.

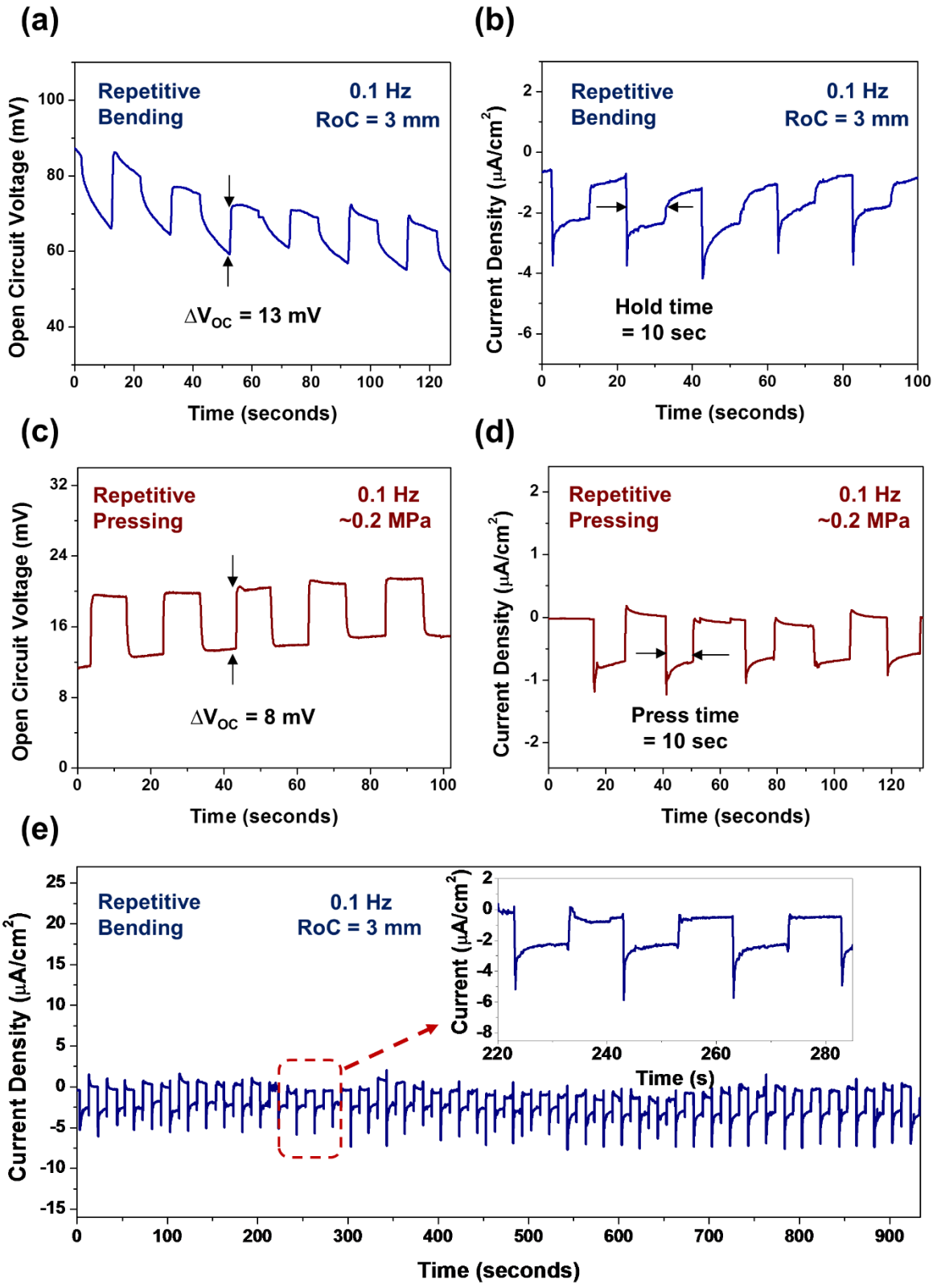
(a)
Repetitive Bending
0.1 Hz
RoC = 3 mm
ΔVOC = 13 mV
Open Circuit Voltage (mV)
Time (seconds)
(b)
Repetitive Bending
0.1 Hz
RoC = 3 mm
Hold time = 10 sec
Current Density (μA/cm2)
Time (seconds)
(c)
Repetitive Pressing
0.1 Hz
~0.2 MPa
ΔVOC = 8 mV
Open Circuit Voltage (mV)
Time (seconds)
(d)
Repetitive Pressing
0.1 Hz
~0.2 MPa
Press time = 10 sec
Current Density (μA/cm2)
Time (seconds)
(e)
Repetitive Bending
0.1 Hz
RoC = 3 mm
Current Density (μA/cm2)
Current (μA/cm2)
Time (s)
Time (seconds)

Figure 5.4. (a) Open circuit voltage response of the energy harvester during bending tests when bent at a radius of 3 mm at a frequency of 0.1 Hz. **(b)** Short circuit current response of the energy harvester during bending tests when bent at a radius of 3 mm at a frequency of 0.1 Hz. **(c)** Open circuit voltage response of the energy harvester during pressing tests with applied load of ~0.2 MPa at a frequency of 0.1 Hz. **(d)** Short circuit current response of the energy harvester during pressing tests with applied load of ~0.2 MPa at a frequency of 0.1 Hz. **(e)** Cycling response of the energy harvester during repeated bending tests when bent at a radius of 3 mm at a frequency of 0.1 Hz.

5.3.5 Performance assessment of the developed strain energy harvester

Unlike piezoelectric energy harvesters that generate maximum power and energy when operating at resonant frequencies of the active materials, our device operates at low frequencies where the performance metrics are dictated by the diffusion characteristics of the sodium ions in the active material, electrolyte, and the separator. The peak power and energy during bending tests (Table 5.1) at 0.1 Hz for a bending radius of 3 mm was determined to be 42 nW/cm^2 and 0.203 $\mu J/cm^2$ respectively. For pressing tests (Table 5.1) at 0.01 Hz under a small loading of ~0.2 MPa, the peak power and energy were determined to be ~9 nW/cm^2 and 0.792 $\mu J/cm^2$ respectively. The peak power and energy obtained significantly exceed the values obtained from state-of-the-art piezoelectric materials that exhibit drastically reduced harvesting performance at low operating frequencies. Compared to other energy harvesting schemes[240-244] (Figure 5.5), the BP nanosheet energy harvester exhibits higher peak power performance than piezoelectrics with operation in frequency ranges directly overlapped with human motion. Whereas piezoelectrics natively exhibit low conversion efficiency in frequency ranges of optimized energy conversion, harvesting energy from human motions at < 5 Hz leads to significantly lower conversion

efficiency. For example, a 1% piezoelectric harvester with operation frequency of 100 Hz can lead to as little as 0.01% efficient operation at 1 Hz, since this device will only be active in harvesting energy from 1% of the total motion duration. In this way, the shading of the panel in Figure 5 indicates the drop-off of efficiency of traditional mechanical energy harvesters due to the mismatch of the operation frequency and the frequency of human motions. Similarly the electrochemical-mechanical harvesters exhibit a drop-off of performance at high frequencies due to the mechanical-chemical response that is correlated with ion diffusion processes in the electrodes. This implies that (1) broadband energy harvesting can be achieved by combinations of traditional harvesters with low-frequency electrochemical harvesters and (2) electrochemical harvesters are well-suited for the conversion of energy associated with human gait into usable electric energy unlike traditional energy harvesting routes. Nonetheless, one challenge in this electrochemical-mechanical system is the low voltage distribution of harvested charge. Whereas research into this class of energy harvesters is presently at its infancy, strategies to improve voltage output could involve (i) the use of larger size ions (K^+, Rb^+ and Cs^+) as these ions have large partial molar volume leading to greater potential differences and (ii) using ion hosts which have high yield strength as greater the yield strength, the greater the voltage output. Other approaches could employ these electrochemical harvesters in series configurations or the use of power electronics, such as buck converters, to shape the voltage output for a desired application.

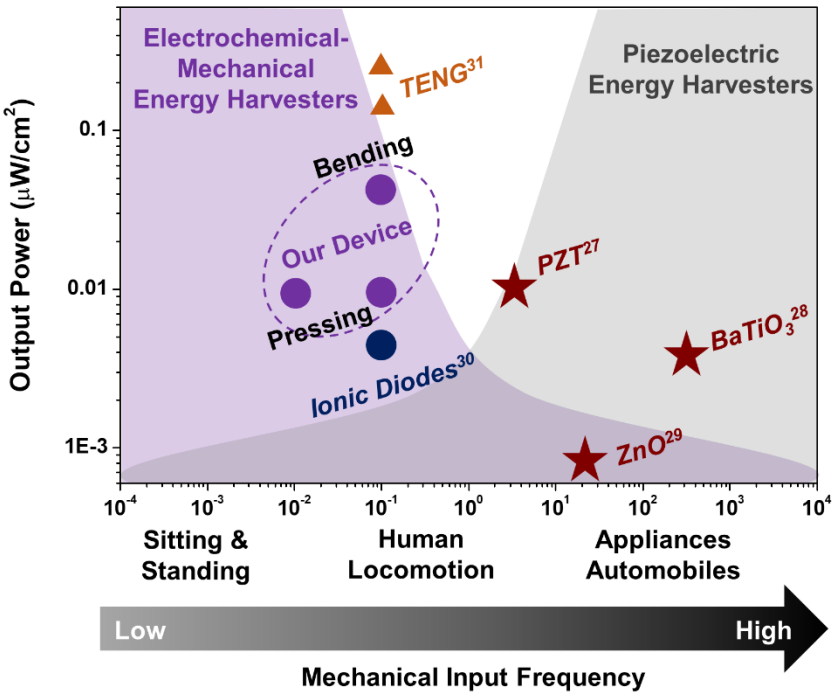

Figure 5.5. Frequency dependent performance plot comparing our 2D black phosphorus energy harvester using nanoscale BP building blocks to other types of devices described in literature. Shaded regions indicate the fall-off of energy harvesting capability at low frequencies outside the range of traditional harvesting routes (left) and at high frequencies outside the range of electrochemical harvesters (right). Note that human gait is described fully by motions with frequency under 10 Hz, where traditional efficiency of traditional harvesting schemes falls off, as represented by the grey shaded region.

Further, our results introduce the use of 2D nanostructures for electrochemical strain energy harvesting, which provides exciting pathways for future research directions. Whereas the theoretical mechanical-to-electrical conversion efficiency can be high in this system (> 30%, Figure 5.13, see Appendix), lack of understanding of the mechanical properties in both 2D materials and ion-intercalated 2D materials remains a bottleneck toward robust quantitative assessment. At the systems level, one can infer that control of assembly of the nanostructured

building blocks will be a critical factor to enable efficient coupling of mechanical energy to electrical energy. At the nanoscale, one can envision a new class of strain harvesters that can be assembled at the single-nanosheet scale. A simple example is a stacked 2D material with locally intercalated ions[165, 166, 175] that can function as a nanoscale strain harvesting device for low-frequency motions at the molecular scale in fabrics, liquids, or other media. Our work emphasizes how 2D building blocks are platforms for the design of future strain energy harvesting schemes tuned to harvest energy from low frequency motions.

Testing Method	Operational Frequency (Hz)	Bending Radius (mm)	Applied Pressure (MPa)	Peak Power (nW/cm^2)	Energy Harvested ($\mu J/cm^2$)	Response Time (s)
Bending	0.1	3		42	0.203	5
Pressing	0.1		~0.2	9.68	0.076	10
	0.01		~0.2	9.12	0.792	100

Table 5.1. Performance of the phosphorene 2D energy harvester described in this work.

5.4 Conclusion

In summary, our work demonstrates a 2D material (phosphorene) strain energy harvester configuration relying on mechano-electrochemical stress-voltage coupling at low frequencies relevant to human motions. The assembled harvester was tested in both bending and pressing modes, with experiments demonstrating a peak power delivery of ~42 nW/cm^2 (0.1 Hz, RoC = 3 mm) and ~9 nW/cm^2 (0.1/0.01 Hz, Load ~0.2 MPa) respectively. The energy output from these devices during bending and pressing were 0.203 $\mu J/cm^2$ (0.1 Hz, RoC = 3mm) and 0.792 $\mu J/cm^2$ (0.01 Hz, Load ~0.2 MPa) respectively with response times (FWHM of current output – 10 s and 100 s) several orders of magnitude greater than conventional piezoelectric systems which

provide highly inefficient harvesting capability at such low frequencies. This provides a framework to exploit (i) the controlled mechanical properties of 2D materials, (ii) the homogenous strain propagation that occurs in 2D material geometries, and (iii) the capability of accessing 2D material energy harvesting tuned to frequencies relevant to human motions. Our results support future work spanning from harvesting mechanical stresses at the nanometer length scales in designer 2D material stacks to designing system-level architectures, such as integrated MEMS-electrochemical harvesting units that can be functional for a broad range of low-frequency energy harvesting applications complimentary to the state-of-the-art piezoelectric or triboeletric system operation.

Acknowledgements

The authors would like to thank Adam Cohn, Keith Share, Anna Douglas, Kate Moyer and Deanna Schauben for useful insights and discussions. We would also like to acknowledge Rizia Bardhan for use of Raman facilities. This work was supported in part by the Vanderbilt University discovery grant program, NSF grant CMMI 1400424, and R.C. was supported by a fellowship through the Vanderbilt Institute for Nanoscale Science and Engineering.

5.5 Appendix

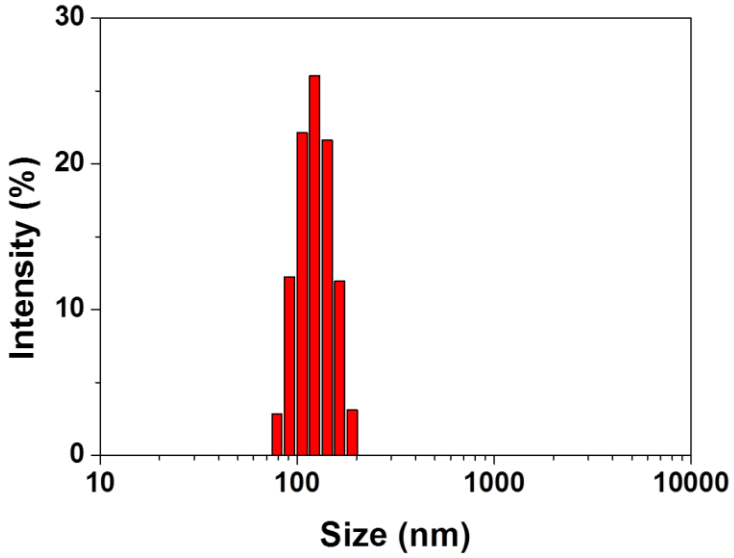

Figure 5.6. Hydrodynamic size distribution of exfoliated BP nanosheets measured by utilizing dynamic light scattering (DLS) technique on a Zetasizer.

Hydrodynamic size distribution data was collected using a Malvern Zetasizer using a dynamic light scattering (DLS) technique by measuring the rate of Brownian motion of the exfoliated BP suspended in NMP solution. The sub-micron size features in Figure 5.6 confirmed with well exfoliation of BP in NMP solution.

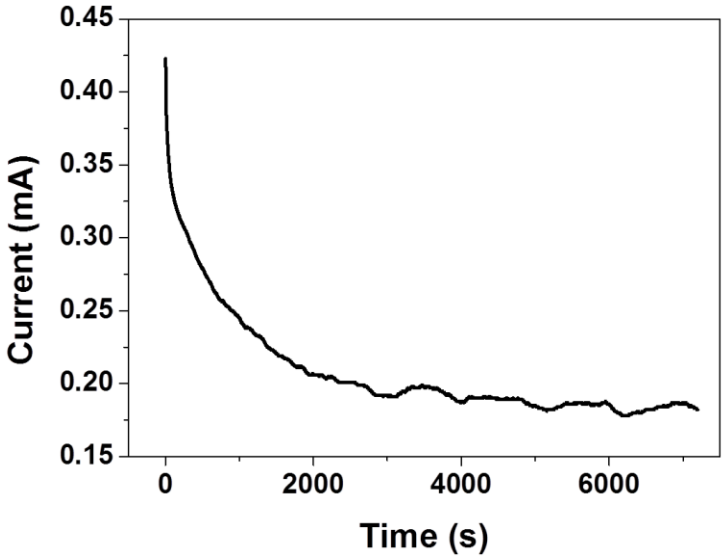

Figure 5.7. I-t curve of electrophoretic deposition of exfoliated BP onto graphene on Cu under constant applied voltage (10 V for 2hrs).

The deposition of black phosphorus on the graphene/Cu substrate using EPD process was monitored using a Keithley 2400 sourcemeter.

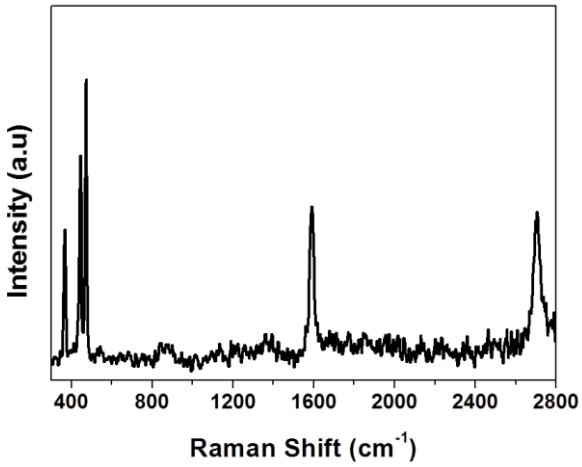

Figure 5.8. Raman spectroscopy of the BP-G electrode.

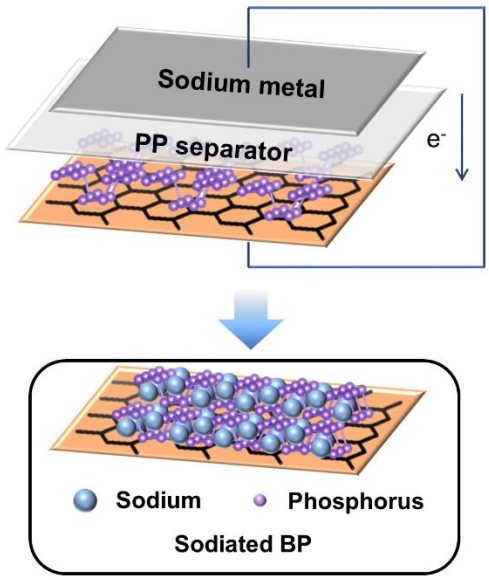

Figure 5.9. Schematic illustration of sodiation process and resulted sodiated black phosphorus electrode.

To obtain sodiated black phosphorus, the deposited black phosphorus on graphene/Cu was connected in short circuit mode against a pure sodium metal for over 4 hours. The sodiated electrode was then cut into two identical halves which form the two electrodes of the energy harvester. The two electrodes were then assembled in a sandwich configuration. The device was then connected in short circuit mode using an external wire for 2 hours to homogenize the composition of both electrodes of the harvester.

5.5.1 Potential safety concerns and strategies to mitigate them

Electrochemical-mechanical energy harvesters generate current through migration of charged ions. In our case, sodium ion from the compressed electrode moves to the tensed electrode resulting in electric current generation. Even though our device operates on the principles of battery electrochemistry, the potential safety issues which affect batteries are less likely to affect this system because of the following reasons:

(i) There is no high energy sodium metal in our harvester as the sodium is in its ionic state in the electrolyte. These ions from the electrolyte alloy with the black phosphorus to form sodiated black phosphorus. Sodium ions are comparatively safer than pure sodium metal.

(ii) The electrochemical – mechanical energy harvesters have electrodes which are identical in composition thereby they are at isopotential. In the isopotential state the energy difference between the two electrodes is zero. Failure mechanisms in batteries are mostly due to short circuiting of the electrodes causing thermal runaway reactions which ignite the organic electrolyte leading to hot gas ejection from the device causing an explosion. As our electrochemical-mechanical energy harvesters have electrodes operating close to isopotential states, short circuiting and thermal runaway are less likely to occur.

(iii) The safety of the device can be improved even further by using solid state electrolytes which are much safer than conventional organic electrolytes.

(iv) Better packaging of the device using reinforced polymer composites can minimize damage during mechanical deformation

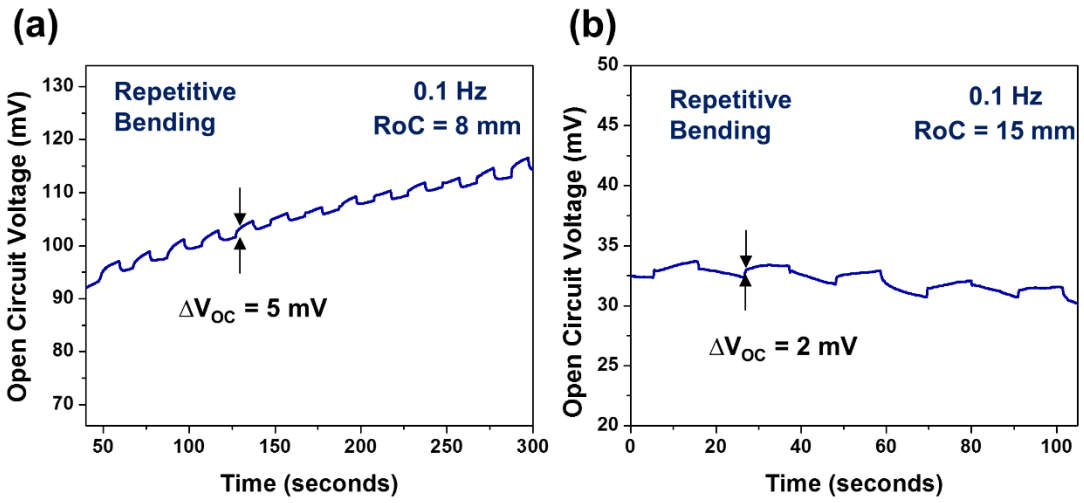

Figure 5.10. (a). Open circuit voltage response of the energy harvester during repeated bending tests when bent at a radius of 8 mm at a frequency of 0.1 Hz. **(b)** Open circuit voltage response of the energy harvester during repeated bending tests when bent at a radius of 15 mm at a frequency of 0.1 Hz.

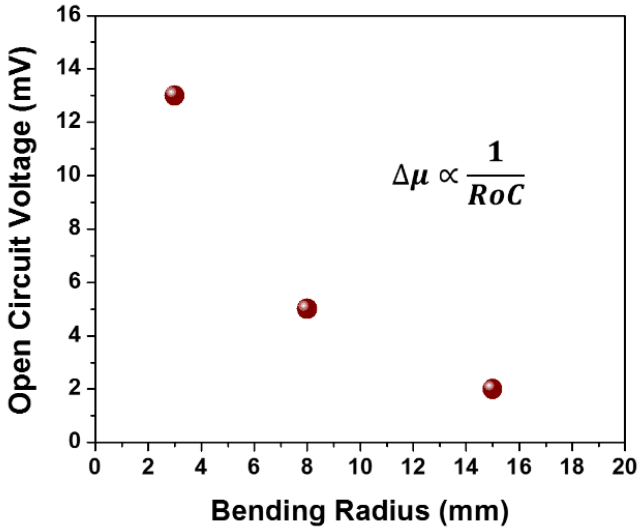

Figure 5.11. Variation of ΔV_{OC} with bending radii

The voltage (ΔV) generated is a function of the chemical potential gradient (Δμ) generated between the two electrodes. The chemical potential gradient between the two electrodes was inversely related to the radius of curvature (RoC) or the bending radius.

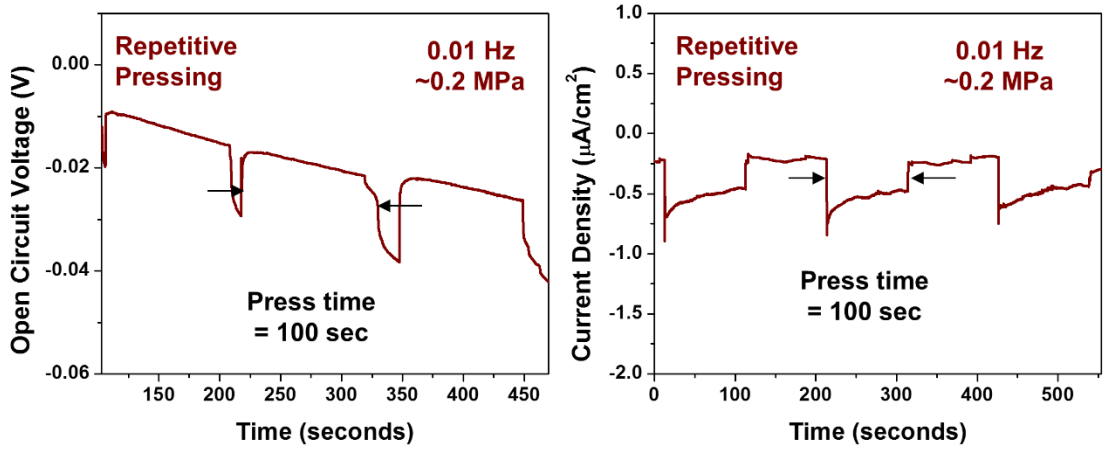

Figure 5.12. (a) Open circuit voltage response of the energy harvester during repeated pressing tests with applied load of ~0.2 MPa at a frequency of 0.01 Hz. **(b)** Short circuit current response of the energy harvester during repeated pressing tests with applied load of ~0.2 MPa at a frequency of 0.01 Hz.

At very low frequencies of 0.01 Hz corresponding to a 100 second hold time, the energy harvester generates comparable voltage and currents in the open circuit and short circuit mode respectively. The FWHM at 0.01Hz is ~100 seconds indicating the applicability of this device in the regime of very low frequencies which are inaccessible to conventional piezoelectric materials.

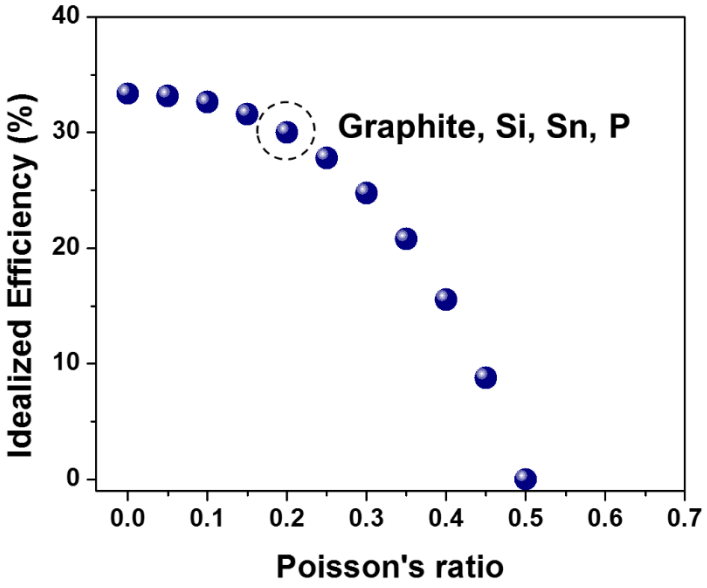

Figure 5.13. Idealized efficiency of these electrochemically driven energy harvesters

The idealized efficiency is obtained from the theoretical constructs provided by S. Kim et al.[229] Bending the device leads to one electrode being compressively strained and the other being tensile strained corresponding to the state $\varepsilon_{xx} = \pm h/RoC$, where RoC is the radius of curvature and h is one half the thickness of the whole device. The stress on one electrode can be written as,

$$\sigma_{xx} = \frac{Eh}{(1-\vartheta^2)(RoC)}, \sigma_{zz} = \frac{\vartheta Eh}{(1-\vartheta^2)(RoC)} \; and \; \sigma_{yy} = 0 \qquad 18$$

σ_{yy} = 0 owing to assumption of a plane stress condition in the y direction. E is the Young's modulus of the electrode and ν is the Poisson's ratio. For materials such as sodiated phosphorus assuming the Na_3P phase, the Poisson's ratio is generally assumed to be ~0.25. The strain energy generated in the system can be coupled into hydrostatic and deviatoric components where,

$$U_{Strain} = U_{Hydrostatic} + U_{Deviatoric} = \frac{E}{2(1-\vartheta^2)}\left(\frac{h}{RoC}\right)^2 \qquad 19$$

$$U_{Hydrostatic} = \frac{\sigma^2_{Hydrostatic}}{2B}, where \; B = \frac{E}{3(1-2\vartheta)} \qquad 20$$

B is the Bulk modulus of the electrode. Assuming only hydrostatic components contribute to energy generation and all of the deviatoric components are wasted, the idealized efficiency is

$$\eta = \frac{U_{Electrical}}{U_{Strain}} = \frac{U_{Hydrostatic}}{U_{Strain}} = \frac{(1-2\vartheta)(1+\vartheta)}{3(1-\vartheta)} \qquad 21$$

The above equation dictates that the efficiency of the device is a function of the Poisson's ratio. Considering a Poisson's ratio of 0.25, the idealized efficiency is about 27.8%. The efficiency maxes out at a Poisson's ratio of 0 to be 33.3%.

Chapter VI

6 Co-Intercalation Electrodes for Harvesting Ambient Mechanical Energy During Human Motion

6.1 Introduction

In recent years, advances in cybernetics, artificial intelligence, and the internet of things has brought forth the idea of integrating a multitude of sensing and actuating systems to complement functionalities in efficient bio-mechanical interfaces.[245-248] To power such integrated electronic systems for long term operation, onboard energy storage architectures are necessary. Using light-weight energy harvesters capitalizing on otherwise wasted ambient mechanical energy provides opportunities for on-demand energy generation rather than energy storage. As the development in cybernetics and human interfaced bio-mechanical architectures increases, powering these devices through energy harvesting by tapping into the ambient mechanical motions of everyday human interactions, specifically those pertaining to human locomotion, is a viable alternative to energy storage.[217, 249-251] These everyday human interactions from sleeping (a low frequency event) to running (a high frequency event) occur entirely at frequencies below 5 Hz. Conventional energy harvesting systems such as most piezoelectric and triboelectric generators operate at frequencies >10 Hz leading to drastically reduced performance at these human interaction frequencies.[217, 222, 242] The emerging class of electrochemical-mechanical energy harvesters on the other hand operate on the principle of mechano-electrochemical coupling in battery electrodes.[40-42, 175, 217, 229, 252-256] The timescale of ion diffusion kinetics of the constituent battery material matches well with operational frequencies <5 Hz.

Human walking depicted by gait cycles occur at frequencies between 0.5Hz to 5Hz.[42, 217, 229] Two types of mechanical impulses occurring as a result of movements of the human body can be potentially harvested: (i) motion generating impact force at the base of the foot and (ii) bending motions of the knee joint. In order to be effectively harnessed the energy harvesting timescale of the harvesters needs to match the duration of mechanical input. Such harvesters would produce energy so long as the mechanical impulse exists, as any sustained energy generation beyond the duration of mechanical input would lead to wastage of the harvested energy.[42, 217, 229] This creates the need for electrochemical-mechanical energy harvesters with high sensitivity and ultrafast kinetics capable of harvesting low mechanical impulses of human locomotion frequencies to deliver high instantaneous power outputs. Previously reported electrode systems for this class of energy harvesters use Li^+ and Na^+ alloying and intercalation materials, which even though effective at capturing high curvature bending impulses, have low power delivery at larger bending motions (low curvatures) of very short durations. These electrodes are primarily limited by ion diffusion kinetics owing to the slow diffusion of the charged ions in these electrodes, causing challenges when considering harvesting energy from human walking.[42, 229, 255]

Although a multitude of reports on high rate battery electrodes exists till date, very few are suited for this application. The ultrafast, large volume change phenomenon of Na^+ co-intercalation into graphitic electrodes (250% - NaC_{16}) makes it an ideal candidate to address the challenges of energy harvesting. The otherwise poor intercalation of Na^+ ions into graphitic electrodes using conventional electrolytes[257] can be enhanced in the presence of ether based electrolytes by co-intercalating solvated Na^+ ions instead of the de-solvated Na^+ during normal intercalation.[166, 258-260] In the case of co-intercalation, the size of the solvated Na^+ ions in co-

intercalation process is larger than de-solvated Na^+ ions resulting in a significantly high volume expansion (250%) of the graphitic host for the fully sodiated state.[166, 261] Additionally, the kinetics of Na^+ co-intercalation process is rapid boasting high diffusion coefficients up to $2x10^{-7}$ $cm^2.s^{-1}$ into graphitic electrodes[166] when compared to the slow lithium diffusion process in previously reported silicon based energy harvesting electrodes (~10^{-10} $cm^2.s^{-1}$).[229]

These factors motivate our work in developing electrochemical-mechanical energy harvesters which can effectively operate in the frequency ranges corresponding to human locomotion (1Hz – 5Hz) using sodiated multilayered graphene (MLG) electrodes utilizing the extreme volume change Na^+ co-intercalation chemistry. We design the energy harvester using two identical sodiated MLG electrodes in a sandwich configuration. Leveraging the large volumetric expansion per charge and the ultrafast kinetics of the Na^+ co-intercalation process higher power outputs can be obtained at low curvatures (low mechanical inputs) when compared to other harvesters of this type. This prototype energy harvester delivers high power output of 0.18 $\mu W.cm^{-2}$ at moderate bending radii of 8 mm as well as good operational stability when harvesting energy during human walking at speeds of 0.25 $m.s^{-1}$ to 1.25 $m.s^{-1}$. Overall, this work highlights the effectiveness in utilizing the extreme volume change, ultrafast Na^+ co-intercalation process into graphitic electrode in harnessing otherwise wasted mechanical energy during human locomotion.

6.2 Experimental methods

6.2.1 Electrode fabrication and characterization

Multilayered graphene (MLG) was grown on Nickel foil (0.03 mm, MTI) using chemical vapor deposition (CVD) process at 850 ^oC using 500 sccm Ar and 10 sccm H_2 gas. After annealing for 1 hour at 850 ^oC, the carbon containing precursor, C_2H_2 at 0.3 sccm was admitted for varying

periods of time (from 6 min to 30 min) to achieve uniform growth of MLG of different thicknesses. Copper foils connected to copper wires were used as the current collectors. Raman spectroscopic analysis was performed using Renishaw inVia MicroRaman system using 532 nm laser excitations and Transmission electron microscopy was performed using FEI Osiris Transmission electron microscope.

6.2.2 Fabrication of the energy harvester and electrochemical testing

To assemble the harvester, as grown MLG on nickel foil was sodiated by contacting sodium metal with 1M $NaPF_6$ (Alfa Aesar) in Diethylene Glycol Dimethyl Ether (DEGDME or Diglyme) electrolyte (Aldrich). A Celgard 2325 separator soaked in the same electrolyte was used and identical sodiated MLG electrodes were assembled in a sandwich configuration with the separator between the two electrodes. Kapton tapes were used as packaging material for the harvester. Owing to the ultrafast nature of the co-intercalation system, the assembled device was connected in short circuit mode using an external wire for only 5 to 10 min. The device was then tested electrochemically using Autolab PGSTAT 101 testing system. To achieve controlled bending and unbending cycles the assembled harvester was bent around pipes of varying diameters using a programmable Arduino set with a Servo motor. For assessing energy harvesting capabilities during human walking, the device was integrated into a wearable knee band and was worn around the knee of a subject. The current response was monitored using the Autolab system at the same time as the bio-mechanical motions involved during walking were collected using motion capture markers attached to the leg.

6.3 *Results and discussion*

6.3.1 *Using graphite co-intercalation electrodes for energy harvesting*

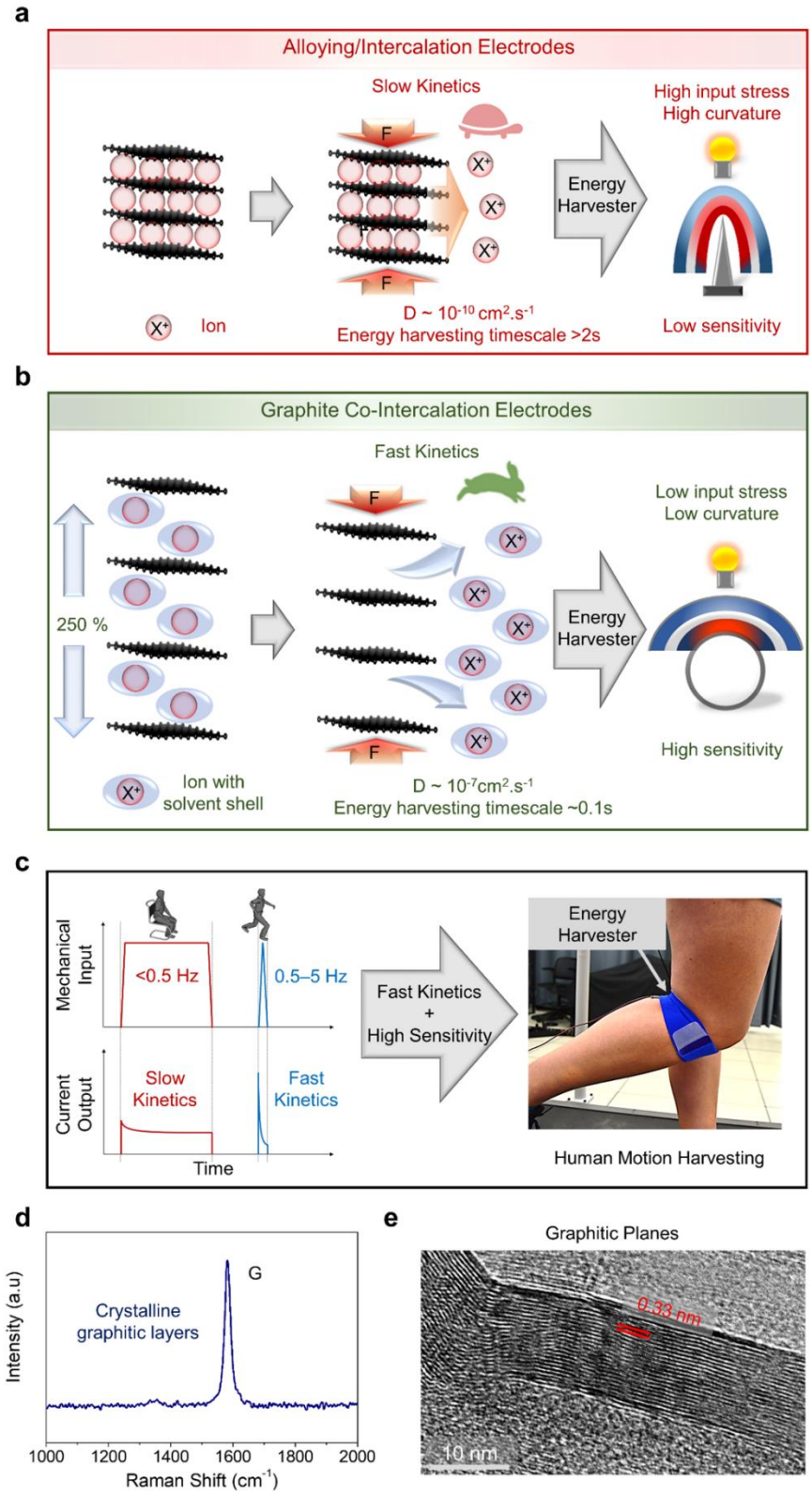

Figure 6.1. (a) Mechano-electrochemical characteristics of conventional alloying/intercalation electrodes. **(b)** Mechano-electrochemical characteristics of graphite co-intercalation electrodes. **(c)** Frequency compatibility of the mechano-electrochemical energy harvesters for human motion harvesting. **(d)** Crystalline nature of the MLG as observed in Raman spectra. **(e)** TEM micrograph showing crystalline graphitic planes of a few layers of MLG exfoliated from the as grown material on Ni-foil.

Figure 6.1a and 6.1b show the differences between conventional alloying/intercalation electrodes (Li-Si, Li-C, Li-Al, Na-P and Na-Sn) when compared to co-intercalation of sodium ions into graphitic electrodes in the presence of glyme based solvents. Conventional alloying/intercalation based electrodes undergo less volumetric expansion per unit charge than the co-intercalating sodium ion. The Na^+ co-intercalated graphitic host (Fig. 6.1b) has stable graphene-diglyme vdw interactions which enables fast ion diffusion kinetics with minimal to no mechanical degradation of host material.[166, 257-262] Rapid ion movement in and out of the host electrode owing to the fast Na^+(DEGDME) ion diffusion rate ($2x10^{-7}$ $cm^2.s^{-1}$) as reported in previous studies implies that the graphitic host undergoes volume expansion and relaxation at extremely fast rates when compared to the slow diffusing Li-Si and Na-P electrodes of the same thickness.[166] The fast kinetics and large mechanical response enables high sensitivity of these Na^+ co-intercalated graphitic electrodes even at small mechanical inputs (low curvatures). These unique characteristics of the sodium co-intercalation chemistry offers possibilities to harvest energy from ambient mechanical inputs of very short durations. As shown in Fig. 6.1c, electrodes with inherently slow kinetics (conventional alloying and intercalation chemistries) are ideally suited for harvesting long duration ambient mechanical inputs of low frequencies (<0.5 Hz) such as sitting and standing events. When considering human interactions such as walking and running, the timescale for

energy generation is <1s as these motions occur at frequencies ranging from 0.5 Hz to 5 Hz. To effectively harness ambient mechanical energy using these mechano-electrochemical energy harvesters during human walking motion, electrodes with fast kinetics (sodium co-intercalation in to graphite) are required. To facilitate effective co-intercalation the graphitic host, the as grown multilayered graphene (MLG) on Ni Foil (see experimental methods) should contain minimal defects[166] in Raman spectroscopic analysis (Fig. 6.1d). A sharp G peak at 1581 cm^{-1} with minimal signature of the defect mode (D peak at ~1300 cm^{-1}) can be observed for the as grown MLG. The corresponding TEM micrograph (Fig. 6.1e) shows a region of the as grown MLG with interlayer spacing of 0.33 nm.

6.3.2 Electrochemical response of the assembled energy harvester

To fabricate the energy harvester, symmetric electrodes Na^+ co-intercalated MLG were assembled in a sandwich configuration separated by a polymer separator (see experimental methods and Appendix. Figure 6.5). Shuttling DEGDME solvated Na^+ ions from one electrode to the other during bending and unbending movements (Appendix Figure. 6.6) produces a chemical potential gradient, allowing the input mechanical energy to be harvested. As the sodiated electrodes are identical to each other in this symmetric configuration, no energy difference exists between the two electrodes and as a result the device exists in an iso-potential state if undisturbed. Application of small mechanical perturbations such as bending causes deviation to this iso-potential state by setting up compressive stresses in one electrode and tensile stresses in the other. This asymmetry in stresses generates a chemical potential gradient owing to the mechano-electrochemical coupling effect observed in such battery electrodes. This mechanically induced chemical potential gradient causes ion migration from the compressed electrode to the tensed electrode which lasts until the stress induced gradient is neutralized. As

migration of a charge carrying ion occurs inside the device across the separator, electrons flow through the external circuit thus harvesting energy during the applied mechanical input.[42, 229]

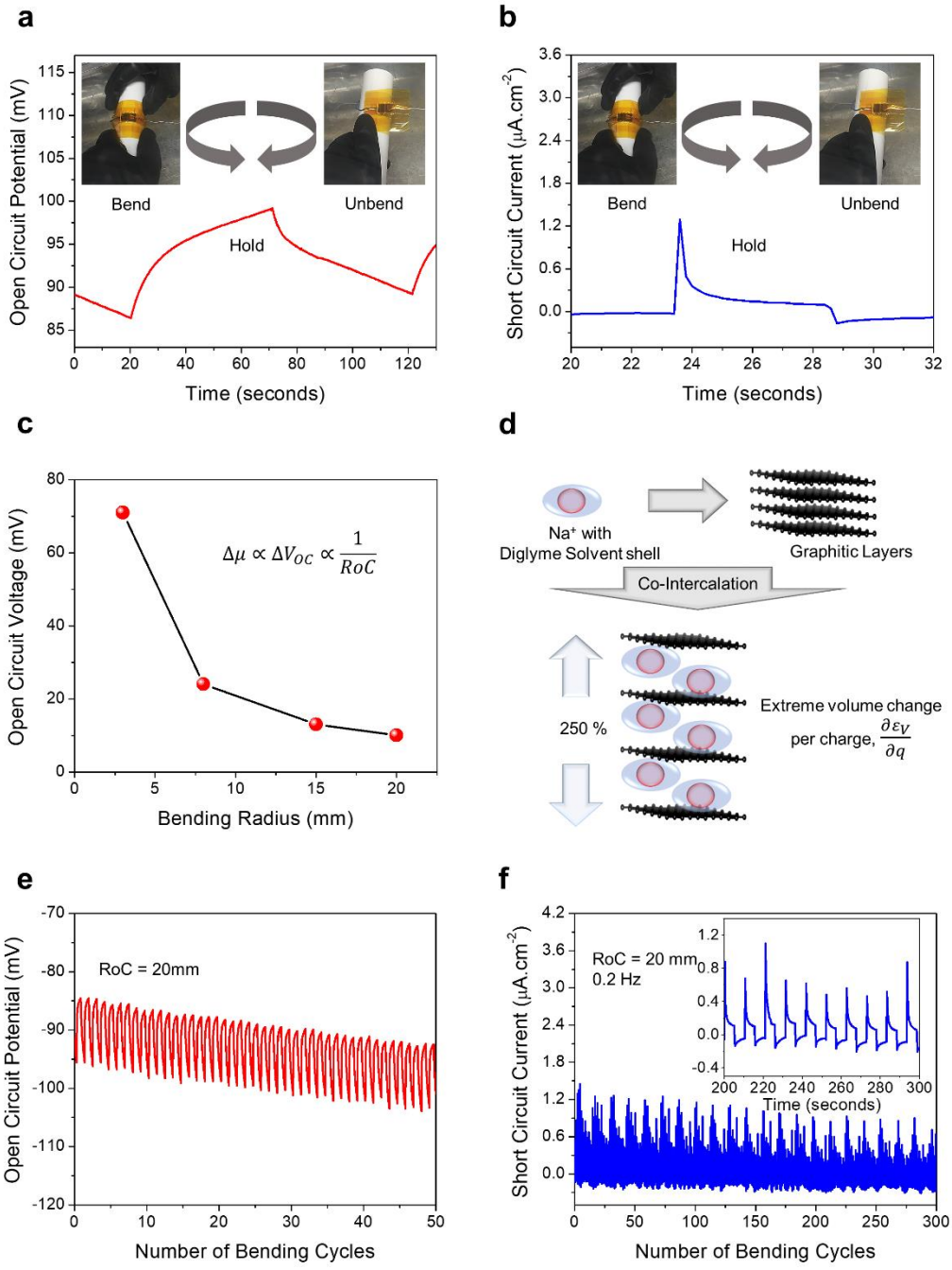

Figure 6.2. (a) Open circuit voltage (V_{OC}) measurements during bending and unbending. **(b)** Short circuit current (SSC) measurements during bending and unbending. **(c)** ΔV_{OC} response

from the harvester at different bending radii. **(d)** Schematic representation of the volumetric strain per charge for the Na^+ co-intercalation process. **(e)** V_{OC} response during repeated bending and unbending. **(f)** SSC response during repeated bending and unbending tests.

The change in the chemical potential gradient between the two electrodes during such mechanical inputs can be observed by measuring the open circuit potential (V_{OC}). As shown in Fig. 6.2a, a sharp rise in voltage output from the device results from bending induced asymmetric stresses. Upon unbending, the chemical potential gradient vanishes and the voltage output returns to the initial state. As is the case with such electrochemical-mechanical energy harvesters, we observe a background potential from the device which could arise from unintended inhomogeneities between the two electrodes. The current output from the harvester during bending and unbending can be observed using short circuit current (SSC) measurements as shown in Fig. 6.2b. When the device is bent, a sharp peak in current is observed which is followed by a gradual decrease in current which lasts as long as the device is held in the bent state. The response time (time scale of energy generation) for the MLG co-intercalation energy harvester, characterized by the FWHM of the current response, is ~0.1 seconds as a result of the ultrafast kinetics of the Na^+ co-intercalation process enabling fast stress gradient relaxations. Upon unbending, the co-intercalation induced concentration differences between the two electrodes result in a reverse current. As the chemical potential gradient is proportional to the induced mechanical stress gradient between the electrodes in the device, low bending geometries (high curvatures) should induce greater stresses resulting in a larger chemical potential gradient. The change in V_{OC} of the device at different bending radii is shown in Fig. 6.2c. Even at very low curvatures (bending radius of 15 mm), we observed higher V_{OC} changes comparable to previously developed electrochemical-mechanical harvesting systems at similar curvatures.[42, 229,

[255] A comparatively higher voltage output is observed in our system compared to Li_XSi, Li_XAl and Na_XP electrodes for the same amount of charge inserted because the voltage output is directly related to the volumetric change per charge in the electrodes during ion insertion (Fig. 6.2d).[42, 217, 229, 255] Upon repeated bending and unbending for (Fig. 6.2e), stable voltage changes were observed. As ions do not migrate between the electrodes to neutralize the stress gradient during the V_{OC} measurements, an overall increase in the background potential results from one electrode constantly being more compressed as cycling progresses while the other electrode is constantly undergoing tension.[42, 229] The SSC response of the device during several bend, hold and unbend cycles is shown in Fig. 6.2f. Similar to the V_{OC} response, we observe a gradually reducing background current arising from unintended inhomogeneities generally observed in this class of electrochemical-mechanical energy harvesters.[42, 229] Current response from the harvester during alternate bending trials is provided in the appendix Figure 6.8.

6.3.3 Response of the energy harvester to varying input mechanical frequencies

To assess the compatibility with the wide frequency range of human interactions, our harvester was bent and unbent at various frequencies ranging from 5Hz (200 millisecond hold time) to 0.03Hz (30 seconds hold time) at a fixed low curvature (bending radius of 15 mm). The current output during this repeated high to low frequency motion on a single harvester is shown in Figure 6.3a. The peak power output from the device determined as the product of the peak current and open circuit voltage is compared with other previously reported electrochemical-mechanical energy harvesters in Fig. 6.3b.[42, 229]

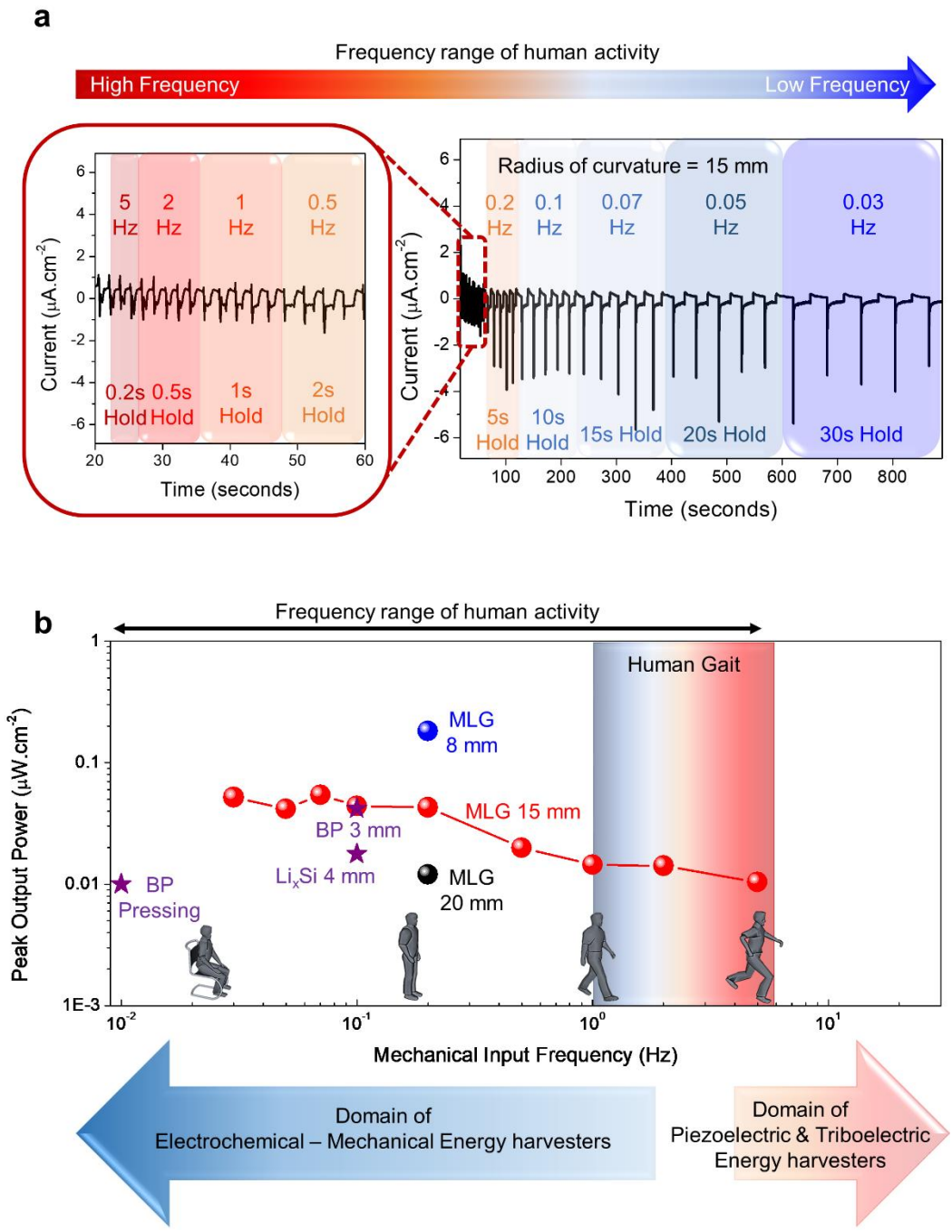

Figure 6.3. (a) Frequency response of the energy harvester at various bend-cycle frequencies at RoC of 15 mm on the same device (Note: The currents were normalized to the active bending area of the harvester). **(b)** Peak output power of the harvester when compared to various electrochemical – mechanical energy harvesters from literature at different frequencies of human activity comparing specific bending radii and pressing modes.

As the current and voltage response from this class of energy harvesters varies directly with the chemical potential gradient which in turn varies inversely with the bending radii, a higher peak power output can be observed at smaller bending radii (large applied mechanical stress resulting from high curvatures). Our harvester generates higher peak power output (0.18 $\mu W.cm^{-2}$) at low curvature (bending radius - 8 mm) when compared to other electrochemical-mechanical energy harvesters operating at high curvatures. Operational stability and good power delivery in a wide range of frequencies is critical for applications such as energy harvesting from human interactions. At frequencies of 5Hz (above human walking range) our harvester delivers a power of 0.01 $\mu W.cm^{-2}$ and at comparatively low frequencies of 0.03Hz (near sitting and standing range), power output of 0.05 $\mu W.cm^{-2}$ was observed at a high bending radius of 15 mm. The average power output (total energy harvested) is provided in the appendix figures 6.8-6.9.

6.3.4 Energy harvesting during human walking

The frequency tests performed on our MLG harvester indicate the feasibility for effective use in harnessing the ambient energy during human walking. We therefore integrated the harvester onto a knee band worn around a human knee and evaluated the current output during different human walking speeds. Figure 4a highlights the major events occurring at the knee joint which can be broadly divided into two: (i) the knee flexure which can be considered as the bending cycle and (ii) the knee extension which can be considered as the unbending cycle (see appendix Figure 6.10. a and b).[263] Using motion sensing markers, simultaneous measurements of the knee velocity (bending rate) and knee angle (bending angle) for various walking speeds ranging from 0.25 $m.s^{-1}$ to 1.25 $m.s^{-1}$ (Fig. 6.4b) were performed. Figure 6.4c highlights the current response from the MLG harvester continuously recorded during human walking at various speeds. The harvester shows good operational stability when switching walking speeds

from low to high as well as high to low. By simultaneously measuring knee angle, knee velocity and current output of the harvester, we observe that the knee angle (bending angle), knee velocity (bending rate) and the magnitude of the peak current increases with increasing walking speeds (Fig. 6.4d and 6.4e) (also see appendix, Figures 6.11 – 6.14). These results indicate bending rate (knee velocity) and bending angle (knee angle) having synergistic effects on the output power of the harvester. At fast walking speeds knee bending angle increases simultaneously with increasing knee velocity (bending rates) resulting in a large stress input as well as fast application of the large stress input respectively. As a cumulative result, an increase in current output of the harvester is observed. During slow walking speeds, a lower knee angle, velocity and current output from the device is observed highlighting the close matching of bio-mechanical and mechano-electrochemical phenomena in our system. Also, these major knee bending events occur in a small percentage of time (10-20% of full walking cycle). The high sensitivity and fast response of the co-intercalation process enables good frequency matching to harvest energy during human walking cycles. These results provide a foundation for further enquiries to integrate such electrochemical-mechanical energy harvesters to other parts of the human body. This configuration can also be integrated into interconnected networks and 3D architectures which translate other forms of mechanical inputs into bending stresses to provide a versatile approach to energy harvesting and sensing.[264-268] As our energy harvester is sensitive to low mechanical movements and stresses with good bio-mechano-electrochemical response matching, these systems can also be used to develop sensors for athletic fitness monitoring.

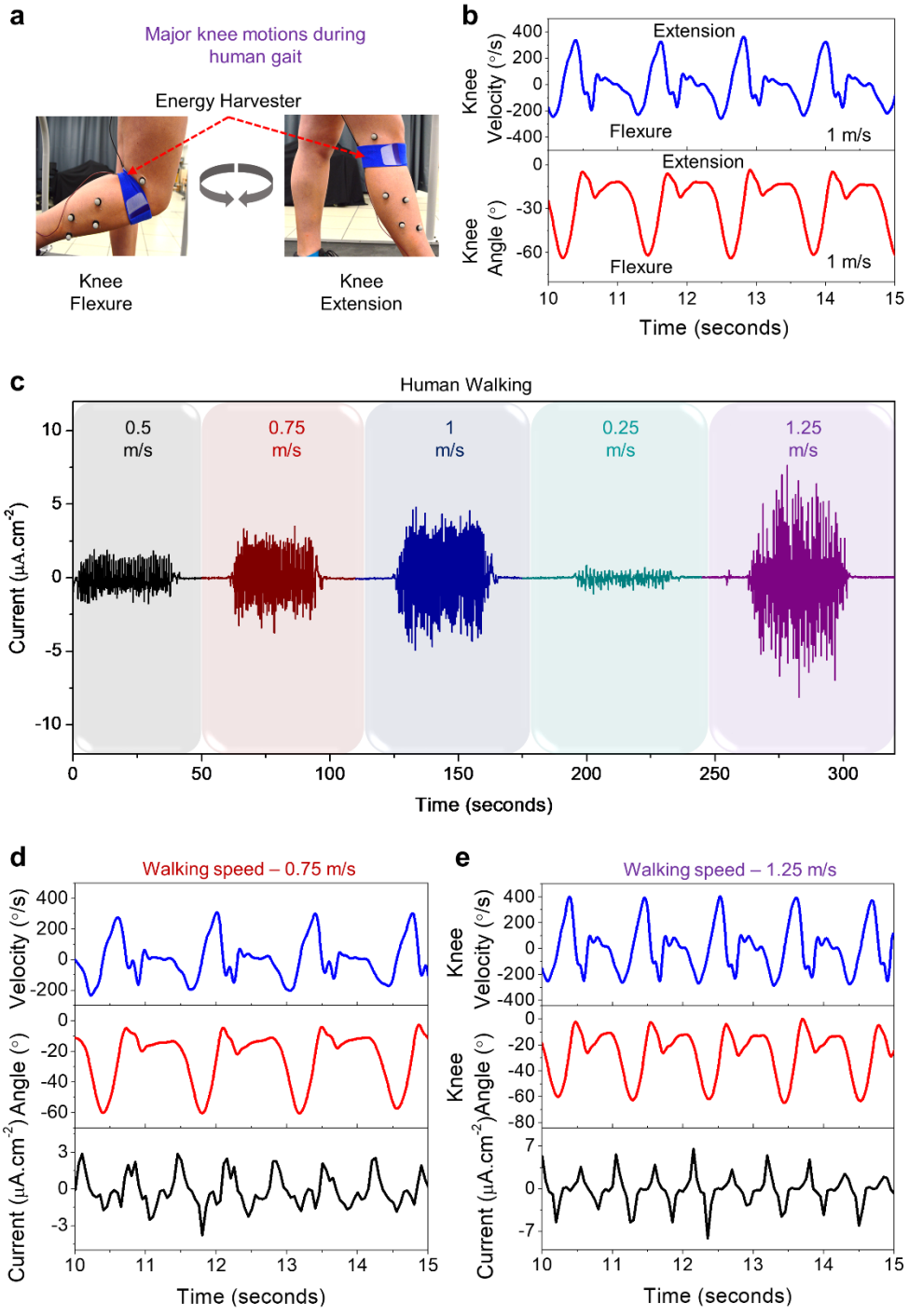

Figure 6.4. (a) Major knee events during human gait. **(b)** Knee velocity and knee angle measurements obtained during different walking speeds. **(c)** Current response of the harvester integrated into a fabric worn around the knee during human walking trials at different speeds.

Simultaneous measurements of knee velocity, knee angle and current response of the harvester at walking speeds of **(d)** 0.75 $m.s^{-1}$ and **e**, 1.25 $m.s^{-1}$.

6.4 Conclusion

In summary, our work demonstrates a highly sensitive, fast responding electrochemical-mechanical energy harvester which utilizes mechano-electrochemical stress-voltage coupling resulting from sodium co-intercalation into graphitic electrodes. The developed energy harvester was tested at various bending conditions delivering peak power output of 0.18 $\mu W.cm^{-2}$ at a moderate bending radius of 8 mm. The device was also tested at multiple frequencies ranging from 0.03Hz to 5Hz at a high bending radius of 15mm where the peak power delivered was 0.05 $\mu W.cm^{-2}$ and 0.01 $\mu W.cm^{-2}$ respectively. The harvester was also assessed to determine the feasibility of harnessing mechanical energy during human walking at various speeds ranging from 0.25 $m.s^{-1}$ to 1.25 $m.s^{-1}$. The current output from the harvester positioned on the knee joint was simultaneously monitored along with bio-mechanical parameters such as knee bending angle and knee velocity. Our results utilize the potential of the ultrafast nature of the co-intercalation reaction in fast, responding energy harvesters, sensors, actuators, and fitness monitoring applications of the future.

Acknowledgements

The authors would like to thank Rachel Carter, Landon Oakes, Mengya Li, Anna Douglas, Deanna Schauben, Jeremiah Afloabi and Chuanzhe Meng for useful insights and discussions. We would also like to acknowledge Rizia Bardhan for use of Raman facilities. This work was supported in part by the Vanderbilt University discovery grant program.

6.5 Appendix

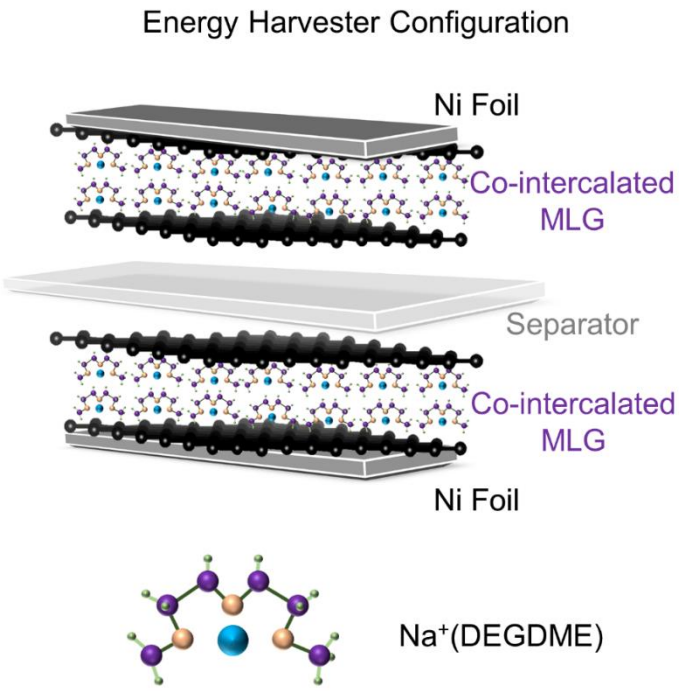

Figure 6.5. Configuration of the energy harvester

The energy harvester is assembled in a symmetric manner with two co-intercalated MLG electrodes on nickel foil separated by a Celgard 2325 tri-layer separator. The active sodium ion is wrapped in a diglyme solvent shell during co-intercalation resulting in large volume expansion per charge inserted.

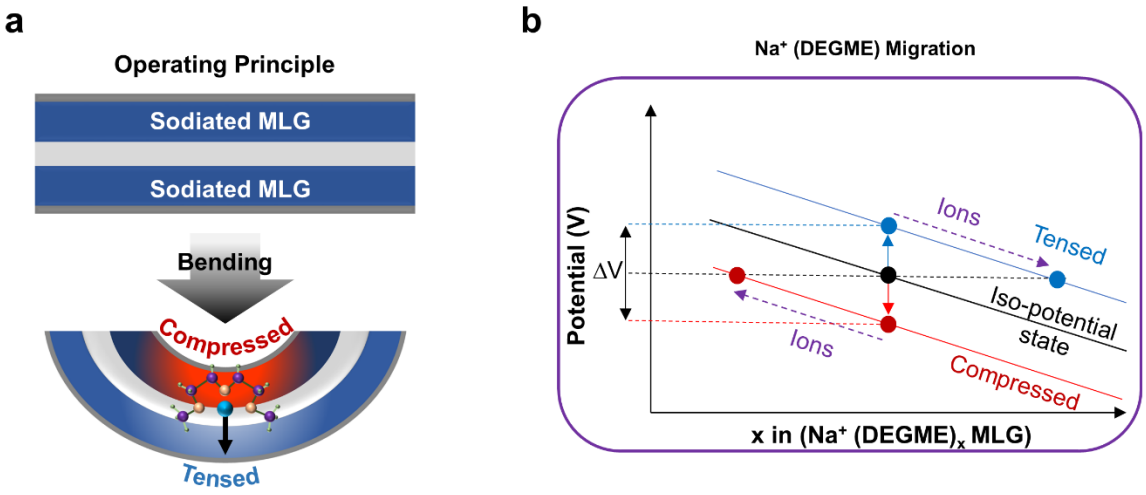

Figure 6.6. (a) Operation mechanics of the energy harvester, **(b)** Electrochemical working principle of the energy harvester

Bending the device (Fig. 6.6. a) generates compressive stresses on one electrode where tensile stresses are set up on the other electrode. Generation of this asymmetric stress gradient creates a decrease in potential of the compressed electrode and increase in potential of the tensed electrode respectively (Fig. 6.6. b). This potential difference drives ions from the compressed side to the tensed side until complete neutralization of the generated stress gradient. During unbending, the concentration induced chemical potential gradient because of ion migration during bending step causes ions to flow in the reverse direction. The migration of charge carrying ions results in electron flow in the external circuit thereby harvesting energy during mechanical inputs.

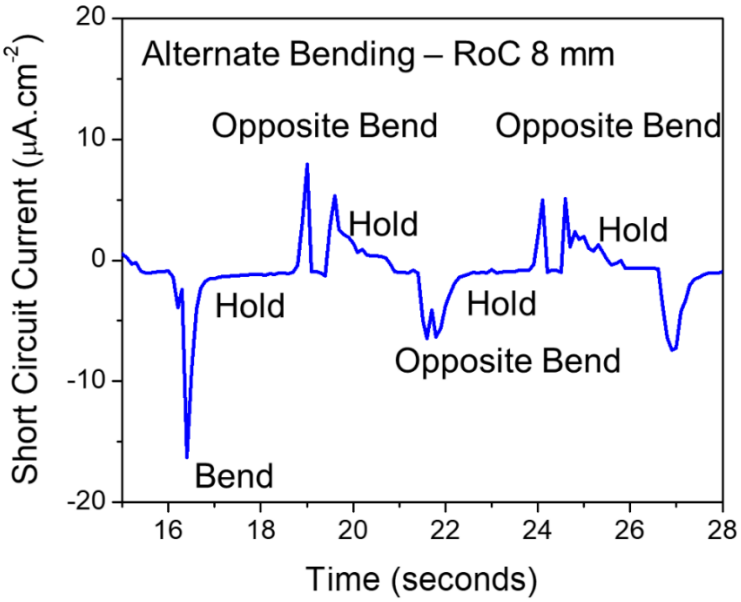

Figure 6.7. Short circuit current response during alternate bending trials

During alternate bending and unbending cycles, the harvester was bent and held one way followed by an alternate bend and hold in the opposite direction at the same bending radius of 8 mm. The observed peak current was similar to bending in one direction, however, during the alternative bending cycle, we observe two peaks in the opposite direction. As the harvester was not unbent in-between bending, holding and alternate bending, the first opposite peak was not followed by a gradual decay of current. This peak can be attributed to the current response arising from the concentration gradient in the two electrodes after the initial bend cycle. The second peak in the opposite direction results from the ion migration to neutralize the compressive and tensile stresses which are now set up opposite to the initial bending. Repeating this alternate bending trials showed the same type of behavior.

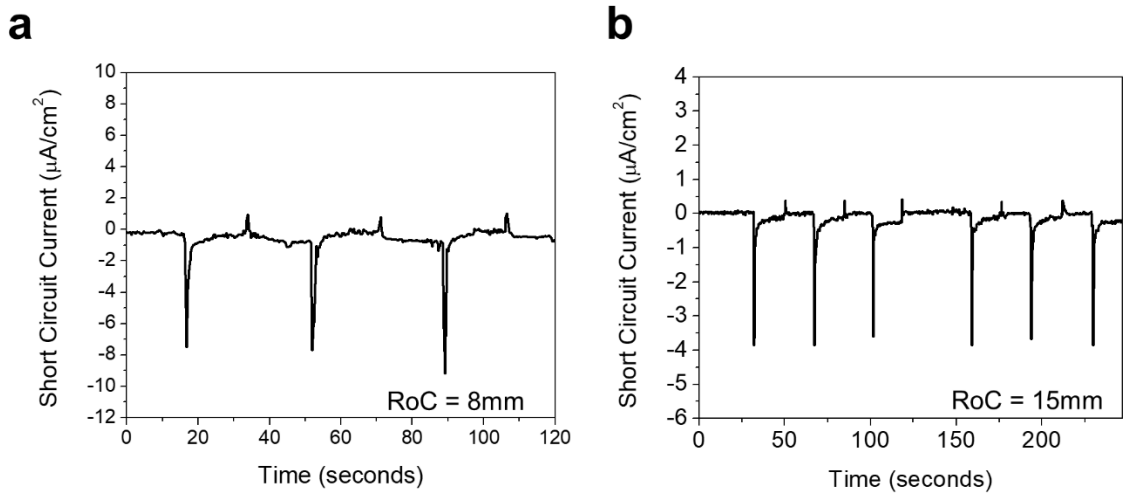

Figure 6.8. Short circuit current response during bending radii of 8mm (a) and 15 mm (b).

Increasing the bending radius results in increased asymmetric stresses on the individual electrodes thereby resulting in larger chemical potential gradient which in turn results in high peak currents.

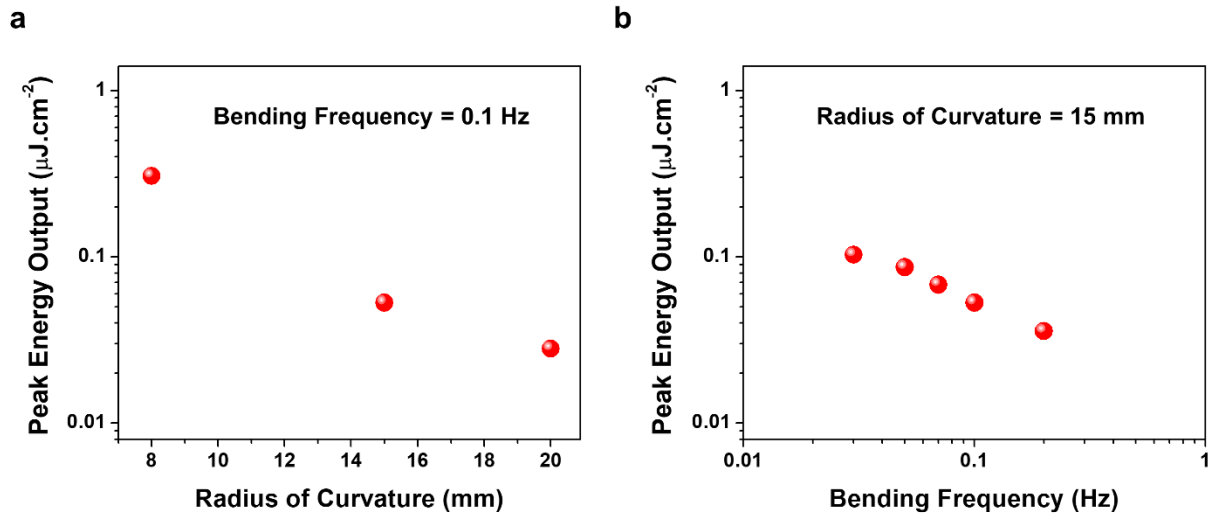

Figure 6.9. (a) Total energy harvested during a 10 second bend and hold time for bending radii of 8mm and 15 mm, **(b)** Total energy harvested during a fixed bending motion with radii of 15 mm and varying hold times

As the MLG system has a fast-kinetic response but low overall energy storage capacity when compared to conventional alloying electrodes such as silicon, black phosphorus and aluminum, the total energy harvested during the mechanical input is lower when compared to these high capacity alloying electrodes. However, as the kinetics of this co-intercalation process is orders of magnitude higher than these alloying electrodes, this device can operate in regimes where the duration of mechanical input is (0.1 seconds to 2 seconds). Owing to the fast-kinetics and high sensitivity, the device can deliver a high power during the short duration of the mechanical input making it suitable for harvesting energy during human motions such as walking and running (1-5 Hz).

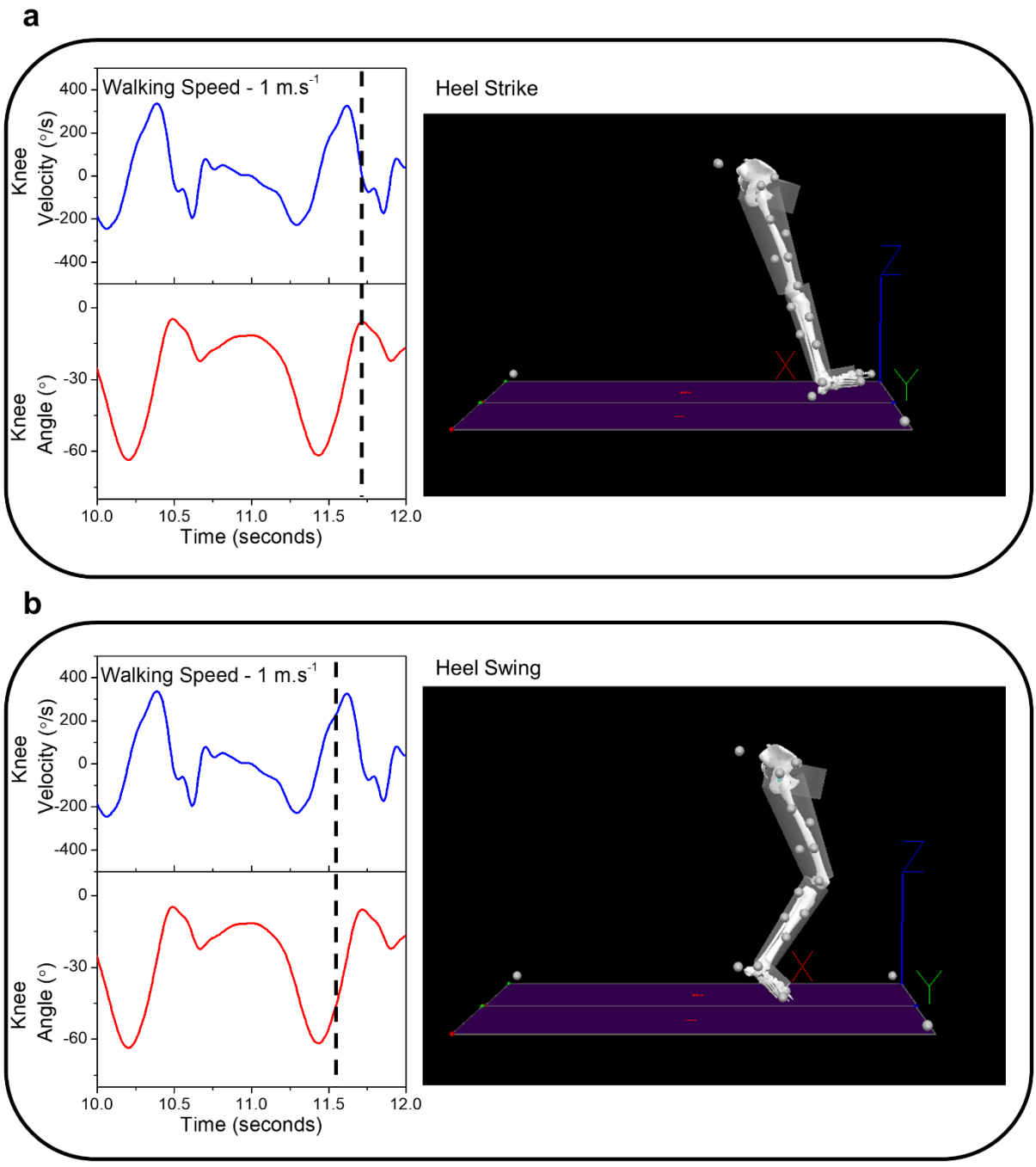

Figure 6.10. Major knee events during human walking at a fixed speed – knee angle and knee velocity observations. **(a)** During heel strike and **(b)** During heel swing

The human gait cycle consists of the following events: (i) initial contact, (ii) loading response, (iii) mid stance, (iv) terminal stance, (v) pre-swing, (vi) initial swing, (vii) mid-swing and (viii)

terminal swing. As our harvester is mounted on the knee joint, the major bending events are characterized by the knee bending movement which comprise ~20% of the gait cycle. The unbending event corresponds to the knee extension movement. The knee joint repeatedly undergoes bending and unbending events during human walking and running.

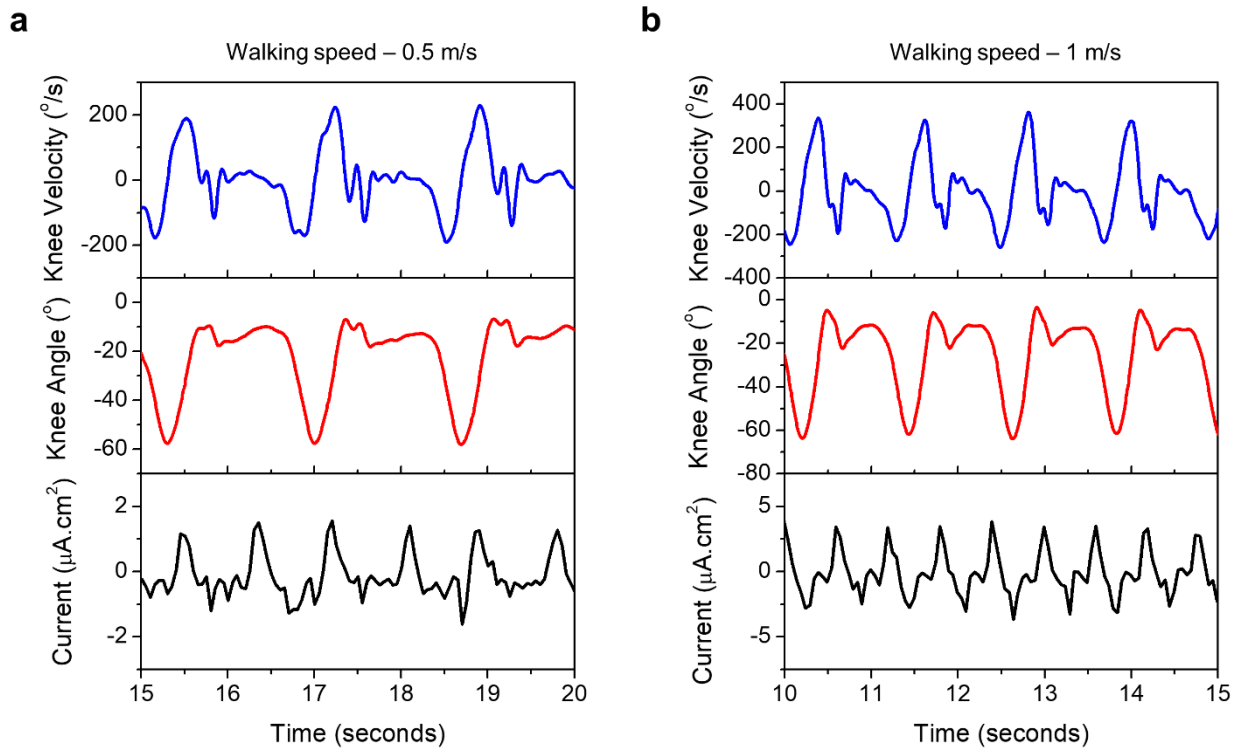

Figure 6.11. Current, knee angle and knee velocity changes during walking speeds: **(a)** 0.5 m/s and **(b)** 1 m/s.

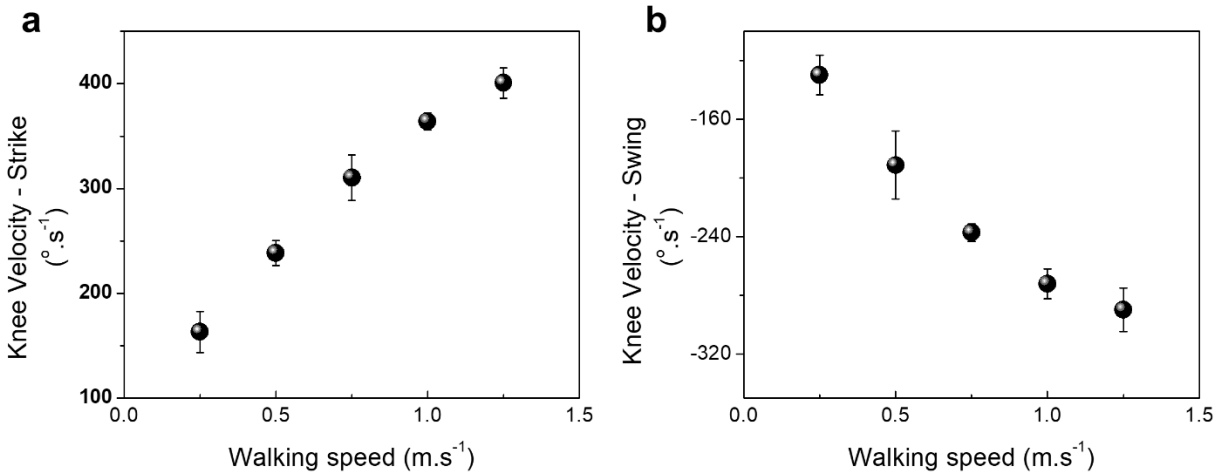

Figure 6.12. Changes to average knee velocity with varying walking speeds: **(a)** during heel strike phase and **(b)** during swing phase

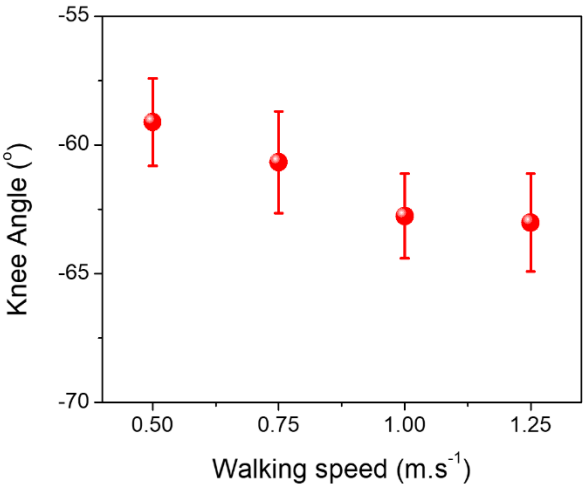

Figure 6.13. Changes to knee angle with varying walking speeds during knee flexure

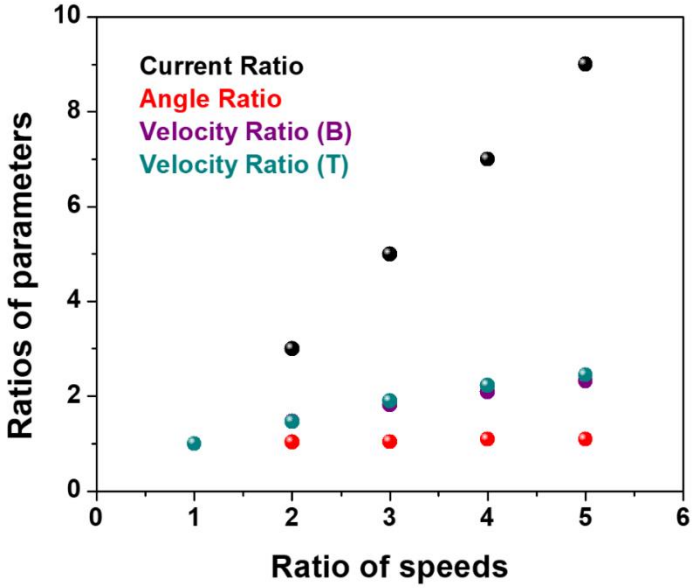

Figure 6.14. Relationship between knee angle, knee velocity and measured current output from the harvester at different walking speeds.

Chapter VII

7 Ultrafast Triggered Transient Energy Storage by Atomic Layer Deposition into Porous Silicon for Integrated Transient Electronics

7.1 Introduction

Transient electronics represents a class of devices where a trigger can be used to dissolve or destroy a device and any information it contains. The premise of a transient system is to exhibit stable and invariant device performance until an external trigger is applied, which can be in the form of pH, light, temperature, or a combination of these stimuli.[269, 270] The trigger initiates a series of reactions or mechanisms in the device that partially or fully dissolves the device, and renders the device inoperable in a manner that destroys the device and any information it may contain. There are many applications that can benefit from transient devices, ranging from information-sensitive electronic devices to biodegradable medical applications. Such a vast array of application areas also brings the requirement of diverse transient properties, including time of dissolution, controlled toxicity, and the type of external trigger source. For example, biological or medical applications may be more centered on toxicity of dissolution products, whereas surveillance and spy applications require fast disablement and dissolution times.

Recent efforts in the development of transient technology have been concentrated in small electronics[271-273] usually centered on silicon materials, silicon based photovoltaics,[269] medical energy harvesters,[274] bioresorbable electronics,[275, 276] and biodegradable primary batteries.[277] The first rechargeable power source with transient behavior has been described by

Fu *et al.* which demonstrates a rechargeable lithium ion battery that dissolves through a chemical cascade reaction.[278] This elegant design involves a power source packaged separately from other electronics or systems that it powers. Building from this work, the intersection of transient energy storage with integrated silicon-based systems could enable facile design of integrated silicon transient electronics and power systems.

Whereas silicon-based materials have been lauded for energy storage capability, stable performance of silicon both in the context of batteries and electrochemical capacitors most often requires surface passivation, usually with carbon or a passive oxide material.[279-283] This presents a challenge for transient behavior since the robust electrochemical stability of carbon leaves it incompatible with triggers used for transience, and incomplete passivation of the surface (that would enable transience) has the adverse effect of compromised function of the device prior to being triggered.[283, 284] However, one material that has been recently investigated for use in batteries and electrochemical (redox) supercapacitors is vanadium oxide, which is active toward lithium ion intercalation through surface reactions.[285-296] Of the methods to produce vanadium oxide materials, atomic layer deposition (ALD) boasts advantages of controllable film thickness and uniform surface morphology.[285, 286, 297-299] Vanadium oxide has also been shown to dissolve in basic solutions, thus making it suitable for transient applications.[278, 300, 301]

Therefore, in this report, we demonstrate the first integrated silicon-based on-chip energy storage system that exhibits transient behavior. This builds from vanadium oxide coated onto the interior of porous silicon that is electrochemically etched into a bulk silicon chip. By controlling the ALD deposition profile in a transient scaffold, ultrafast deactivation of the device occurs when exposed to an alkaline trigger solution, and full dissolution of all components occurs

within 30 minutes. This identifies a general route of combining the versatility of ALD with porous silicon transient materials to design integrated silicon transient power storage systems.

7.2 Experimental methods

7.2.1 Etching of porous Silicon

Preparation of porous silicon was carried using electrochemical etching technique. Highly p-doped porous silicon wafers (0.01-0.02 Ω/cm) were etched using an AMMT wafer-scale silicon etching system in a 3:8 v/v hydrofluoric acid and ethanol. An etching current of 45 mA/cm^2 was applied for 180 seconds on the silicon wafer to obtain a 5 µm deep porous layer. In general, depth of the porous structure can be tailored varying the etching time and etching current. Further optimization of these parameters can enable selective control of pore morphology tuned selectively to obtain desired coatings as well as good device performance

7.2.2 VO_x deposition using ALD

Vanadium oxide (VO_x) was coated on the obtained porous silicon structure using a GemStar 6" ALD system. The precursor, (98+%) Vanadium(V)tri-i-propoxy oxide (VTIP) with a chemical formula, $VO(OC_3H_7)_3$ was preheated to 55 ^oC before the process. Nanopure water (H_2O) obtained using a Millipore water purifier was used as the oxidizer. The precursor and the oxidizer manifolds were heated to 115 ^oC to prevent condensation effects. Ultra-high pure Argon was used as the carrier gas and a reaction temperature of 150 ^oC was maintained throughout the process. To obtain the gradient in thickness of VO_x coating on the 3D of porous silicon from pore tip to pore depth, VTIP and water pulses of 2 seconds each and short residence times of 2 seconds for both reactants in the reaction chamber was employed. Based on previous reports, residence times of about 20 seconds or greater is required for complete saturation of VTIP and

water in the reaction chamber. The overall reaction between VTIP and water can be split into two half reactions.

$$(V\text{-}OH)_{surface} + VO(OC_3H_7)_3 \rightarrow (O\text{-}V\text{-}(OC_3H_7))_{surface} + HOC_3H_7 \quad 22$$

$$(V\text{-}(OC_3H_7))_{surface} + H_2O \rightarrow (V\text{-}OH)_{surface} + HOC_3H_7 \quad 23$$

Gradient coatings on 3D porous structures using ALD can be generated using this concept which proves beneficial in the immediate disabling of the transient device. To determine the mass of the VO_x deposited per cycle, a silicon wafer (Diameter: 100 mm) was etched under the aforementioned conditions and subjected to 500 ALD cycles of VO_x deposition. The mass of the wafer before and after the ALD process gives an estimation of the mass of VO_x deposited per cycle on the porous structure.

7.2.3 Preparation of the gel electrolyte

3g of poly(vinyl alcohol) (PVA) was dissolved in 30ml of water and 0.5M $LiClO_4$ was added to the solution under constant stirring at 80 ^oC. This solution was cooled to room temperature to obtain the consistency of a gel. A freshly prepared gel electrolyte was used as the electrolyte for the transient device.

7.2.4 Preparation of the separator

5g of poly(ethylene oxide) (PEO) was dissolved in 8g of propylene carbonate containing 0.5M $LiClO_4$ was stirred overnight at 60 ^oC. The viscous solution was then doctor bladed onto a glass slide followed by drying in a vacuum over at 60^oC. The film was then peeled off and used as the separator for the transient device.

7.2.5 Electrochemical measurements

Electrochemical measurements were performed in a symmetric two-electrode configuration with identical electrodes of similar geometrical area. The PEO/$LiClO_4$ separator with the PVA/$LiClO_4$ electrolyte was

sandwiched between the two VO_x coated porous silicon electrodes. Cyclic voltammetry (CV) technique was used to analyze the redox behavior of the electrochemically active VO_x coating between -0.6 V to 0.6 V at a scan rate of 100 mV/s. 19 nm thick VO_x coated porous silicon corresponding to 400 ALD cycles which showed a reversible redox behavior was cycled at 100 mV/s using CV technique to understand the stability of the redox couple. Galvanostatic charge discharge (CD) analysis was performed at on all samples a current density of 0.1 mA/cm^2 to evaluate the performance of these transient devices. In a symmetric two electrode configuration both the electrodes contribute to the total capacitance of the device. Specific capacitance of these devices in the symmetric two electrode configuration was estimated from the average slope of the discharge curves according to:

$$C_{electrode} = 2C_{cell} = \left(\frac{2I}{\left(\frac{dV}{dt}\right)m}\right) \qquad 24$$

where m is the mass of the active material on both electrodes, dV/dt is the average slope of the discharge curve and I is the total discharging current. All electrochemical data was normalized to the area of the electrodes tested.

7.3 Results and Discussion

7.3.1 Concept of the transient energy storage device

Schematic representation of the concept of an integrated device as shown in Figure 7.1 gives insight into fabrication and the transient behavior of the fabricated device. The active energy storage material (VO_x) is deposited to play a dual role that both (1) inhibits corrosion-based deactivation of nanoscale silicon in electrochemical environments, and (2) provides active redox storage as an electrochemical capacitor. This architecture is designed so that in a triggering environment, the VO_x will dissolve and expose the unstable porous silicon material to corrosive conditions that dissolve and remove all materials except the bulk silicon. However, in the electrolyte environment, the VO_x/porous silicon system will exhibit stable, invariant

performance. Here, porous silicon plays a role of a tunable, high surface area transient template for the coating of active material, and can be integrated directly into bulk silicon materials using standard semiconductor processing technology. This means that this material can be processed into the backside of silicon electronics, or even coupled with other silicon-based transient electronics, which is schematically illustrated in Figure 7.1. A gel based PVA/0.5M $LiClO_4$ electrolyte (supplementary information) was used as an electrolyte to couple VO_x coated porous silicon transient devices. Additionally, for this system to be fully transient, a polyethylene oxide (PEO) based separator (appendix), which dissolves in the aqueous trigger media, was used. This leads to a device that can be a functional energy storage material until an external trigger (1 M NaOH) disables and disintegrates the device.

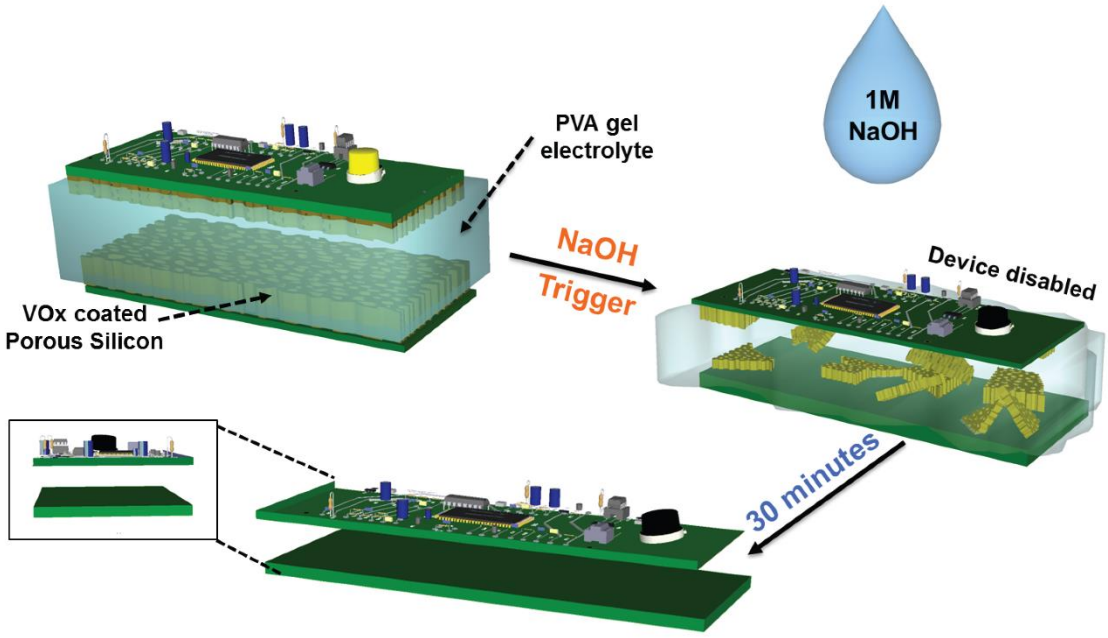

Figure 7.1. Schematic representation demonstrating the integration of transient energy storage into silicon-based (transient or non-transient) electronics. Triggering the system with 1 M NaOH

aqueous solution leads to near-immediate disablement of the device, and full dissolution within 30 minutes.

7.3.2 Ultrafast transience enabled by engineering VO_x – porous silicon architecture

A key aspect of this transient device design is the ALD deposition of VO_x materials.[302, 303] To accomplish this, we utilized sequential pulses of $VO(OC_3H_7)_3$ and H_2O with 2 second residence times. Due to the diffusion-limited growth of ALD coatings on the interior of high aspect ratio nanoporous materials, longer residence times are required for uniform coatings.[304] However, to design a material with optimized transient performance, we reverted to shorter residence times which yield a thickness gradient from top of the porous material to the bottom. Thickness of the films was measured based on ellipsometry of films coated on planar silicon surfaces (appendix) and penetration of the VO_x coatings was confirmed based on scanning electron microscopy (SEM) characterization. Full details of the ALD chemistry and experimental parameters are detailed in the supplementary information. Uncoated porous silicon with 5 μm deep pores is shown in Figure 7.2a. VO_x deposition on the porous silicon for 100 and 400 ALD cycles and the resulting pore morphology is shown in Figure 7.2b and 7.2c, respectively. The total areal mass loading of vanadium oxide in these composites is 0.057 mg/cm^2 and .229 mg/cm^2 for 100 and 400 ALD cycles, respectively. Evidence of a thicker VO_x coating is visually apparent in the case of 400 ALD cycles when compared to 100 ALD cycles, noting that the underlying porous silicon template is identical between Figs. 7.2a – 7.2c. Energy dispersive X-ray (EDS) on the cross-section of the porous silicon was performed, and line profiles corresponding to EDS scans are shown in Figures 7.2d and 7.2e. Based on EDS analysis, relative weight and atomic percentages of Vanadium and Oxygen are 64% Vanadium and 36% Oxygen (weight) and 36% and 64% (atomic), respectively.

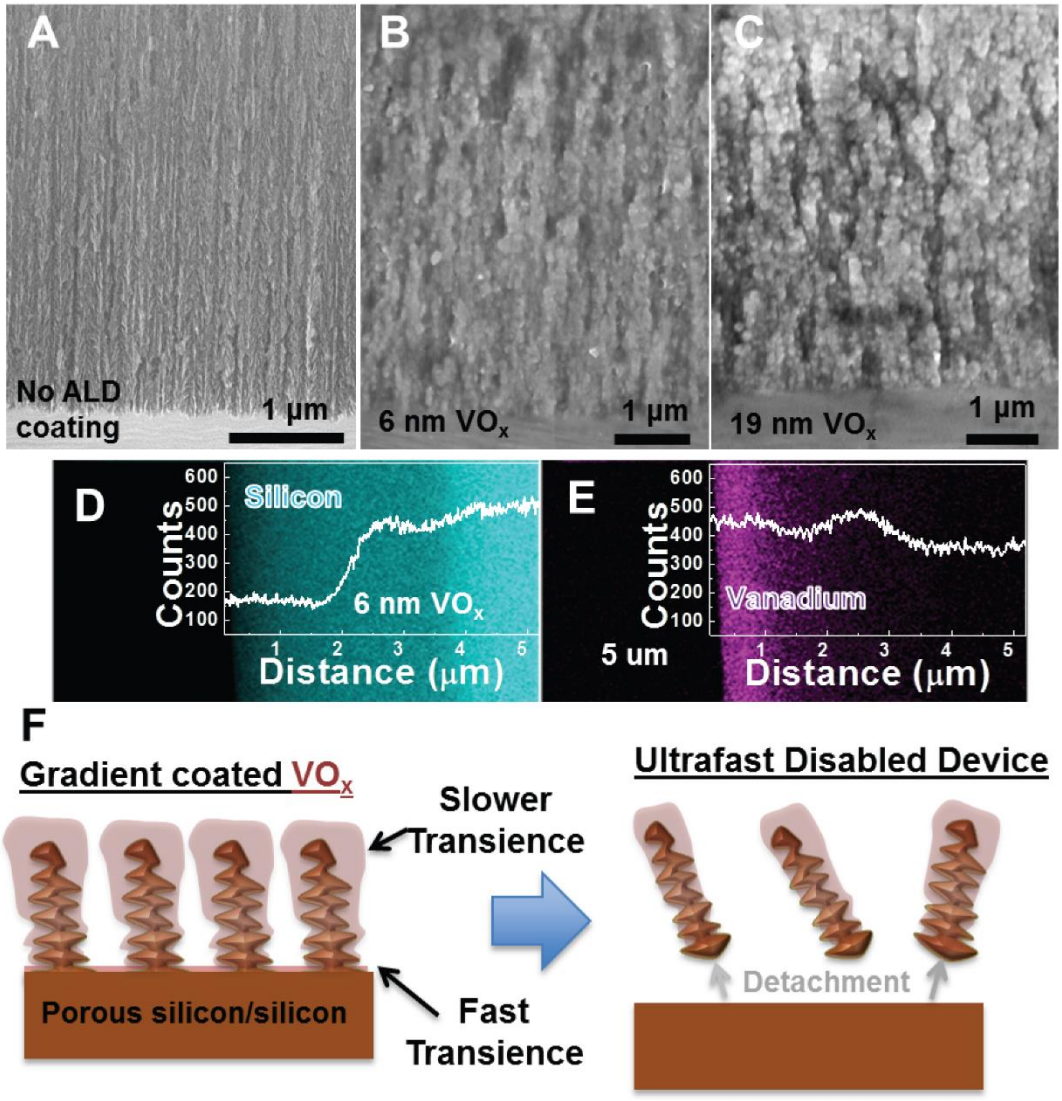

Figure 7.2. (A-C) SEM images of uncoated and coated porous silicon: **(A)** uncoated porous silicon, **(B)** 100 ALD cycles (6 nm) of VOx ALD coated on porous silicon, and **(C)** 400 ALD cycles (19 nm) of VO¬x ALD coated on porous silicon. **(D-E)** Cross sectional EDX maps of VOx coated porous silicon showing: **(D)** silicon and **(E)** vanadium down the cross-section of the porous silicon. **(F)** Scheme showing how the thinner coating at the porous silicon base leads to ultrafast disablement.

To further analyze the state of the VO_x material, we annealed ALD deposited VO_x in air at 450 °C for 1 hour and characterized the material using Raman spectroscopy (see appendix) before and after annealing. Due to the highly Raman active modes of crystalline vanadium oxide, Raman analysis demonstrates the transition from a non-crystalline or amorphous state of vanadium oxide to crystalline V_2O_5.[303] We therefore associate the ALD material to a non-stoichiometric and non-crystalline form of vanadium oxide which we label as VO_x. Notably, a greater concentration of VO_x is observed at the top of the porous silicon material, and this slightly decreases near the base of the porous silicon. Whereas this effect is due to diffusion-limited ALD growth that can be improved with higher vapor pressure precursors, longer residence times, or higher temperatures, such asymmetric thickness profiles bring a distinct benefit to the function of a transient device. In this design, the thin coating of the VO_x active material near the base of the porous silicon will dissolve away more rapidly than the thicker coating near the top of the material, (Figure 7.2f) and this will in-turn expose the base of the porous silicon – which is highly reactive in aqueous basic solutions. This causes the rapid detachment of the active material from the base (within seconds), which deactivates the energy storage function of the material. Therefore, transience occurs through a two-step process with rapid deactivation on the timescale of a few seconds, and eventual full dissolution on longer scales of minutes. To explicitly demonstrate this mechanism, we produced a control sample where the residence time was increased, leading to a uniform VO_x coating in the porous silicon. This system exhibited no rapid deactivation and a 4X longer transience time than the gradient coated samples (see appendix). Notably, this highlights the principle that engineered coating processes can enable wide versatility in the utility of transient functions in energy storage systems.

7.3.3 Electrochemical assessment of the transient energy storage device

Electrochemical measurements were carried out to assess the energy storage capability of these transient devices. This device was tested in a symmetric two-electrode configuration to assess the storage capability of the VO_x, as three-electrode measurements can over exaggerate the measured results.[302, 305] As the focus of this work is a transient, integrated energy storage platform, further development asymmetric designs can build upon the same general approach and enable a tunable range of operating voltages relative to that measured for VO_x. To characterize the electrochemical performance of these devices, we compared the same ALD parameters using 300, 400, and 500 ALD cycles, which corresponds to ~ 15, 19, and 24 nm thick coatings based on extrapolated from ellipsometry analysis (appendix). Cyclic voltammograms (CV) taken at 100 mV/s and galvanostatic charge-discharge curves taken at 0.1 mA/cm^2 corresponding to VO_x coated onto porous silicon templates at these three thicknesses are shown in Figures 7.3a and 7.3b. Analysis of both CV and charge-discharge curves emphasizes that a 19 nm thick VO_x layer corresponding to 400 ALD cycles exhibits the most fully developed stable redox peaks centered around 0 V which is expected for faradaic redox capacitors in symmetric two-electrode configurations. Compared to other thicknesses, this coating thickness also minimizes the resistance polarization in the device that is attributed to power loss on fast charge cycling. This coating thickness also leads to the highest total measured capacitance based on galvanostatic measurements. As the electrolyte used in this system is $PVA/LiClO_4$, the redox behavior of VO_x arises from the near- surface redox intercalation of Li^+ represented by:

$$xLi^+ + yVO_x + e^- \leftrightarrow Lix(VO_x)y \qquad 25$$

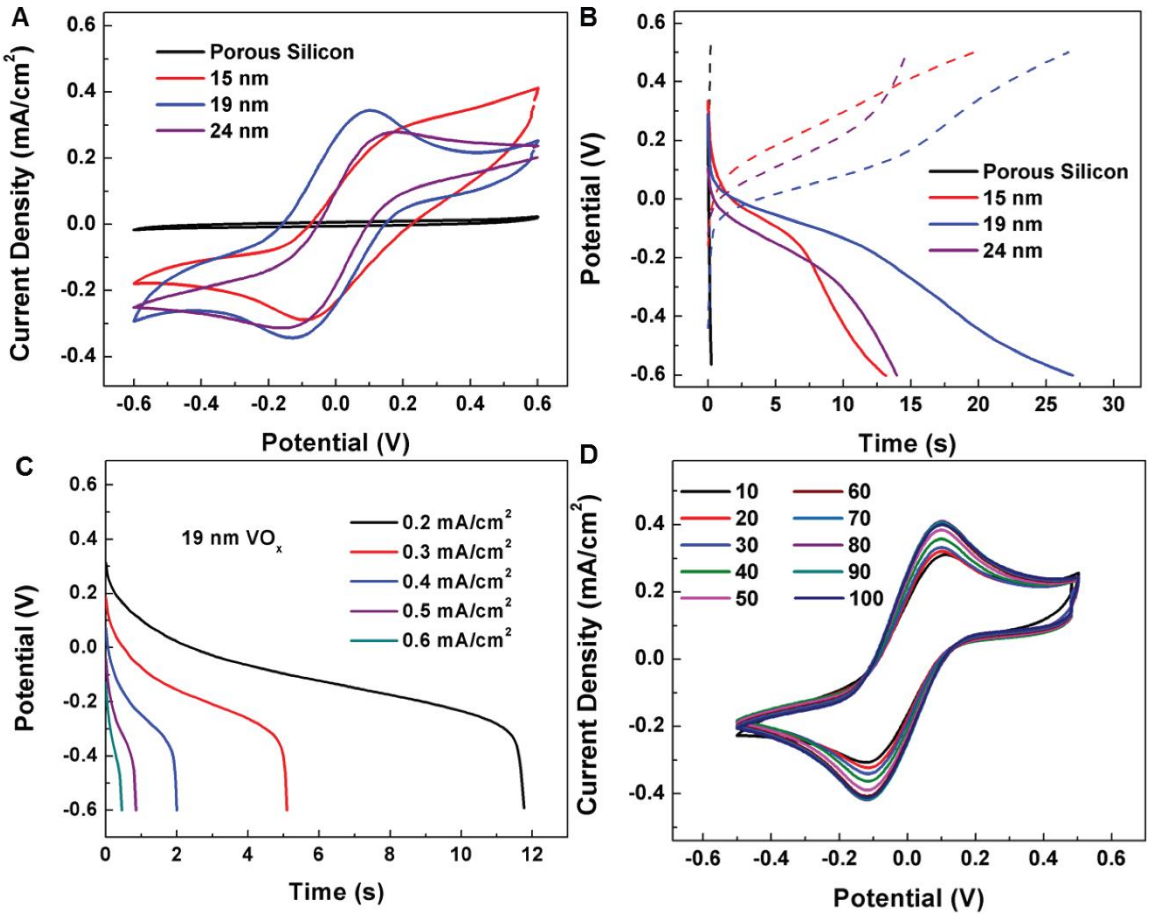

Figure 7.3. (A) Cyclic voltammograms of VO_x coated porous silicon at different coating thicknesses compared to uncoated porous silicon reference, **(B)** galvanostatic charge-discharge curves showing the 5th cycle for each coating thickness, and **(C)** galvanostatic rate study showing discharge performance as a function of discharge current, and **(D)** voltammetric cycling performance for transient energy storage device with 19 nm VO_x coating on porous silicon.

Two key variables represent the total energy storage capability of these materials: (1) the total mass of VO_x coated onto porous silicon that is optimized with thick coatings, and (2) the ability for the electrolyte to penetrate into the pore structure that is inhibited when thick coatings are applied. For the sample with 400 ALD cycles, specific capacitance based on charge-discharge

curves is measured as ~ 21 F/g. Whereas this specific capacitance is lower than that achieved using materials such as RuO_2 or $Ni(OH)_2$, the VO_x provides a distinct medium between transient behavior, the surface passivation role for electrochemical use of porous silicon, and a versatile ALD chemistry that can enable the ultrafast transience on silicon templates. These thickness studies hence establish an optimized VO_x thickness for this system near ~ 19 nm, and less than 24 nm. Charge-discharge tests at various current densities were performed on the devices with 19 nm VO_x coatings. The discharge curves at various current densities (Figure 7.3c) indicate stable near-surface redox intercalation reactions represented by the plateau region. Increasing current densities decreases the plateau region corresponding to decreased charge storage which is a result of the nature of these coated 3D porous electrodes. At higher rates, not all redox active VO_x sites on the 3D porous silicon structure are accessed resulting in decreased charge storage. The VO_x coatings on the porous silicon substrate were optimally chosen to achieve good transience as well as respectable electrochemical performance for integrated applications. Durability measurements were performed on devices prepared with the optimal coating thickness (Figure 7.3d) for over 100 CV cycles, showing stable cycling behavior. Based on the electrochemical tests, 19 nm thick VO_x coated porous silicon was used to demonstrate the transient behavior of the device. Electrochemical Impedance Spectroscopy (EIS) measurements were further performed in a symmetric two electrode setup with 19 nm VO_x coatings and the results indicate low equivalent series resistance and charge transfer resistance indicating stable charge storage capability (see appendix).

7.3.4 Transient behavior of the energy storage device

Demonstration of the transient behavior of the VO_x based porous silicon system (Figure 7.4) highlights the potential application of integrated transient energy storage using this

technique. Transient behavior triggered by an alkaline solution (1M NaOH) disables the VO_x-porous silicon electrode in less than 5 seconds due to the electrode design discussed in Fig. 7.2. This is in part due to the reactive nature of porous silicon in the triggering solution, with the full (uncoated) porous silicon material dissolution occurring in well under 1 min (Figure 7.4a). Coating the porous silicon surface with VO_x enables surface passivation in the electrolyte environment, but rapid dissolution of the full material when exposed to the trigger solution. The VO_x gradient that results in a thinner coating near the bottom of the porous material results in faster dissolution of this bottom section of the material, causing deactivation to occur within 5 seconds due to detachment of this material. Such ultrafast triggering can be highly beneficial for applications requiring immediate transience. Following the dissolution of the porous silicon/bulk silicon interface, the VO_x coated layer was observed to fully dissolve in around 30 minutes. In a full device, the penetration of the trigger solution into the device happens due to the initial swelling of the gel electrolyte. The transient behavior of the PEO/$LiClO_4$ separator is given in Figure 7.4c. The polymer separator dissolves within 30 minutes following the initial swelling in the trigger solution. Whereas a 1 M NaOH (pH=13) triggering solution ensures rapid dissolution, certain applications of transient electronics require low toxicity trigger solutions. We have therefore included dissolution tests of .1 M (pH=11) and .01 M (pH=9) NaOH solutions (see Supplementary Information), which show similar rapid transient deactivation except with longer time to achieve full dissolution. Such transient systems may also be ideally suited to operate in ambient humid conditions since the transient VO_x/porous silicon electrode itself is stable in such conditions.

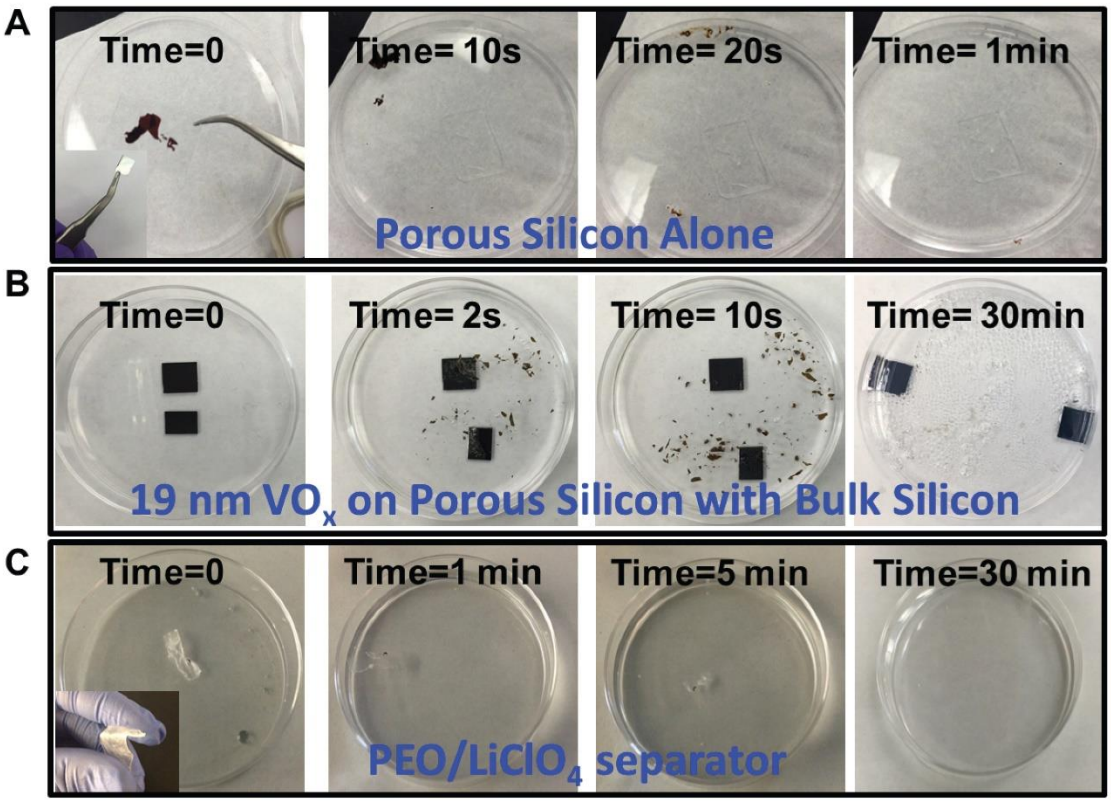

Figure 7.4. Transient dissolution of device components including **(A)** uncoated porous silicon (control), **(B)** 19 nm VOx gradient coating on porous silicon with bulk silicon substrate (left behind after 30 mins), and **(C)** PEO/LiClO4 separator. Dissolution tests with uniformly coated VOx (appendix) support the mechanism of the gradient coating in rapid deactivation of the energy storage material that is illustrated in these dissolution studies.

7.3.5 Integration of the transient energy storage with microelectronic systems

Whereas this effort so far demonstrates the transience of VO_x/porous silicon electrodes, we further performed experiments to demonstrate the direct integration of transient energy storage into microelectronic systems. To accomplish this, we used a commercially obtained integrated silicon microchip made with copper processing. To produce a fully integrated transient energy storage electrode, we etched porous silicon into the backside of the microchip,

and coated the porous silicon with 19 nm VO_x in a similar manner as described previously (Figures 7.5A-B). This leads to a configuration where the energy stored in the backside of the microchip can power the front-side components, and operation of the total system can be systematically deactivated based on the transient energy storage material.

To demonstrate transient behavior of the integrated electrode, it was exposed to identical triggering environments (1 M NaOH) and after 30 minutes, full dissolution of VO_x/porous silicon active material was observed. This demonstrates integration of transient energy storage with silicon electronics for the first time. In addition to fully transient systems, this also provides a route toward integrated transient electronics where the electronic components by themselves may not be transient, but their electronic function can be disabled by the transient behavior of the integrated power source.

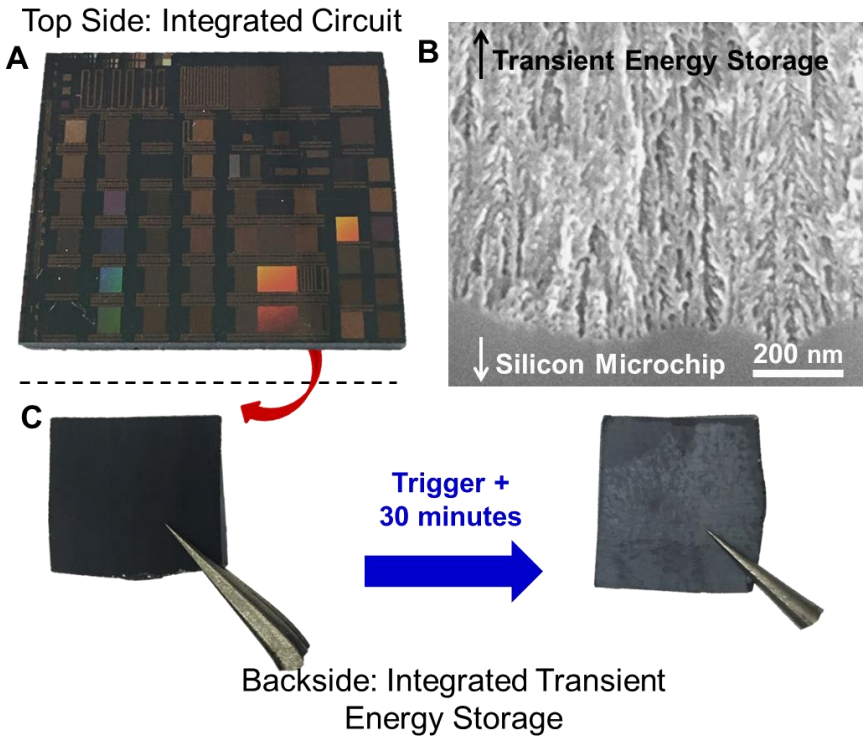

Figure 7.5. Transient behavior of an integrated circuit microchip where the backside is directly etched and coated with VO_x to provide on-board integrated storage. **(A)** Front side image of the integrated circuit microchip, **(B)** SEM image showing the interface between the silicon material in the microchip and the on-board transient energy storage material, and **(C)** image showing the backside of the microchip before and after triggering, where the transient energy storage material is visually fully dissolved. This opens a new class of transient electronics where on-board transient power sources that power integrated electronics can enable transient operation even when the electronic components themselves do not exhibit transience.

Overall, whereas we highlight this route for VO_x coated onto porous silicon, we emphasize that porous silicon is a universal template for transient energy storage. The ability to coat other metal oxides or nitrides that exhibit energy storage capability into the interior of transient porous silicon materials opens a full design space to engineer new transient systems for

electronics, biomedical applications, or defense applications. This builds on the principle that any system that is designed to dissolve or disappear when triggered still requires a power source to facilitate operation prior to triggering – with the most elegant design being an integrated and fully transient power system. Here we demonstrate the first such integrated power source into silicon materials, with promise to diverse transient applications.

7.4 Conclusions

In summary, we demonstrate the first design for a transient energy storage electrode material that is integrated seamlessly into silicon material that can dually function for either transient or non-transient silicon-based electronics. By combining the native transient properties of porous silicon with the controlled gradient coatings of active materials using atomic layer deposition, our work highlights the capability to achieve stable energy storage (> 20 F/g) until a trigger is applied, which deactivates the energy storage function in a matter of seconds, with full dissolution occurring within 30 minutes. We demonstrate this specifically for vanadium oxide (VO_x) coated onto porous silicon, where the VO_x plays a role to protect the reactive porous silicon and provide active redox storage until a trigger is applied, which dissolves both the porous silicon and the VO_x materials. We further explicitly demonstrate the integration of transient energy storage using this approach into the backside of a silicon integrated circuit, emphasizing the simplicity in transitioning this approach to integrated applications. As silicon is a benchmark material for evolving efforts in transient electronics, this technique is generalizable to a wide range of different coatings that can be coupled with porous silicon using ALD for stable performance and triggered transience. In the circumstance that not all components in a circuit may be transient, the utility of a transient power source is that all on-board components

being powered will ultimately be disabled in concert with the integrated power system – a feat that we show can be achieved in a matter of seconds using this design.

Acknowledgements

We gratefully acknowledge helpful discussions with Dr. Sanjay Mathur and Ms. Shuangzhou Wang regarding ALD processing, and Dr. Huazhi Li and Dr. Stephen Bachman at Arradiance for critical insight into ALD VO_x process development. We also thank Adam P. Cohn, Landon Oakes, Andrew Westover, and Mengya Li for useful discussions regarding this work, and Dr. Rizia Bardhan for the use of lab facilities and insights regarding material fabrication and characterization. This work was supported by National Science Foundation grant CMMI 1334269. A.D. and K.S. are supported in part by the National Science Foundation Graduate Research Fellowship under Grant No. 1445197.

7.5 Appendix

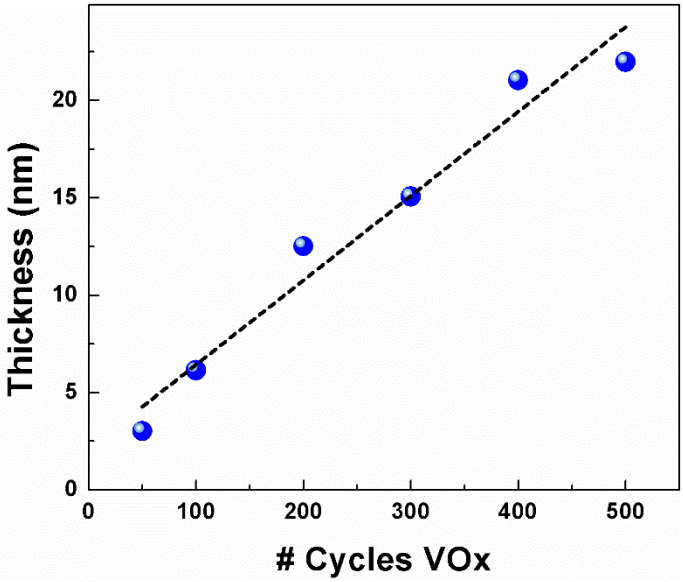

Figure 7.6. Plot of VOx coating thickness as a function of the total number of ALD cycles showing the expected overall linear increase in thickness expected for ALD processes.

Thickness estimation of the VO_x coatings after the ALD process was performed using a JA Woollam M2000VI Spectroscopic Ellipsometer. The measurements were performed on a silicon wafer with VO_x depositions for various ALD cycles (50-500) using the same process conditions followed in the deposition process of VO_x on porous silicon.

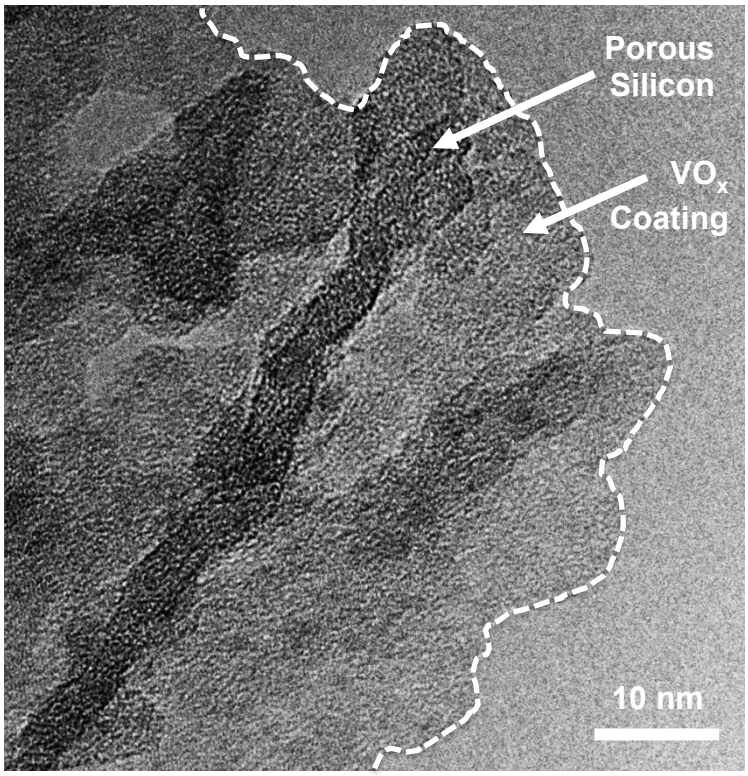

Figure 7.7. TEM image of VOx coatings on porous silicon.

As labeled, the porous silicon material is darker than the VO_x in bright field images. TEM images are acquired using an FEI Osiris TEM at a beam voltage of 200 kV and a screen current of 1.3 nA.

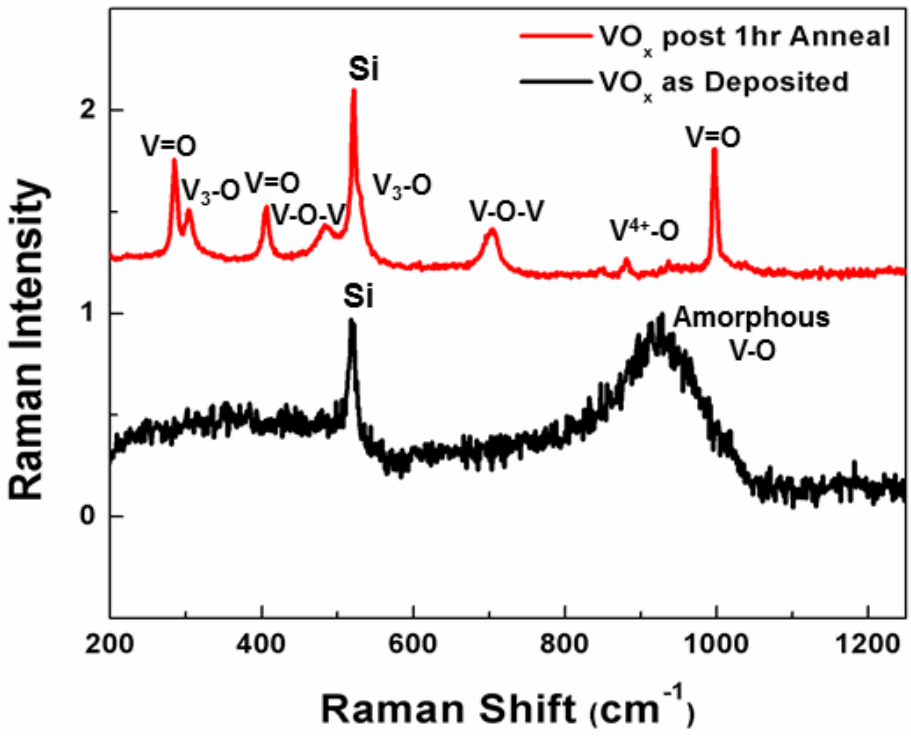

Figure 7.8. Raman spectroscopic analysis of the VO_x material before and after annealing at 450^{o}C in air, with stretch modes labeled.

Prior to annealing, broad spectral features, such as the peak centered at 900 cm^{-1}, elucidate the presence of a state of VO_x that is disordered or amorphous. After annealing, the distinct Raman characteristics of V_2O_5 emerge, indicating the crystallization to the orthorhombic crystalline phase of V_2O_5. Raman modes at 283 cm^{-1}, 404 cm^{-1}, 1006 cm^{-1} correspond to the V=O bond and the modes at 304 cm-^{1} and 529 cm^{-1} indicate the presence of V_3-O bonds. The Raman modes corresponding to the V-O-V bonds are located around 481 cm^{-1} and 710 cm^{-1}.[306] In turn, this implies, in correlation with EDS measurements, that the VO_x material is an oxygen-deficient and non-crystalline form of a material related to V_2O_5.

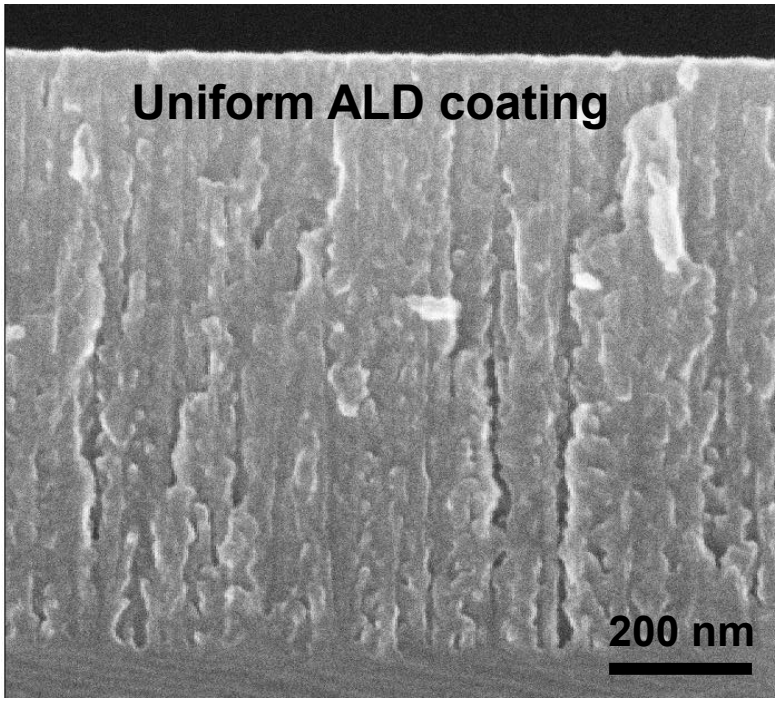

Figure 7.9. Cross section SEM image of a porous silicon material with VO_x

Cross section SEM image of a porous silicon material with VO_x distributed uniformly across the length, as opposed to a gradient distribution as described earlier. Uniform ALD coatings of VO_x were achieved by doubling the residence time of the precursors in the reaction chamber. The resulting sample was tested to understand the transient behavior from the uniform coating.

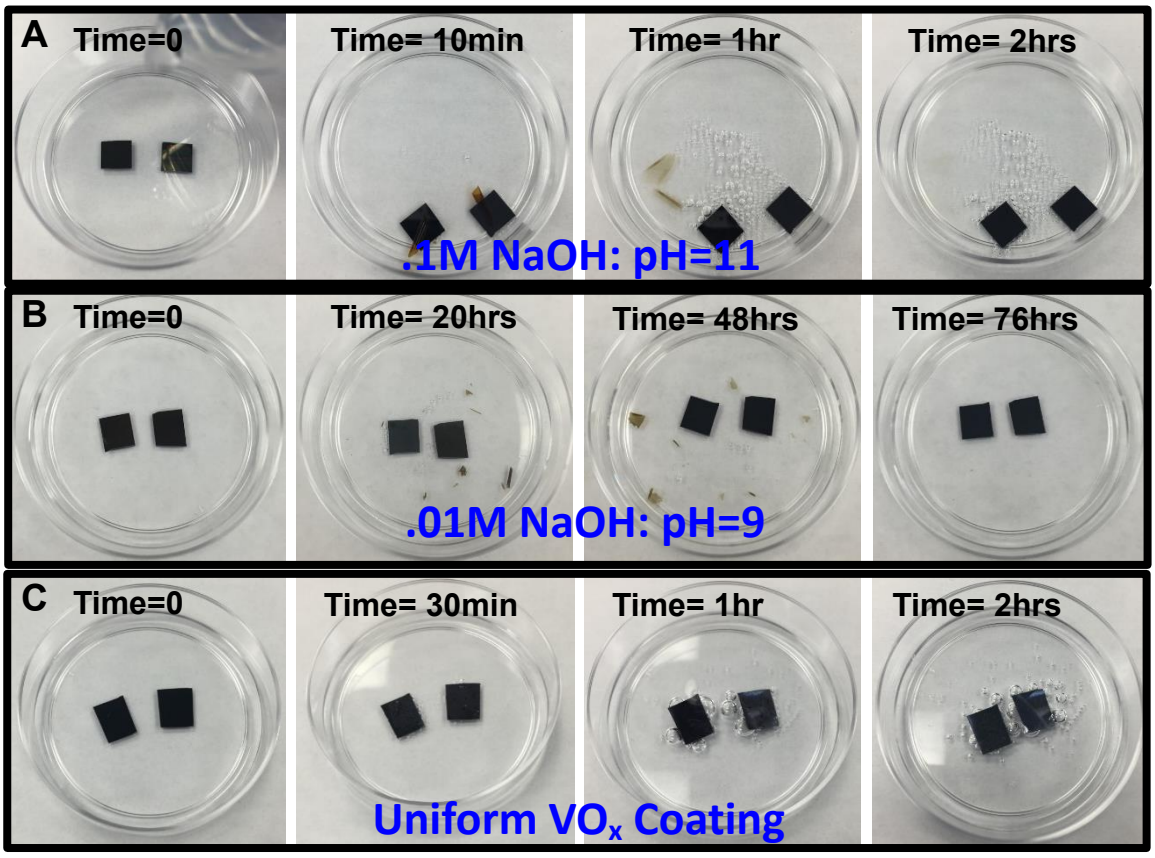

Figure 7.10. Transience of gradient coated VO_x/porous silicon energy storage electrodes in different triggering solutions

Transience of gradient coated VO_x/porous silicon energy storage electrodes in different triggering solutions (A, B) and uniformly coated VOx/porous silicon electrodes in 1 M NaOH triggering solutions. From A-B, as the pH decreases, the rapid triggering effect is evident based on the detachment of the active material from the silicon electrode, even though the time required to achieve full dissolution is significantly increased – especially for 0.01 M NaOH which takes up to 76 hours to fully dissolve. In contrast to this mechanism, uniformly coated VO_x/porous silicon transient electrodes do not exhibit the rapid deactivation step observed in the gradient coated electrodes, and fully dissolve while retaining their on-chip configuration in a

period of 2 hours. This demonstrates the nature of the gradient ALD coating of VO_x in allowing ultrafast deactivation that can be useful in transient systems.

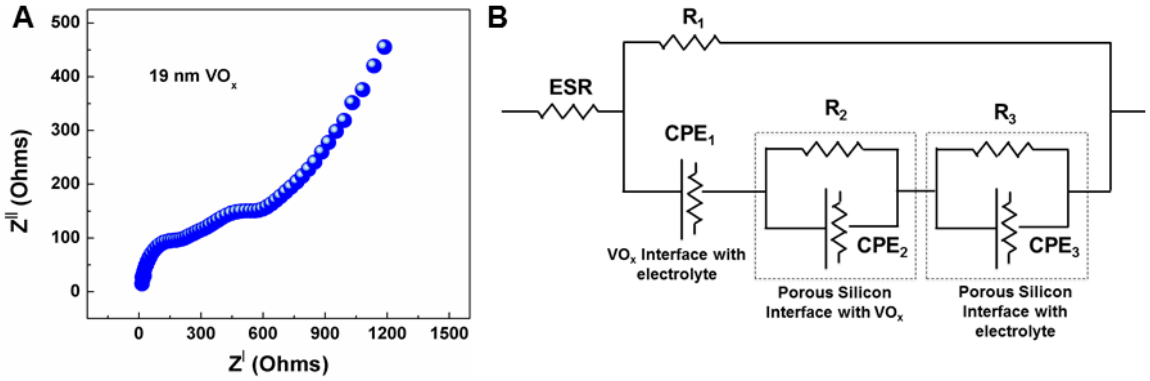

Figure 7.11. (A) Electrochemical Impedance Spectroscopy of the 19 nm VO_x coated porous silicon electrode and **(B)** Equivalent circuit representation that describes the EIS spectra of 19 nm VO_x coated porous silicon.

Electrochemical Impedance Spectroscopy was performed on the 19 nm VO_x coated porous silicon. The symmetric electrode system was subjected to a DC bias of 0 V at an amplitude 10 mV RMS in the frequency range of 100 kHz to 0.01 Hz. The resulting Nyquist plot comprising of the real and imaginary impedances is given in Figure S6A. The VO_x coated porous silicon has a relatively low ESR value (20 Ω) which is evident from the Nyquist curve. Equivalent circuit representing the resistances observed in the system arising from various interfaces is shown in Figure S6B. The polymer electrolyte gel and VO_x interface, the interface of VO_x and porous silicon and the interface of porous silicon and the electrolyte resulting from the gradient coating of VO_x comprise the resistances in this system. As the measurements were performed in a symmetric two electrode configuration, the resistance corresponding to the VO_x electrolyte interface has a moderate value of about 170 Ω.

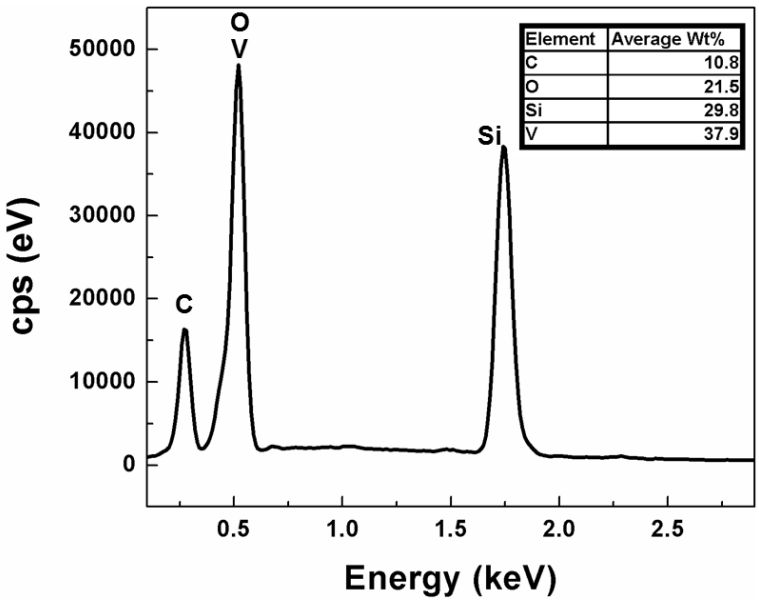

Figure 7.12. Representative Energy Dispersive X-Ray Spectroscopy cross-sectional spectrum of VO_x coated porous silicon electrode.

The EDS spectrum shows elements of Vanadium, Oxygen, Silicon, and Carbon (from the carbon tape substrate). Based on compositional analysis of the vanadium oxide material, assumed to only contain V and O, this indicates relative weight percentage of Vanadium and Oxygen as 64% Vanadium and 36% Oxygen within the VO_x composite.

Chapter VIII

8 A Fully Transient Mechanical Energy Harvester

8.1 Introduction

Despite the recent emergence of the field of transient technologies, numerous prototype biomedical/environmental sensors, actuators, sensitive data storage, analysis and transmitting systems have already been developed with transient capabilities.[307-310] These transient devices carry out the specific task for which they are designed until triggered with some controlled external stimulus to undergo complete dissolution or destruction.[308, 311-313] In this area, two broad categories can be defined for transient devices. First is transience that leads to elimination of a specific device and all its components along with all the functionalities or data it may contain. The second form of transience is relying on architecture-integrated security measures of valuable systems and implement an absolute and irreversible power cutoff triggering a chain of events that halt operation of the device preventing transmission or access to any sensitive data, without physically destroying the data or system. The latter case has only been recently investigated, with efforts concentrated toward transient batteries or energy storage materials.[39, 314-316] However, this route is advantageous over full system and data destruction in that power systems are cheap, replaceable, and easily customizable to the system they power. Further, for most electronics or data-containing systems, disablement of the power system is sufficient to halt unwarranted access or transmission of data from the device until it is intercepted by a trusted source.

In this regard, recent state-of-the-art efforts have focused on cascade reactions that render dissolvable Li-ion batteries or ultrafast disablement mechanisms for energy storage platforms.[314,

[315, 317] However, with the emergence of portable data-containing technologies that can be wearable, integrated, or systematically coupled or powered with human motion, new opportunities for transient systems emerge. Capturing ambient mechanical energy that is otherwise wasted is an attractive form of energy harvesting that is not limited by the situational dependence of solar, wind or thermal systems. While conventional mechanical energy harvesters, such as piezoelectric and triboelectric devices, are best suited for operation at resonant frequencies commonly orders of magnitude higher than those exhibited in human motion (e.g. < 5 Hz)[217, 318, 319] recent studies have focused on systems tailored to low frequencies that are advantageous for such application.[256, 318, 320] Specifically, devices that leverage the stress-induced mechanical-electrochemical coupling of alloying materials presents a new class of harvester device that can operate at low frequencies and exhibit high performance.[229, 321] By exploiting the design of such systems to focus on materials that are uniquely compatible with transient operation, this opens the door for devices that are capable of harvesting mechanical energy, being implemented in directions combined with wearable technology, and having the capability to be fully transient and dissolve when triggered with an external stimulus.

Here, we report the design and performance of the first transient energy harvester that builds upon a mechanical-electrochemical harvesting mechanism to enable low-frequency operation. This utilizes two identical alloyed aluminum-lithium electrodes separated by an electrolyte soaked polyvinyl alcohol (PVA) separator and combined in a sandwich configuration that, upon triggering, fully dissolves in 30 min. This prototype harvester delivers a peak power output of 0.208 $\mu W\ cm^{-2}$ and a peak energy output of 1.762 $\mu J\ cm^{-2}$ at low bending frequencies of 0.1 Hz with continuous energy generation (energy generation timescale of 10s). Our studies

demonstrate this design does not pose any performance trade-off by moving to a transient system, with performance competitive with state-of-the-art results reported in the literature.

8.2 Experimental methods

8.2.1 Fabrication, testing and dissolution

Aluminum foils (MTI Corporation - thickness 15 µm, purity >99.3 %) were ultrasonically cleaned in acetone, ethanol and DI water followed by lithiation at 0.1C (80% assuming 500 nm thickness) in a custom-made cell using $LiPF_6$ (1M) obtained from Sigma Aldrich) in 1:1 vol% ethylene carbonate (EC, Sigma Aldrich) and diethyl carbonate (DEC, Sigma Aldrich) with a lithium foil counter electrode using a Celgard 2500 separator. Following lithiation the lithiated foil was cut into two identical halves and was assembled in a sandwich configuration using an electrolyte (1M $LiPF_6$ in 1:1 vol% EC:DEC) soaked PVA film (Monosol). This configuration was packaged using PVA film (Monosol) and the two identical lithiated aluminum electrodes in the configuration were connected in short circuit mode for over 2 hours using an external wire to homogenize the composition and achieve equilibrium. Mechanical bending and pressing tests were performed using finger tapping as well as using a custom-made setup employing an arduino and servo motor. Electrochemical tests were performed using a PGSTAT 101 potentiostat using an Autolab interface. Transient behavior of the device was assessed in KOH (Sigma Aldrich) 2M solution. X-Ray diffraction and SEM/EDS characterization were performed using Rigaku Smart Lab and Zeiss Merlin respectively.

8.3 *Results and discussion*

8.3.1 *Device configuration and operational principle*

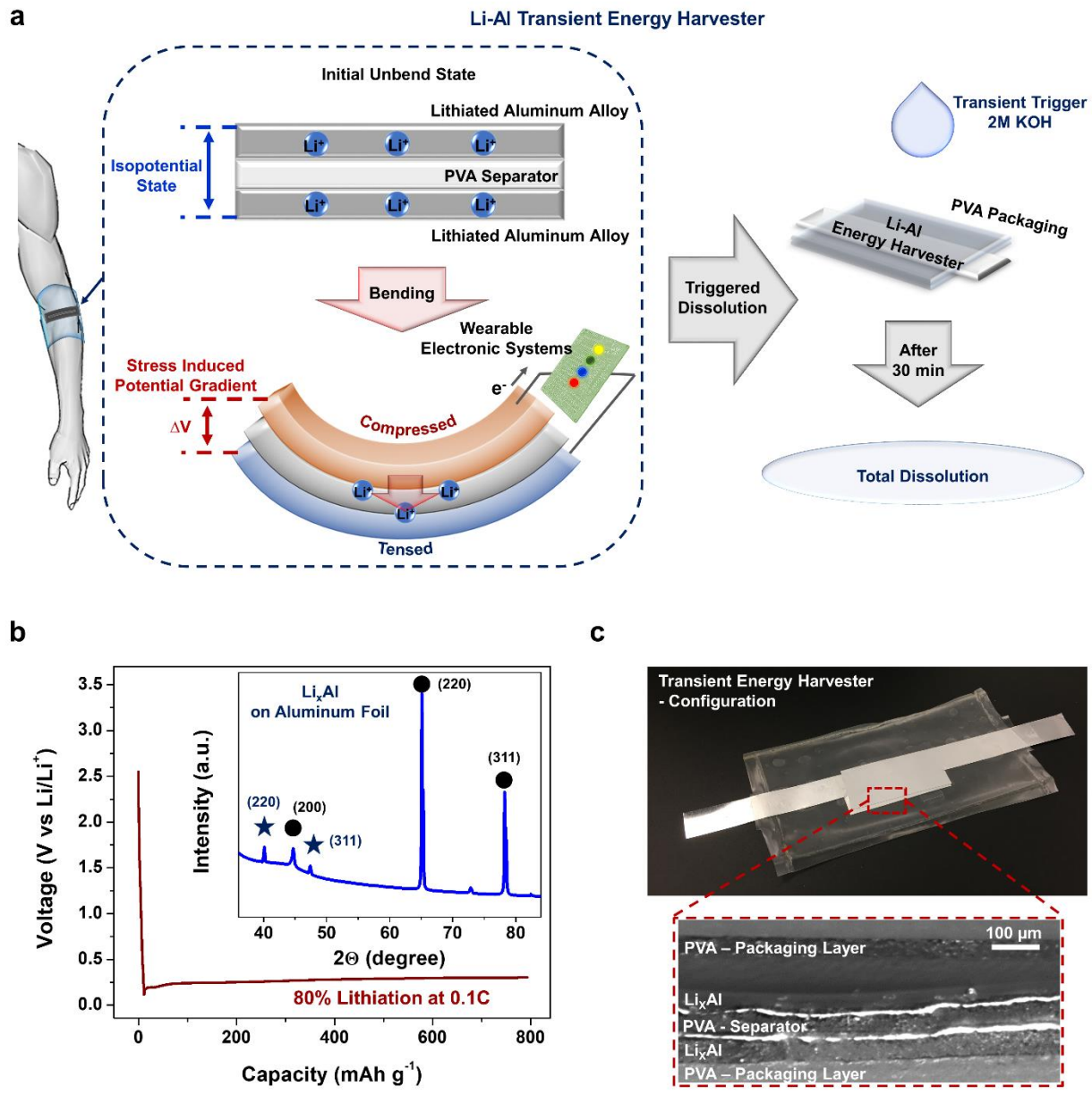

Figure 8.1. (a) Schematic representation of the working and dissolution behavior of the Li_xAl transient energy harvester, **(b)** Lithiation profile of the aluminum electrode, inset: X-ray diffractogram showing the lithiated aluminum phase on the aluminum foil, and **(c)** Optical

micrograph of the prototype transient energy harvester with cross-sectional image showing the different constituent layers in the sandwich configuration.

The device configuration used in the transient energy harvester involves a sandwich configuration comprising two identical alloyed aluminum-lithium (Li_xAl) electrodes (Figure 8.1a) prepared from aluminum foils. Though many materials employed in conventional battery systems are known show dissolution behavior in certain solutions, aluminum-based electrodes were chosen owing to the versatile dual functionality it offers: (i) performing the role of current collector as well as, (ii) controllably alloying with lithium electrochemically, forming active lithium aluminum alloys. The device, assembled in this sandwich configuration, when bent, induces asymmetric stresses that results in compression on one electrode and tension on the other, producing a chemical potential gradient as a result of the mechano-electrochemical coupling[41, 105, 217, 229, 319, 321-323] (Appendix, Figure 8.5). The relationship between stress induced chemical potential gradient and bending mechanics of the device is provided in the supporting information (also see appendix, figure 8.6). The induced chemical potential gradient facilitates the migration of the Li^+ ions from the compressed side to the tensed side resulting in electron flow in the outer circuit thus generating energy output. Moreover, this occurs with all components in the design amenable to full dissolution when a basic aqueous trigger is applied. The identical partially charged electrodes are fabricated using two halves of a single lithiated aluminum foil (Appendix, Figure 8.7). The aluminum foil (thickness ~15 μm) was galvanostatically lithiated (Figure 1b) to 80% (792 mAh g^{-1}) of its theoretical capacity (990 mAh g^{-1}). X-Ray diffractogram (Figure 8.1b – inset) verifies the presence of the lithiated phase with peaks corresponding to Li-Al alloy ((220) at 40^o and (311) at ~47^o) on aluminum foil ((200) at 44.7^o (220) at 65^o and (311) at 78.2^o).[315] SEM/EDS elemental maps of the cross-section of the

lithiated aluminum foil indicates the presence of Li-Al alloy, and is also provided in the appendix, figure 8.8. The separator used in this prototype is a PVA film soaked in $LiPF_6$ (1M) in EC: DEC (1:1 vol%) electrolyte (see experimental section). The prototype harvester was packaged using PVA films to ensure air stability of the constituents during operation, yet allow transience owing to the known dissolution behavior of PVA in basic solutions.[39, 315] A cross sectional optical micrograph shown in figure 8.1c illustrates the different layers of the assembled energy harvester.

8.3.2 Electrochemical response of the device

The working principle in these devices is due to mechanical stimuli induced asymmetric stress generation in the two constituent lithiated electrodes (see appendix), which is transferrable to both bending and pressing operation modes.[321] To assess the chemical potential gradient and the resulting ion flow corresponding to mechanical energy input, open circuit voltage (V_{OC}) and short circuit current (SSC) measurements were performed on the device respectively. Figure 8.2a and 8.2b show V_{OC} and SSC during pressing mode where repeated mechanical inputs of ~0.2 MPa were applied to the harvester. Similar tests were performed during bending mode (Figure 8.2c and 8.2d) resulting in repeatable changes to voltage and current which uniquely correlate with the frequency of the input mechanical stimuli. The V_{OC} of the device increases gradually upon application of a mechanical stress and decreases upon release reaching the initial resting potential. The very nature of the open circuit voltage test implies that the lithium ions do not migrate across the separator and therefore no electrons are owing from one electrode to the other in the external circuit. Thus, we detect the gradual change in voltage corresponding to the changes in lithium concentration near the surface of the active electrode resulting from the stress experienced by the electrodes.

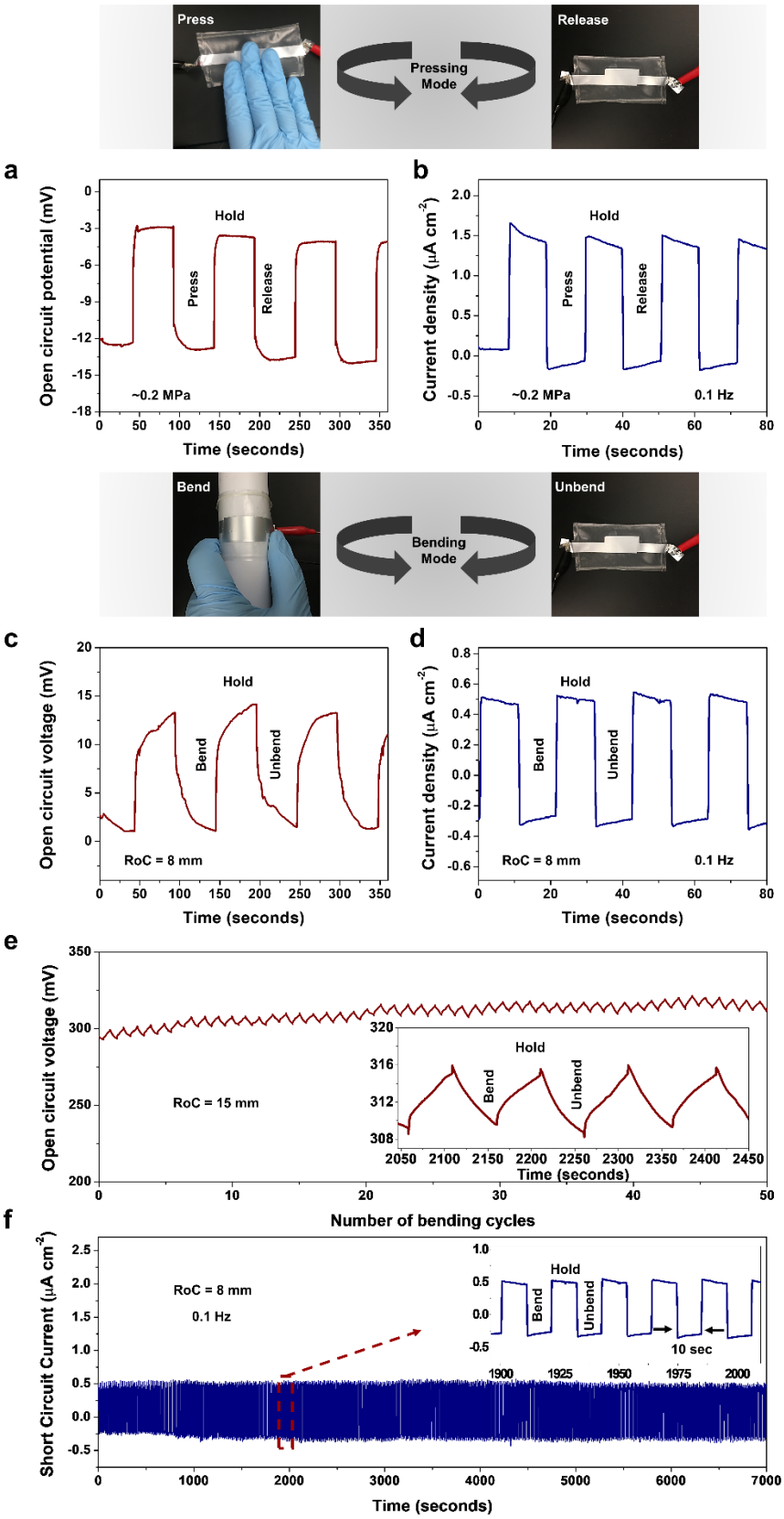
Press
Release
Pressing Mode
a
Open circuit potential (mV)
Hold
Press
Release
~0.2 MPa
Time (seconds)
b
Current density (μA cm-2)
Hold
Press
Release
~0.2 MPa
0.1 Hz
Time (seconds)
Bend
Unbend
Bending Mode
c
Open circuit voltage (mV)
Hold
Bend
Unbend
RoC = 8 mm
Time (seconds)
d
Current density (μA cm-2)
Hold
Bend
Unbend
RoC = 8 mm
0.1 Hz
Time (seconds)
e
Open circuit voltage (mV)
RoC = 15 mm
Hold
Bend
Unbend
Time (seconds)
Number of bending cycles
f
Short Circuit Current (μA cm-2)
RoC = 8 mm
0.1 Hz
Hold
Bend
Unbend
10 sec
Time (seconds)

Figure 8.2. (a) and **(b)** Open circuit voltage and short circuit current measurements during the pressing tests, **(c)** and **(d)** Open circuit voltage and short circuit current measurements during the bending tests, **(e)** and **(f)** Open circuit voltage and short circuit current measurements during bending – cycling study.

The theoretical voltage output of lithiated aluminum alloys at the different radii of curvatures compared to other battery electrode materials is provided in the appendix (Figure 8.9) for comparison. The SSC response (also, see appendix, figure 8.10) of the device shows an increase in current in one direction during application of mechanical stimuli corresponding to the chemical potential induced ion migration toward a peak value followed by gradual decrease in current observed as long as the mechanical input is maintained (holding phase). During short circuit measurements however, the lithium ions migrate across the separator. Therefore, as soon as the device is bent, an asymmetric stress gradient is set up between the electrodes resulting in lithium ions migrating from one side to the other accompanied by the flow of electrons in the external circuit thereby a resulting in a sharp peak in SSC response (see appendix). Owing to the nature of battery electrochemistry, when lithium ions are extracted/inserted from the electrodes of the device, volumetric changes to compensate for the ion extraction/insertion process occurs. This ion extraction/insertion induced stress results in gradual reduction of the initial bending induced stress gradient causing the initial sharp current peak to then gradually decreases. However, when the device is unbent, ion extraction/insertion induced compositional gradient now drive the reverse migration resulting in an AC-type current response from the device. Control tests using unlithiated aluminum electrodes is provided in the appendix, figure 8.11 to validate the mechanism of stress induced lithium migration as the primary working principle of our energy harvester. As lithium ion migration in our electrochemical system is limited by the

diffusion of lithium ions through the solid electrode material, controlling this parameter can enable design strategies for effectively matching the frequencies of several types of ambient mechanical inputs. In general, the diffusion coefficient of lithium in Li_xAl alloy is in the order of 10^{-10} cm^2 s^{-1} at 293 K.[324] Considering a characteristic diffusion distance of 500 nm (given by the thickness of active Li_xAl on aluminum foil), we estimate a diffusion time of 25 seconds (given the expression, $t = l^2/D$, where 't' is the diffusion time, 'l' is the diffusion length and 'D' is the diffusion coefficient). As these electrochemical systems employ tunable diffusion-controlled reactions for energy harvesting, the energy generation timescale given by the full width at half maximum of the current response (10 seconds in our system at 0.1 Hz input mechanical stimuli) and can be optimized to last as long as the mechanical input is applied. For example, the duration of mechanical input to the harvester during human walking (0.5 - 5 Hz) is different from other low frequency inputs during human activities such as sitting and standing (<0.5 Hz).[229, 321] This feature allows for optimized frequency tuning of energy generation timescales to match specific low frequency mechanical inputs. Assessment of cyclability was performed on the device in bending mode at 15 mm and 8 mm radius of curvatures (RoC) using a custom-made Arduino-servo motor system providing bending and unbending mechanical inputs to the device with 10 second hold period (0.1 Hz bending frequency). The device exhibits stable trends in both V_{OC} (Figure 8.2e) and SSC (Figure 8.2f) performance during repeated bending and unbending tests (also see appendix, figure 8.12). The SSC response during repeated bending and unbending show stable responses maintaining FWHM of 10 seconds after several hundred bending cycles.

8.3.3 Performance assessment of the transient energy harvester

While traditional energy harvesting systems such as piezoelectric devices show effective operation at high frequencies (>10 Hz), their performance drops off by orders of magnitude at

low frequencies away from their inherent resonant frequencies. Comparatively, due to the reliance of ion transport in our system, the performance is poor at high frequencies > 10 Hz and compliments the operation window of traditional piezoelectric harvesters.

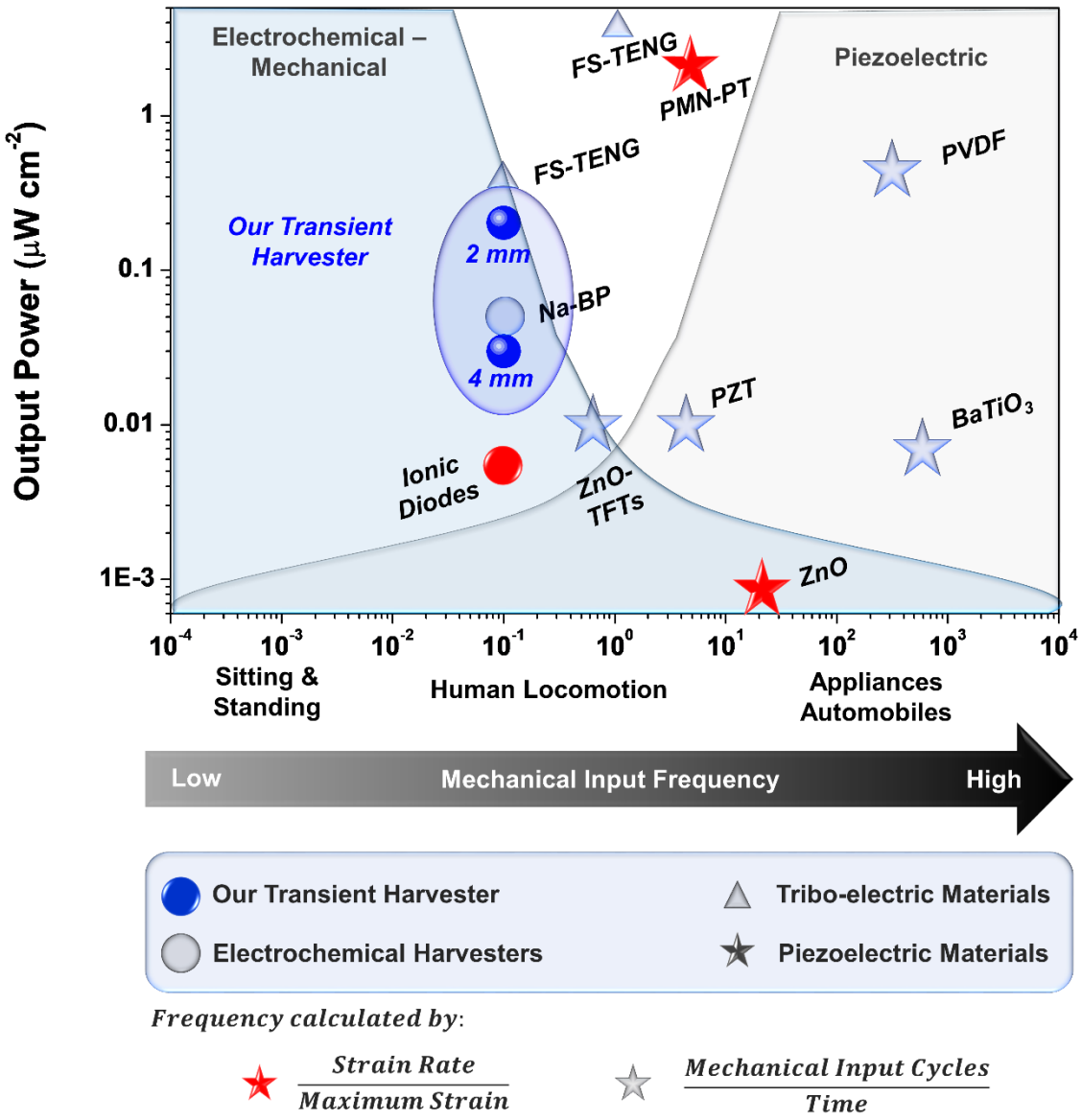

Figure 8.3. Peak output power as a function of mechanical energy input frequency comparing the transient energy harvester to some of the other devices in literature. Peak output power at two specific bending radii (2 mm and 4 mm) are displayed in the figure for comparison. Colors of

points reflect means by which the frequency is assessed, either using strain rate or the mechanical input cycles measured over time.

Comparing specifically to recently reported low-frequency energy harvesting devices [240, 242, 316, 318, 320, 321, 325-327] (Figure 8.3), the transient energy harvester shows improved performance at low mechanical input frequencies. It should be noted that even though triboelectric and piezoelectric systems can be operated at low mechanical input frequencies, their energy generation timescales are significantly lower (in milliseconds) when compared to electrochemical energy harvesters. The response time or the time scale of energy generation (FWHM of the SSC response – appendix, figure 8.13) compared to other ambient mechanical energy harvesting platforms is provided in the appendix (Table 8.2). The peak power and energy output of the harvester during bending tests at different bending radii (Table 8.1 and see appendix, figure 8.14) show an inverse dependence of power and energy harvested with increasing curvature (decreasing bending radii).[229, 321]

Radius of curvature [mm]	Peak power [$\mu W\ cm^{-2}$]	Energy harvested [$\mu J\ cm^{-2}$]	Response time [seconds]
2	0.208	1.762	10
4	0.03	0.301	10
8	0.006	0.063	10
15	0.002	0.02	10

Table 8.1. Performance of our transient energy harvester during bending tests at different radii of curvatures at 0.1 Hz

The peak output power measured is the product of the open circuit voltage difference and the maximum peak current of the short circuit current response observed during one bending

event ($Peak\ power = \Delta V_{OC} \times SSC_{Max}$). The total energy harvested during one bending event is the product of the charge transferred (area encompassed by the SSC response) and the open circuit voltage difference observed ($Energy = \Delta V_{OC} \int_0^t idt$, where 't' is the hold time).[229, 318] The obtained peak output power and energy puts an upper limit of the maximum power and energy delivered by our device during the specific conditions of testing. At the highest curvature (bending radii, 2 mm) our device delivers a peak output power of 0.208 μW cm^{-2} harvesting a peak output energy of 1.762 μJ cm^{-2} at a frequency of 0.1 Hz whereas at low curvatures (bending radii, 15 mm) output power and the harvested energy at 0.1 Hz was 2 nW cm^{-2} and 20 nJ cm^{-2} respectively. In both scenarios, continuous energy generation during the full duration of the mechanical input can be observed characterized by the FWHM of the current response (10 seconds at 0.1 Hz). By selectively tuning the ion diffusion properties in the electrode by optimizing kinetic parameters through nano-structuring and nanoscale architectures, effective energy harvesting at broad range of low frequencies with continuous energy generation can potentially be achieved using this system. Moreover, the power and energy output of the transient harvester can be improved through two approaches, (i) Material selection approach: using larger ions (Na^+, K^+) and alloying compounds with higher mechanical properties in the partially charged state would improve the voltage output of the harvester and using alternative ions (Mg^{2+} and Ca^{2+}), more electrons per unit charge can be transferred thereby more energy can be harvested, (ii) Systems level design approach: leveraging the high performance of the harvester at high curvatures (very low volume of electrochemically active material required) arrays of interconnected harvesters can be fabricated using e-beam and lithography techniques. Such design approaches pioneered by John Rogers' and team[328-331] can be readily adapted for developing such integrated harvester arrays (one possible design provided in the appendix, figure

8.15) which would significantly boost the practical viability of the electrochemical-mechanical energy harvester platforms.

8.3.4 Transient behavior of the fabricated energy harvester

The transient capability of our prototype harvester in a KOH (2M) trigger solution was assessed using dissolution tests (Figure 8.4). As long as the device is not made to contact the specific trigger solution, transient behavior initiation will not occur and security is guaranteed. Triggering the transient behavior of the energy harvester can be achieved by pouring the trigger solution onto the harvester or by immersing the device in it whenever the desired functionalities of the system has been fulfilled. Notably, the individual components of the harvester (Figure 8.4a and 8.4b) can completely dissolve, leaving no trace of the harvester system after being triggered. The two major components of our harvester are PVA film (used for packaging and separator) and alloyed aluminum foil. These two materials were chosen as the only components owing to their known dissolution behavior in KOH solutions.[39, 315] The PVA film (Figure 8.4a) dissolves completely in 5 min while the lithiated aluminum foil (Figure 8.4b) requires 30 min to achieve total dissolution indicating that the limiting component for complete dissolution is the aluminum foil. The fully assembled device was triggered for dissolution in a KOH (2M) solution (Figure 8.4c), and becomes completely inoperable within 5 min of soaking owing to the full dissolution of PVA-based components, and achieves complete transience in around 30 min. As the 30-minute duration is limited by the lithiated aluminum, we anticipate complete transience could be reached more rapidly by using thinner Al layers, such as those prepared by physical vapor deposition methods.

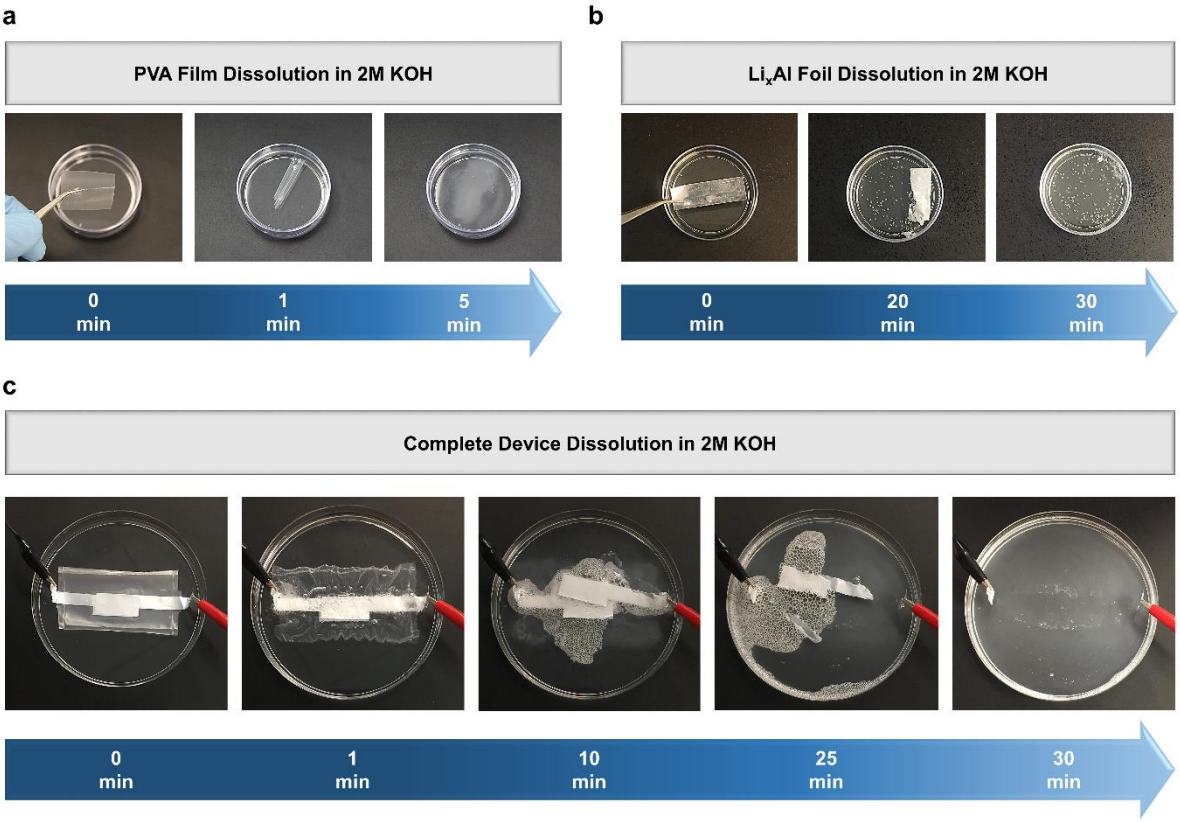

Figure 8.4. Dissolution behavior in 2M KOH trigger solution of **(a)** PVA film, **(b)** Lithiated aluminum foil and **(c)** prototype transient energy harvester

8.4 Conclusion

In summary, this study demonstrates a prototype mechanical energy harvester that is fully transient, optimized for low frequency harvesting relevant to wearable or integrated technologies, and exhibiting performance competitive with state-of-the-art reports in the literature for energy harvester performance. This device builds upon the mechanical stress - electrochemical coupling in a symmetric cell involving two alloyed aluminum-lithium electrodes prepared from bulk Al foils. The harvester delivers a peak output power of 0.208 μW cm^{-2} and a peak output energy of 1.762 μJ cm^{-2} at a frequency of 0.1 Hz at a radius of curvature of 2 mm. The current profiles dictated by ion-diffusion kinetics enable continuous energy generation,

harvesting energy during the full duration of the mechanical input stimuli (FWHM of 10 seconds at 0.1 Hz), a feature unique to this class of electrochemical harvesters. Our device configuration exhibits complete dissolution of all the components in KOH-based aqueous trigger solution in 30 minutes. Apart from the proposed concept of an energy harvester, the mechano-electrochemical coupling effect where specific electrochemical inputs translate to mechanical outputs can also be leveraged using similar configurations for development of transient actuators.[332-334] Further, we envision these device configurations to be an intriguing future avenue for implementing security in next-generation devices, where dissolution of a tailored power system can preserve sensitive data, but eliminate all capability to access or transmit that data until the system is recovered. Our work demonstrates for the first time that power harvesters, and particularly those which could be integrated with wearable technologies, present a viable route toward this vision.

Acknowledgements

We would like to acknowledge and thank all members of Dr. Gilbert Nessim's research group for their insights and fabrication of materials. We would also like to thank Robin Midgett, Adam Cohn, Thomas Metke, Siyuan Jiang and Jennifer Donohue for their insights and useful discussions. We also acknowledge Dr. Rizia Bardhan for use of optical microscopy and Raman spectroscopy as well as VINSE staff for assistance with user facilities. This work was supported in part by the Vanderbilt Discovery Grant and NSF grant CMMI 1400424. A. P. C. and K. S. are supported in part by the National Science Foundation Graduate Research Fellowship under Grant No. 1445197.

8.5 Appendix

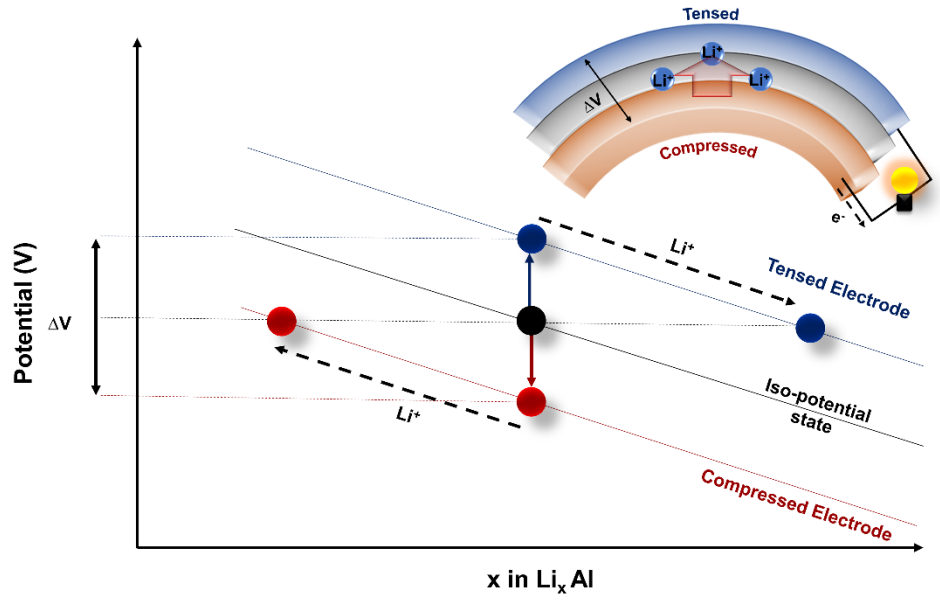

Figure 8.5. Operating principle of the electrochemical-mechanical energy harvesters

Our harvester operates on the principle of mechano-electrochemical coupling observed in energy storage electrodes. When the device is bent or pressed, asymmetric stresses are generated in the two electrodes leading to a chemical potential difference. Charged ions, Li^+ migrate from the compressed side to the tensed side resulting in electron flow in the outer circuit thereby harvesting energy. This energy generation lasts as long as the stress generated chemical potential difference is neutralized.

8.5.1 Stress-induced chemical potential gradient

Based on the work of Sangtae Kim et al.,[229] the mechanics of the device when bending and the induced chemical potential gradient can be described as follows. Bending induces asymmetric stresses where one electrode becomes tensed and the other becomes compressed as shown in figure S2.

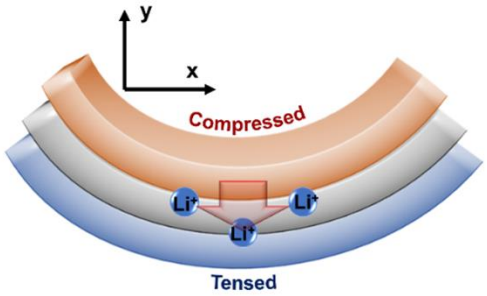

Figure 8.6. Schematic representation of the bending geometry

The stress, 'σ' generated on the compressed and tensed electrode can be written as,

$$\sigma_{xx} = \frac{E}{(1-\upsilon^2)}\frac{h}{R}, \sigma_{zz} = \frac{\upsilon E}{(1-\upsilon^2)}\frac{h}{R} \; and \; \sigma_{yy} = 0 \qquad 26$$

Where, 'E' is the Young's modulus and 'ν' is the Poisson's ratio. A plane-stress condition is assumed along the 'y' direction. As deviatoric stress components are assumed to not contribute to the chemical potential gradient, only hydrostatic stress components are considered. Thus the hydrostatic component can be deduced as,

$$\sigma_{\text{hydro}} \equiv \frac{\text{Tr}(\sigma)}{3} \qquad 27$$

As the chemical potential gradient, 'Δμ', can be related to the output voltage, the chemical potential gradient is the product of hydrostatic stress component and the partial molar volume of lithium in the alloy.

$$\Delta\mu = \Delta V = \Omega_{\text{Li}}\Delta\sigma_{\text{hydro}} \qquad 28$$

Therefore, the chemical potential gradient, '$\Delta\mu$', developed between the two electrodes is given by the following expression,

$$\Delta\mu = \Omega_{\mathrm{Li}} \left(\frac{\mathrm{E}}{1-\upsilon}\right) \frac{2\mathrm{h}}{3\mathrm{R}} \qquad 29$$

Where, 'Ω_{Li}', $(\Omega_{\mathrm{Li}} \equiv (\partial \mathrm{V}/\partial \mathrm{N}_{\mathrm{Li}}))$ is the partial molar volume of lithium in alloying electrodes such as aluminum (14.5 A^3), N_{Li} is the amount of lithium ions, 'E' is the Young's modulus of the lithium aluminum alloy, 'ν' is the Poisson's ratio, 'h' is the half thickness of the device and 'R' is the radius of curvature."

8.5.2 Migration of lithium during bending

The stress induced chemical potential gradient is given by the expression (3). This expression is developed by assuming that only hydrostatic stress components take part in energy generation. Therefore, lithium ions have to migrate from one electrode to the other to relax the induced chemical potential gradient. The amount of lithium ions, 'ΔN_{Li}', transferred is given by the expression,[229]

$$\Delta N_{Li} = \frac{V_{one\ electrode}}{\Omega_{Li}} \left(\frac{1-2\upsilon}{1-\upsilon}\right) \left(\frac{h}{R}\right) \qquad 30$$

Where '$V_{one\ electrode}$' is the volume of electrode of the device which is subjected to stress owing to the applied curvature.

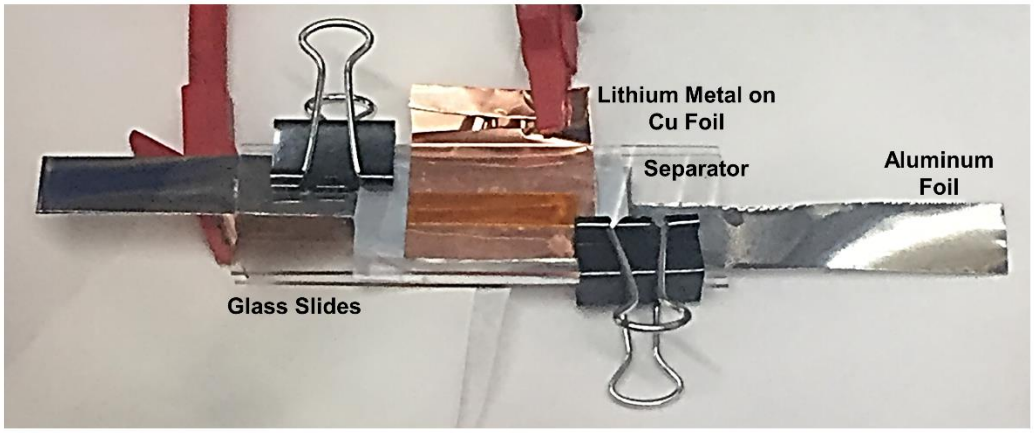

Figure 8.7. Custom-made lithiation cell

A custom-made electrochemical cell was used to lithiate the aluminum foil to 80% of the first 500 nm thickness. This custom-made cell was used inside an argon glove box with 1M $LiPF_6$ in 1:1 vol% EC:DEC electrolyte.

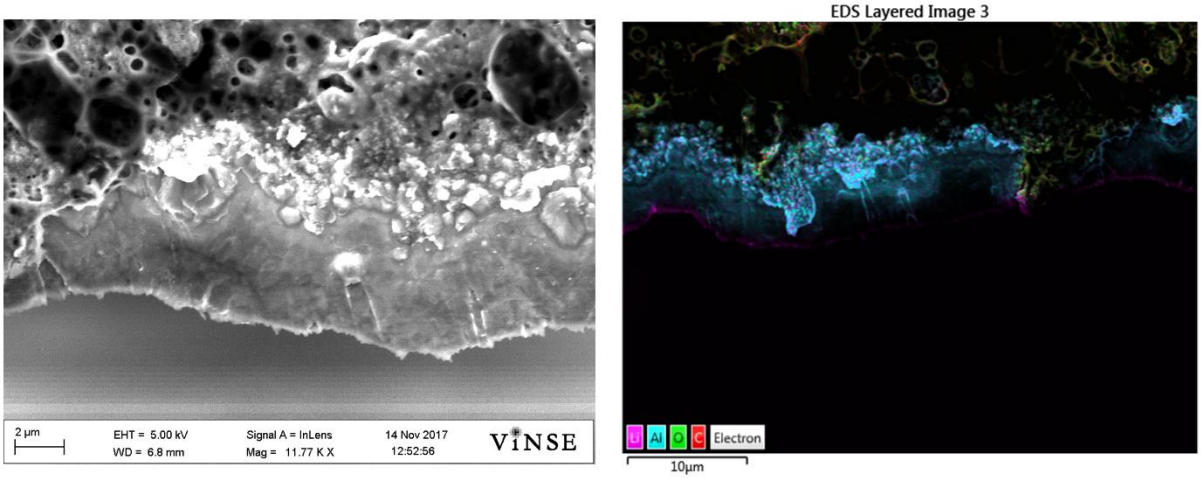

Figure 8.8. SEM and EDS elemental map of the cross-sectional region of the lithiated aluminum alloy on aluminum foil

SEM micrograph and EDS elemental mapping were performed on the cross-section of the lithium aluminum alloy. The rough features in the SEM were due to unforeseen and unintended

air exposure to the lithiated alloy during SEM imaging. However, elemental mapping revealed lithium rich phase only on the outer edge of the alloy corresponding to a thickness <1 μm indicating successful lithiation.

8.5.3 Theoretical output voltage predictions – comparison with other electrochemical systems

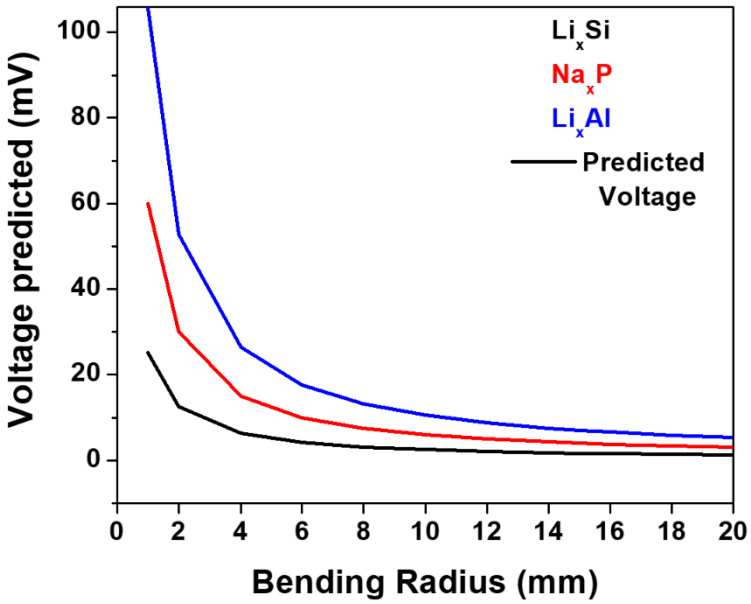

Figure 8.9. Theoretically predicted output voltages with different bending radii for the lithium aluminum systems compared to other similar electrochemical systems.

The theoretical voltage output can be obtained using the following expression as developed from the work of Sangtae Kim et al.[229]

$$\Delta V_{OC} \equiv \Delta\mu = \Omega_{Li}\left(\frac{E}{1-\nu}\right)\left(\frac{2h}{3R}\right) \qquad 31$$

Where, Ω_{Li} is the partial molar volume of lithium ion (volume change per unit charge) in aluminum which is similar for most lithium alloys with the value of 14.5 A^{o3}, E is the Young's

modulus of the active alloy (Li_xAl-105 GPa)[335], ν is the Poisson's ratio, h is the half thickness of the device and R is the radius of curvature.

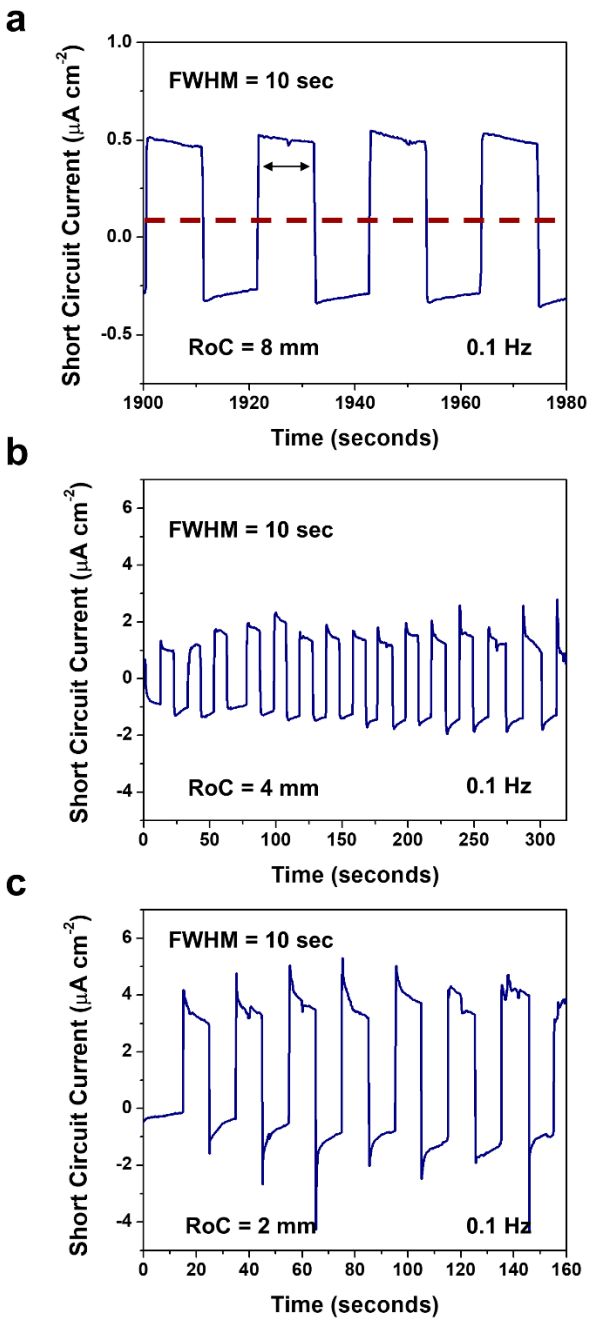

Figure 8.10. Short circuit current measurements at frequency 0.1 Hz at radii of curvatures of **(a)** 8 mm, **(b)** 4 mm and **(c)** 2 mm

Short circuit current measurements at the different bending radii at 0.1 Hz revealed an inverse relationship with bending radii. Lower the bending radii (high curvature) higher the current output. In all cases the FWHM was around 10 seconds corresponding to the hold time in the bend-hold-unbend cycles corresponding to a frequency of 0.1 Hz. The response time or the energy generation timescale characterized by the FWHM of the current response indicates continuous energy generation during the full duration of the applied mechanical input, a characteristic feature of electrochemical energy harvesters.

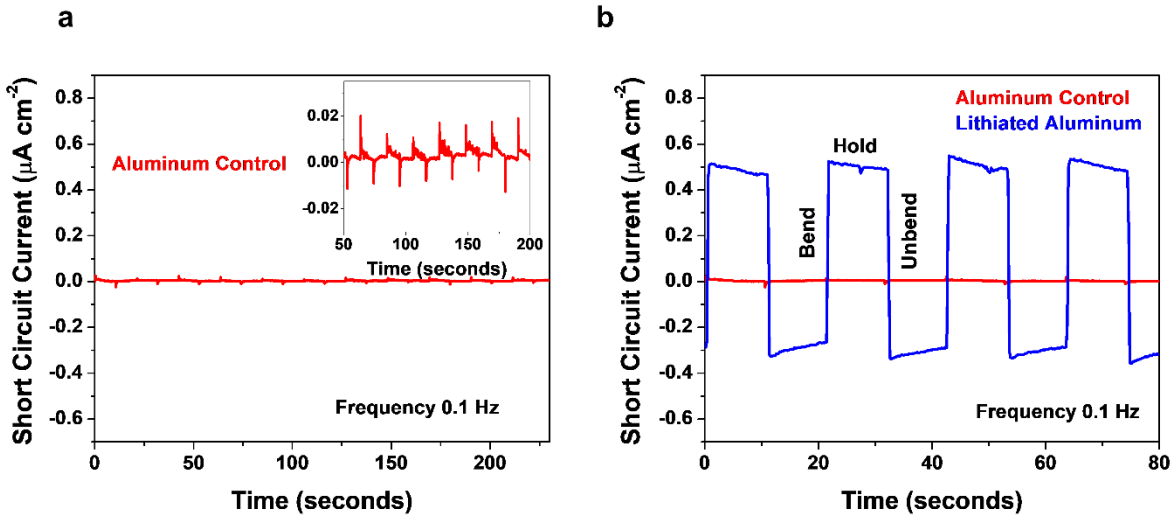

Figure 8.11. (a) Short circuit current response of unlithiated aluminum control (inset showing a magnified region of the current response indicating very small responses during bending, holding and unbending cycles and **(b)** SSC comparison of the lithiated aluminum alloy when compared to the aluminum control overlaid showing bending, holding and unbending phases

The short circuit current response of the unlithiated aluminum electrodes (control sample), shows low current densities with sharp spikes in current during onset of bending (figure 8.11. a.). During the hold phase the response rapidly declines followed by a sharp spike in current during the unbending cycle. When compared to the lithiated aluminum alloy shown in figure 8.11. b, we

observe the difference in current densities owing to the energy dense charge transfer process of lithiation and delithiation in lithiated aluminum alloy. Moreover, continuous energy generation for the entire duration of the holding phase (10 seconds – 0.1 Hz) is observed in the case of the lithiated aluminum alloy. Even if there are any small triboelectric energy generation possibilities in our system, the differences in the current densities between the control sample and the lithiated aluminum sample highlights the benefit of using the Li_xAl battery electrode for low frequency energy generation. These tests validate the fact that the response of our device is primarily the result of mechano-electrochemical coupling induced lithium ion migration.

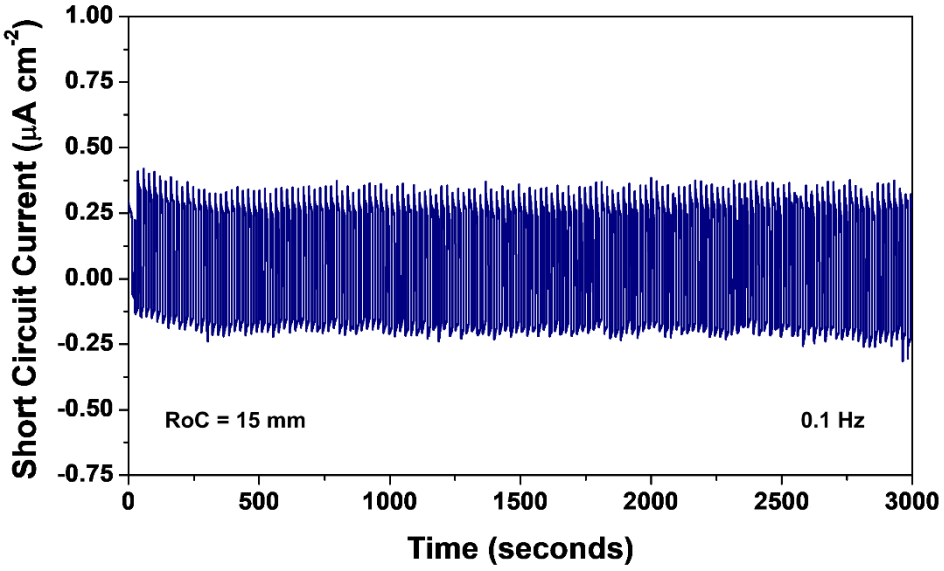

Figure 8.12. Short circuit current measurements – cycling stability tests during repeated bending at 0.1 Hz with radius of curvature 15 mm

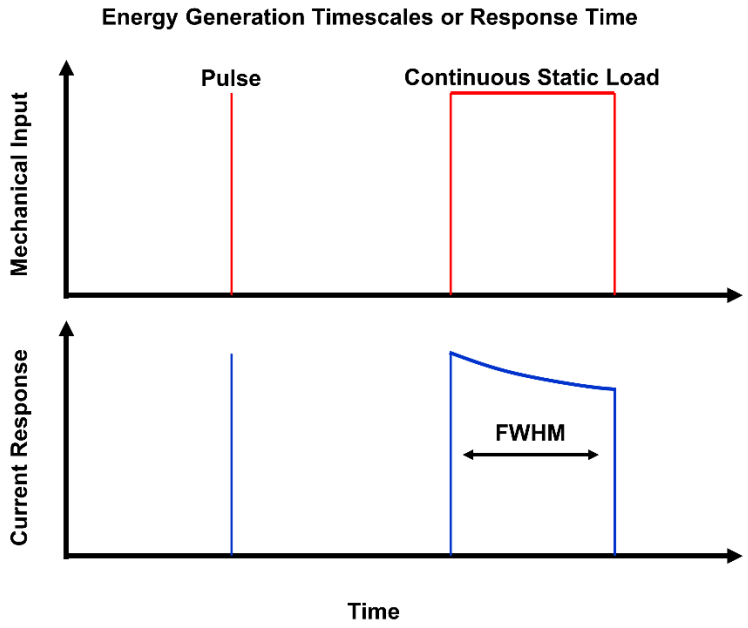

Figure 8.13. Energy generation timescales comparing high frequency pulse loads and low frequency continuous static load

The response times or the energy generation timescales is given by the full width at half-maximum value of the current response of the energy harvesting device. Figure 8.13 depicts typical expected response times of a pulse type mechanical input and continuous static loading input. The extracted values of response times from the reports of the different ambient mechanical energy harvesters in literature is provided in the table 8.2. These values highlight the continuous energy generation capabilities of the electrochemical systems

Type of Energy Harvester	Operational Frequency [Hz]	Response Time [s]
Our Transient Energy Harvester	0.1	10
BP - Electrochemical Energy Harvester[321]	0.1	10
Ionic Diodes[318]	0.1	5
ZnO Nanowires[242]	11.2	<0.1
$BaTiO_3$ Nanowires[325]	160	<0.1
PZT[240]	3.2	<1
ZnO-TFTs[316]	0.5	<1
PMN-PT[327]	6.3	~0.1
PVDF[326]	146	–
FS-TENG[320]	0.1, 1	–

Table 8.2. Comparison of response times of the different energy harvesters

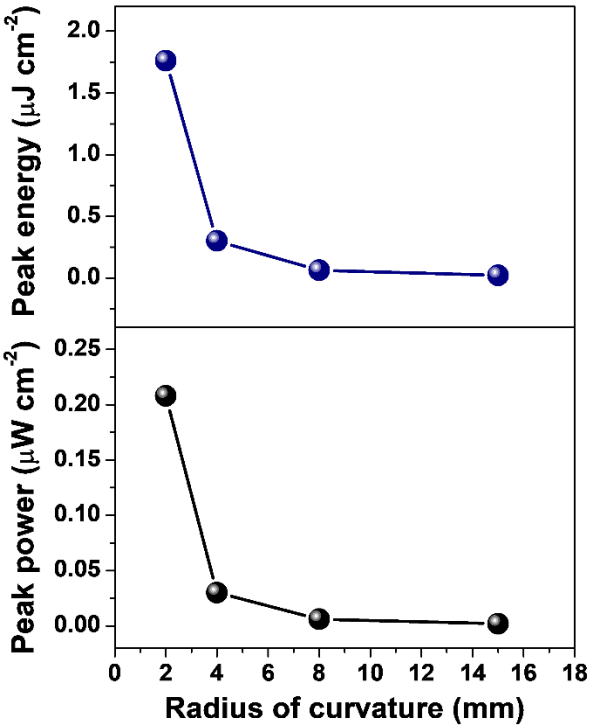

Figure 8.14. Peak power and peak energy outputs of the transient energy harvester as a function of bending radii at 0.1 Hz

Peak output power, the product of ΔV_{OC} and peak SSC as well as peak output energy, the product of charge transferred during in SSC and ΔV_{OC} show an inverse dependence with increasing radius of curvatures. As high stresses are generated at high curvatures (low bending radii), the set-up chemical potential gradient is higher leading to comparatively high power and energy output at the low bending radii.

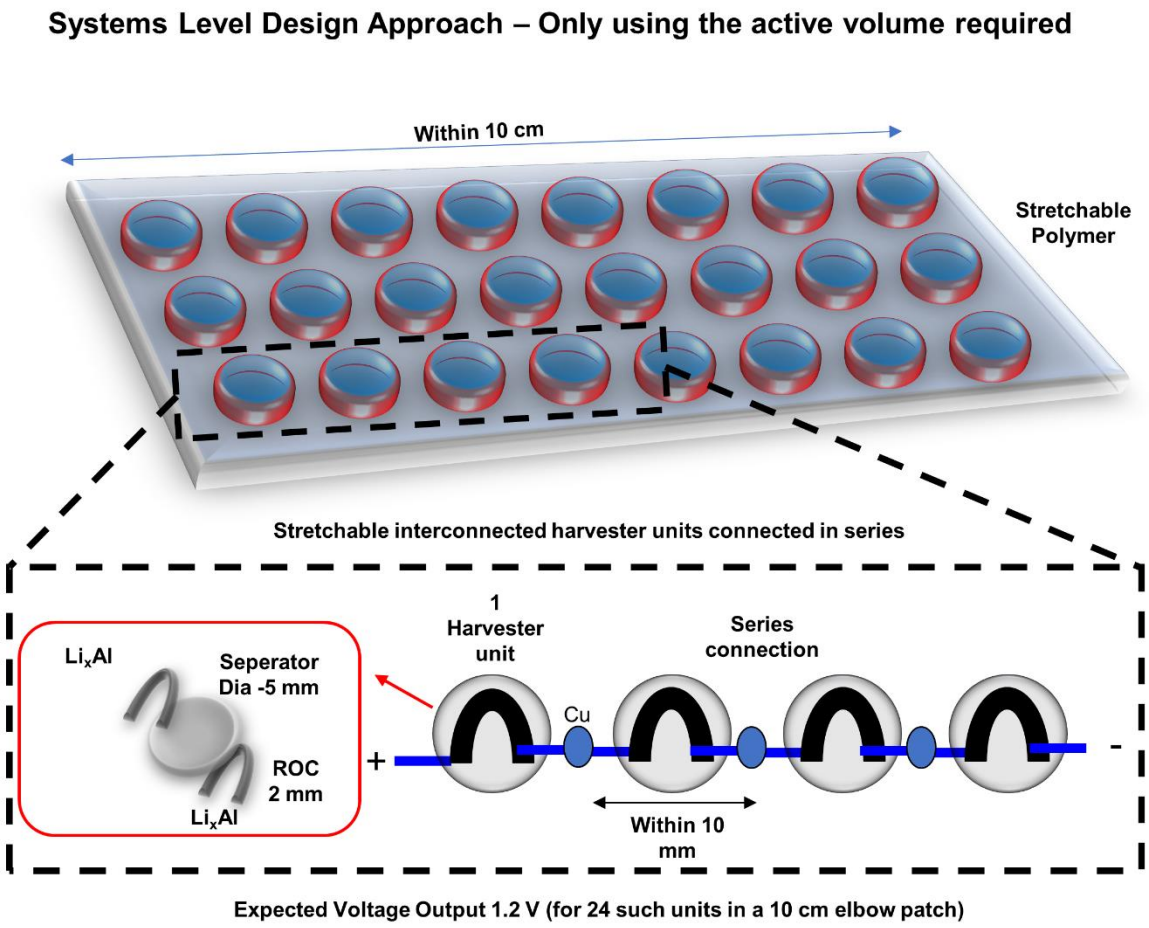

Figure 8.15. Systems level design approach for developing arrays of integrated Li_xAl electrochemical energy harvesters

Figure 8.15 provides a framework for fabricating arrays of devices to make practically relevant performance possible. This builds upon the advantages that, maximum peak performance in

terms of energy and power are obtained at the highest bending radii. At the highest bending radii, 2 mm in our experiments, the device generates a high OCV of ~50 mV. At this extremely high curvature scenario, the electrochemically active volume of an ~1 cm^2 device would be ~ 12.46 μm^3 (assuming 500 nanometers thick active Li_xAl alloy for both the electrodes). From the total active volume 100 μm^3 (for 1 cm^2 device), ~ 13 % is only utilized in such a scenario and the remaining ~ 87% active material remains not utilized. This provides opportunities for developing systems level design adapted from the recent works of John Rogers and team who showcased their battery arrays connected using serpentine interconnects (Sheng Xu et al., Nat. Commun. 4, 1543 (2013))[328] and many other techniques of nano and microfabrication of arrays of devices. Employing the same strategies and using the advantages of our electrochemical systems, a design approach for fabricating arrays of devices for practical viability can be achieved. Using conservative estimates for the preliminary design (packing 1 harvester unit with electrical connections in a 1 cm^2 area, we propose e-beam sputtering of active material and current collectors using patterned masks onto PVA films. As given in the schematic, using the conservative design approach, we could potentially pack 24 harvesters in a 10 cm X 3 cm patch which could potentially be integrated onto textile fabrics, structural architectures and long duration (low frequency) mechanical input platforms. This configuration is specifically envisioned for stretching applications and is expected to deliver 1.2 V output voltage which would potentially be used for low power electronics such as other transient electronic systems. Apart from this, commercially available voltage boost converters can be employed to ramp up the voltage to ‘’trickle charge’ a supercapacitor or a low energy battery.

Chapter IX

9 A Multifunctional Structural Ultra-Battery Composite

9.1 Introduction

The advent of electric vehicles, portable and wearable electronics, drones, advanced defense platforms, long range satellites and advanced extraterrestrial rovers have prompted increased research efforts in the field of robust, multifunctional energy storage devices.[38, 39, 321, 336-339] The term multifunctional when coupled to energy storage architectures implies devices that incorporate new functions and features as well as perform their respective energy storage requirement. As digitization and internet of things rapidly push the boundaries of the current technological revolution, development of energy storage systems with multiple functionalities are crucial. Structural load-bearing energy storage is one such concept where energy storage devices integrated into structural architectures perform load-bearing function in addition to energy storage.[340-342] Currently, this approach is pursued with rejuvenated enthusiasm owing to the promise of minimizing weight of applications at the same time offset the need to house bulky present-day energy storage devices. As the potential end-use technologies are being developed at a rapid rate, researchers have begun to ask the question – how to achieve a practical multifunctional structural energy storage system with comparable performance metrics to present mono-functional devices? Despite some progress in the field with regards to structural batteries[343-345] and supercapacitors,[342, 346-358] most approaches, envision structural supercapacitors, primarily, electrochemical double layer capacitors (EDLC) to fulfill this role owing to their ease of fabrication, safety and relatively low cost. Most current EDLC based structural energy storage devices, though significant advances in the field, still suffer from low

practical energy and power densities. Faradaic pseudocapacitive energy storage electrodes have been long considered as the bridge between conventional EDLCs and batteries boasting high energy densities at the same time maintaining high power densities.[104, 359] Pseudocapacitive electrodes store more energy per atom of active material than EDLCs. Their relative ease of fabrication, operation in safe aqueous based electrolytes and comparable low cost of materials are characteristics that make them attractive candidates for consideration.

Although many faradaic redox chemistries have been reported in literature,[360-364] the century-old Ni-Fe battery system with energy densities of ~30-50 Wh/kg and power densities of ~3-50 W/kg has long fascinated many researchers owing to its durability and robust energy storage capabilities even under harsh conditions.[365, 366] More recently, Wang et al,[21] revisited this century-old system with the goal of improving the energy and power capabilities. By employing inorganic/carbon hybrid pseudocapacitive electrode materials, they developed an Ni-Fe system with an increased energy density of >120 Wh/kg and power density of >15 W/kg (1000 times higher rate than conventional Ni-Fe cells). With energy densities significantly higher than EDLC systems and power densities significantly higher than conventional batteries, this approach gave momentum to the field of ultra-batteries. Several reports on Ni-Fe ultra-battery chemistries exists till date focused on electrode fabrication approaches, binder free approaches and electrolyte optimization approaches.[367-370] However, integration of such systems into structural composites have remained unexplored so far.

One of the most important findings from previous works on Ni-Fe ultra-battery systems is that employing inorganic active material/carbon hybrid micro/nano-structures deliver high energy and power performance metrics. The carbon framework provides an ultrafast electron conduction pathway at the same time provide a high surface area for the inorganic active

material enabling better ion conduction resulting in fast redox reactions at the surface.[21, 370] With regards to structural architectures, most approaches have primarily focused on carbon fiber laminate-based systems with impressive mechanical properties but inferior electrochemical properties.[340, 341] In recent years, alternative approaches using carbon nanotubes (CNTs) and CNT-fiber systems have garnered great interest owing to the promise of improved mechanical and electrochemical performance metrics.[351, 356, 357] Therefore, approaches using a CNT based carbon framework coupled with inorganic redox active species would, in theory, be the one stop solution to the present challenges facing structural energy storage systems.

Building off this rationale, here, we demonstrate the fabrication, mechanical and electrochemical performance of a multifunctional structural ultra-battery composite using electrodeposited faradaic redox active species of nickel and iron onto carbon nanotubes grown on stainless steel meshes. The composite fabricated using wet lay-up process with fiberglass or Kevlar separators and an ion conducting polymer electrolyte delivers good energy and power densities with stable performance. Using faradaic redox active species of nickel and iron provides an increase in energy and power densities when compared to other EDLC based structural composites in literature owing to the ultrafast and energy dense reactions of the pseudocapacitive redox couples $Ni^{2+/3+}$ and $Fe^{2+/3+}$. Simultaneous in-situ mechano-electrochemical tests performed on the fabricated ultra-battery composites reveal stable electrochemical performance as well as good mechanical integrity until mechanical failure. Our work thus highlights the next advance in the field of multifunctional structural energy storage devices employing faradaic electrodes in an ultra-battery composite.

9.2 Experimental methods

9.2.1 Growth of CNTs on stainless steel meshes

Stainless-steel meshes (316, 400x400) was used as the substrate to grow CNTs. The nanotube growth was carried out in a three zone furnace initially heated to the growth temperature. Preheating the gases was done in zones 1 and 2 where the temperature was maintained constant at 770 ^{o}C. In the zone 3 or the growth zone, the temperature was varied between 740 ^{o}C and 790 ^{o}C depending upon requirement. 400 SCCM of H_2 and 100 SCCM of Ar was admitted for 15 min to purge the furnace. After purging, stainless steel meshes were inserted into the growth zone of the furnace. This was followed by an annealing step under 1000 SCCM of Ar/O_2 (99% / 1%) and 100 SCCM of pure Ar for 45 min. Following this step, the Ar/O_2 was turned off and the stainless steel surface was reduced under a flow of 100 SCCM of Ar, and 400 SCCM of H_2 for 40 min. This was followed by a gas flow of 100 SCCM of Ethylene, 250 SCCM of Ar/O_2 (99%/1%), 400 SCCM of H_2 and 100 SCCM of Ar for 15 min to initiate the growth of carbon nanotubes.

9.2.2 Development of CNT/NiO_x carbon/inorganic framework

NiO_x was electrochemical deposited on CNT/Stainless-steel from 250 mM $Ni(NO_3)_2$ aqueous solution at a scan rate of 100 mV/s with voltage windows from -1.2 to 0 V (with respect to SCE). The deposition was varied between 100-500 voltammetry cycles to yield the desired mass. Platinum was used as counter electrode and the resulting CNT/Stainless-steel/NiO_x framework was then washed thoroughly, dried, and then used as the cathode.

9.2.3 Development of CNTs/FeO_x carbon/inorganic framework

NiO_x was electrochemical deposited on CNT/Stainless-steel from 0.5 M $Ni(NO_3)_2$ aqueous solution at a scan rate of 100 mV/s with voltage windows from -1.35 to 0 V (with respect to

SCE). The deposition was varied between 100-500 voltammetry cycles to yield the desired mass. Platinum was used as counter electrode and the electrode was then washed with DI water and annealed at 550 °C for 1.5 hours in 1 SLM Ar to obtain CNT/Stainless-steel/FeO_x framework. Characterization of the deposited electrodes were performed using SEM/EDS (Zeiss Merlin) and Raman spectroscopic techniques (Renishaw).

9.2.4 Electrochemical testing of the electrodes

Electrochemical measurements for both electrodes were obtained in a beaker cell using 1 M KOH solution as the electrolyte. A three-electrode system was used for testing, with Platinum as the counter electrode and SCE as the reference electrode. Cyclic voltammetry and galvanostatic charge/discharge testing were performed on the electrodes to evaluate the electrochemical performance.

9.2.5 Assembling the ultra-battery composite

The fabricated electrodes were assembled into a composite using a wet lay-up process with 1M KOH/PVA electrolyte similar to previous reports. Fiber glass or Kevlar mats were used as separators depending upon the type of composite fabricated. Vacuum or mechanical pressure was applied to facilitate good bonding between the composite layers and the ion conducting polymer. Cyclic voltammetry and galvanostatic charge/discharge testing was performed on the electrodes to evaluate the electrochemical performance of the full cell.

9.2.6 In-situ mechano-electrochemical tests

In-situ mechano-electrochemical tests were performed using an Instron mechanical testing device. Autolab PGSTAT101 was used as the electrochemical testing station. The fabricated composite was gripped between the grips of the Instron and connected to electrical leads to facilitate simultaneous measurement. All composites were subjected to tensile strain rates of 1

mm/min to aid ease of characterizing the electrochemical data as well as assess the electrochemical performance in different zones of the stress-strain behavior of the composite.

9.3 Results and discussion

9.3.1 Multifunctional energy storage composites – CNTs on stainless steel

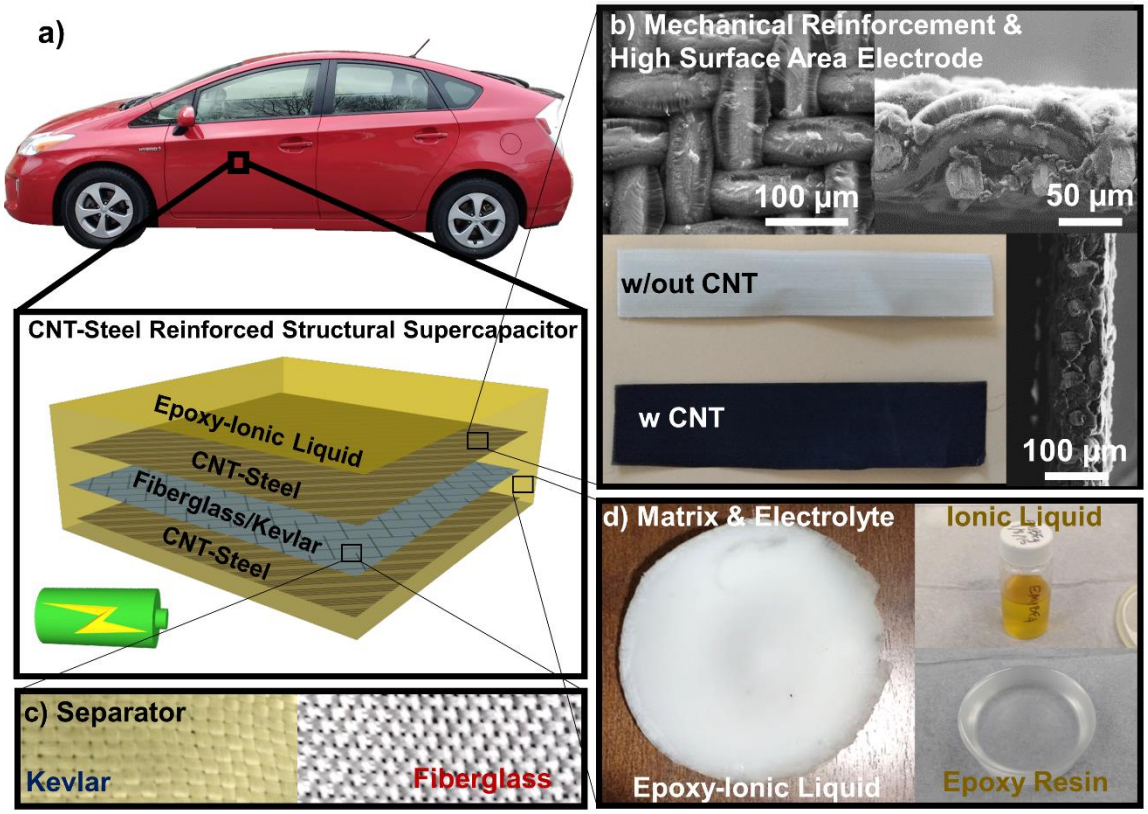

Figure 9.1. (a) Schematic showing the structural supercapacitor with the vision of a reinforced composite material that could be used in a vehicle chassis. **(b)** SEM and optical images of a CNT-steel mesh. **c)** Photograph of fiberglass and Kevlar separators **(d)** Photographs of the epoxy-IL electrolyte on the left and the individual components on the right.

Figure 9.1 shows the design aspects of the structural composite and schematic representation of a structural supercapacitor developed using plain CNTs grown on stainless steel mesh (Figure 9.1a). CNTs were grown on stainless steel meshes *via* chemical vapor deposition (CVD)

technique.[371-374] CNTs grown on the 316 SS 400 mesh at 790°C and the growth on the 304 SS 200 mesh at 770°C were adopted for our device studies based on the highest CNT growth density (see Appendix, figure 9.12, 9.13 and table 9.1). Figure 9.1b shows SEM images of the best CNT growth as well as an optical image of the CNTs coated SS steel when compared to the uncoated stainless steel. The approximate length of the as grown CNTs were 15-30 µm. The electrolyte used for this particular type of super capacitive device was a mixture of epoxy and ionic liquid as shown in Figure 9.1c. Figure 9.1d shows images of the two different types of separator materials used in fabricating these multifunctional composites, namely fiberglass and Kevlar.

9.3.2 Multifunctional performance of the energy storage composite – CNTs on stainless steel

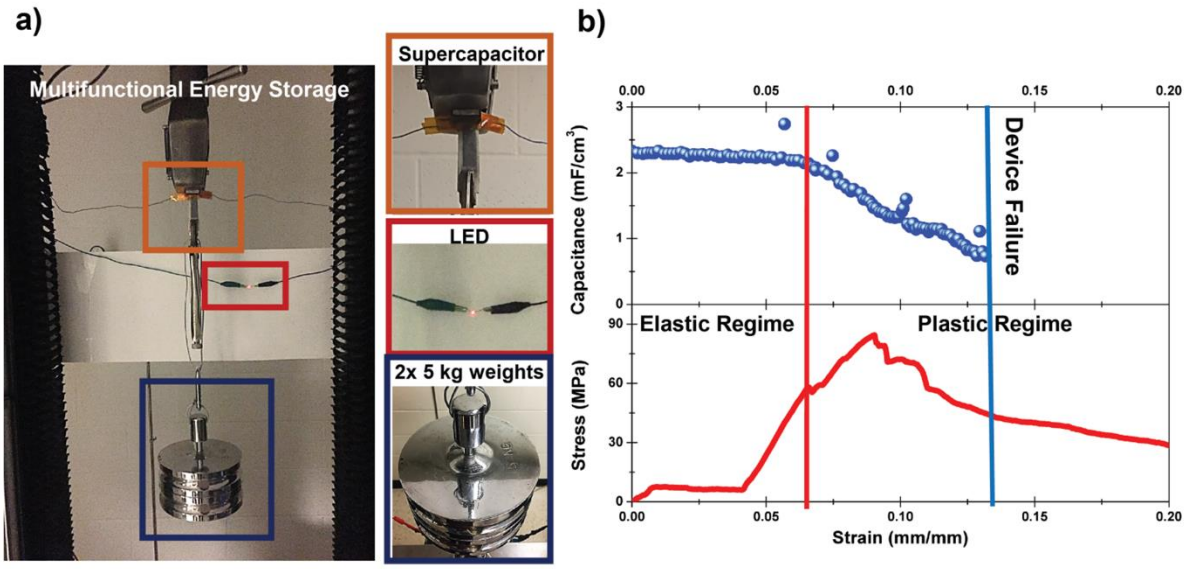

Figure 9.2. (a) Photograph of a structural supercapacitor material supporting 10 kg of weight in a load cell while simultaneously powering a red LED. **(b)** In-situ mechano-electro-chemical measurement showing a simultaneous tensile test with the capacitance measurements from charge discharge curves.

To visualize the simultaneous dual functionality of the CNT-steel multifunctional energy composite, an Instron load cell was configured such that two 5 kg weights (10 kg in total) were suspended from a material composed of two structural supercapacitors connected in series, which were discharged to power a red LED (Figure 9.2a). This reflects a consistent observation made in these materials that demonstrates a critical operation condition of a multifunctional energy storage composite, which is to store and release energy while under mechanical stress. To illustrate the potential applicability of this prototype device in load bearing applications, a concrete block (~10 Kg) was suspended attached to the device (see Appendix, 9.14). The device maintained good mechanical integrity providing feasible routes for future work on systems level engineering approaches for integrating such devices into practical load bearing applications. To further mechanistically explore the dual electrochemical-mechanical performance, *in-situ* tests were conducted where energy storage performance and mechanical performance were measured simultaneously (Figure 9.2b). Here, within the elastic regime of the material we observe invariant electrochemical and charge storage performance. However, as the device enters the plastic regime, a steady degradation in capacitance is observed until the device is no longer able to charge and complete electrochemical failure occurs. The results indicate the important concept that electrochemical device failure precedes mechanical device failure, and this occurs at the onset of the plastic regime.

9.3.3 Interface re-enforcement provided by the CNTs

A key feature of our approach is the presence of CNTs which not only imparts energy storage properties to our composites but also provides effective reinforcement at the interface with the polymer matrix. Numerous previous reports have illuminated the role of CNTs as an effective reinforcing material in polymer composite laminates.[375, 376] In particular the research

works from John Hart's'[377] and Brian Wardle's[378, 379] research groups have proven the lamellar reinforcement properties of CNTs in polymer composites in some cases providing ~153%[380] effective reinforcement when compared to the cases without CNTs. For determining interface properties of the as grown CNTs on the stainless steel meshes, we performed lap-joint shear measurements (Figure 9.3) which indicated increased toughness for the meshes with CNTs when compared to the plain stainless steel meshes. These observations imply that the CNTs in our system perform the dual function of energy storage at the same time providing structural reinforcement to the structural supercapacitor.

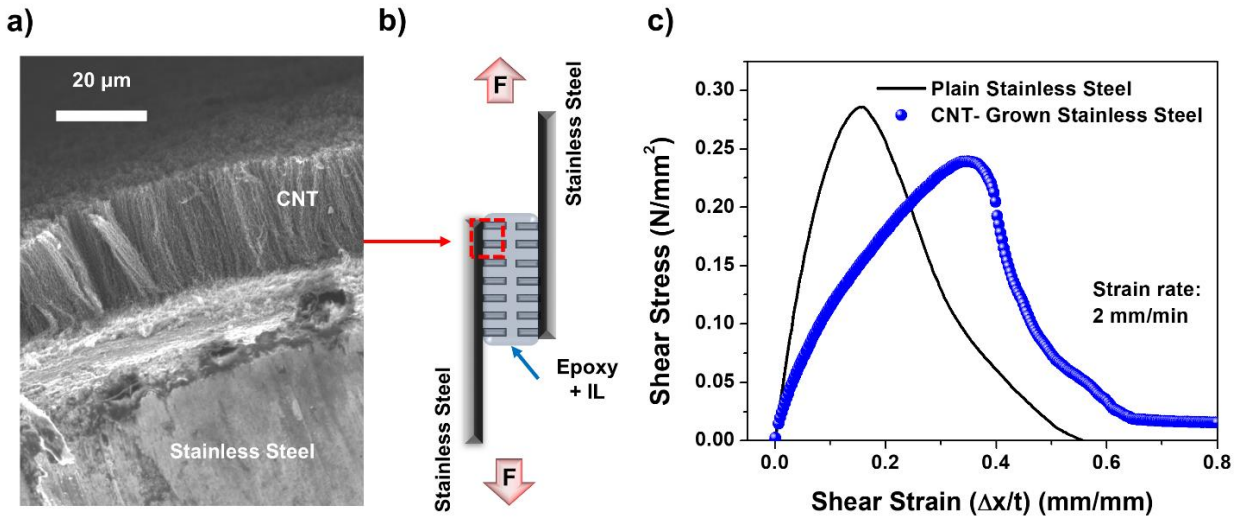

Figure 9.3. (a) SEM cross-sectional image of CNTs grown on stainless steel sheets for analyzing the reinforcement at the interface. **(b)** Schematic representation of the methodology of the lap-joint shear test. **(c)** The shear stress against shear strain response of the plain stainless-steel sample when compared to the CNT-grown stainless-steel sample showing increased shear toughness (area encompassed by the curve) for the CNT grown samples (strain rate: 2 mm/min).

For analyzing interface reinforcement effects, CNTs were grown on stainless steel sheets (Type – 316) as observed from the cross-sectional SEM image shown in Figure 9.3a. Following this, lap-

joint shear tests (Figure 9.3b) were performed on the CNT-grown stainless-steel samples as well as plain stainless-steel samples as a control. Epoxy-Ionic liquid (55 wt%:45 wt%) was used as the polymer matrix to facilitate better detection of interface properties. The shear measurements were performed on an Instron 5944 mechanical testing system at a standard strain rate of 2 mm/min. The test parameters and polymer/IL ratios were chosen such that the reinforcing effect of CNTs at the interface of the polymer matrix can be effectively isolated. The shear toughness of the samples was calculated from the area encompassed by the stress-strain curve (Figure 9.3c) before failure (minimum load detection). Comparing the best samples, we observe that the plain stainless-steel sample had a shear toughness value of 0.0073 J/mm^3 when compared to the CNT grown stainless steel which had a value of 0.0082 J/mm^3. These tests indicated a ~12% increase in toughness for the samples which had the CNTs reinforcing the interface.

9.3.4 Performance assessment of the CNT-stainless steel multifunctional supercapacitor

Comparing to other multifunctional supercapacitors in literature (Figure 9.4), for our device, we obtain energy densities up to 3 mWh/kg (10 μWh/cm^3) and power densities of 1 W/kg (70 mW/cm^3) from the discharge profiles of the device. We have also compared this with equivalent devices having liquid electrolytes with 10 mWh/kg (30 μWh/cm^3) energy and 10 W/kg (700 mW/cm^3) power densities. Notably, our devices exhibit comparable performance to other state-of-the-art reports in literature.[350, 353, 356, 357, 381] We have also included projected values of energy and power densities based on an assumed increase in voltage window for the previously reported carbon aerogel devices[350] and assuming only mass of the active components for the CNT Fiber based devices from the work of Senokos et al.[356]

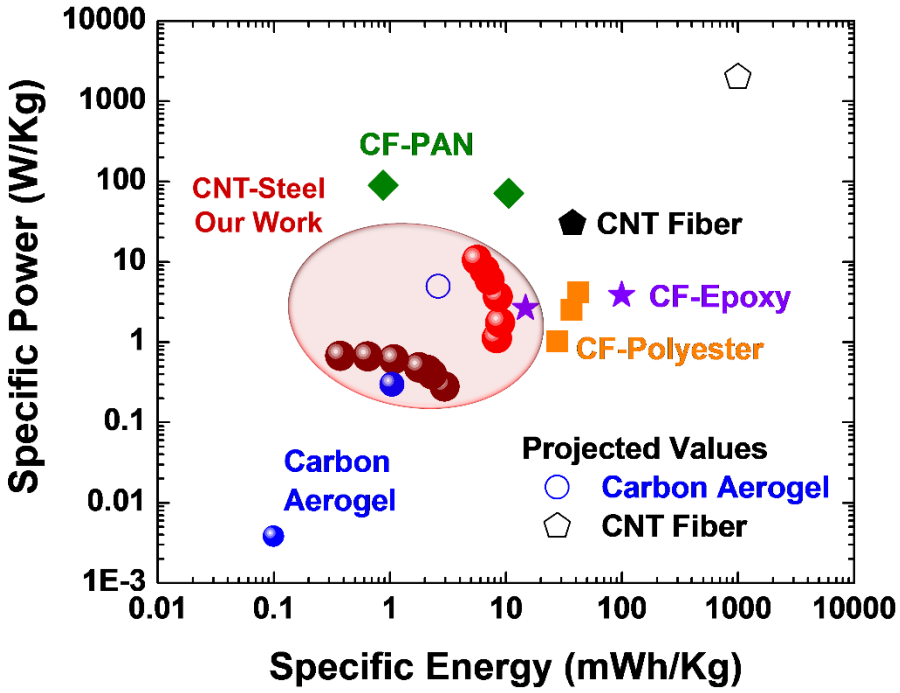

Figure 9.4. Ragone plot showing specific energy and power density of CNT-Steel mesh performance with a Kevlar separator and a 100% IL electrolyte and an Epoxy-IL electrolyte compared to the liquid/solid state performance of the best structural supercapacitor composites in literature.

These results indicate a clear need for improved energy densities to be viable in practical multifunctional energy storage applications. Specifically using faradaic systems instead of electrochemical double layer systems can store more energy per atom of active material owing to the energy dense redox reactions of faradaic electrodes. Building off this work, we developed multifunctional Ni-Fe based redox electrodes for use in multifunctional load-bearing applications.

9.3.5 *Multifunctional Ni-Fe ultra-battery composites*

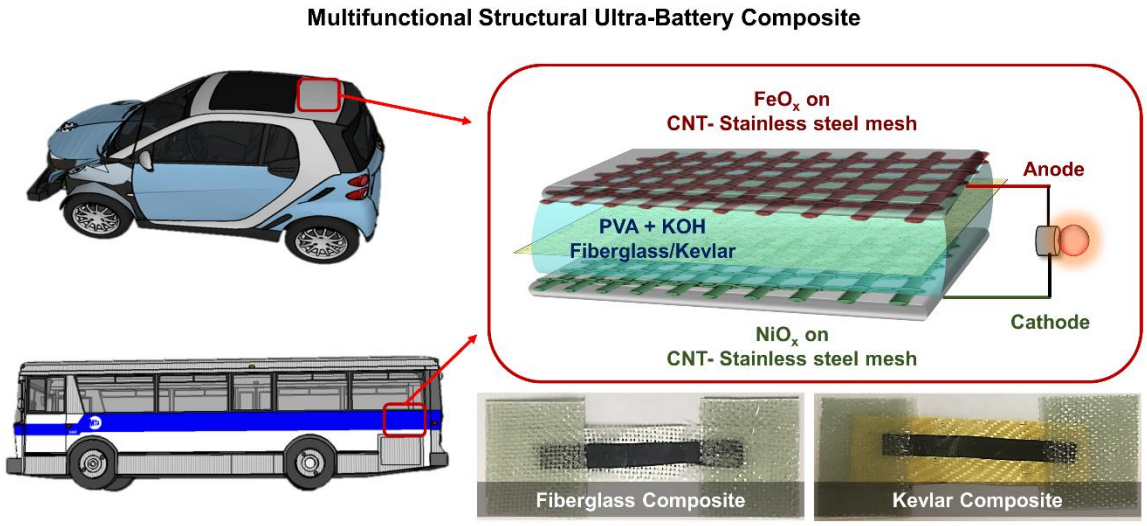

Figure 9.5. Multifunctional ultra-battery composite using fiberglass or Kevlar as the separator

The schematic representation of the concept of an ultra-battery composite is given in figure 9.5. This ultra-battery composite employs faradaic energy storage compared to conventional double layer based structural energy storage systems. Oxides/hydroxides of iron and nickel deposited on CNTs grown on stainless steel meshes comprises the anode and cathode respectively. The composite is assembled using wet lay-up process using potassium hydroxide - poly(vinyl alcohol) (PVA-KOH) gel as the electrolyte.[367, 382] Depending upon the requirement fiber glass or Kevlar (aramid fiber) can be employed as separators. The cured composite is intended to be integrated into structural architectures such as door panel, hood, chassis of vehicles and many other applications. Images of the ultra-battery composites employing both fiber glass and Kevlar separators used in this study are given in figure.

9.3.6 *Development and characterization of Ni-Fe redox active species on CNT-Stainless steel*

The redox active electrodes used in our study are oxides/hydroxides of nickel and iron which were deposited on carbon nanotubes grown on stainless steel meshes. Figure 9.6a shows

the carbon nanotubes grown on the stainless steel meshes using CVD technique. SEM micrographs of the CNT grown stainless steel meshes are show the presence of vertically aligned tubes (also, see appendix, figure 9.15). Raman spectroscopy performed on the tubes (appendix, figure 9.16) reveals sp^3 along with sp^2 carbon atoms characterized by the 'D' and 'G' peaks indicating the presence of active sites which can be further exploited to electrochemically deposit oxides/hydroxides of nickel and iron. Electrochemical deposition of nickel and iron were performed using the respective nitrate precursor solution (see methods) to obtain NiO_x and FeO_x coated CNTs as observed in the SEM micrographs (figure 9.6b and 9.6c). EDS elemental mapping (figures 9.6d-f) and (figures 9.6g-i) reveals the presence of nickel and iron species on the CNTs grown on stainless steel. This is further corroborated using Raman spectroscopic analysis (figure 9.6j) which shows peaks corresponding to α-nickel hydroxide and iron oxide signatures.[383-385]

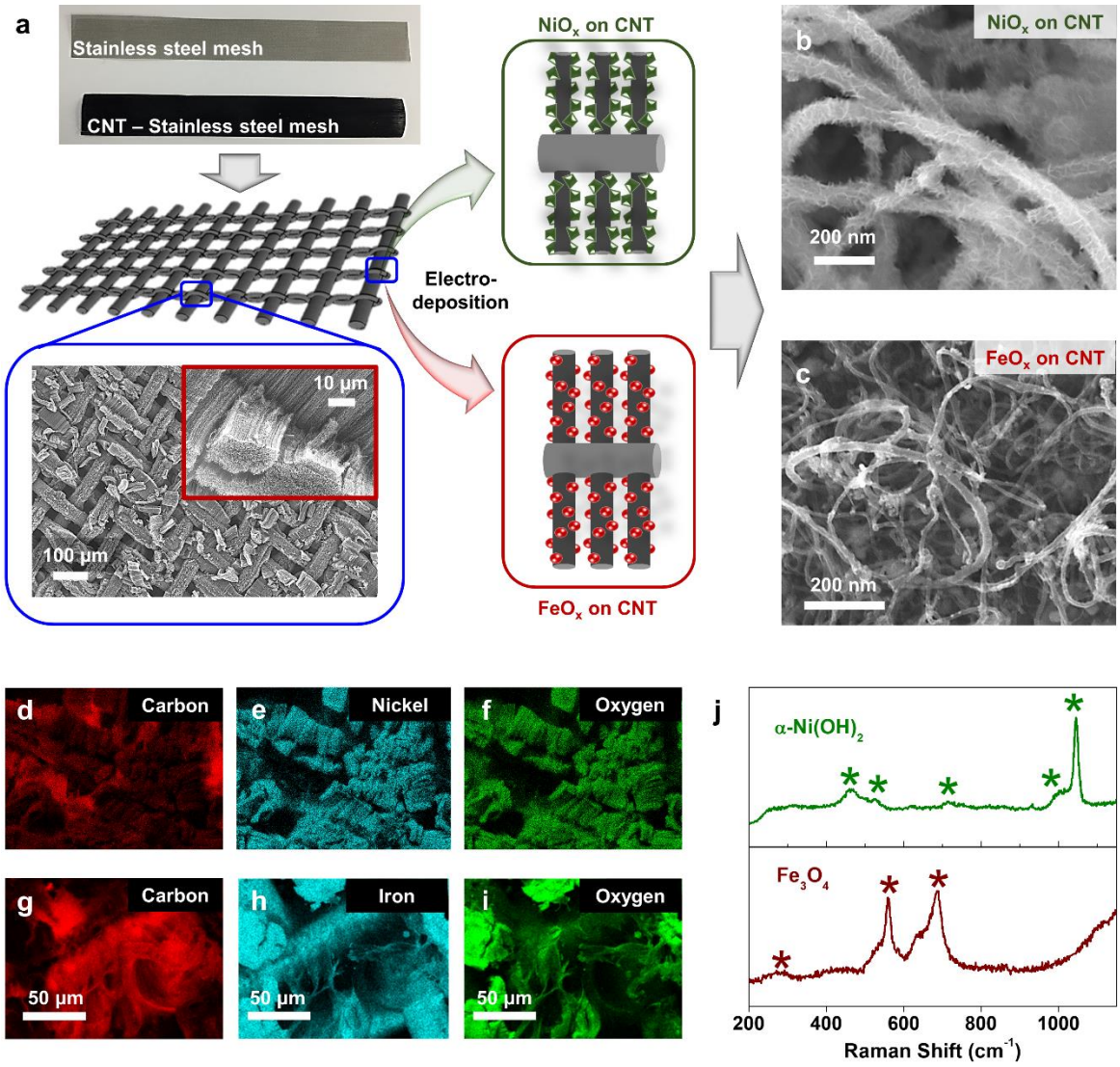

Figure 9.6. (a) Schematic representation of the electrodeposition process for depositing NiO_x and FeO_x on the surface of CNTs grown on stainless steel (SEM micrographs), **(b)** and **(c)** SEM micrographs of the deposited NiO_x and FeO_x on CNTs, **(d-f)** SEM-EDS elemental maps showing the presence of nickel rich species on CNTs, **(g-i)** SEM-EDS elemental maps showing the presence of iron rich species on CNTs, **(j)** Raman spectra of the deposited material on CNTs.

9.3.7 Electrochemical characterization of the individual electrodes

Electrochemical characterization of the redox active materials in KOH aqueous electrolytes (1M) were performed to assess the energy storage capability of the individual electrodes. Cyclic voltammograms at scan rates (5 mV/s to 100 mV/s) of the nickel hydroxide – CNT/SS electrode (figure 9.7a) reveals oxidation and reduction reactions corresponding to the reversible conversion of $Ni(OH)_2$ to NiOOH. The anodic and cathodic peaks are centered around ~0.3V vs SCE. At scan rates of 5 mV/s the electrode delivers a high capacity of 86 mAh/g (capacitance of 394 F/g) based on active material mass. The electrode exhibits high rate capability maintaining ~90% of the capacity observed at 5 mV/s at high scan rates of 100 mV/s as shown in figure 9.7b. We attribute this high capacity maintenance at high scan rates to the architecture of CNTs on stainless steel meshes providing superfast electron conduction pathways for the redox reaction occurring at the surface coatings on the CNTs as shown in the inset of figure 9.7b. Galvanostatic discharge curves at different current densities were performed on the electrode to assess the discharge characteristics (figure 9.7c). A capacity over 50 mAh/g is maintained even at high current densities of 20 mA/cm^2 (active area) indicating the good energy storage capability of the nickel hydroxide electrode. Similar tests starting with cyclic voltammetry were performed on the iron oxide CNT-SS electrode in aqueous 1M KOH electrolyte. The cyclic voltammograms (figure 9.7d) at various scan rates (from 5 mV/s to 100 mV/s) show anodic and cathodic peak corresponding to reversible redox reaction of FeOOH $\leftrightarrow$ $Fe(OH)_2$ centered around ~0.9V vs SCE. Similar to the nickel hydroxide electrode, the iron redox electrode shows high capacity maintenance with over 130 mAh/g at a scan rate of 100 mV/s (figure 9.7e). The superfast electron conduction pathways (figure 9.7e inset) owing to the architecture of aligned conducting CNTs on stainless steel mesh facilitates the high rate redox

reaction of the surface oxide. Galvanostatic discharge curves (figure 9.7f) show a capacity maintenance of over 130 mAh/g at a high current density of 20 mA/cm^2. Electrochemical measurements of the individual electrodes in a half cell configuration in aqueous electrolytes highlights the potential of this system when paired together in a full cell configuration. Cycling performance of the individual electrodes (figure 9.17) and full cell electrochemical performance of the Ni-Fe system with the developed NiO_x cathode and FeO_x anode in the liquid electrolyte (figure 9.18) is provided in the appendix.

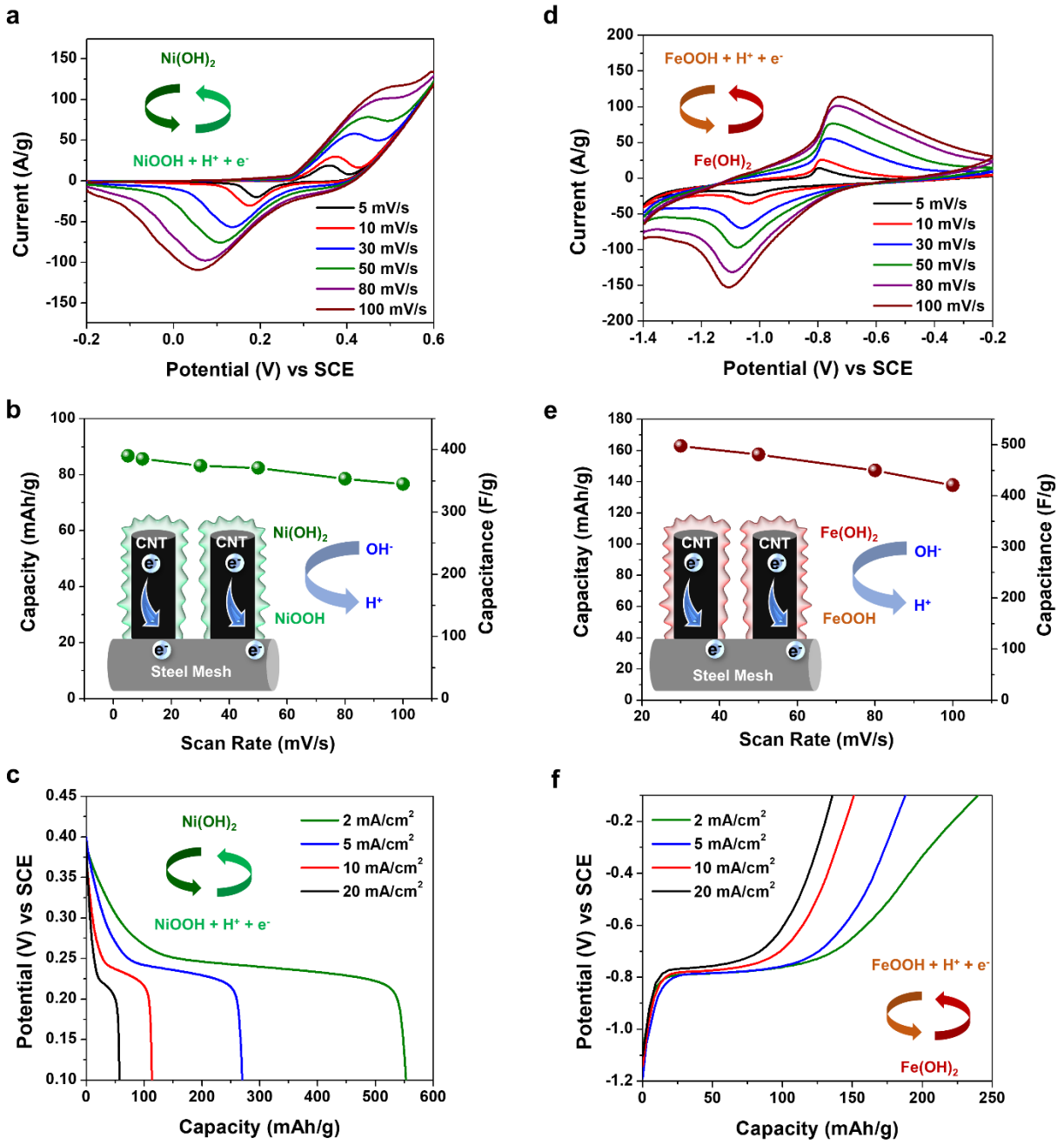

Figure 9.7. (a) Cyclic voltammograms at various scan rates, **(b)** Capacity and capacitance variation with scan rates (inset- schematic representation of the ultrafast electron conduction pathways as a result of the CNT-SS framework) and **(c)** Galvanostatic discharge curves for the deposited nickel hydroxide on CNT-SS electrode, **(d)** Cyclic voltammograms at various scan rates, **(e)** Capacity and capacitance variation with scan rates (inset- schematic representation of

the ultrafast electron conduction pathways as a result of the CNT-SS framework) and **(f)** Galvanostatic discharge curves for the iron oxide on CNT-SS electrode.

9.3.8 Electrochemical performance of the ultra-battery composite

To demonstrate the multifunctional capability of the Ni-Fe system, the NiO_x and FeO_x – CNT/SS meshes were assembled in a sandwich configuration with fiberglass/Kevlar separator using PVA-KOH (1M) gel electrolyte in a wet lay-up process (see experimental methods). The gel electrolyte cures to form an ion conducting solid electrolyte holding the composite together thus forming the ultra-battery composite. Electrochemical performance of the ultra-battery composite using a fiber glass separator layer was determined using cyclic voltammetry and galvanostatic charge discharge tests. Voltammograms at various scan rates (5 mV/s to 100 mV/s) given in figure 9.8a indicate the redox reaction corresponding to $Ni^{2+ \rightarrow 3+}$ and $Fe^{3+ \rightarrow 2+}$ as a result of the cathode undergoing reduction while the anode undergoes oxidation during one half sweep and the reverse occurring in the reverse sweep. The variation of capacitance and capacity with scan rate is provided in figure 9.8b. The lower capacity and rate performance in a full cell configuration when compared to the half cells can be attributed to two reasons: (i) in a full cell (2 electrode measurement), the electrolyte resistance is not excluded owing to the absence of a reference electrode (SCE) present in a three-electrode measurement and (ii) the addition of the fiberglass or Kevlar separators add additional resistances to the system which lowers performance. Nevertheless, the composite shows good galvanostatic charge/discharge characteristics (figure 9.8c) with a capacity of ~22 mAh/g at a current density of 0.5 A/g. Cycling performance of the fiber-glass based composite and the electrochemical performance of the ultra-battery composite with the Kevlar separator is provided in the appendix (figure 9.19 and 9.20 respectively).

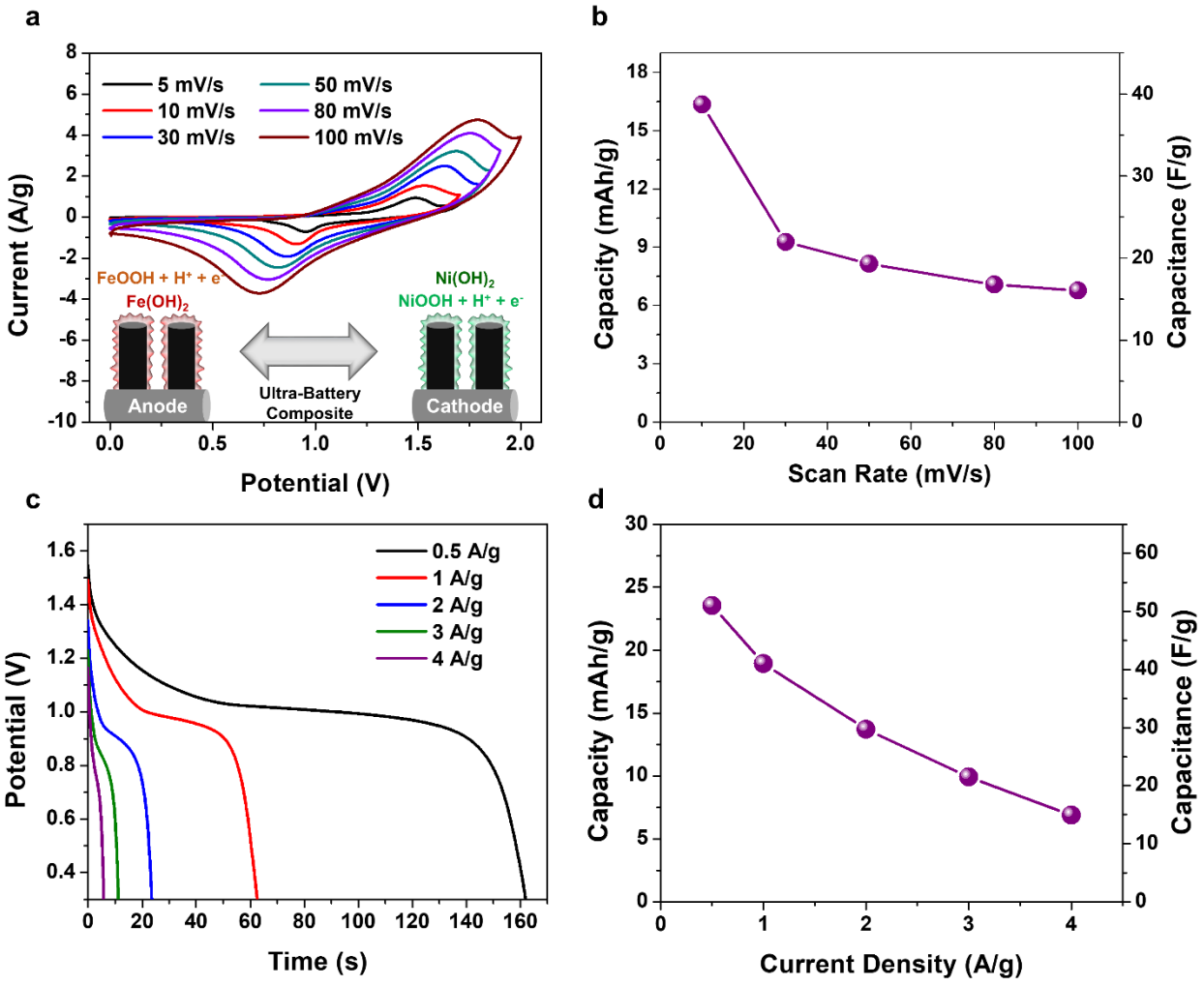

Figure 9.8. (a) Cyclic voltammograms at various scan rates (inset- schematic representation of the iron-based anode and nickel-based cathode for the ultra-battery composite), **(b)** Capacity and capacitance variation with scan rates and **(c)** Galvanostatic discharge curves, **(d)** Capacity and capacitance variation with different applied current densities.

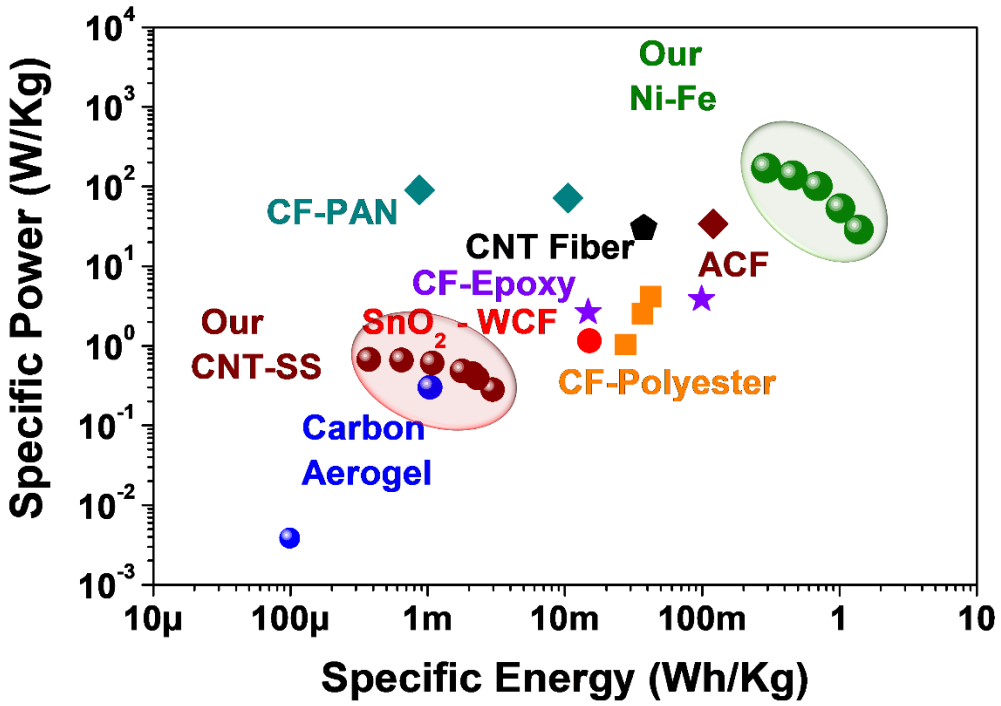

Figure 9.9. Energy and power density of the Ni-Fe ultra-battery composite compared to state-of the art structural energy storage composites in literature

The most important performance metric for a structural energy storage composite are the energy and power densities. Our ultra-battery composite delivers a peak energy of 1.38 Wh/kg at power densities of 29 W/kg and 293 mWh/kg at 170 W/kg respectively based on total mass of all the components in the composite (figure 9.9). Our performance when compared to several other structural energy storage devices in literature, highlights the significant improvement achieved when using the ultra-battery composite instead of EDLC based systems.[342, 350, 353, 354, 356, 357, 381, 386] To emphasis the potential of this redox chemistry, energy and power densities based on active mass is provided in figure 9.10. The ultra-battery composite has peak energy density of 23 Wh/kg and peak power density 2.8 kW/kg respectively based on mass of the redox active species (see appendix figure 9.21, 9.22 and 9.23 for active mass and total mass energy densities of fiber

glass and Kevlar-based Ni-Fe ultra-battery composite respectively). Comparing other state of the art systems such as CNT-Fiber based structural composite and its projected highest reported performance (projected energy density of ~11 Wh/kg)[357] based on active mass indicates the Ni-Fe system (projected energy density of ~120 Wh/kg)[21] to have the potential for significant further improvements. Nevertheless, energy and power density projections based on active mass indicates the room for further development, however practical performance metrics for structural energy storage devices should take into account the total mass of all the components.

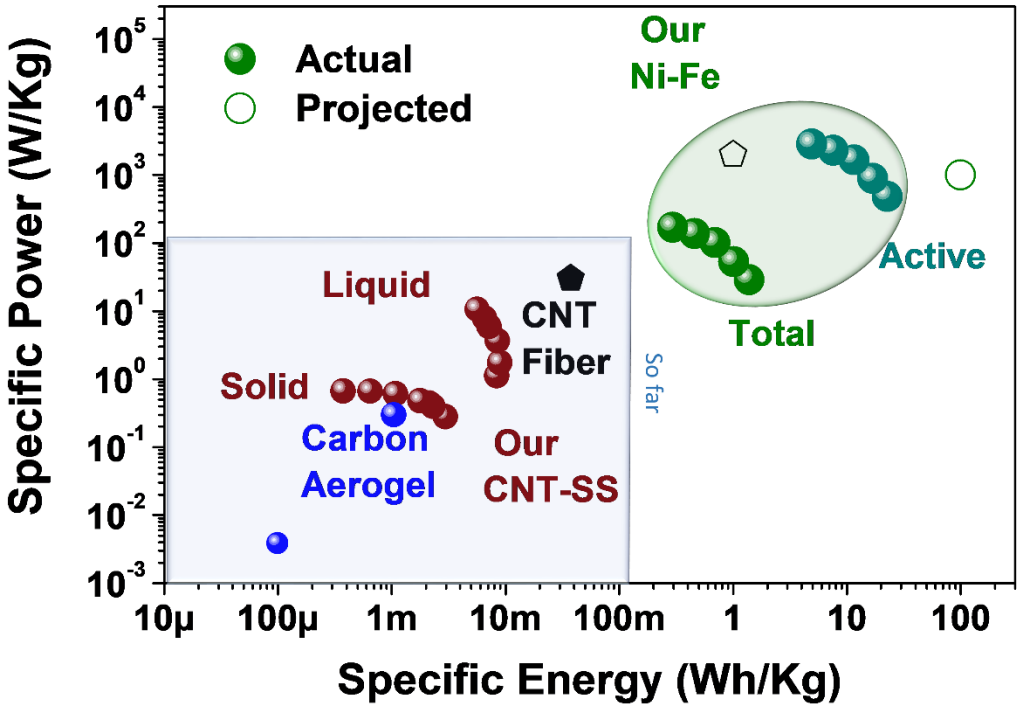

Figure 9.10. Energy and power density projections for the Ni-Fe ultra-battery composite (based on active mass and highest reported values) compared to state-of the art structural energy storage composites in literature.

9.3.9 In-situ mechano-electrochemical performance of the ultra-battery composite

Multifunctional capabilities of the ultra-battery composite were assessed using in-situ mechano-electrochemical tests where simultaneous determination of electrochemical and mechanical performance was determined. The dynamic nature of electrochemical energy storage where mechanics and electrochemistry are inseparable components, simultaneous measurements of the two properties gives insights into the interfaces and stability of the system. To perform the in-situ mechano-electrochemical tests, the ultra-battery composite (using the fiber glass separator) was initially subjected to galvanostatic charge/discharge cycles clamped in an Instron (tensile mode) mechanical tester (figure 9.11a). The composite was subjected to tensile stresses at the rate of 1 mm/min (figure 9.11b) after several stable charge/discharge cycles (figure 9.11c), The different stages observed in the stress strain curve during testing is provided in the supporting information (figure 9.24). The fiber glass-based Ni-Fe ultra-battery composite had an ultimate tensile strength of 23 MPa and modulus of elasticity of 0.023 GPa. The device failure is characterized by the failure of the composite to electrochemically store energy characterized by the abrupt break of the charge/discharge cycle which occurs in the plastic region (figure 9.11d). The observed mechanical performance can be further improved by switching to a Kevlar based Ni-Fe ultra-battery composite (figure 9.11e). In-situ mechano-electrochemical tests were performed in the same manner as the fiber glass-based composite following some initial cycles to attain stability (figure 9.11f). The device failure is characterized by a sharp decrease in the capacity retained during the charge discharge cycling which occurs at the onset of mechanical failure (figure 9.11g).

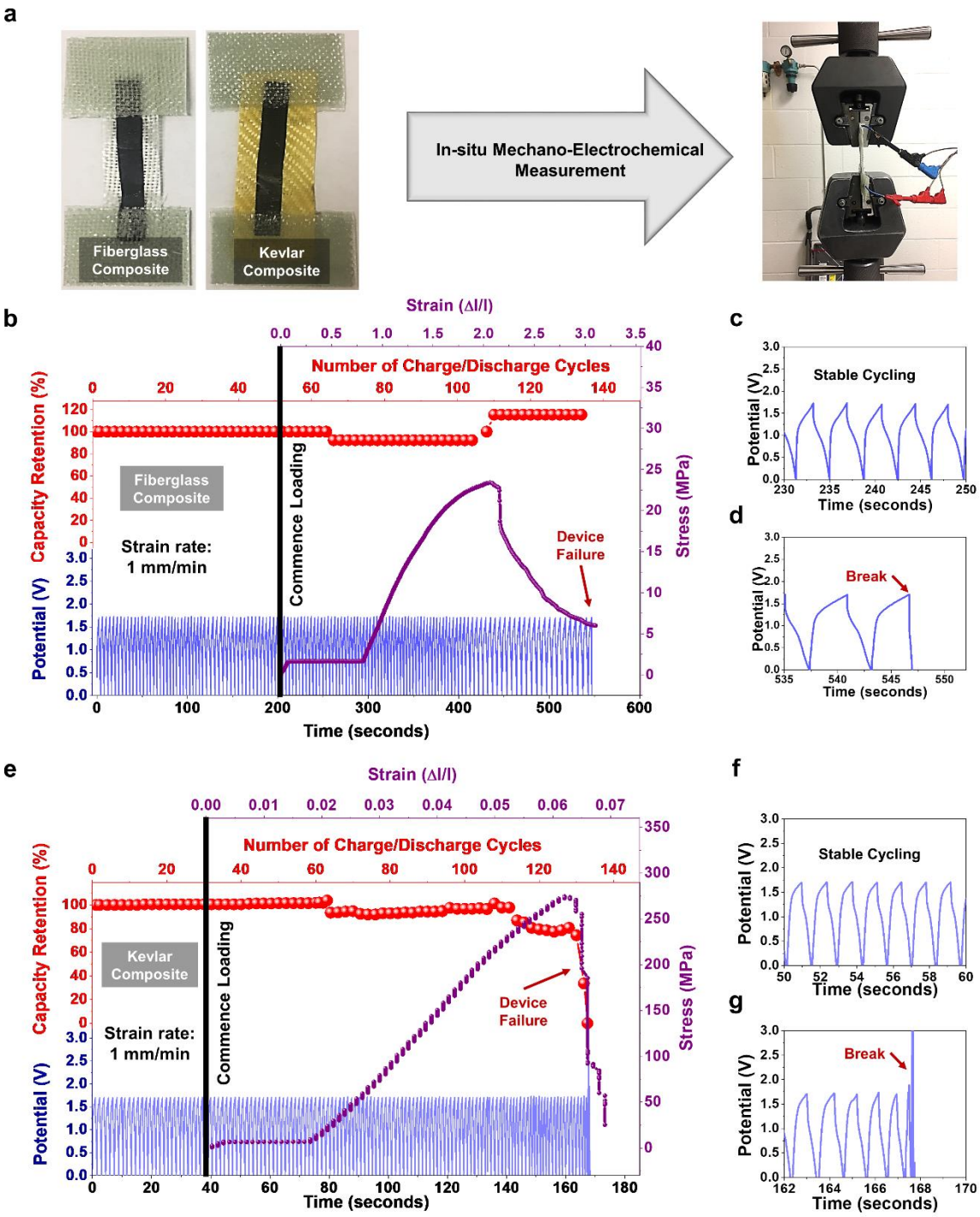

Figure 9.11. (a) Images of the ultra-battery composites based on fiberglass and Kevlar clamped in tensile mode in an Instron mechanical tester, **(b)** In-situ mechano-electrochemical measurements of the fiberglass composite during simultaneous charge discharge measurements

along with dynamic tensile tests, **(c)** Galvanostatic charge/discharge profiles from a region showing stable cycling performance of the fiberglass composite, **(d)** Galvanostatic charge/discharge profiles from the region showing the failure of the fiberglass-based ultra-battery composite, **(e)** In-situ mechano-electrochemical measurements of the kevlar composite during simultaneous charge discharge measurements along with dynamic tensile tests, **(f)** Galvanostatic charge/discharge profiles from a region showing stable cycling performance of the Kevlar composite, **(g)** Galvanostatic charge/discharge profiles from the region showing the failure of the kevlar-based ultra-battery composite.

The Kevlar-based composite had an ultimate tensile strength of 274 MPa with an elastic modulus of 7.3 GPa. This improvement in mechanical performance is achieved at the expense of reduced electrochemical performance when compared to fiber glass composites. Nevertheless, this approach employing faradaic pseudocapacitive redox active materials deposited on aligned carbon nanotubes grown on stainless steel meshes presents a viable route to engineer high performance multifunctional structural energy storage composites.

9.4 Conclusion

Summarizing, our work demonstrates a faradaic nickel-iron based ultra-battery structural composite which exhibits stable electrochemical performance far surpassing conventional double layer based structural supercapacitors. Using CNTs grown on stainless steel meshes functioning as engineered current collectors with superfast electron conduction pathways provides a robust platform for integrating faradaic pseudocapacitive redox active materials on to the nanotube surfaces. The resulting electrodes exhibit high capacity maintenance and good rate capabilities tested in a half cell configuration. The structural ultra-battery composite fabricated through a wet lay-up process using a fiberglass separator, boasts peak energy densities of 1.38 Wh/kg at power

densities of 29 W/kg and 293 mWh/kg at 170 W/kg respectively based on total mass of all the components in the composite. These metrics are significantly higher than conventional state-of the art structural energy storage devices in literature. The fiber glass-based composite has good ultimate tensile strength of 23 MPa which can be further improved by using Kevlar separators resulting in the Ni-Fe ultra-battery composite exhibiting a high ultimate tensile strength of 274 MPa. The true potential of this approach is based on the fact that there are numerous other reported faradaic energy storage materials which can be paired appropriately in full cell configurations. This possibility warrants further investigations into integration of such systems into multifunctional structural composites. Our work on Ni-Fe based ultra-battery composite represents the next advancement in the field of multifunctional energy storage materials as observed by the high energy and power densities. This approach using CNT-steel architectures as supports for a wide range of energy dense electrochemically active redox material pairs coupled with woven polymeric/carbon-based textiles such as glass fiber, Kevlar and carbon fiber provides a framework for further development of multifunctional energy storage systems.

Acknowledgements

We would like to acknowledge and thank all members of Dr. Gilbert Nessim's research group at Bar Ilan University, Israel, for their insights and material fabrication. We would also like to thank Robin Midgett, Adam Cohn, Keith Share, Mengya Li, Janna Eaves, Thomas Metke, Siyuan Jiang and Jennifer Donohue for their insights and useful discussions. We also acknowledge Dr. Rizia Bardhan for use of optical microscopy and Raman spectroscopy as well as VINSE staff for assistance with user facilities. This work was supported in part by the Vanderbilt Discovery Grant and BSF grant.

9.5 Appendix

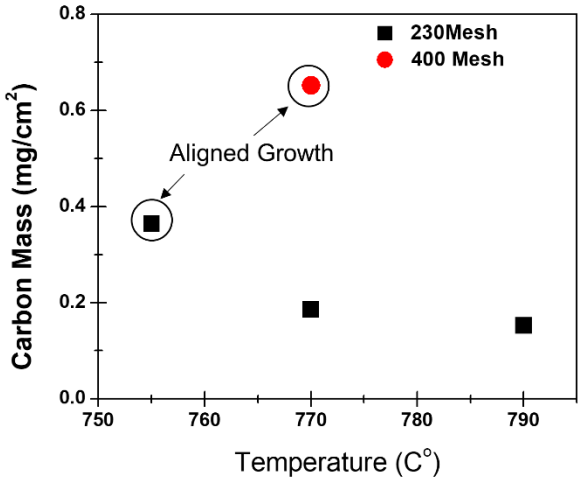

Figure 9.12. Comparison of CNTs grown on 230 mesh and 400 mesh stainless steel samples.

Mass of the carbon nanotubes grown and information regarding the nature of growth is provided.

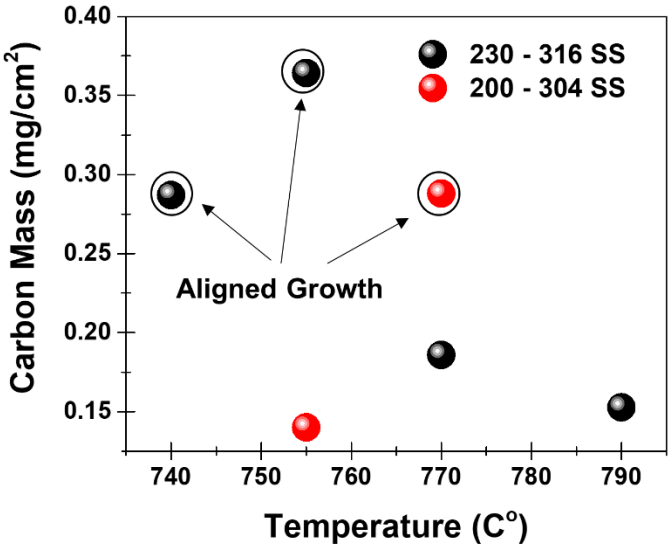

Figure 9.13. Comparison of CNTs grown on 316 and 304 stainless steel samples.

Mass of the carbon nanotubes grown and information regarding the nature of growth is provided.

Elements	304 SS (%)	316 SS (%)
Fe	Balance	Balance
C	0.08 max	0.08 max
Cr	18.0-20.0	16.0-18.0
Ni	8.0-12.0	10.0-14.0
Mo	-----	2.00-3.00
Mn	2.00 max	2.00 max
N	0.10 max	0.10 max
P	0.045 max	0.045 max
S	0.030 max	0.03 max
Si	0.75 max	0.75 max

Table 9.1. Comparison of elemental composition of the 304 and 316 steel meshes.

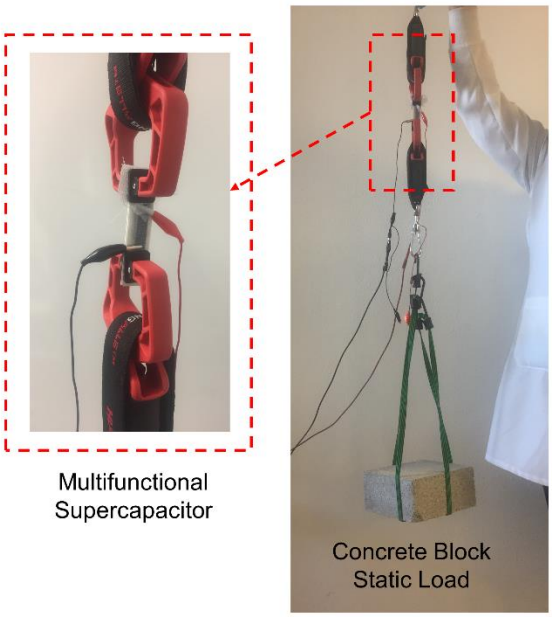

Figure 9.14. Photograph of a structural supercapacitor material supporting ~10 kg of weight concrete block.

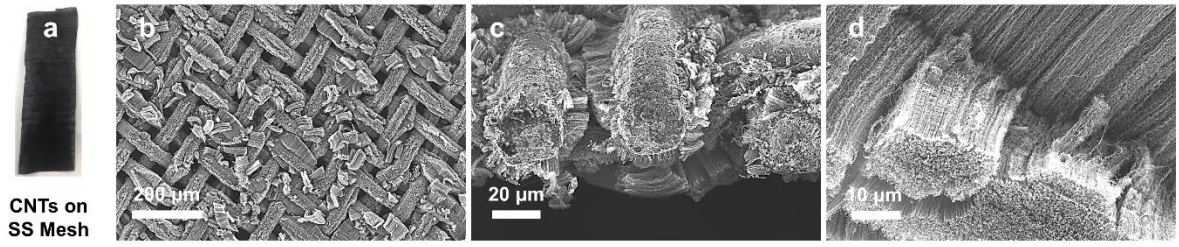

Figure 9.15. (a) Image of a CNT-stainless steel mesh, **(b-d)** SEM micrographs of the CNTs grown on stainless steel mesh

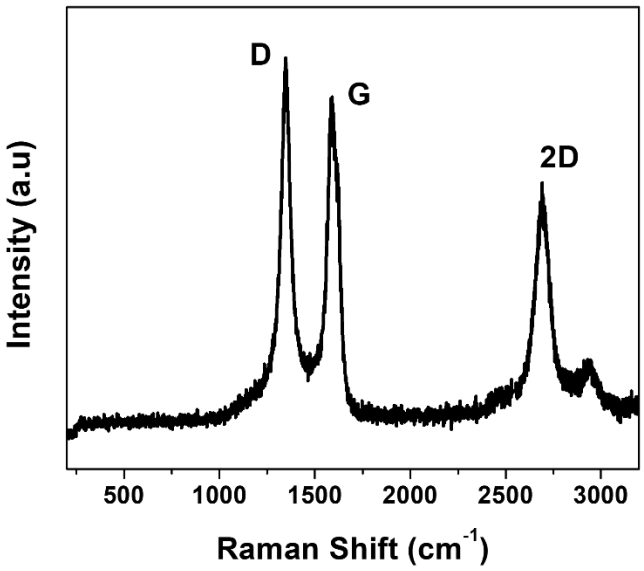

Figure 9.16. Raman spectra of the carbon nanotubes grown on the stainless-steel samples.

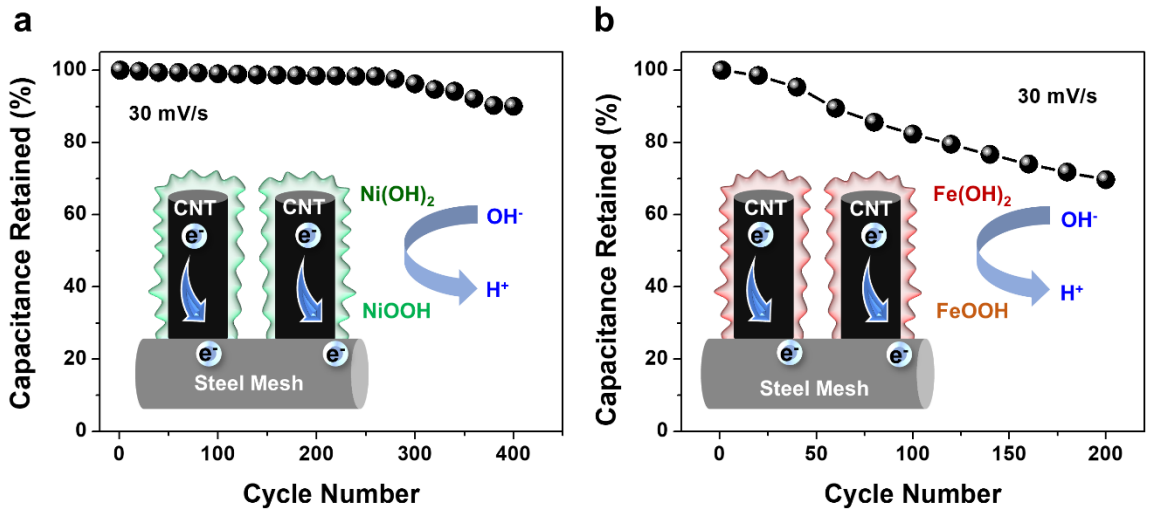

Figure 9.17. Capacitance retention of the individual nickel and iron electrodes at scan rate of 30 mV/s.

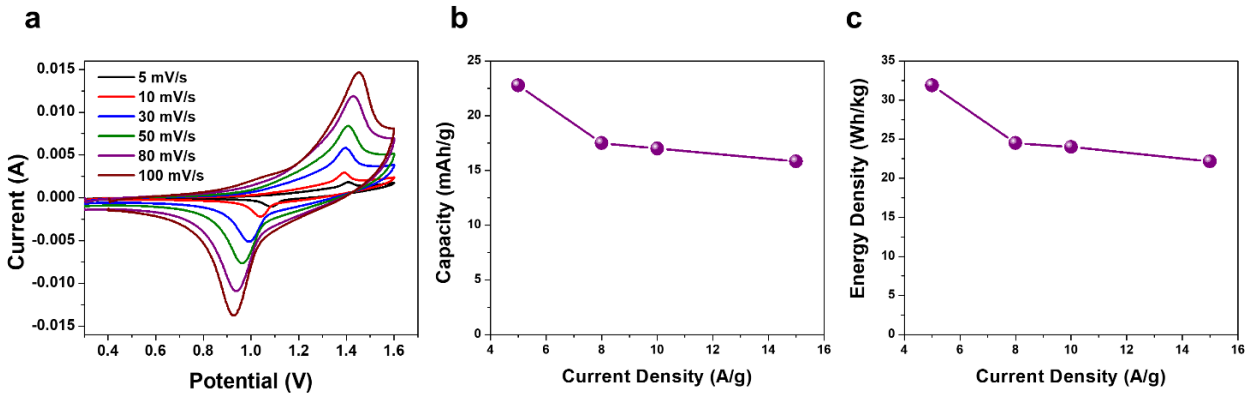

Figure 9.18. (a) Cyclic voltammograms at various scan rates, **(b)** capacity variation with current density and **(c)** energy density variation with current density for the Ni-Fe full cell in liquid 1M KOH electrolyte.

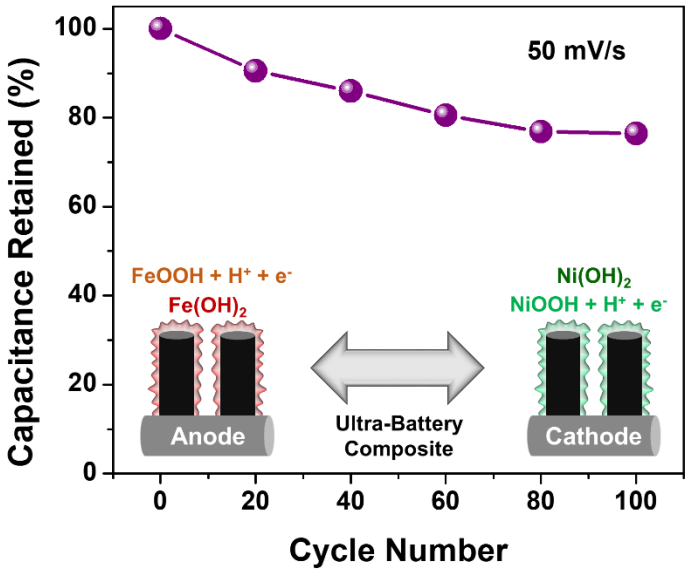

Figure 9.19. Capacitance retention of the fiber glass-based Ni-Fe ultra-battery composite at scan rate of 50 mV/s.

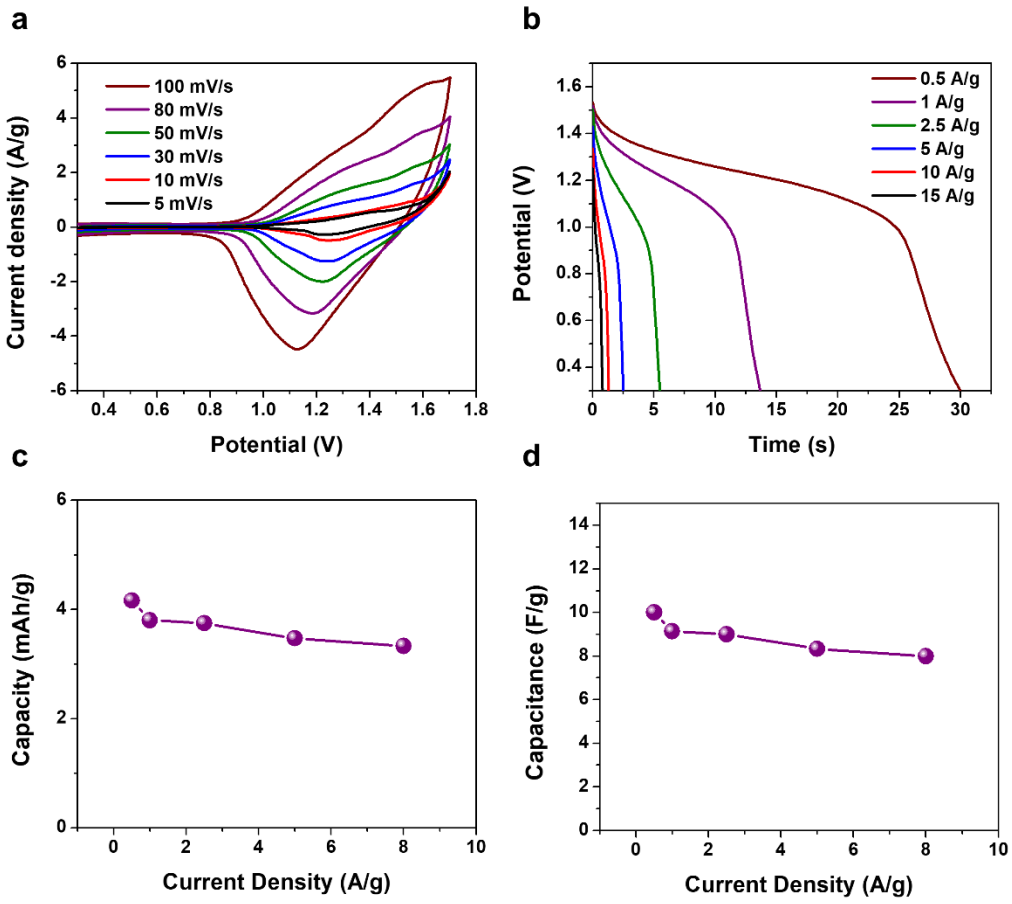

Figure 9.20. (a) Cyclic voltammograms at various scan rates, **(b)** Galvanostatic discharge curves at various current densities, **(c)** Capacity variation with current density and **(d)** Capacitance variation with current density for the Ni-Fe ultra-battery composite using a Kevlar separator based on mass of the active materials.

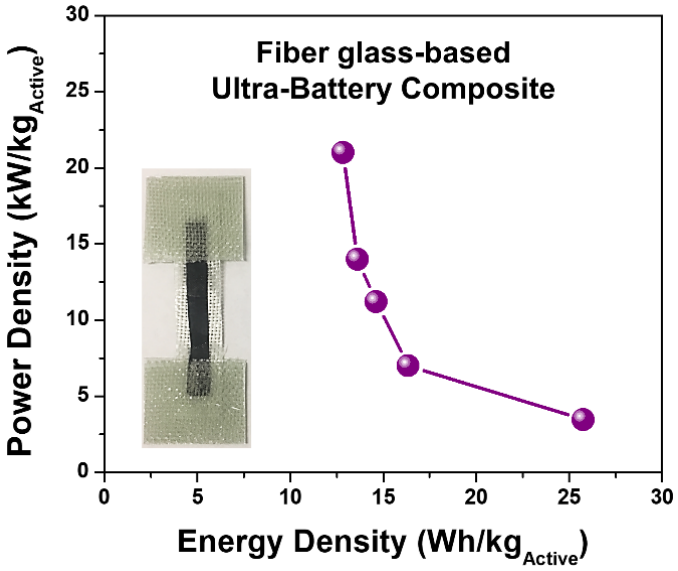

Figure 9.21. Energy and power densities of the fiber glass-based Ni-Fe ultra-battery composite based on active mass.

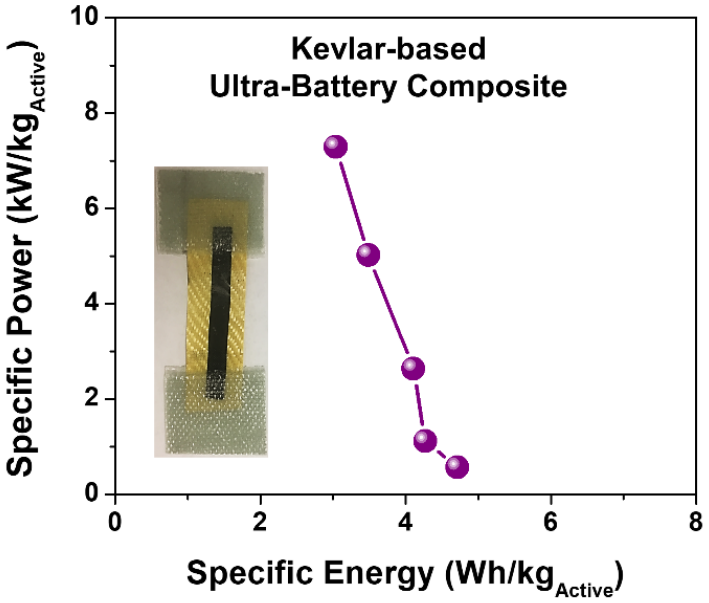

Figure 9.22. Energy and power densities of the Kevlar-based Ni-Fe ultra-battery composite based on active mass.

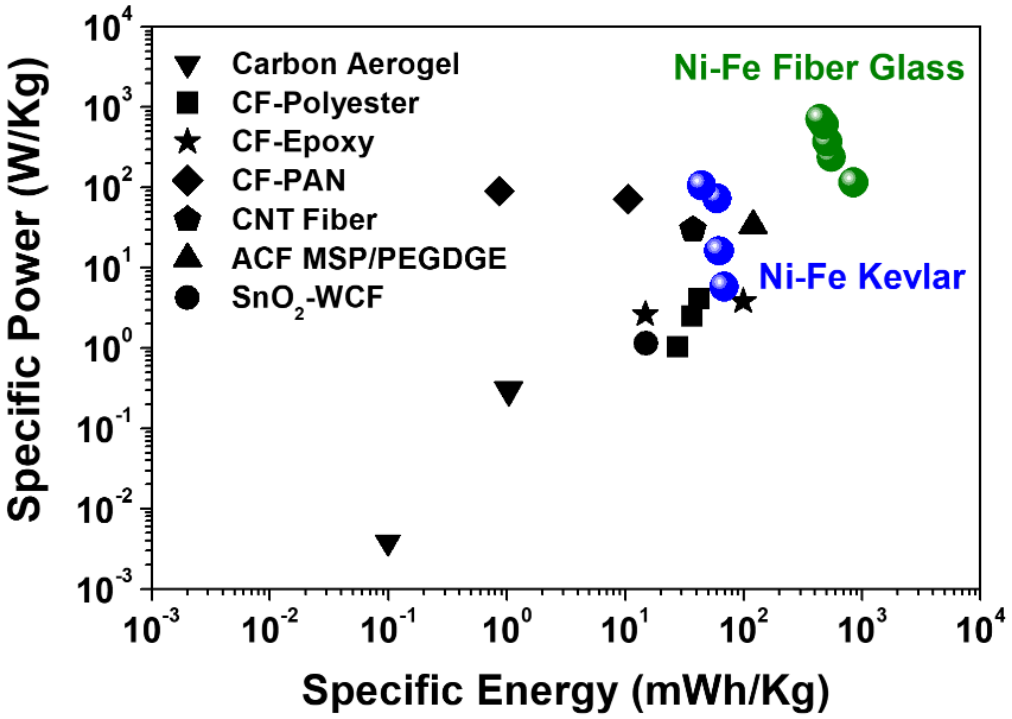

Figure 9.23. Energy and power densities of the fiberglass and Kevlar-based Ni-Fe ultra-battery composite based on total mass of all the components compared to state-of the art devices in literature.

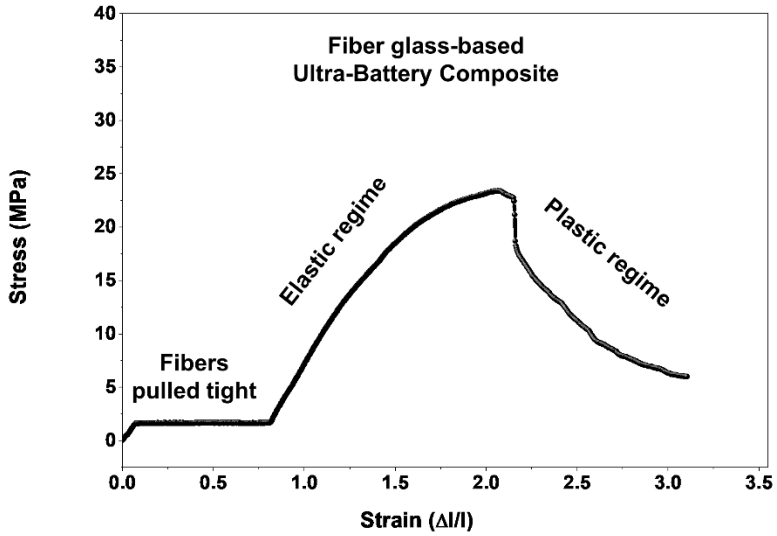

Figure 9.24. Regions of the stress-strain curve for the fiberglass-based ultra-battery composite

Chapter X

10 Conclusions

10.1 Summary

The focus of this research work was to explore the concept of mechano-electrochemical coupling in energy storage electrodes. Fundamental understanding of the effect of mechanical stress and strain on electrochemical energy storage parameters using principles of strain engineering has been successfully demonstrated for the first time in chapters III and IV. Leveraging this new fundamental mechanistic insight, I developed electrochemical-mechanical strain energy harvesters capable of harvesting low frequency ambient mechanical energy. These harvesters described in chapter V and VI using 2D black phosphorus and graphite co-intercalation electrodes can effectively harvest the otherwise wasted ambient mechanical energy from everyday human activities such as walking, running, sitting, sleeping and many more. Furthermore, I developed multifunctional energy storage and harvesting architectures for (i) transient energy storage/harvesting applications (chapters VII and VIII) and (ii) multifunctional load-bearing energy storage applications (Chapter IX). The first half of this work provides new fundamental insights into relatively unexplored mechanisms such as structure-electrochemical relationships and mechano-electrochemical relationships in electrochemical energy storage systems. The second half of this work provides insights and developmental understanding of devices and systems (energy harvesters and multifunctional energy storage) which build off the concepts explored in the first half. Overall, this work provides a broad framework for developing wearable technologies and multifunctional energy storage devices of the future.

10.2 Outlook for strain engineering in energy storage

To understand and thereby control the interplay of mechanics and electrochemistry using concepts of strain engineering in other energy systems requires effective isolation of the expected effects. The proposed strategies in this work are versatile enough to be applied to 'beyond lithium' (Na^+/K^+),[158, 387-389] multivalent (Mg^{2+}, Ca^{2+}) ion and sulfur (Li-S/Na-S)[390-395] and air battery[396, 397] architectures. Successful development of the developed strategies of this work would provide new fundamental understanding to the role of interface mechanics even in solid state battery systems. Fundamental unravelling of the relationship between mechanics and electrochemistry can lead to a variety of solutions to challenges in other electrochemical systems such as solid-state sulfur batteries, solid state alternative ion/multivalent ion batteries, plating batteries, thin film batteries and energy harvesting systems.

10.3 Outlook for electrochemical-mechanical energy harvesters

Low frequency (<5Hz) ambient mechanical energy harvesting is a challenging area for the present state of the art piezoelectric and triboelectric systems. One of the most viable alternative is the novel class of electrochemical-mechanical strain energy harvesters. As discussed in chapter VIII, the volume of active material required for energy harvesting at high mechanical stresses where high power and energy output are obtained indicates that a systems level engineering approach can be used to fabricate arrays of tiny energy harvesters in a small area. Such approaches can compensate for the low voltage output of these systems making them viable for practical applications. Moreover, integration of such devices into textiles and fabrics could provide attractive avenues for further development of these new class of energy harvesting systems.

10.4 Outlook for multifunctional energy storage/harvesting devices

In the case of transient energy storage devices, the concept of on-demand energy supply using a transient energy harvester has huge potential. Transient energy harvesting storage and harvesting systems which can be integrated directly into textiles and fabrics would provide further benefits. By systems level engineering approaches, individual fibers of fabrics can be made into energy storage/harvesting architectures thereby increasing the feasibility and practical viability of such systems.

In the case of multifunctional structural load-bearing energy storage systems, increasing energy densities to reach values >100 Wh/kg based on total weight of the device is going to be the primary focus of this field. To have better load bearing capabilities, transition to carbon fiber-based technologies developed hierarchical carbon nanotube[398-408] interconnected interfaces would be beneficial for both mechanical strength improvements and energy storage improvements.[409] Engineering nano-material architectures[239, 410] at the interface between carbon fibers and active materials would be essential for effective load transfer and also prevent delamination of active materials during load-bearing scenarios. Improving energy densities can be achieved by using lithium ion battery materials deposited on such architectures. Using lithium ion battery chemistries however, requires packaging that would remain a challenge as it adds dead mass to the device which hurts energy densities. Moreover, in most approaches in literature, simultaneous performance (in-situ) testing is not given sufficient attention. Static loading conditions which are commonly used to test such systems though very useful do not provide a complete picture of the full capability of a multifunctional system. The electrochemical - mechanical interactions which contribute to a major failure mode in batteries are not considered in most of the present existing works in literature. As mechanics and battery/pseudocapacitor

electrochemistry are related, the cause of failure is amplified when developing multifunctional energy storage structures which stems from a lack of understanding of mechano-chemical interactions at the fundamental levels of battery operation.

10.5 Conclusion and boarder perspective

Electrochemical energy storage devices have been the driving force behind the ongoing technological revolution which gave us advanced platforms such as electric vehicles, laptops, mobile phones and wearable health monitors. These energy storage devices such as batteries and supercapacitors are dynamic mechano-electrochemical systems where the mechanical component cannot be ignored. Novel formulations, battery designs and systems level designs of the next generation energy storage devices require foundational understanding of the mechanics involved at both the lattice level as well as bulk level. My dissertation is therefore aimed at creating a paradigm shift towards understanding, isolating and thereby controlling mechanical process occurring in such systems. Utilizing such mechanical processes in the new class of electrochemical-mechanical energy harvesters operating at low frequencies, effective on-demand energy generation capability can be integrated with several multifunctional energy storage device architectures. Such multifunctional systems including transient devices and load-bearing energy storage composites could potentially enable innovative technologies which are yet to be envisioned.

REFERENCES

1. ISO, C. What the Duck Curve Tells Us About Managing a Green Grid. *Calif. ISO, Shap. a Renewed Futur.* 1-4.

2. Denholm, P.; O'Connell, M.; Brinkman, G.; Jorgenson, J. *Overgeneration from Solar Energy in California. A Field Guide to the Duck Chart*; National Renewable Energy Lab.(NREL), Golden, CO (United States): 2015.

3. Srinivasan, V. The Three Laws of Batteries (and a Bonus Zeroth Law). https://gigaom.com/2011/03/18/the-three-laws-of-batteries-and-a-bonus-zeroth-law/ (Accessed: July, 2018),

4. Li, J.; Shan, Z.; Ma, E. Elastic Strain Engineering for Unprecedented Materials Properties. *MRS Bulletin.* **2014,** *39*, 108-114.

5. Chung, S. Extension of Moore's Law Via Strained Technologies-the Strategies and Challenges. *ECS Transactions.* **2011,** *41*, 27-41.

6. Schlenker, J. L.; Gibbs, G.; Boisen, M. Strain-Tensor Components Expressed in Terms of Lattice Parameters. *Acta Crystallographica Section A: Crystal Physics, Diffraction, Theoretical and General Crystallography.* **1978,** *34*, 52-54.

7. Rose, J. H.; Ferrante, J.; Smith, J. R. Universal Binding Energy Curves for Metals and Bimetallic Interfaces. *Physical Review Letters.* **1981,** *47*, 675.

8. Schlom, D. G.; Chen, L.-Q.; Fennie, C. J.; Gopalan, V.; Muller, D. A.; Pan, X.; Ramesh, R.; Uecker, R. Elastic Strain Engineering of Ferroic Oxides. *MRS Bulletin.* **2014,** *39*, 118-130.

9. Hao, S.; Cui, L.; Wang, H.; Jiang, D.; Liu, Y.; Yan, J.; Ren, Y.; Han, X.; Brown, D. E.; Li, J. Retaining Large and Adjustable Elastic Strains of Kilogram-Scale Nb Nanowires. *ACS applied materials & interfaces.* **2016,** *8*, 2917-2922.

10. Qiao, L.; Bi, X., *Epitaxial Integration of Ferroelectric Batio3 with Semiconductor Si: From a Structure-Property Correlation Point of View*. INTECH Open Access Publisher: 2011.

11. Lu, J.; Neto, A. C.; Loh, K. P. Transforming Moiré Blisters into Geometric Graphene Nano-Bubbles. *Nature communications.* **2012,** *3*, 823.

12. Bedell, S.; Khakifirooz, A.; Sadana, D. Strain Scaling for Cmos. *MRS Bulletin.* **2014,** *39*, 131-137.

13. Yildiz, B. "Stretching" the Energy Landscape of Oxides—Effects on Electrocatalysis and Diffusion. *Mrs Bulletin.* **2014,** *39*, 147-156.

14. Hausbrand, R.; Cherkashinin, G.; Ehrenberg, H.; Gröting, M.; Albe, K.; Hess, C.; Jaegermann, W. Fundamental Degradation Mechanisms of Layered Oxide Li-Ion Battery Cathode Materials: Methodology, Insights and Novel Approaches. *Materials Science and Engineering: B.* **2015,** *192*, 3-25.

15. Wu, H.; Cui, Y. Designing Nanostructured Si Anodes for High Energy Lithium Ion Batteries. *Nano Today.* **2012,** *7*, 414-429.

16. Ravnsbæk, D. B.; Xiang, K.; Xing, W.; Borkiewicz, O. J.; Wiaderek, K. M.; Gionet, P.; Chapman, K. W.; Chupas, P. J.; Tang, M.; Chiang, Y.-M. Engineering the Transformation Strain in Limn Y Fe1–Y Po4 Olivines for Ultrahigh Rate Battery Cathodes. *Nano letters.* **2016,** *16*, 2375-2380.

17. Tao, X.; Wang, J.; Liu, C.; Wang, H.; Yao, H.; Zheng, G.; Seh, Z. W.; Cai, Q.; Li, W.; Zhou, G. Balancing Surface Adsorption and Diffusion of Lithium-Polysulfides on Nonconductive Oxides for Lithium-Sulfur Battery Design. *Nat. Commun.* **2016,** *7*, 11203.

18. Chan, C. K.; Peng, H.; Liu, G.; McIlwrath, K.; Zhang, X. F.; Huggins, R. A.; Cui, Y. High-Performance Lithium Battery Anodes Using Silicon Nanowires. *Nature nanotechnology.* **2008,** *3*, 31-35.

19. SaifuláIslam, M. Feeling the Strain: Enhancing Ionic Transport in Olivine Phosphate Cathodes for Li-and Na-Ion Batteries through Strain Effects. *Journal of Materials Chemistry A.* **2016,** *4*, 6998-7004.

20. Lee, J.; Pennycook, S. J.; Pantelides, S. T. Simultaneous Enhancement of Electronic and Li+ Ion Conductivity in Lifepo4. *Applied Physics Letters.* **2012,** *101*, 033901.

21. Wang, H.; Liang, Y.; Gong, M.; Li, Y.; Chang, W.; Mefford, T.; Zhou, J.; Wang, J.; Regier, T.; Wei, F. An Ultrafast Nickel–Iron Battery from Strongly Coupled Inorganic Nanoparticle/Nanocarbon Hybrid Materials. *Nat. Commun.* **2012,** *3*, 917.

22. Li, H.; Yu, M.; Wang, F.; Liu, P.; Liang, Y.; Xiao, J.; Wang, C.; Tong, Y.; Yang, G. Amorphous Nickel Hydroxide Nanospheres with Ultrahigh Capacitance and Energy Density as Electrochemical Pseudocapacitor Materials. *Nat. Commun.* **2013,** *4*, 1894.

23. Augustyn, V.; Simon, P.; Dunn, B. Pseudocapacitive Oxide Materials for High-Rate Electrochemical Energy Storage. *Energy Environ. Sci.* **2014,** *7*, 1597-1614.

24. Augustyn, V.; Come, J.; Lowe, M. A.; Kim, J. W.; Taberna, P.-L.; Tolbert, S. H.; Abruna, H. D.; Simon, P.; Dunn, B. High-Rate Electrochemical Energy Storage through Li+ Intercalation Pseudocapacitance. *Nat. Mater.* **2013,** *12*, 518-522.

25. Muralidharan, N.; Westover, A. S.; Sun, H.; Galioto, N.; Carter, R.; Cohn, A. P.; Oakes, L.; Pint, C. L. From the Junkyard to the Power Grid: Ambient Processing of Scrap Metals into Nanostructured Electrodes for Ultrafast Rechargeable Batteries. *ACS Energy Lett.* **2016,** *1*, 1034–1041.

26. Wang, H.; Liang, Y.; Gong, M.; Li, Y.; Chang, W.; Mefford, T.; Zhou, J.; Wang, J.; Regier, T.; Wei, F. An Ultrafast Nickel–Iron Battery from Strongly Coupled Inorganic Nanoparticle/Nanocarbon Hybrid Materials. *Nat. Commun.* **2012,** *3*, 917.

27. Chao, D.; Zhu, C.; Yang, P.; Xia, X.; Liu, J.; Wang, J.; Fan, X.; Savilov, S. V.; Lin, J.; Fan, H. J. Array of Nanosheets Render Ultrafast and High-Capacity Na-Ion Storage by Tunable Pseudocapacitance. *Nat. Commun.* **2016,** *7*, 12122.

28. Lukatskaya, M. R.; Kota, S.; Lin, Z.; Zhao, M.-Q.; Shpigel, N.; Levi, M. D.; Halim, J.; Taberna, P.-L.; Barsoum, M. W.; Simon, P. Ultra-High-Rate Pseudocapacitive Energy Storage in Two-Dimensional Transition Metal Carbides. *Nat. Energy.* **2017,** *2*, 17105.

29. Anasori, B.; Lukatskaya, M. R.; Gogotsi, Y. 2d Metal Carbides and Nitrides (Mxenes) for Energy Storage. *Nat. Rev. Mater.* **2017,** *2*, 16098.

30. Jiang, Q.; Kurra, N.; Alhabeb, M.; Gogotsi, Y.; Alshareef, H. N. All Pseudocapacitive Mxene-Ruo2 Asymmetric Supercapacitors. *Adv. Energy Mater.* **2018**, 1703043.

31. Dar, F. I.; Moonooswamy, K. R.; Es-Souni, M. Morphology and Property Control of Nio Nanostructures for Supercapacitor Applications. *Nanoscale Res. lett.* **2013,** *8*, 1-7.

32. Jiang, H.; Zhao, T.; Li, C.; Ma, J. Hierarchical Self-Assembly of Ultrathin Nickel Hydroxide Nanoflakes for High-Performance Supercapacitors. *J. Mater. Chem.* **2011,** *21*, 3818-3823.

33. Cheng, J.; Zhang, J.; Liu, F. Recent Development of Metal Hydroxides as Electrode Material of Electrochemical Capacitors. *RSC Adv.* **2014,** *4*, 38893-38917.

34. Kim, S.-I.; Thiyagarajan, P.; Jang, J.-H. Great Improvement in Pseudocapacitor Properties of Nickel Hydroxide Via Simple Gold Deposition. *Nanoscale.* **2014,** *6*, 11646-11652.

35. Huang, L.; Chen, D.; Ding, Y.; Feng, S.; Wang, Z. L.; Liu, M. Nickel–Cobalt Hydroxide Nanosheets Coated on Nico2o4 Nanowires Grown on Carbon Fiber Paper for High-Performance Pseudocapacitors. *Nano Lett.* **2013,** *13*, 3135-3139.

36. Zhu, Y.; Cao, C.; Tao, S.; Chu, W.; Wu, Z.; Li, Y. Ultrathin Nickel Hydroxide and Oxide Nanosheets: Synthesis, Characterizations and Excellent Supercapacitor Performances. *Sci. Rep.* **2014,** *4*, 5787

37. Ma, X.; Li, Y.; Wen, Z.; Gao, F.; Liang, C.; Che, R. Ultrathin B-Ni (Oh) 2 Nanoplates Vertically Grown on Nickel-Coated Carbon Nanotubes as High-Performance Pseudocapacitor Electrode Materials. *ACS applied materials & interfaces.* **2014,** *7*, 974-979.

38. Cohn, A. P.; Erwin, W. R.; Share, K.; Oakes, L.; Westover, A. S.; Carter, R. E.; Bardhan, R.; Pint, C. L. All Silicon Electrode Photocapacitor for Integrated Energy Storage and Conversion. *Nano Lett.* **2015,** *15*, 2727-2731.

39. Douglas, A.; Muralidharan, N.; Carter, R.; Share, K.; Pint, C. L. Ultrafast Triggered Transient Energy Storage by Atomic Layer Deposition into Porous Silicon for Integrated Transient Electronics. *Nanoscale.* **2016,** *8*, 7384-7390.

40. Muralidharan, N.; Brock, C.; Cohn, A. P.; Schauben, D.; Carter, R. E.; Oakes, L.; Walker, D. G.; Pint, C. L. Tunable Mechanochemistry of Lithium Battery Electrodes. *ACS Nano.* **2017,** *11*, 6243–6251.

41. Muralidharan, N.; Carter, R.; Oakes, L.; Cohn, A. P.; Pint, C. L. Strain Engineering to Modify the Electrochemistry of Energy Storage Electrodes. *Sci. Rep.* **2016,** *6*, 27542.

42. Muralidharan, N.; Li, M.; Carter, R. E.; Galioto, N.; Pint, C. L. Ultralow Frequency Electrochemical–Mechanical Strain Energy Harvester Using 2d Black Phosphorus Nanosheets. *ACS Energy Lett.* **2017,** *2*, 1797–1803.

43. Li, J.; Wang, G.; Geng, H.; Zhu, H.; Zhang, M.; Di, Z.; Liu, X.; Chu, P. K.; Wang, X. Cvd Growth of Graphene on Niti Alloy for Enhanced Biological Activity. *ACS Appl. Mater. Interfaces.* **2015,** *7*, 19876-19881.

44. Hao, S.; Cui, L.; Jiang, J.; Guo, F.; Xiao, X.; Jiang, D.; Yu, C.; Chen, Z.; Zhou, H.; Wang, Y. A Novel Multifunctional Niti/Ag Hierarchical Composite. *Sci. Rep.* **2014,** *4*, 5267

45. Barnett, B. P.; Arepally, A.; Karmarkar, P. V.; Qian, D.; Gilson, W. D.; Walczak, P.; Howland, V.; Lawler, L.; Lauzon, C.; Stuber, M. Magnetic Resonance–Guided, Real-Time Targeted Delivery and Imaging of Magnetocapsules Immunoprotecting Pancreatic Islet Cells. *Nat. Med.* **2007,** *13*, 986-991.

46. Shabalovskaya, S.; Anderegg, J.; Van Humbeeck, J. Critical Overview of Nitinol Surfaces and Their Modifications for Medical Applications. *Acta Biomater.* **2008,** *4*, 447-467.

47. Chen, P. C.; Hsieh, S. J.; Zou, J.; Chen, C. C. Selectively Dealloyed Ti/Tio2 Network Nanostructures for Supercapacitor Application. *Mater. Lett.* **2014,** *133*, 175-178.

48. Qi, Z.; Weissmüller, J. r. Hierarchical Nested-Network Nanostructure by Dealloying. *ACS Nano.* **2013,** *7*, 5948-5954.

49. Erlebacher, J.; Aziz, M. J.; Karma, A.; Dimitrov, N.; Sieradzki, K. Evolution of Nanoporosity in Dealloying. *Nature.* **2001,** *410*, 450-453.

50. Cheng, F. T.; Shi, P.; Man, H. C. Nature of Oxide Layer Formed on Niti by Anodic Oxidation in Methanol. *Mater. Lett.* **2005,** *59*, 1516-1520.

51. Kawakita, J.; Stratmann, M.; Hassel, A. W. High Voltage Pulse Anodization of a Niti Shape Memory Alloy. *J. Electrochem. Soc.* **2007,** *154*, C294-C298.

52. Hang, R. Q.; Liu, Y. L.; Zhao, L. Z.; Gao, A.; Bai, L.; Huang, X. B.; Zhang, X. Y.; Tang, B.; Chu, P. K. Fabrication of Ni-Ti-O Nanotube Arrays by Anodization of Niti Alloy and Their Potential Applications. *Sci. Rep.* **2014,** *4*, 7547

53. Yang, Z. D.; Wei, X. J.; Gao, W.; Cao, P. Anodization of Niti Alloy in an Ethylene Glycol Electrolyte. *Surf. Coating Tech.* **2014,** *252*, 142-147.

54. Chu, C. L.; Wang, R. M.; Hu, T.; Yin, L. H.; Pu, Y. P.; Lin, P. H.; Dong, Y. S.; Guo, C.; Chung, C. Y.; Yeung, K. W. K.; Chu, P. K. Xps and Biocompatibility Studies of Titania Film on Anodized Niti Shape Memory Alloy. *J. Mater. Sci. -Mater. Med.* **2009,** *20*, 223-228.

55. Kim, J. H.; Zhu, K.; Yan, Y. F.; Perkins, C. L.; Frank, A. J. Microstructure and Pseudocapacitive Properties of Electrodes Constructed of Oriented Nio-Tio2 Nanotube Arrays. *Nano Lett.* **2010,** *10*, 4099-4104.

56. Gao, Z. D.; Han, Y. Y.; Wang, Y. M.; Xu, J. W.; Song, Y. Y. One-Step to Prepare Self-Organized Nanoporous Nio/Tio2 Layers and Its Use in Non-Enzymatic Glucose Sensing. *Sci. Rep.* **2013,** *3*, 3323.

57. Zhang, G.; Li, W.; Xie, K.; Yu, F.; Huang, H. A One-Step and Binder-Free Method to Fabricate Hierarchical Nickel-Based Supercapacitor Electrodes with Excellent Performance. *Adv. Funct. Mater.* **2013,** *23*, 3675-3681.

58. Wu, S.; Hui, K.; Hui, K. N. One-Dimensional Core–Shell Architecture Composed of Silver Nanowire@ Hierarchical Nickel–Aluminum Layered Double Hydroxide Nanosheet as Advanced Electrode Materials for Pseudocapacitor. *J. Phys. Chem. C.* **2015,** *119*, 23358-23365.

59. Kim, D.; Lee, K.; Roy, P.; Birajdar, B. I.; Spiecker, E.; Schmuki, P. Formation of a Non-Thickness-Limited Titanium Dioxide Mesosponge and Its Use in Dye-Sensitized Solar Cells. *Angew. Chem.* **2009,** *121*, 9490-9493.

60. Shabalovskaya, S.; Anderegg, J.; Van Humbeeck, J. Critical Overview of Nitinol Surfaces and Their Modifications for Medical Applications. *Acta Biomater.* **2008,** *4*, 447-467.

61. Duerig, T. W.; Melton, K.; Stöckel, D., *Engineering Aspects of Shape Memory Alloys*. *Butterworth-Heinemann*: 2013.

62. Aaronson, H. I.; Enomoto, M.; Lee, J. K., *Mechanisms of Diffusional Phase Transformations in Metals and Alloys*. *CRC Press*: 2010.

63. Hang, R. Q.; Liu, Y. L.; Gao, A.; Bai, L.; Huang, X. B.; Zhang, X. Y.; Lin, N. M.; Tang, B.; Chu, P. K. Highly Ordered Ni-Ti-O Nanotubes for Non-Enzymatic Glucose Detection. *Mater. Sci. Eng., C.* **2015,** *51*, 37-42.

64. Yang, M.; Huo, L.; Pei, L. J.; Pan, K.; Gan, Y. Enhanced Photoelectrochemical Performance and Charge Transfer Properties in Self-Organized Niox-Doped Tio2 Nanotubes. *Electrochim. Acta.* **2014,** *125*, 288-293.

65. Lo, Y. L.; Hwang, B. J. In Situ Raman Studies on Cathodically Deposited Nickel Hydroxide Films and Electroless Ni-P Electrodes in 1 M Koh Solution. *Langmuir.* **1998,** *14*, 944-950.

66. Hermet, P.; Gourrier, L.; Bantignies, J.-L.; Ravot, D.; Michel, T.; Deabate, S.; Boulet, P.; Henn, F. Dielectric, Magnetic, and Phonon Properties of Nickel Hydroxide. *Phys. Rev. B.* **2011,** *84*, 235211.

67. Lu, M.-L.; Lin, T.-Y.; Weng, T.-M.; Chen, Y.-F. Large Enhancement of Photocurrent Gain Based on the Composite of a Single N-Type Sno 2 Nanowire and P-Type Nio Nanoparticles. *Opt. Express.* **2011,** *19*, 16266-16272.

68. Li, C. P.; Proctor, A.; Hercules, D. M. Curve Fitting Analysis of Esca Ni 2p Spectra of Nickel-Oxygen Compounds and Ni/Al 2 O 3 Catalysts. *Appl. Spectrosc.* **1984,** *38*, 880-886.

69. Kim, K.; Winograd, N. X-Ray Photoelectron Spectroscopic Studies of Nickel-Oxygen Surfaces Using Oxygen and Argon Ion-Bombardment. *Surf. Sci.* **1974,** *43*, 625-643.

70. Venezia, A.; Bertoncello, R.; Deganello, G. X-Ray Photoelectron Spectroscopy Investigation of Pumice-Supported Nickel Catalysts. *Surf. Interface Anal.* **1995,** *23*, 239-247.

71. Wang, X.; Sebastian, P.; Millan, A.-C.; Parkhutik, P.; Gamboa, S. Electrochemical Study of Nanostructured Multiphase Nickel Hydroxide. *J. New Mater. Electrochem. Syst.* **2005,** *8*, 101-108.

72. Bourgault, P.; Conway, B. The Electrochemical Behavior of the Nickel Oxide Electrode: Part Ii. Quasi-Equilibrium Behavior. *Can. J. Chem.* **1960,** *38*, 1557-1575.

73. Yi, H.; Chen, X.; Wang, H. W.; Wang, X. F. Hierarchical Tin@Ni(Oh)(2) Core/Shell Nanowire Arrays for Supercapacitor Application. *Electrochim. Acta.* **2014,** *116*, 372-378.

74. Jiang, H.; Ma, J.; Li, C. Hierarchical Porous Nico 2 O 4 Nanowires for High-Rate Supercapacitors. *Chem. Commun.* **2012,** *48*, 4465-4467.

75. Xiong, S.; Yuan, C.; Zhang, X.; Qian, Y. Mesoporous Nio with Various Hierarchical Nanostructures by Quasi-Nanotubes/Nanowires/Nanorods Self-Assembly: Controllable Preparation and Application in Supercapacitors. *CrystEngComm.* **2011,** *13*, 626-632.

76. Qin, R.; Ding, D. Y.; Ning, C. Q.; Liu, H. G.; Zhu, B. S.; Li, M.; Mao, D. L. Ni-Doped Tio2 Nanotube Arrays on Shape Memory Alloy. *Appl. Surf. Sci.* **2011,** *257*, 6308-6313.

77. Liu, Q.; Ding, D. Y.; Ning, C. Q. Anodic Fabrication of Ti-Ni-O Nanotube Arrays on Shape Memory Alloy. *Materials.* **2014,** *7*, 3262-3273.

78. Dai, X.; Chen, D.; Fan, H.; Zhong, Y.; Chang, L.; Shao, H.; Wang, J.; Zhang, J.; Cao, C.-n. Ni (Oh) 2/Nio/Ni Composite Nanotube Arrays for High-Performance Supercapacitors. *Electrochim. Acta.* **2015,** *154*, 128-135.

79. Salari, M.; Aboutalebi, S. H.; Konstantinov, K.; Liu, H. K. A Highly Ordered Titania Nanotube Array as a Supercapacitor Electrode. *Phys. Chem. Chem. Phys.* **2011,** *13*, 5038-5041.

80. Lu, X. H.; Wang, G. M.; Zhai, T.; Yu, M. H.; Gan, J. Y.; Tong, Y. X.; Li, Y. Hydrogenated Tio2 Nanotube Arrays for Supercapacitors. *Nano Lett.* **2012,** *12*, 1690-1696.

81. Arico, A. S.; Bruce, P.; Scrosati, B.; Tarascon, J.-M.; Van Schalkwijk, W. Nanostructured Materials for Advanced Energy Conversion and Storage Devices. *Nat. Mater.* **2005,** *4*, 366-377.

82. Larcher, D.; Tarascon, J. Towards Greener and More Sustainable Batteries for Electrical Energy Storage. *Nat. Chem.* **2015,** *7*, 19–29.

83. Jain, A.; Hautier, G.; Ong, S. P.; Dacek, S.; Ceder, G. Relating Voltage and Thermal Safety in Li-Ion Battery Cathodes: A High-Throughput Computational Study. *Phys. Chem. Chem. Phys.* **2015,** *17*, 5942-5953.

84. Mo, Y.; Ong, S. P.; Ceder, G. Insights into Diffusion Mechanisms in P2 Layered Oxide Materials by First-Principles Calculations. *Chem. Mater.* **2014,** *26*, 5208-5214.

85. Fu, X.; Su, C.; Fu, Q.; Zhu, X.; Zhu, R.; Liu, C.; Liao, Z.; Xu, J.; Guo, W.; Feng, J. Tailoring Exciton Dynamics by Elastic Strain-Gradient in Semiconductors. *Adv. Mater.* **2014,** *26*, 2572-2579.

86. Feng, J.; Qian, X.; Huang, C.-W.; Li, J. Strain-Engineered Artificial Atom as a Broad-Spectrum Solar Energy Funnel. *Nat. Photonics.* **2012,** *6*, 866-872.

87. Li, J.; Shan, Z.; Ma, E. Elastic Strain Engineering for Unprecedented Materials Properties. *MRS Bull.* **2014,** *39*, 108-114.

88. Li, H.; Contryman, A. W.; Qian, X.; Ardakani, S. M.; Gong, Y.; Wang, X.; Weisse, J. M.; Lee, C. H.; Zhao, J.; Ajayan, P. M. Optoelectronic Crystal of Artificial Atoms in Strain-Textured Molybdenum Disulphide. *Nat. Commun.* **2015,** *6*, 7381.

89. Li, H.; Tsai, C.; Koh, A. L.; Cai, L.; Contryman, A. W.; Fragapane, A. H.; Zhao, J.; Han, H. S.; Manoharan, H. C.; Abild-Pedersen, F. Activating and Optimizing Mos2 Basal Planes for Hydrogen Evolution through the Formation of Strained Sulphur Vacancies. *Nat. Mater.* **2016,** *15*, 48-53.

90. Bissett, M. A.; Tsuji, M.; Ago, H. Strain Engineering the Properties of Graphene and Other Two-Dimensional Crystals. *Phys. Chem. Chem. Phys.* **2014,** *16*, 11124-11138.

91. Lu, J.; Neto, A. C.; Loh, K. P. Transforming Moiré Blisters into Geometric Graphene Nano-Bubbles. *Nat. Commun.* **2012,** *3*, 823.

92. Liu, Z.; Amani, M.; Najmaei, S.; Xu, Q.; Zou, X.; Zhou, W.; Yu, T.; Qiu, C.; Birdwell, A. G.; Crowne, F. J. Strain and Structure Heterogeneity in Mos2 Atomic Layers Grown by Chemical Vapour Deposition. *Nat. Commun.* **2014,** *5*, 5246.

93. Wang, L.; Liu, P.; Guan, P.; Yang, M.; Sun, J.; Cheng, Y.; Hirata, A.; Zhang, Z.; Ma, E.; Chen, M. In Situ Atomic-Scale Observation of Continuous and Reversible Lattice Deformation Beyond the Elastic Limit. *Nat. Commun.* **2013,** *4*, 2413.

94. Wang, L.; Zhang, Z.; Han, X. In Situ Experimental Mechanics of Nanomaterials at the Atomic Scale. *NPG Asia Mater.* **2013,** *5*, e40.

95. Gong, M.; Jin, X.; Sakidja, R.; Ren, S. Synergistic Strain Engineering Effect of Hybrid Plasmonic, Catalytic and Magnetic Core-Shell Nanocrystals. *Nano Lett.* **2015,** *15*, 8347–8353.

96. Kibler, L. A.; El-Aziz, A. M.; Hoyer, R.; Kolb, D. M. Tuning Reaction Rates by Lateral Strain in a Palladium Monolayer. *Angew. Chem. Int. Ed. Engl.* **2005,** *44*, 2080-2084.

97. Du, M.; Cui, L.; Cao, Y.; Bard, A. J. Mechanoelectrochemical Catalysis of the Effect of Elastic Strain on a Platinum Nanofilm for the Orr Exerted by a Shape Memory Alloy Substrate. *J. Am. Chem. Soc.* **2015,** *137*, 7397–7403.

98. Sneed, B. T.; Young, A. P.; Tsung, C.-K. F. Building up Strain in Colloidal Metal Nanoparticle Catalysts. *Nanoscale.* **2015,** *7*, 12248-12265.

99. Amakawa, K.; Sun, L.; Guo, C.; Hävecker, M.; Kube, P.; Wachs, I. E.; Lwin, S.; Frenkel, A. I.; Patlolla, A.; Hermann, K. How Strain Affects the Reactivity of Surface Metal Oxide Catalysts. *Angew. Chem. Int. Ed. Engl.* **2013,** *52*, 13553-13557.

100. Aidhy, D. S.; Sachan, R.; Zarkadoula, E.; Pakarinen, O.; Chisholm, M. F.; Zhang, Y.; Weber, W. J. Fast Ion Conductivity in Strained Defect-Fluorite Structure Created by Ion Tracks in Gd2ti2o7. *Sci. Rep.* **2015,** *5*, 16297

101. Han, J. W.; Yildiz, B. Enhanced One Dimensional Mobility of Oxygen on Strained Lacoo 3 (001) Surface. *J. Mater. Chem.* **2011,** *21*, 18983-18990.

102. Tsvetkov, N.; Lu, Q.; Chen, Y.; Yildiz, B. Accelerated Oxygen Exchange Kinetics on Nd2nio4+ Δ Thin Films with Tensile Strain Along C-Axis. *ACS Nano.* **2015,** *9*, 1613-1621.

103. Kim, S.; Choi, S. J.; Zhao, K.; Yang, H.; Gobbi, G.; Zhang, S.; Li, J. Electrochemically Driven Mechanical Energy Harvesting. *Nat. Commun.* **2016,** *7*.

104. Simon, P.; Gogotsi, Y. Materials for Electrochemical Capacitors. *Nat. Mater.* **2008,** *7*, 845-854.

105. Sheldon, B. W.; Soni, S. K.; Xiao, X.; Qi, Y. Stress Contributions to Solution Thermodynamics in Li-Si Alloys. *Electrochem. Solid State Lett.* **2011,** *15*, A9-A11.

106. Chon, M. J.; Sethuraman, V. A.; McCormick, A.; Srinivasan, V.; Guduru, P. R. Real-Time Measurement of Stress and Damage Evolution During Initial Lithiation of Crystalline Silicon. *Phys. Rev. Lett.* **2011,** *107*, 045503.

107. Zeng, Z.; Liu, N.; Zeng, Q.; Lee, S. W.; Mao, W. L.; Cui, Y. In Situ Measurement of Lithiation-Induced Stress in Silicon Nanoparticles Using Micro-Raman Spectroscopy. *Nano Energy.* **2016,** *22*, 105-110.

108. Azizi, A.; Zou, X.; Ercius, P.; Zhang, Z.; Elías, A. L.; Perea-López, N.; Stone, G.; Terrones, M.; Yakobson, B. I.; Alem, N. Dislocation Motion and Grain Boundary Migration in Two-Dimensional Tungsten Disulphide. *Nat. Commun.* **2014,** *5*, 4867.

109. Liu, Y.; Merinov, B. V.; Goddard, W. A. Origin of Low Sodium Capacity in Graphite and Generally Weak Substrate Binding of Na and Mg among Alkali and Alkaline Earth Metals. *Proc. Natl. Acad. Sci. USA.* **2016,** *113*, 3735-3739.

110. Hansen, A. W.; Beltrami, L. V. R.; Antonini, L. M.; Villarinho, D. J.; Neves, J. C. K. d.; Marino, C. E. B.; Malfatti, C. d. F. Oxide Formation on Niti Surface: Influence of the Heat Treatment Time to Achieve the Shape Memory. *Materials Research.* **2015,** *18*, 1053-1061.

111. Firstov, G.; Vitchev, R.; Kumar, H.; Blanpain, B.; Van Humbeeck, J. Surface Oxidation of Niti Shape Memory Alloy. *Biomaterials.* **2002,** *23*, 4863-4871.

112. Tan, G.; Liu, Y.; Sittner, P.; Saunders, M. Lüders-Like Deformation Associated with Stress-Induced Martensitic Transformation in Niti. *Scr. Mater.* **2004,** *50*, 193-198.

113. Liu, Q.; Ding, D.; Ning, C. Anodic Fabrication of Ti-Ni-O Nanotube Arrays on Shape Memory Alloy. *Materials.* **2014,** *7*, 3262-3273.

114. Santara, B.; Giri, P.; Imakita, K.; Fujii, M. Evidence of Oxygen Vacancy Induced Room Temperature Ferromagnetism in Solvothermally Synthesized Undoped Tio 2 Nanoribbons. *Nanoscale.* **2013,** *5*, 5476-5488.

115. Kim, S.-J.; Yun, Y.-U.; Oh, H.-J.; Hong, S. H.; Roberts, C. A.; Routray, K.; Wachs, I. E. Characterization of Hydrothermally Prepared Titanate Nanotube Powders by Ambient and in Situ Raman Spectroscopy. *J. Phys. Chem. Lett.* **2009,** *1*, 130-135.

116. Bellat, V.; Chassagnon, R.; Heintz, O.; Saviot, L.; Vandroux, D.; Millot, N. A Multi-Step Mechanism and Integrity of Titanate Nanoribbons. *Dalton Trans.* **2015,** *44*, 1150-1160.

117. Byrne, M. T.; McCarthy, J. E.; Bent, M.; Blake, R.; Gun'ko, Y. K.; Horvath, E.; Konya, Z.; Kukovecz, A.; Kiricsi, I.; Coleman, J. N. Chemical Functionalisation of Titania Nanotubes and Their Utilisation for the Fabrication of Reinforced Polystyrene Composites. *J. Mater. Chem.* **2007,** *17*, 2351-2358.

118. Baraton, M.; Busca, G.; Prieto, M.; Ricchiardi, G.; Escribano, V. S. On the Vibrational Spectra and Structure of Fecro 3 and of the Ilmenite-Type Compounds Cotio 3 and Nitio 3. *J. Solid State Chem.* **1994,** *112*, 9-14.

119. GallardoáAmores, J. M.; SanchezáEscribano, V. Ft Raman and Ftir Studies of Titanias and Metatitanate Powders. *J. Chem. Soc. Faraday Trans.* **1994,** *90*, 3181-3190.

120. Nguyen-Phan, T.-D.; Huy, C. N.; Kim, C.-K.; Shin, E. W. Facile Microwave-Assisted Synthesis and Controllable Architecture of Three-Dimensional Nickel Titanate. *CrystEngComm.* **2015,** *17*, 4562-4574.

121. Bellam, J. B.; Ruiz-Preciado, M. A.; Edely, M.; Szade, J.; Jouanneaux, A.; Kassiba, A. H. Visible-Light Photocatalytic Activity of Nitrogen-Doped Nitio 3 Thin Films Prepared by a Co-Sputtering Process. *RSC Adv.* **2015,** *5*, 10551-10559.

122. Yan, J.; Wu, G.; Guan, N.; Li, L.; Li, Z.; Cao, X. Understanding the Effect of Surface/Bulk Defects on the Photocatalytic Activity of Tio 2: Anatase Versus Rutile. *Phys. Chem. Chem. Phys.* **2013,** *15*, 10978-10988.

123. Li, L.; Yan, J.; Wang, T.; Zhao, Z.-J.; Zhang, J.; Gong, J.; Guan, N. Sub-10 Nm Rutile Titanium Dioxide Nanoparticles for Efficient Visible-Light-Driven Photocatalytic Hydrogen Production. *Nat. Commun.* **2015,** *6*, 5881.

124. Zhou, M.; Chai, H.; Jia, D.; Zhou, W. The Glucose-Assisted Synthesis of a Graphene Nanosheet–Nio Composite for High-Performance Supercapacitors. *New J. Chem.* **2014,** *38*, 2320-2326.

125. Luo, C.; Li, D.; Wu, W.; Zhang, Y.; Pan, C. Preparation of Porous Micro–Nano-Structure Nio/Zno Heterojunction and Its Photocatalytic Property. *RSC Adv.* **2014,** *4*, 3090-3095.

126. Feng, C.; Zhao, J.; Yang, F.; Gong, K.; Hao, S.; Cao, Y.; Hu, C.; Zhang, J.; Wang, Z.; Chen, L. Nonvolatile Modulation of Electronic Structure and Correlative Magnetism of L10-Fept Films Using Significant Strain Induced by Shape Memory Substrates. *Sci. Rep.* **2016,** *6*, 20199

127. Feng, C.; Zhao, J.; Yang, F.; Hao, S.; Gong, K.; Hu, D.; Cao, Y.; Jiang, X.; Wang, Z.; Chen, L. Reversible and Nonvolatile Modulations of Magnetization Switching Characteristic and Domain Configuration in L10-Fept Films Via Nonelectrically Controlled Strain Engineering. *ACS Appl. mater. Interfaces.* **2016,** *8*, 7545-7552.

128. Racek, J.; Stora, M.; Šittner, P.; Heller, L.; Kopeček, J.; Petrenec, M. Monitoring Tensile Fatigue of Superelastic Niti Wire in Liquids by Electrochemical Potential. *Shap. Mem. Superelasticity.* **2015,** *1*, 204-230.

129. Jen, S.-H.; Bertrand, J. A.; George, S. M. Critical Tensile and Compressive Strains for Cracking of Al_2O_3 Films Grown by Atomic Layer Deposition. *J. Appl. Phys.* **2011,** *109*, 084305.

130. Hang, R.; Liu, Y.; Zhao, L.; Gao, A.; Bai, L.; Huang, X.; Zhang, X.; Tang, B.; Chu, P. K. Fabrication of Ni-Ti-O Nanotube Arrays by Anodization of Niti Alloy and Their Potential Applications. *Sci. Rep.* **2014,** *4*.

131. Gao, Z.-D.; Han, Y.; Wang, Y.; Xu, J.; Song, Y.-Y. One-Step to Prepare Self-Organized Nanoporous Nio/Tio2 Layers and Its Use in Non-Enzymatic Glucose Sensing. *Sci. Rep.* **2013,** *3*, 3323.

132. Gu, Y.; Lu, Z.; Chang, Z.; Liu, J.; Lei, X.; Li, Y.; Sun, X. Niti Layered Double Hydroxide Thin Films for Advanced Pseudocapacitor Electrodes. *J. Mater. Chem.* **2013,** *1*, 10655-10661.

133. Stamenkovic, V.; Mun, B. S.; Mayrhofer, K. J.; Ross, P. N.; Markovic, N. M.; Rossmeisl, J.; Greeley, J.; Nørskov, J. K. Changing the Activity of Electrocatalysts for Oxygen Reduction by Tuning the Surface Electronic Structure. *Angew. Chem.* **2006,** *118*, 2963-2967.

134. Strasser, P.; Koh, S.; Anniyev, T.; Greeley, J.; More, K.; Yu, C.; Liu, Z.; Kaya, S.; Nordlund, D.; Ogasawara, H. Lattice-Strain Control of the Activity in Dealloyed Core–Shell Fuel Cell Catalysts. *Nat. Chem.* **2010,** *2*, 454-460.

135. Svedruzic, D.; Gregg, B. A. Mechano-Electrochemistry and Fuel-Forming Mechano-Electrocatalysis on Spring Electrodes. *J. Phys. Chem. C.* **2014,** *118*, 19246-19251.

136. Lee, H. J.; Lee, J. H.; Chung, S. Y.; Choi, J. W. Enhanced Pseudocapacitance in Multicomponent Transition-Metal Oxides by Local Distortion of Oxygen Octahedra. *Angew. Chem.* **2016,** *55*, 1-6.

137. Wang, Q.; Liu, S.; Sun, H.; Lu, Q. Synthesis of a Flower-Like Co-Doped Ni (Oh) 2 Composite for High-Performance Supercapacitors. *RSC Adv.* **2015,** *5*, 48181-48186.

138. Hu, G.; Tang, C.; Li, C.; Li, H.; Wang, Y.; Gong, H. The Sol-Gel-Derived Nickel-Cobalt Oxides with High Supercapacitor Performances. *J. Electrochem. Soc.* **2011,** *158*, A695-A699.

139. Undisz, A.; Schrempel, F.; Wesch, W.; Rettenmayr, M. In Situ Observation of Surface Oxide Layers on Medical Grade Ni-Ti Alloy During Straining. *J. Biomed. Mater. Res. Part A.* **2009,** *88*, 1000-1009.

140. Racek, J.; Šittner, P.; Heller, L.; Pilch, J.; Petrenec, M.; Sedlák, P. Corrosion of Niti Wires with Cracked Oxide Layer. *J. Mater. Eng. Perform.* **2014,** *23*, 2659-2668.

141. Racek, J.; Stora, M.; Šittner, P.; Heller, L.; Kopeček, J.; Petrenec, M. Monitoring Tensile Fatigue of Superelastic Niti Wire in Liquids by Electrochemical Potential. *Shape Memory and Superelasticity.* **2015,** *1*, 204-230.

142. Danczuk, M.; Nunes Jr, C. V.; Araki, K.; Anaissi, F. J. Influence of Alkaline Cation on the Electrochemical Behavior of Stabilized Alpha-Ni (Oh) 2. *J. Solid State Electrochem.* **2014,** *18*, 2279-2287.

143. Hang, R.; Liu, Y.; Zhao, L.; Gao, A.; Bai, L.; Huang, X.; Zhang, X.; Tang, B.; Chu, P. K. Fabrication of Ni-Ti-O Nanotube Arrays by Anodization of Niti Alloy and Their Potential Applications. *Sci. Rep.* **2014,** *4*, 7547

144. Tavassol, H.; Jones, E. M.; Sottos, N. R.; Gewirth, A. A. Electrochemical Stiffness in Lithium-Ion Batteries. *Nat. Mater.* **2016,** *15*, 1182-1187.

145. Sasaki, T.; Ukyo, Y.; Novák, P. Memory Effect in a Lithium-Ion Battery. *Nat. Mater.* **2013,** *12*, 569-575.

146. Kumar, R.; Tokranov, A.; Sheldon, B. W.; Xiao, X.; Huang, Z.; Li, C.; Mueller, T. In Situ and Operando Investigations of Failure Mechanisms of the Solid Electrolyte Interphase on Silicon Electrodes. *ACS Energy Lett.* **2016,** *1*, 689-697.

147. Ulvestad, A.; Cho, H.; Harder, R.; Kim, J.; Dietze, S.; Fohtung, E.; Meng, Y.; Shpyrko, O. Nanoscale Strain Mapping in Battery Nanostructures. *Appl. Phys. Lett.* **2014,** *104*, 073108.

148. Xu, R.; de Vasconcelos, L. S.; Zhao, K. Computational Analysis of Chemomechanical Behaviors of Composite Electrodes in Li-Ion Batteries. *J. Mater. Res.* **2016,** *31*, 2715-2727.

149. Ravnsbæk, D. B.; Xiang, K.; Xing, W.; Borkiewicz, O. J.; Wiaderek, K. M.; Gionet, P.; Chapman, K. W.; Chupas, P. J.; Tang, M.; Chiang, Y.-M. Engineering the Transformation Strain in $Limn_yfe_{1-Y}po_4$ Olivines for Ultrahigh Rate Battery Cathodes. *Nano Lett.* **2016,** *16*, 2375-2380.

150. Palacín, M.; de Guibert, A. Why Do Batteries Fail? *Science.* **2016,** *351*, 1253292.

151. Zhao, K.; Pharr, M.; Cai, S.; Vlassak, J. J.; Suo, Z. Large Plastic Deformation in High-Capacity Lithium-Ion Batteries Caused by Charge and Discharge. *J. Am. Ceram. Soc.* **2011,** *94*, s226–s235.

152. Choi, J. W.; McDonough, J.; Jeong, S.; Yoo, J. S.; Chan, C. K.; Cui, Y. Stepwise Nanopore Evolution in One-Dimensional Nanostructures. *Nano Lett.* **2010,** *10*, 1409-1413.

153. Huang, X.; Yang, H.; Liang, W.; Raju, M.; Terrones, M.; Crespi, V. H.; Van Duin, A. C.; Zhang, S. Lithiation Induced Corrosive Fracture in Defective Carbon Nanotubes. *Appl. Phys. Lett.* **2013,** *103*, 153901.

154. Park, M. S.; Wang, G. X.; Kang, Y. M.; Wexler, D.; Dou, S. X.; Liu, H. K. Preparation and Electrochemical Properties of Sno_2 Nanowires for Application in Lithium-Ion Batteries. *Angew. Chem. Int. Ed.* **2007,** *119*, 764-767.

155. Li, Y.; Yao, J.; Uchaker, E.; Zhang, M.; Tian, J.; Liu, X.; Cao, G. Sn-Doped V_2o_5 Film with Enhanced Lithium-Ion Storage Performance. *J. Phys. Chem. C.* **2013,** *117*, 23507-23514.

156. Zheng, Y.-Z.; Ding, H.; Uchaker, E.; Tao, X.; Chen, J.-F.; Zhang, Q.; Cao, G. Nickel-Mediated Polyol Synthesis of Hierarchical V_2o_5 Hollow Microspheres with Enhanced Lithium Storage Properties. *J. Mater. Chem. A.* **2015,** *3*, 1979-1985.

157. Wan, N.; Lu, X.; Wang, Y.; Zhang, W.; Bai, Y.; Hu, Y.-S.; Dai, S. Improved Li Storage Performance in Sno_2 Nanocrystals by a Synergetic Doping. *Sci. Rep.* **2016,** *6*, 18978.

158. Share, K.; Cohn, A. P.; Carter, R.; Rogers, B.; Pint, C. L. Role of Nitrogen Doped Graphene for Improved High Capacity Potassium Ion Battery Anodes. *ACS Nano.* **2016,** *10*, 9738–9744.

159. Liu, C.; Gillette, E. I.; Chen, X.; Pearse, A. J.; Kozen, A. C.; Schroeder, M. A.; Gregorczyk, K. E.; Lee, S. B.; Rubloff, G. W. An All-in-One Nanopore Battery Array. *Nat. Nanotechnol.* **2014,** *9*, 1031-1039.

160. Palanisamy, K.; Um, J. H.; Jeong, M.; Yoon, W.-S. Porous V_2o_5/Rgo/Cnt Hierarchical Architecture as a Cathode Material: Emphasis on the Contribution of Surface Lithium Storage. *Sci. Rep.* **2016,** *6*, 31275.

161. Cui, L.-F.; Yang, Y.; Hsu, C.-M.; Cui, Y. Carbon− Silicon Core− Shell Nanowires as High Capacity Electrode for Lithium Ion Batteries. *Nano Lett.* **2009,** *9*, 3370-3374.

162. Chan, C. K.; Peng, H.; Liu, G.; McIlwrath, K.; Zhang, X. F.; Huggins, R. A.; Cui, Y. High-Performance Lithium Battery Anodes Using Silicon Nanowires. *Nat. Nanotechnol.* **2008,** *3*, 31-35.

163. Zhu, Y.; Peng, L.; Chen, D.; Yu, G. Intercalation Pseudocapacitance in Ultrathin $Vopo_4$ Nanosheets: Toward High-Rate Alkali-Ion-Based Electrochemical Energy Storage. *Nano Lett.* **2015,** *16*, 742-747.

164. Luo, L.; Zhao, P.; Yang, H.; Liu, B.; Zhang, J.-G.; Cui, Y.; Yu, G.; Zhang, S.; Wang, C.-M. Surface Coating Constraint Induced Self-Discharging of Silicon Nanoparticles as Anodes for Lithium Ion Batteries. *Nano Lett.* **2015,** *15*, 7016-7022.

165. Liu, Q.; Li, Z.-F.; Liu, Y.; Zhang, H.; Ren, Y.; Sun, C.-J.; Lu, W.; Zhou, Y.; Stanciu, L.; Stach, E. A. Graphene-Modified Nanostructured Vanadium Pentoxide Hybrids with Extraordinary Electrochemical Performance for Li-Ion Batteries. *Nat. Commun.* **2015,** *6*, 6127.

166. Cohn, A. P.; Share, K.; Carter, R.; Oakes, L.; Pint, C. L. Ultrafast Solvent-Assisted Sodium Ion Intercalation into Highly Crystalline Few-Layered Graphene. *Nano Lett.* **2015,** *16*, 543-548.

167. Zhu, Y.; Wang, C. Strain Accommodation and Potential Hysteresis of $Lifepo_4$ Cathodes During Lithium Ion Insertion/Extraction. *J. Power Sources.* **2011,** *196*, 1442-1448.

168. Chen, X.; Pomerantseva, E.; Banerjee, P.; Gregorczyk, K.; Ghodssi, R.; Rubloff, G. Ozone-Based Atomic Layer Deposition of Crystalline V_2o_5 Films for High Performance Electrochemical Energy Storage. *Chem. Mater.* **2012,** *24*, 1255-1261.

169. Chen, C.; Wen, Y.; Hu, X.; Ji, X.; Yan, M.; Mai, L.; Hu, P.; Shan, B.; Huang, Y. Na^+ Intercalation Pseudocapacitance in Graphene-Coupled Titanium Oxide Enabling Ultra-Fast Sodium Storage and Long-Term Cycling. *Nat. Commun.* **2015,** *6*, 6929.

170. Zhu, H.; Jia, Z.; Chen, Y.; Weadock, N.; Wan, J.; Vaaland, O.; Han, X.; Li, T.; Hu, L. Tin Anode for Sodium-Ion Batteries Using Natural Wood Fiber as a Mechanical Buffer and Electrolyte Reservoir. *Nano Lett.* **2013,** *13*, 3093-3100.

171. Muralidharan, N.; Carter, R.; Oakes, L.; Cohn, A.; Pint, C. Strain Engineering to Modify the Electrochemistry of Energy Storage Electrodes. *Sci. Rep.* **2016,** *6*, 27542.

172. Benson, E. E.; Miller, E. M.; Nanayakkara, S. U.; Svedruzic, D.; Ferrere, S.; Neale, N. R.; van de Lagemaat, J.; Gregg, B. A. Semiconductor-to-Metal Transition in Rutile Tio_2 Induced by Tensile Strain. *Chem. Mater.* **2017,** *29*, 2173–2179.

173. Wang, H.; Xu, S.; Tsai, C.; Li, Y.; Liu, C.; Zhao, J.; Liu, Y.; Yuan, H.; Abild-Pedersen, F.; Prinz, F. B. Direct and Continuous Strain Control of Catalysts with Tunable Battery Electrode Materials. *Science.* **2016,** *354*, 1031-1036.

174. Du, M.; Cui, L.; Cao, Y.; Bard, A. J. Mechanoelectrochemical Catalysis of the Effect of Elastic Strain on a Platinum Nanofilm for the Orr Exerted by a Shape Memory Alloy Substrate. *J. Am. Chem. Soc.* **2015,** *137*, 7397-7403.

175. Oakes, L.; Carter, R.; Hanken, T.; Cohn, A. P.; Share, K.; Schmidt, B.; Pint, C. L. Interface Strain in Vertically Stacked Two-Dimensional Heterostructured Carbon-Mos_2 Nanosheets Controls Electrochemical Reactivity. *Nat. Commun.* **2016,** *7*, 11796.

176. SaifuláIslam, M. Feeling the Strain: Enhancing Ionic Transport in Olivine Phosphate Cathodes for Li-and Na-Ion Batteries through Strain Effects. *J. Mater. Chem. A.* **2016,** *4*, 6998-7004.

177. Lee, J.; Pennycook, S. J.; Pantelides, S. T. Simultaneous Enhancement of Electronic and Li^+ Ion Conductivity in Lifepo4. *Appl. Phys. Lett.* **2012,** *101*, 033901.

178. Ma, C.; Liu, M.; Chen, C.; Lin, Y.; Li, Y.; Horwitz, J.; Jiang, J.; Meletis, E.; Zhang, Q. The Origin of Local Strain in Highly Epitaxial Oxide Thin Films. *Sci. Rep.* **2013,** *3*, 3092

179. Yang, M.; Yang, Y.; Hong, B.; Wang, L.; Luo, Z.; Li, X.; Kang, C.; Li, M.; Zong, H.; Gao, C. Surface-Growth-Mode-Induced Strain Effects on the Metal–Insulator Transition in Epitaxial Vanadium Dioxide Thin Films. *RSC Adv.* **2015,** *5*, 80122-80128.

180. Pertsev, N.; Zembilgotov, A.; Hoffmann, S.; Waser, R.; Tagantsev, A. Ferroelectric Thin Films Grown on Tensile Substrates: Renormalization of the Curie–Weiss Law and Apparent Absence of Ferroelectricity. *J. Appl. Phys.* **1999,** *85*, 1698-1701.

181. Østreng, E.; Gandrud, K. B.; Hu, Y.; Nilsen, O.; Fjellvåg, H. High Power Nano-Structured V_2O_5 Thin Film Cathodes by Atomic Layer Deposition. *J. Mater. Chem. A.* **2014,** *2*, 15044-15051.

182. Musschoot, J.; Deduytsche, D.; Poelman, H.; Haemers, J.; Van Meirhaeghe, R.; Van den Berghe, S.; Detavernier, C. Comparison of Thermal and Plasma-Enhanced Ald/Cvd of Vanadium Pentoxide. *J. Electrochem. Soc.* **2009,** *156*, P122-P126.

183. Badot, J.; Ribes, S.; Yousfi, E.; Vivier, V.; Pereira-Ramos, J.; Baffier, N.; Lincotb, D. Atomic Layer Epitaxy of Vanadium Oxide Thin Films and Electrochemical Behavior in Presence of Lithium Ions. *Electrochem. Solid State Lett.* **2000,** *3*, 485-488.

184. Blanquart, T.; Niinistö, J.; Gavagnin, M.; Longo, V.; Heikkilä, M.; Puukilainen, E.; Pallem, V. R.; Dussarrat, C.; Ritala, M.; Leskelä, M. Atomic Layer Deposition and Characterization of Vanadium Oxide Thin Films. *RSC Adv.* **2013,** *3*, 1179-1185.

185. Lee, D.; Yoon, A.; Jang, S.; Yoon, J.-G.; Chung, J.-S.; Kim, M.; Scott, J.; Noh, T. Giant Flexoelectric Effect in Ferroelectric Epitaxial Thin Films. *Phys. Rev. Lett.* **2011,** *107*, 057602.

186. Gao, M.; Du, H.; Ma, C.; Liu, M.; Collins, G.; Zhang, Y.; Dai, C.; Chen, C.; Lin, Y. Strain Relaxation in Epitaxial $Srruo_3$ Thin Films on $Laalo_3$ Substrates. *Appl. Phys. Lett.* **2013,** *103*, 141901.

187. Xu, Y.; Tang, Y.; Zhu, Y.; Liu, Y.; Li, S.; Zhang, S.; Ma, X. Misfit Strain Relaxation of Ferroelectric $Pbtio_3$/$Laalo_3$ (111) Thin Film System. *Sci. Rep.* **2016,** *6*, 35172

188. Greaves, G. N.; Greer, A.; Lakes, R.; Rouxel, T. Poisson's Ratio and Modern Materials. *Nat. Mater.* **2011,** *10*, 823-837.

189. Zhang, K.; Regoutz, A.; Palgrave, R.; Payne, D.; Egdell, R.; Walsh, A.; Collins, S.; Wermeille, D.; Cowley, R. Determination of the Poisson Ratio of (001) and (111) Oriented Thin Films of In_2o_3 by Synchrotron-Based X-Ray Diffraction. *Phys. Rev. B.* **2011,** *84*, 233301.

190. Baddour-Hadjean, R.; Marzouk, A.; Pereira-Ramos, J. Structural Modifications of $Li_xv_2o_5$ in a Composite Cathode ($0 \leq X < 2$) Investigated by Raman Microspectrometry. *J. Raman Spectrosc.* **2012,** *43*, 153-160.

191. Baddour-Hadjean, R.; Smirnov, M.; Smirnov, K.; Kazimirov, V. Y.; Gallardo-Amores, J.; Amador, U.; Arroyo-de Dompablo, M.; Pereira-Ramos, J. Lattice Dynamics of B-V_2o_5: Raman Spectroscopic Insight into the Atomistic Structure of a High-Pressure Vanadium Pentoxide Polymorph. *Inorg. Chem.* **2012,** *51*, 3194-3201.

192. Ichitsubo, T.; Yagi, S.; Doi, T.; Yukitani, S.; Hirai, K.; Matsubara, E. Influence of Mechanical Strain on the Electrochemical Lithiation of Aluminum-Based Electrode Materials. *J. Electrochem. Soc.* **2011,** *159*, A14-A17.

193. Laref, S.; Laref, A. Theoretical Insight into the Strain Effect on the Intercalation Potential of Li–$Fepo_4$ Materials. *RSC Adv.* **2015,** *5*, 35667-35674.

194. Armstrong, E.; McNulty, D.; Geaney, H.; O'Dwyer, C. Electrodeposited Structurally Stable V_2o_5 Inverse Opal Networks as High Performance Thin Film Lithium Batteries. *ACS Appl. Mater. Interfaces.* **2015,** *7*, 27006-27015.

195. Tong, Z.; Hao, J.; Zhang, K.; Zhao, J.; Su, B.-L.; Li, Y. Improved Electrochromic Performance and Lithium Diffusion Coefficient in Three-Dimensionally Ordered Macroporous V_2o_5 Films. *J. Mater. Chem. C.* **2014,** *2*, 3651-3658.

196. Chan, C. K.; Peng, H.; Twesten, R. D.; Jarausch, K.; Zhang, X. F.; Cui, Y. Fast, Completely Reversible Li Insertion in Vanadium Pentoxide Nanoribbons. *Nano Lett.* **2007,** *7*, 490-495.

197. De Jesus, L. R.; Horrocks, G. A.; Liang, Y.; Parija, A.; Jaye, C.; Wangoh, L.; Wang, J.; Fischer, D. A.; Piper, L. F.; Prendergast, D. Mapping Polaronic States and Lithiation Gradients in Individual V_2O_5 Nanowires. *Nat. Commun.* **2016,** *7*, 12022.

198. Decker, F.; Donsanti, F.; Salvi, A. M.; Ibris, N.; Castle, J. E.; Martin, F.; Alamarguy, D.; Vuk, A. S.; Orel, B.; Lourenco, A. Li+ Distribution into V_2O_5 Films Resulting from Electrochemical Intercalation Reactions. *J. Braz. Chem. Soc.* **2008,** *19*, 667-671.

199. Cohn, A. P.; Muralidharan, N.; Carter, R.; Share, K.; Oakes, L.; Pint, C. L. Durable Potassium Ion Battery Electrodes from High-Rate Cointercalation into Graphitic Carbons. *J. Mater. Chem. A.* **2016,** *4*, 14954-14959.

200. Sai Gautam, G.; Canepa, P.; Abdellahi, A.; Urban, A.; Malik, R.; Ceder, G. The Intercalation Phase Diagram of Mg in V_2O_5 from First-Principles. *Chem. Mater.* **2015,** *27*, 3733-3742.

201. Yoo, H. D.; Shterenberg, I.; Gofer, Y.; Gershinsky, G.; Pour, N.; Aurbach, D. Mg Rechargeable Batteries: An on-Going Challenge. *Energy Environ. Sci.* **2013,** *6*, 2265-2279.

202. Kang, H.; Song, W.; Sohn, S.; Jin, H.; Lee, S.; Chung, Y. Polarization State-Dependent Stress Effect on the Dielectric Properties of Lead Zirconate Titanite Thin Films. *Appl. Phys. Lett.* **2006,** *88*, 172905.

203. Stanford, M. K. Thermophysical Properties of 60-Nitinol for Mechanical Component Applications. **2012**.

204. Schuerch, H. U. *Certain Physical Properties and Applications of Nitinol*; DTIC Document: 1968; pp ARC-R-280.

205. Østreng, E.; Gandrud, K. B.; Hu, Y.; Nilsen, O.; Fjellvåg, H. High Power Nano-Structured V 2 O 5 Thin Film Cathodes by Atomic Layer Deposition. *J. Mater. Chem. A.* **2014,** *2*, 15044-15051.

206. Laref, S.; Laref, A. Theoretical Insight into the Strain Effect on the Intercalation Potential of Li–Fepo 4 Materials. *RSC Adv.* **2015,** *5*, 35667-35674.

207. Gonze, X.; Amadon, B.; Anglade, P.-M.; Beuken, J.-M.; Bottin, F.; Boulanger, P.; Bruneval, F.; Caliste, D.; Caracas, R.; Côté, M. Abinit: First-Principles Approach to Material and Nanosystem Properties. *Comput. Phys. Commun.* **2009,** *180*, 2582-2615.

208. Torrent, M.; Jollet, F.; Bottin, F.; Zérah, G.; Gonze, X. Implementation of the Projector Augmented-Wave Method in the Abinit Code: Application to the Study of Iron under Pressure. *Comput. Mater. Sci.* **2008,** *42*, 337-351.

209. Kohn, W.; Sham, L. J. Self-Consistent Equations Including Exchange and Correlation Effects. *Phys. Rev. Lett.* **1965,** *140*, A1133.

210. Blöchl, P. E. Projector Augmented-Wave Method. *Phys. Rev. B.* **1994,** *50*, 17953.

211. Jollet, F.; Torrent, M.; Holzwarth, N. Generation of Projector Augmented-Wave Atomic Data: A 71 Element Validated Table in the Xml Format. *Comput. Phys. Commun.* **2014,** *185*, 1246-1254.

212. Holzwarth, N.; Tackett, A.; Matthews, G. A Projector Augmented Wave (Paw) Code for Electronic Structure Calculations, Part I: Atompaw for Generating Atom-Centered Functions. *Comput. Phys. Commun.* **2001,** *135*, 329-347.

213. Laubach, S.; Schmidt, P. C.; Thißen, A.; Fernandez-Madrigal, F. J.; Wu, Q.-H.; Jaegermann, W.; Klemm, M.; Horn, S. Theoretical and Experimental Determination of the Electronic Structure of V 2 O 5, Reduced V 2 O 5− X and Sodium Intercalated Nav 2 O 5. *Phys. Chem. Chem. Phys.* **2007,** *9*, 2564-2576.

214. Braithwaite, J.; Catlow, C.; Gale, J.; Harding, J. Lithium Intercalation into Vanadium Pentoxide: A Theoretical Study. *Chem. Mater.* **1999,** *11*, 1990-1998.

215. Aydinol, M.; Kohan, A.; Ceder, G. Ab Initio Calculation of the Intercalation Voltage of Lithium-Transition-Metal Oxide Electrodes for Rechargeable Batteries. *J. Power Sources.* **1997,** *68*, 664-668.

216. Rocquefelte, X.; Boucher, F.; Gressier, P.; Ouvrard, G. First-Principle Study of the Intercalation Process in the Li X V2o5 System. *Chem. Mater.* **2003,** *15*, 1812-1819.

217. Cannarella, J.; Arnold, C. B. Toward Low-Frequency Mechanical Energy Harvesting Using Energy-Dense Piezoelectrochemical Materials. *Adv. Mater.* **2015,** *27*, 7440-7444.

218. Orrego, S.; Shoele, K.; Ruas, A.; Doran, K.; Caggiano, B.; Mittal, R.; Kang, S. H. Harvesting Ambient Wind Energy with an Inverted Piezoelectric Flag. *Appl. Energ.* **2017,** *194*, 212-222.

219. Qin, Y.; Wang, X.; Wang, Z. L. Microfibre–Nanowire Hybrid Structure for Energy Scavenging. *Nature.* **2008,** *451*, 809-813.

220. Anton, S. R.; Sodano, H. A. A Review of Power Harvesting Using Piezoelectric Materials (2003–2006). *Smart Mater. Struct.* **2007,** *16*, R1-R21.

221. Wu, H.; Huang, Y.; Xu, F.; Duan, Y.; Yin, Z. Energy Harvesters for Wearable and Stretchable Electronics: From Flexibility to Stretchability. *Adv. Mater.* **2016,** *28*, 9881–9919.

222. Li, H.; Tian, C.; Deng, Z. D. Energy Harvesting from Low Frequency Applications Using Piezoelectric Materials. *Appl. Phys. Rev.* **2014,** *1*, 041301.

223. Mummolo, C.; Mangialardi, L.; Kim, J. H. Quantifying Dynamic Characteristics of Human Walking for Comprehensive Gait Cycle. *J. Biomech. Eng.* **2013,** *135*, 091006.

224. Danion, F.; Varraine, E.; Bonnard, M.; Pailhous, J. Stride Variability in Human Gait: The Effect of Stride Frequency and Stride Length. *Gait Posture.* **2003,** *18*, 69-77.

225. Schiffer, Z.; Arnold, C. Characterization and Model of Piezoelectrochemical Energy Harvesting Using Lithium Ion Batteries. *Exp. Mech.* **2017,** *DOI: 10.1007/s11340-017-0291-1*.

226. Liu, X. M.; Arnold, C. B. Effects of Cycling Ranges on Stress and Capacity Fade in Lithium-Ion Pouch Cells. *J. Electrochem. Soc.* **2016,** *163*, A2501-A2507.

227. Schiffer, Z. J.; Cannarella, J.; Arnold, C. B. Strain Derivatives for Practical Charge Rate Characterization of Lithium Ion Electrodes. *J. Electrochem. Soc.* **2016,** *163*, A427-A433.

228. Muralidharan, N.; Brock, C. N.; Cohn, A. P.; Schauben, D.; Carter, R. E.; Oakes, L.; Walker, D. G.; Pint, C. L. Tunable Mechanochemistry of Lithium Battery Electrodes. *ACS Nano.* **2017,** *11*, 6243-6251.

229. Kim, S.; Choi, S. J.; Zhao, K.; Yang, H.; Gobbi, G.; Zhang, S.; Li, J. Electrochemically Driven Mechanical Energy Harvesting. *Nat. Commun.* **2016,** *7*, 10146.

230. Zhang, S. Chemomechanical Modeling of Lithiation-Induced Failure in High-Volume-Change Electrode Materials for Lithium Ion Batteries. *NPJ Comput. Mater.* **2017,** *3*, 1-11.

231. Castellanos-Gomez, A.; Roldán, R.; Cappelluti, E.; Buscema, M.; Guinea, F.; van der Zant, H. S.; Steele, G. A. Local Strain Engineering in Atomically Thin Mos2. *Nano Lett.* **2013,** *13*, 5361-5366.

232. Çakır, D.; Sahin, H.; Peeters, F. M. Tuning of the Electronic and Optical Properties of Single-Layer Black Phosphorus by Strain. *Phys. Rev. B.* **2014,** *90*, 205421.

233. Jiang, J.-W.; Park, H. S. Negative Poisson's Ratio in Single-Layer Black Phosphorus. *Nat. Commun.* **2014,** *5*, 4727.

234. Fei, R.; Yang, L. Strain-Engineering the Anisotropic Electrical Conductance of Few-Layer Black Phosphorus. *Nano Lett.* **2014,** *14*, 2884-2889.

235. Dahbi, M.; Yabuuchi, N.; Fukunishi, M.; Kubota, K.; Chihara, K.; Tokiwa, K.; Yu, X.-F.; Ushiyama, H.; Yamashita, K.; Son, J.-Y.; Cui, Y.-T.; Oji, H.; Komaba, S. Black Phosphorus as a High-Capacity, High-Capability Negative Electrode for Sodium-Ion Batteries: Investigation of the Electrode/Electrolyte Interface. *Chem. Mater.* **2016,** *28*, 1625-1635.

236. Li, M.; Muralidharan, N.; Moyer, K.; Pint, C. Solvent Mediated Hybrid 2d Materials: Black Phosphorus-Graphene Heterostructured Building Blocks Assembled for Sodium Ion Batteries. *Nanoscale.* **2018**.

237. Chen, T.; Zhao, P.; Guo, X.; Zhang, S. Two-Fold Anisotropy Governs Morphological Evolution and Stress Generation in Sodiated Black Phosphorus for Sodium Ion Batteries. *Nano Lett.* **2017,** *17*, 2299–2306.

238. Oakes, L.; Zulkifli, D.; Azmi, H.; Share, K.; Hanken, T.; Carter, R.; Pint, C. L. One Batch Exfoliation and Assembly of Two-Dimensional Transition Metal Dichalcogenide Nanosheets Using Electrophoretic Deposition. *J. Electrochem. Soc.* **2015,** *162*, D3063-D3070.

239. Oakes, L.; Hanken, T.; Carter, R.; Yates, W.; Pint, C. L. Roll-to-Roll Nanomanufacturing of Hybrid Nanostructures for Energy Storage Device Design. *ACS Appl. Mater. Interfaces.* **2015,** *7*, 14201-14210.

240. Qi, Y.; McAlpine, M. C. Nanotechnology-Enabled Flexible and Biocompatible Energy Harvesting. *Energy Environ. Sci.* **2010,** *3*, 1275-1285.

241. Koka, A.; Zhou, Z.; Sodano, H. A. Vertically Aligned Batio3 Nanowire Arrays for Energy Harvesting. *Energy Environ. Sci.* **2014,** *7*, 288-296.

242. Xu, S.; Qin, Y.; Xu, C.; Wei, Y.; Yang, R.; Wang, Z. L. Self-Powered Nanowire Devices. *Nat. Nanotechnol.* **2010,** *5*, 366-373.

243. Hou, Y.; Zhou, Y.; Yang, L.; Li, Q.; Zhang, Y.; Zhu, L.; Hickner, M. A.; Zhang, Q.; Wang, Q. Flexible Ionic Diodes for Low-Frequency Mechanical Energy Harvesting. *Adv. Energy Mater.* **2016,** *7*, 1601983.

244. Zi, Y.; Guo, H.; Wen, Z.; Yeh, M. H.; Hu, C.; Wang, Z. L. Harvesting Low-Frequency (<5 Hz) Irregular Mechanical Energy: A Possible Killer Application of Triboelectric Nanogenerator. *ACS Nano.* **2016,** *10*, 4797-805.

245. Robu, V.; Flynn, D. Artificial Intelligence: Outsmart Supply Dips in Renewable Energy. *Nature.* **2017,** *544*, 161-161.

246. Dagdeviren, C.; Su, Y.; Joe, P.; Yona, R.; Liu, Y.; Kim, Y.-S.; Huang, Y.; Damadoran, A. R.; Xia, J.; Martin, L. W. Conformable Amplified Lead Zirconate Titanate Sensors with Enhanced Piezoelectric Response for Cutaneous Pressure Monitoring. *Nat. Commun.* **2014,** *5*, 4496.

247. Xu, S.; Zhang, Y.; Jia, L.; Mathewson, K. E.; Jang, K.-I.; Kim, J.; Fu, H.; Huang, X.; Chava, P.; Wang, R. Soft Microfluidic Assemblies of Sensors, Circuits, and Radios for the Skin. *Science.* **2014,** *344*, 70-74.

248. Webb, R. C.; Bonifas, A. P.; Behnaz, A.; Zhang, Y.; Yu, K. J.; Cheng, H.; Shi, M.; Bian, Z.; Liu, Z.; Kim, Y.-S. Ultrathin Conformal Devices for Precise and Continuous Thermal Characterization of Human Skin. *Nat. Mater.* **2013,** *12*, 938-944.

249. Dagdeviren, C.; Joe, P.; Tuzman, O. L.; Park, K.-I.; Lee, K. J.; Shi, Y.; Huang, Y.; Rogers, J. A. Recent Progress in Flexible and Stretchable Piezoelectric Devices for Mechanical Energy Harvesting, Sensing and Actuation. *Extreme Mech. Lett.* **2016,** *9*, 269-281.

250. Lu, B.; Chen, Y.; Ou, D.; Chen, H.; Diao, L.; Zhang, W.; Zheng, J.; Ma, W.; Sun, L.; Feng, X. Ultra-Flexible Piezoelectric Devices Integrated with Heart to Harvest the Biomechanical Energy. *Sci. Rep.* **2015,** *5*, 16065

251. Dagdeviren, C.; Yang, B. D.; Su, Y.; Tran, P. L.; Joe, P.; Anderson, E.; Xia, J.; Doraiswamy, V.; Dehdashti, B.; Feng, X. Conformal Piezoelectric Energy Harvesting and Storage from Motions of the Heart, Lung, and Diaphragm. *Proc. Natl. Acad. Sci. U.S.A.* **2014,** *111*, 1927-1932.

252. Schiffer, Z. J.; Arnold, C. B. Characterization and Model of Piezoelectrochemical Energy Harvesting Using Lithium Ion Batteries. *Experimental Mechanics.* **2017**.

253. Bucci, G.; Swamy, T.; Bishop, S.; Sheldon, B. W.; Chiang, Y.-M.; Carter, W. C. The Effect of Stress on Battery-Electrode Capacity. *J. Electrochem. Soc.* **2017,** *164*, A645-A654.

254. Benson, E. E.; Miller, E. M.; Nanayakkara, S. U.; Svedruzic, D.; Ferrere, S.; Neale, N. R.; van de Lagemaat, J.; Gregg, B. A. Semiconductor-to-Metal Transition in Rutile Tio_2 Induced by Tensile Strain. *Chem. Mater.* **2017,** *29*, 2173-2179.

255. Chen, T.; Yang, H.; Li, J.; Zhang, S. Mechanics of Electrochemically Driven Mechanical Energy Harvesting. *Extreme Mech Lett.* **2017,** *15*, 78-82.

256. Kim, S. H.; Haines, C. S.; Li, N.; Kim, K. J.; Mun, T. J.; Choi, C.; Di, J.; Oh, Y. J.; Oviedo, J. P.; Bykova, J. Harvesting Electrical Energy from Carbon Nanotube Yarn Twist. *Science.* **2017,** *357*, 773-778.

257. Liu, Y.; Merinov, B. V.; Goddard, W. A. Origin of Low Sodium Capacity in Graphite and Generally Weak Substrate Binding of Na and Mg among Alkali and Alkaline Earth Metals. *Proc. Natl. Acad. Sci. U.S.A.* **2016,** *113*, 3735-3739.

258. Jung, S. C.; Kang, Y.-J.; Han, Y.-K. Origin of Excellent Rate and Cycle Performance of Na^+-Solvent Cointercalated Graphite Vs. Poor Performance of Li^+-Solvent Case. *Nano Energy.* **2017,** *34*, 456-462.

259. Yoon, G.; Kim, H.; Park, I.; Kang, K. Conditions for Reversible Na Intercalation in Graphite: Theoretical Studies on the Interplay among Guest Ions, Solvent, and Graphite Host. *Adv. Energy Mater.* **2017,** *7*, 1601519.

260. Jache, B.; Adelhelm, P. Use of Graphite as a Highly Reversible Electrode with Superior Cycle Life for Sodium-Ion Batteries by Making Use of Co-Intercalation Phenomena. *Angew. Chem. Int. Ed.* **2014,** *53*, 10169-10173.

261. Kim, H.; Hong, J.; Yoon, G.; Kim, H.; Park, K.-Y.; Park, M.-S.; Yoon, W.-S.; Kang, K. Sodium Intercalation Chemistry in Graphite. *Energy Environ. Sci.* **2015,** *8*, 2963-2969.

262. Guan, Z.; Shen, X.; Yu, R.; Wang, Z.; Chen, L. Chemical Intercalation of Solvated Sodium Ions in Graphite. *Electrochim. Acta.* **2016,** *222*, 1365-1370.

263. Ahn, J.; Hogan, N. Walking Is Not Like Reaching: Evidence from Periodic Mechanical Perturbations. *PLOS ONE.* **2012,** *7*, e31767.

264. Jang, K.-I.; Li, K.; Chung, H. U.; Xu, S.; Jung, H. N.; Yang, Y.; Kwak, J. W.; Jung, H. H.; Song, J.; Yang, C. Self-Assembled Three Dimensional Network Designs for Soft Electronics. *Nat. Commun.* **2017,** *8*, 15894.

265. Jang, K.-I.; Chung, H. U.; Xu, S.; Lee, C. H.; Luan, H.; Jeong, J.; Cheng, H.; Kim, G.-T.; Han, S. Y.; Lee, J. W. Soft Network Composite Materials with Deterministic and Bio-Inspired Designs. *Nat. Commun.* **2015,** *6*, 6566.

266. Fan, J. A.; Yeo, W.-H.; Su, Y.; Hattori, Y.; Lee, W.; Jung, S.-Y.; Zhang, Y.; Liu, Z.; Cheng, H.; Falgout, L. Fractal Design Concepts for Stretchable Electronics. *Nat. Commun.* **2014,** *5*, 3266.

267. Sha, J.; Li, Y.; Villegas Salvatierra, R.; Wang, T.; Dong, P.; Ji, Y.; Lee, S.-K.; Zhang, C.; Zhang, J.; Smith, R. H. Three-Dimensional Printed Graphene Foams. *ACS Nano.* **2017,** *11*, 6860–6867.

268. Chortos, A.; Liu, J.; Bao, Z. Pursuing Prosthetic Electronic Skin. *Nat. Mater.* **2016,** *15*, 937–950.

269. Hwang, S. W.; Tao, H.; Kim, D. H.; Cheng, H. Y.; Song, J. K.; Rill, E.; Brenckle, M. A.; Panilaitis, B.; Won, S. M.; Kim, Y. S.; Song, Y. M.; Yu, K. J.; Ameen, A.; Li, R.; Su, Y. W.; Yang, M. M.; Kaplan, D. L.; Zakin, M. R.; Slepian, M. J.; Huang, Y. G.; Omenetto, F. G.; Rogers, J. A. A Physically Transient Form of Silicon Electronics. *Science.* **2012,** *337*, 1640-1644.

270. Yin, L.; Cheng, H. Y.; Mao, S. M.; Haasch, R.; Liu, Y. H.; Xie, X.; Hwang, S. W.; Jain, H.; Kang, S. K.; Su, Y. W.; Li, R.; Huang, Y. G.; Rogers, J. A. Dissolvable Metals for Transient Electronics. *Advanced Functional Materials.* **2014,** *24*, 645-658.

271. Huang, X.; Liu, Y. H.; Hwang, S. W.; Kang, S. K.; Patnaik, D.; Cortes, J. F.; Rogers, J. A. Biodegradable Materials for Multilayer Transient Printed Circuit Boards. *Adv. Mater.* **2014,** *26*, 7371-7377.

272. Hwang, S. W.; Huang, X.; Seo, J. H.; Song, J. K.; Kim, S.; Hage-Ali, S.; Chung, H. J.; Tao, H.; Omenetto, F. G.; Ma, Z. Q.; Rogers, J. A. Materials for Bioresorbable Radio Frequency Electronics. *Adv. Mater.* **2013,** *25*, 3526-3531.

273. Park, C. W.; Kang, S. K.; Hernandez, H. L.; Kaitz, J. A.; Wie, D. S.; Shin, J.; Lee, O. P.; Sottos, N. R.; Moore, J. S.; Rogers, J. A. Thermally Triggered Degradation of Transient Electronic Devices. *Adv. Mater.* **2015,** *27*, 3783–3788.

274. Dagdeviren, C.; Hwang, S. W.; Su, Y. W.; Kim, S.; Cheng, H. Y.; Gur, O.; Haney, R.; Omenetto, F. G.; Huang, Y. G.; Rogers, J. A. Transient, Biocompatible Electronics and Energy Harvesters Based on Zno. *Small.* **2013,** *9*, 3398-3404.

275. Son, D.; Lee, J.; Lee, D. J.; Ghaffari, R.; Yun, S.; Kim, S. J.; Lee, J. E.; Cho, H. R.; Yoon, S.; Yang, S. X.; Lee, S.; Qiao, S. T.; Ling, D. S.; Shin, S.; Song, J. K.; Kim, J.; Kim, T.; Lee, H.; Kim, J.; Soh, M.; Lee, N.; Hwang, C. S.; Nam, S.; Lu, N. S.; Hyeon, T.; Choi, S. H.; Kim, D. H. Bioresorbable Electronic Stent Integrated with Therapeutic Nanoparticles for Endovascular Diseases. *Acs Nano.* **2015,** *9*, 5937-5946.

276. Hwang, S. W.; Kim, D. H.; Tao, H.; Kim, T. I.; Kim, S.; Yu, K. J.; Panilaitis, B.; Jeong, J. W.; Song, J. K.; Omenetto, F. G.; Rogers, J. A. Materials and Fabrication Processes for Transient and Bioresorbable High-Performance Electronics. *Advanced Functional Materials.* **2013,** *23*, 4087-4093.

277. Yin, L.; Huang, X.; Xu, H. X.; Zhang, Y. F.; Lam, J.; Cheng, J. J.; Rogers, J. A. Materials, Designs, and Operational Characteristics for Fully Biodegradable Primary Batteries. *Adv. Mater.* **2014,** *26*, 3879-3884.

278. Fu, K.; Liu, Z.; Yao, Y. G.; Wang, Z. Y.; Zhao, B.; Luo, W.; Dai, J. Q.; Lacey, S. D.; Zhou, L. H.; Shen, F.; Kim, M.; Swafford, L.; Sengupta, L.; Hu, L. B. Transient Rechargeable Batteries Triggered by Cascade Reactions. *Nano Lett.* **2015,** *15*, 4664-4671.

279. Westover, A. S.; Freudiger, D.; Gani, Z. S.; Share, K.; Oakes, L.; Carter, R. E.; Pint, C. L. On-Chip High Power Porous Silicon Lithium Ion Batteries with Stable Capacity over 10 000 Cycles. *Nanoscale.* **2015,** *7*, 98-103.

280. Oakes, L.; Westover, A.; Mares, J. W.; Chatterjee, S.; Erwin, W. R.; Bardhan, R.; Weiss, S. M.; Pint, C. L. Surface Engineered Porous Silicon for Stable, High Performance Electrochemical Supercapacitors. *Scientific Reports.* **2013,** *3*, 3020.

281. Son, I. H.; Park, J. H.; Kwon, S.; Park, S.; Rummeli, M. H.; Bachmatiuk, A.; Song, H. J.; Ku, J.; Choi, J. W.; Choi, J. M.; Doo, S. G.; Chang, H. Silicon Carbide-Free Graphene Growth on Silicon for Lithium-Ion Battery with High Volumetric Energy Density. *Nature Communications.* **2015,** *6*, 7393.

282. Meng, X. B.; Yang, X. Q.; Sun, X. L. Emerging Applications of Atomic Layer Deposition for Lithium-Ion Battery Studies. *Advanced Materials.* **2012,** *24*, 3589-3615.

283. Chatterjee, S.; Carter, R.; Oakes, L.; Erwin, W. R.; Bardhan, R.; Pint, C. L. Electrochemical and Corrosion Stability of Nanostructured Silicon by Graphene Coatings: Toward High Power Porous Silicon Supercapacitors. *Journal of Physical Chemistry C.* **2014,** *118*, 10893-10902.

284. Carter, R.; Chatterjee, S.; Gordon, E.; Share, K.; Erwin, W. R.; Cohn, A. P.; Bardhan, R.; Pint, C. L. Corrosion Resistant Three-Dimensional Nanotextured Silicon for Water Photo-Oxidation. *Nanoscale.* **2015,** *7*, 16755-16762.

285. Badot, J. C.; Ribes, S.; Yousfi, E. B.; Vivier, V.; Pereira-Ramos, J. P.; Baffier, N.; Lincot, D. Atomic Layer Epitaxy of Vanadium Oxide Thin Films and Electrochemical Behavior in Presence of Lithium Ions. *Electrochem. Solid State Lett.* **2000,** *3*, 485-488.

286. Boukhalfa, S.; Evanoff, K.; Yushin, G. Atomic Layer Deposition of Vanadium Oxide on Carbon Nanotubes for High-Power Supercapacitor Electrodes. *Energy Environ. Sci.* **2012,** *5*, 6872-6879.

287. Dong, W.; Rolison, D. R.; Dunn, B. Electrochemical Properties of High Surface Area Vanadium Oxide Aerogels. *Electrochem. Solid State Lett.* **2000,** *3*, 457-459.

288. Dong, W.; Sakamoto, J.; Dunn, B. Electrochemical Properties of Vanadium Oxide Aerogels and Aerogel Nanocomposites. *J. Sol-Gel Sci. Technol.* **2003,** *26*, 641-644.

289. Huang, C. M.; Hu, C. C.; Chang, K. H.; Li, J. M.; Li, Y. F. Pseudocapacitive Characteristics of Vanadium Oxide Deposits with a Three-Dimensional Porous Structure. *J. Electrochem. Soc.* **2009,** *156*, A667-A671.

290. Lao, Z. J.; Konstantinov, K.; Tournaire, Y.; Ng, S. H.; Wang, G. X.; Liu, H. K. Synthesis of Vanadium Pentoxide Powders with Enhanced Surface-Area for Electrochemical Capacitors. *J. Power Sources.* **2006,** *162*, 1451-1454.

291. Perera, S. D.; Patel, B.; Nijem, N.; Roodenko, K.; Seitz, O.; Ferraris, J. P.; Chabal, Y. J.; Balkus, K. J. Vanadium Oxide Nanowire-Carbon Nanotube Binder-Free Flexible Electrodes for Supercapacitors. *Adv. Energy Mater.* **2011,** *1*, 936-945.

292. Sun, D.; Kwon, C. W.; Baure, G.; Richman, E.; MacLean, J.; Dunn, B.; Tolbert, S. H. The Relationship between Nanoscale Structure and Electrochemical Properties of Vanadium Oxide Nanorolls. *Adv. Energy Mater.* **2004,** *14*, 1197-1204.

293. Wang, B.; Konstantinov, K.; Wexler, D.; Liu, H.; Wang, G. X. Synthesis of Nanosized Vanadium Pentoxide/Carbon Composites by Spray Pyrolysis for Electrochemical Capacitor Application. *Electrochim. Acta.* **2009,** *54*, 1420-1425.

294. Mai, L. Q.; Xu, L.; Han, C. H.; Xu, X.; Luo, Y. Z.; Zhao, S. Y.; Zhao, Y. L. Electrospun Ultralong Hierarchical Vanadium Oxide Nanowires with High Performance for Lithium Ion Batteries. *Nano Letters.* **2010,** *10*, 4750-4755.

295. Tian, X. C.; Xu, X.; He, L.; Wei, Q. L.; Yan, M. Y.; Xu, L.; Zhao, Y. L.; Yang, C. C.; Mai, L. Q. Ultrathin Pre-Lithiated V6o13 Nanosheet Cathodes with Enhanced Electrical Transport and Cyclability. *Journal of Power Sources.* **2014,** *255*, 235-241.

296. Rauda, I. E.; Augustyn, V.; Saldarriaga-Lopez, L. C.; Chen, X. Y.; Schelhas, L. T.; Rubloff, G. W.; Dunn, B.; Tolbert, S. H. Nanostructured Pseudocapacitors Based on Atomic Layer Deposition of V2o5 onto Conductive Nanocrystal-Based Mesoporous Ito Scaffolds. *Advanced Functional Materials.* **2014,** *24*, 6717-6728.

297. Baddour-Hadjean, R.; Golabkan, V.; Pereira-Ramos, J. P.; Mantoux, A.; Lincot, D. A Raman Study of the Lithium Insertion Process in Vanadium Pentoxide Thin Films Deposited by Atomic Layer Deposition. *J. Raman Spectrosc.* **2002,** *33*, 631-638.

298. Le Van, K.; Groult, H.; Mantoux, A.; Perrigaud, L.; Lantelme, F.; Lindstrom, R.; Badour-Hadjean, R.; Zanna, S.; Lincot, D. Amorphous Vanadium Oxide Films Synthesised by Alcvd for Lithium Rechargeable Batteries. *J. Power Sources.* **2006,** *160*, 592-601.

299. Willinger, M. G.; Neri, G.; Rauwel, E.; Bonavita, A.; Micali, G.; Pinna, N. Vanadium Oxide Sensing Layer Grown on Carbon Nanotubes by a New Atomic Layer Deposition Process. *Nano Lett.* **2008,** *8*, 4201-4204.

300. Liu, Y.; Clark, M.; Zhang, Q.; Yu, D.; Liu, D.; Liu, J.; Cao, G. V2o5 Nano-Electrodes with High Power and Energy Densities for Thin Film Li-Ion Batteries. *Adv. Energy Mater.* **2011,** *1*, 194-202.

301. Wang, Y.; Cao, G. Developments in Nanostructured Cathode Materials for High-Performance Lithium-Ion Batteries. *Adv. Mater.* **2008,** *20*, 2251-2269.

302. Boukhalfa, S.; Evanoff, K.; Yushin, G. Atomic Layer Deposition of Vanadium Oxide on Carbon Nanotubes for High-Power Supercapacitor Electrodes. *Energy & Environmental Science.* **2012,** *5*, 6872-6879.

303. Singh, T.; Wang, S.; Aslam, N.; Zhang, H.; Hoffmann-Eifert, S.; Mathur, S. Atomic Layer Deposition of Transparent Vox Thin Films for Resistive Switching Applications. *Chemical vapor deposition.* **2014,** *20*, 291-297.

304. Elam, J. W.; Routkevitch, D.; Mardilovich, P. P.; George, S. M. Conformal Coating on Ultrahigh-Aspect-Ratio Nanopores of Anodic Alumina by Atomic Layer Deposition. *Chemistry of Materials.* **2003,** *15*, 3507-3517.

305. Khomenko, V.; Frackowiak, E.; Beguin, F. Determination of the Specific Capacitance of Conducting Polymer/Nanotubes Composite Electrodes Using Different Cell Configurations. *Electrochim. Acta.* **2005,** *50*, 2499-2506.

306. Bhat, B. A.; Khan, G. R.; Asokan, K. Role of Substrate Effects on the Morphological, Structural, Electrical and Thermoelectrical Properties of V2o5 Thin Films. *RSC Adv.* **2015,** *5*, 52602-52611.

307. Hwang, S. W.; Kim, D. H.; Tao, H.; Kim, T. i.; Kim, S.; Yu, K. J.; Panilaitis, B.; Jeong, J. W.; Song, J. K.; Omenetto, F. G. Materials and Fabrication Processes for Transient and Bioresorbable High-Performance Electronics. *Adv. Funct. Mater.* **2013,** *23*, 4087-4093.

308. Gao, Y.; Zhang, Y.; Wang, X.; Sim, K.; Liu, J.; Chen, J.; Feng, X.; Xu, H.; Yu, C. Moisture-Triggered Physically Transient Electronics. *Sci. Adv.* **2017,** *3*, e1701222.

309. Lee, C. H.; Jeong, J. W.; Liu, Y.; Zhang, Y.; Shi, Y.; Kang, S. K.; Kim, J.; Kim, J. S.; Lee, N. Y.; Kim, B. H. Materials and Wireless Microfluidic Systems for Electronics Capable of Chemical Dissolution on Demand. *Adv. Funct. Mater.* **2015,** *25*, 1338-1343.

310. Hwang, S.-W.; Lee, C. H.; Cheng, H.; Jeong, J.-W.; Kang, S.-K.; Kim, J.-H.; Shin, J.; Yang, J.; Liu, Z.; Ameer, G. A. Biodegradable Elastomers and Silicon Nanomembranes/Nanoribbons for Stretchable, Transient Electronics, and Biosensors. *Nano Lett.* **2015,** *15*, 2801-2808.

311. Hwang, S.-W.; Tao, H.; Kim, D.-H.; Cheng, H.; Song, J.-K.; Rill, E.; Brenckle, M. A.; Panilaitis, B.; Won, S. M.; Kim, Y.-S. A Physically Transient Form of Silicon Electronics. *Science.* **2012,** *337*, 1640-1644.

312. Hwang, S. W.; Song, J. K.; Huang, X.; Cheng, H.; Kang, S. K.; Kim, B. H.; Kim, J. H.; Yu, S.; Huang, Y.; Rogers, J. A. High-Performance Biodegradable/Transient Electronics on Biodegradable Polymers. *Adv. Mater.* **2014,** *26*, 3905-3911.

313. Fu, K. K.; Wang, Z.; Dai, J.; Carter, M.; Hu, L. Transient Electronics: Materials and Devices. *Chem. Mater.* **2016,** *28*, 3527-3539.

314. Fu, K.; Liu, Z.; Yao, Y.; Wang, Z.; Zhao, B.; Luo, W.; Dai, J.; Lacey, S. D.; Zhou, L.; Shen, F. Transient Rechargeable Batteries Triggered by Cascade Reactions. *Nano Lett.* **2015,** *15*, 4664-4671.

315. Liu, Z.; Fu, K.; Wang, Z.; Zhu, Y.; Wan, J.; Yao, Y.; Dai, J.; Kim, M.; Swafford, L.; Wang, C. Cut-and-Stack Nanofiber Paper toward Fast Transient Energy Storage. *Inorg. Chem. Front.* **2016,** *3*, 681-688.

316. Dagdeviren, C.; Hwang, S. W.; Su, Y.; Kim, S.; Cheng, H.; Gur, O.; Haney, R.; Omenetto, F. G.; Huang, Y.; Rogers, J. A. Transient, Biocompatible Electronics and Energy Harvesters Based on Zno. *Small.* **2013,** *9*, 3398-3404.

317. Chen, Y.; Jamshidi, R.; White, K.; Cınar, S.; Gallegos, E.; Hashemi, N.; Montazami, R. Physical–Chemical Hybrid Transiency: A Fully Transient Li-Ion Battery Based on Insoluble Active Materials. *J. Polym. Sci. B.* **2016,** *54*, 2021-2027.

318. Hou, Y.; Zhou, Y.; Yang, L.; Li, Q.; Zhang, Y.; Zhu, L.; Hickner, M. A.; Zhang, Q.; Wang, Q. Flexible Ionic Diodes for Low-Frequency Mechanical Energy Harvesting. *Adv. Energy Mater.* **2017,** *7*.

319. Schiffer, Z.; Arnold, C. Characterization and Model of Piezoelectrochemical Energy Harvesting Using Lithium Ion Batteries. *Exp. Mech.* **2017**.

320. Zi, Y.; Guo, H.; Wen, Z.; Yeh, M.-H.; Hu, C.; Wang, Z. L. Harvesting Low-Frequency (< 5 Hz) Irregular Mechanical Energy: A Possible Killer Application of Triboelectric Nanogenerator. *ACS Nano.* **2016,** *10*, 4797-4805.

321. Muralidharan, N.; Li, M.; Carter, R. E.; Galioto, N.; Pint, C. L. Ultralow Frequency Electrochemical–Mechanical Strain Energy Harvester Using 2d Black Phosphorus Nanosheets. *ACS Energy Lett.* **2017,** *2*, 1797-1803.

322. Muralidharan, N.; Brock, C. N.; Cohn, A. P.; Schauben, D.; Carter, R. E.; Oakes, L.; Walker, D. G.; Pint, C. L. Tunable Mechanochemistry of Lithium Battery Electrodes. *ACS Nano.* **2017,** *11*, 6243-6251.

323. Yang, H.; Liang, W.; Guo, X.; Wang, C.-M.; Zhang, S. Strong Kinetics-Stress Coupling in Lithiation of Si and Ge Anodes. *Extreme Mech. Lett.* **2015,** *2*, 1-6.

324. Kumagai, N.; Kikuchi, Y.; Tanno, K.; Lantelme, F.; Chemla, M. Electrochemical Investigation of the Diffusion of Lithium in B-Lial Alloy at Room Temperature. *J. Appl. Electrochem.* **1992,** *22*, 728-732.

325. Koka, A.; Zhou, Z.; Sodano, H. A. Vertically Aligned Batio 3 Nanowire Arrays for Energy Harvesting. *Energy Environ. Sci.* . **2014,** *7*, 288-296.

326. Li, B.; Laviage, A. J.; You, J. H.; Kim, Y.-J. Harvesting Low-Frequency Acoustic Energy Using Quarter-Wavelength Straight-Tube Acoustic Resonator. *Appl. Acoust.* **2013,** *74*, 1271-1278.

327. Hwang, G. T.; Park, H.; Lee, J. H.; Oh, S.; Park, K. I.; Byun, M.; Park, H.; Ahn, G.; Jeong, C. K.; No, K. Self-Powered Cardiac Pacemaker Enabled by Flexible Single Crystalline Pmn-Pt Piezoelectric Energy Harvester. *Adv. Mater.* **2014,** *26*, 4880-4887.

328. Xu, S.; Zhang, Y.; Cho, J.; Lee, J.; Huang, X.; Jia, L.; Fan, J. A.; Su, Y.; Su, J.; Zhang, H. Stretchable Batteries with Self-Similar Serpentine Interconnects and Integrated Wireless Recharging Systems. *Nat. Commun.* **2013,** *4*, 1543.

329. Jeong, Y. R.; Kim, J.; Xie, Z.; Xue, Y.; Won, S. M.; Lee, G.; Jin, S. W.; Hong, S. Y.; Feng, X.; Huang, Y. A Skin-Attachable, Stretchable Integrated System Based on Liquid Gainsn for Wireless Human Motion Monitoring with Multi-Site Sensing Capabilities. *NPG Asia Mater.* **2017,** *9*, e443.

330. Kim, D.-H.; Ahn, J.-H.; Choi, W. M.; Kim, H.-S.; Kim, T.-H.; Song, J.; Huang, Y. Y.; Liu, Z.; Lu, C.; Rogers, J. A. Stretchable and Foldable Silicon Integrated Circuits. *Science.* **2008,** *320*, 507-511.

331. Zhang, Y.; Fu, H.; Su, Y.; Xu, S.; Cheng, H.; Fan, J. A.; Hwang, K.-C.; Rogers, J. A.; Huang, Y. Mechanics of Ultra-Stretchable Self-Similar Serpentine Interconnects. *Acta Mater.* **2013,** *61*, 7816-7827.

332. Chin, T. E.; Rhyner, U.; Koyama, Y.; Hall, S. R.; Chiang, Y.-M. Lithium Rechargeable Batteries as Electromechanical Actuators. *Electrochem. Solid State Lett.* **2006,** *9*, A134-A138.

333. Lang, J.; Ding, B.; Zhu, T.; Su, H.; Luo, H.; Qi, L.; Liu, K.; Wang, K.; Hussain, N.; Zhao, C. Cycling of a Lithium-Ion Battery with a Silicon Anode Drives Large Mechanical Actuation. *Adv. Mater.* **2016,** *28*, 10236-10243.

334. Koyama, Y.; Chin, T. E.; Rhyner, U.; Holman, R. K.; Hall, S. R.; Chiang, Y. M. Harnessing the Actuation Potential of Solid-State Intercalation Compounds. *Adv. Funct. Mater.* **2006,** *16*, 492-498.

335. Noble, B.; Harris, S.; Dinsdale, K. The Elastic Modulus of Aluminium-Lithium Alloys. *J. Mater. Sci.* **1982,** *17*, 461-468.

336. Huang, Y.; Zhu, M.; Huang, Y.; Pei, Z.; Li, H.; Wang, Z.; Xue, Q.; Zhi, C. Multifunctional Energy Storage and Conversion Devices. *Adv. Mater.* **2016,** *28*, 8344-8364.

337. Aboutalebi, S. H.; Jalili, R.; Esrafilzadeh, D.; Salari, M.; Gholamvand, Z.; Aminorroaya Yamini, S.; Konstantinov, K.; Shepherd, R. L.; Chen, J.; Moulton, S. E. High-Performance Multifunctional Graphene Yarns: Toward Wearable All-Carbon Energy Storage Textiles. *ACS Nano.* **2014,** *8*, 2456-2466.

338. Song, T.; Sun, B. Towards Photo-Rechargeable Textiles Integrating Power Conversion and Energy Storage Functions: Can We Kill Two Birds with One Stone? *ChemSusChem.* **2013,** *6*, 408-410.

339. Ramadoss, A.; Saravanakumar, B.; Lee, S. W.; Kim, Y.-S.; Kim, S. J.; Wang, Z. L. Piezoelectric-Driven Self-Charging Supercapacitor Power Cell. *ACS Nano.* **2015,** *9*, 4337-4345.

340. González, C.; Vilatela, J.; Molina-Aldareguía, J.; Lopes, C.; LLorca, J. Structural Composites for Multifunctional Applications: Current Challenges and Future Trends. *Prog. Mater. Sci.* **2017,** *89*, 194-251.

341. Asp, L. E.; Greenhalgh, E. S. Structural Power Composites. *Compos. Sci. Technol.* **2014,** *101*, 41-61.

342. Chan, K.-Y.; Jia, B.; Lin, H.; Hameed, N.; Lee, J.-H.; Lau, K.-T. A Critical Review on Multifunctional Composites as Structural Capacitors for Energy Storage. *Compos. Struct.* **2018,** *188*, 126-142.

343. Liu, P.; Sherman, E.; Jacobsen, A. Design and Fabrication of Multifunctional Structural Batteries. *J. Power Sources.* **2009,** *189*, 646-650.

344. Ekstedt, S.; Wysocki, M.; Asp, L. Structural Batteries Made from Fibre Reinforced Composites. *Plast. Rubber Compos.* **2010,** *39*, 148-150.

345. Kjell, M. H.; Jacques, E.; Zenkert, D.; Behm, M.; Lindbergh, G. Pan-Based Carbon Fiber Negative Electrodes for Structural Lithium-Ion Batteries. *J. Electrochem. Soc.* **2011,** *158*, A1455-A1460.

346. Westover, A. S.; Shabab, F. N.; Tian, J. W.; Bernath, S.; Oakes, L.; Erwin, W. R.; Carter, R.; Bardhan, R.; Pint, C. L. Stretching Ion Conducting Polymer Electrolytes: In-Situ Correlation of Mechanical, Ionic Transport, and Optical Properties. *J. Electrochem. Soc.* **2014,** *161*, E112-E117.

347. Westover, A. S.; Baer, B.; Bello, B. H.; Sun, H.; Oakes, L.; Bellan, L. M.; Pint, C. L. Multifunctional High Strength and High Energy Epoxy Composite Structural Supercapacitors with Wet-Dry Operational Stability. *J. Mater. Chem. A.* **2015,** *3*, 20097-20102.

348. Westover, A. S.; Tian, J. W.; Bernath, S.; Oakes, L.; Edwards, R.; Shabab, F. N.; Chatterjee, S.; Anilkumar, A. V.; Pint, C. L. A Multifunctional Load-Bearing Solid-State Supercapacitor. *Nano Lett.* **2014,** *14*, 3197-3202.

349. Shirshova, N.; Bismarck, A.; Carreyette, S.; Fontana, Q. P.; Greenhalgh, E. S.; Jacobsson, P.; Johansson, P.; Marczewski, M. J.; Kalinka, G.; Kucernak, A. R. Structural Supercapacitor Electrolytes Based on Bicontinuous Ionic Liquid–Epoxy Resin Systems. *J. Mater. Chem. A.* **2013,** *1*, 15300-15309.

350. Qian, H.; Kucernak, A. R.; Greenhalgh, E. S.; Bismarck, A.; Shaffer, M. S. Multifunctional Structural Supercapacitor Composites Based on Carbon Aerogel Modified High Performance Carbon Fiber Fabric. *ACS Appl. Mater. Interfaces.* **2013,** *5*, 6113-6122.

351. Shirshova, N.; Qian, H.; Houllé, M.; Steinke, J. H.; Kucernak, A. R.; Fontana, Q. P.; Greenhalgh, E. S.; Bismarck, A.; Shaffer, M. S. Multifunctional Structural Energy Storage Composite Supercapacitors. *Faraday Discuss.* **2014,** *172*, 81-103.

352. Javaid, A.; Ho, K.; Bismarck, A.; Shaffer, M.; Steinke, J.; Greenhalgh, E. Multifunctional Structural Supercapacitors for Electrical Energy Storage Applications. *J. Compos. Mater.* **2014,** *48*, 1409-1416.

353. Shirshova, N.; Qian, H.; Shaffer, M. S.; Steinke, J. H.; Greenhalgh, E. S.; Curtis, P. T.; Kucernak, A.; Bismarck, A. Structural Composite Supercapacitors. *Compos. Part A Appl. Sci. Manuf.* **2013,** *46*, 96-107.

354. Qian, H.; Diao, H.; Shirshova, N.; Greenhalgh, E. S.; Steinke, J. G.; Shaffer, M. S.; Bismarck, A. Activation of Structural Carbon Fibres for Potential Applications in Multifunctional Structural Supercapacitors. *J. Colloid Interface Sci.* **2013,** *395*, 241-248.

355. Benson, J.; Kovalenko, I.; Boukhalfa, S.; Lashmore, D.; Sanghadasa, M.; Yushin, G. Multifunctional Cnt-Polymer Composites for Ultra-Tough Structural Supercapacitors and Desalination Devices. *Adv. Mater.* **2013,** *25*, 6625-6632.

356. Senokos, E.; Reguero, V.; Cabana, L.; Palma, J.; Marcilla, R.; Vilatela, J. J. Large-Area, All-Solid, and Flexible Electric Double Layer Capacitors Based on Cnt Fiber Electrodes and Polymer Electrolytes. *Adv. Mater.Technol.* **2017,** *2*.

357. Senokos, E.; Ou, Y.; Torres, J. J.; Sket, F.; González, C.; Marcilla, R.; Vilatela, J. J. Energy Storage in Structural Composites by Introducing Cnt Fiber/Polymer Electrolyte Interleaves. *Sci Rep.* **2018,** *8*, 3407.

358. Deka, B. K.; Hazarika, A.; Kim, J.; Park, Y.-B.; Park, H. W. Multifunctional Cuo Nanowire Embodied Structural Supercapacitor Based on Woven Carbon Fiber/Ionic Liquid–Polyester Resin. *Compos. A Appl. Sci. Manuf.* **2016,** *87*, 256-262.

359. Simon, P.; Gogotsi, Y.; Dunn, B. Where Do Batteries End and Supercapacitors Begin? *Science.* **2014,** *343*, 1210-1211.

360. Muralidharan, N.; Westover, A. S.; Sun, H.; Galioto, N.; Carter, R. E.; Cohn, A. P.; Oakes, L.; Pint, C. L. From the Junkyard to the Power Grid: Ambient Processing of Scrap Metals into Nanostructured Electrodes for Ultrafast Rechargeable Batteries. *ACS Energy Lett.* **2016,** *1*, 1034-1041.

361. Fan, Z.; Yan, J.; Wei, T.; Zhi, L.; Ning, G.; Li, T.; Wei, F. Asymmetric Supercapacitors Based on Graphene/Mno2 and Activated Carbon Nanofiber Electrodes with High Power and Energy Density. *Adv. Funct. Mater.* **2011,** *21*, 2366-2375.

362. Zhou, C.; Zhang, Y.; Li, Y.; Liu, J. Construction of High-Capacitance 3d Coo@ Polypyrrole Nanowire Array Electrode for Aqueous Asymmetric Supercapacitor. *Nano Lett.* **2013,** *13*, 2078-2085.

363. Wang, Y.-G.; Wang, Z.-D.; Xia, Y.-Y. An Asymmetric Supercapacitor Using Ruo2/Tio2 Nanotube Composite and Activated Carbon Electrodes. *Electrochim. Acta.* **2005,** *50*, 5641-5646.

364. Qu, Q.; Shi, Y.; Tian, S.; Chen, Y.; Wu, Y.; Holze, R. A New Cheap Asymmetric Aqueous Supercapacitor: Activated Carbon//Namno2. *J. Power Sources.* **2009,** *194*, 1222-1225.

365. Halpert, G. Past Developments and the Future of Nickel Electrode Cell Technology. *J. Power Sources.* **1984,** *12*, 177-192.

366. Chakkaravarthy, C.; Periasamy, P.; Jegannathan, S.; Vasu, K. The Nickel/Iron Battery. *J. Power Sources.* **1991,** *35*, 21-35.

367. Liu, J.; Chen, M.; Zhang, L.; Jiang, J.; Yan, J.; Huang, Y.; Lin, J.; Fan, H. J.; Shen, Z. X. A Flexible Alkaline Rechargeable Ni/Fe Battery Based on Graphene Foam/Carbon Nanotubes Hybrid Film. *Nano Lett.* **2014,** *14*, 7180-7187.

368. Lei, D.; Lee, D.-C.; Magasinski, A.; Zhao, E.; Steingart, D.; Yushin, G. Performance Enhancement and Side Reactions in Rechargeable Nickel–Iron Batteries with Nanostructured Electrodes. *ACS Appl. Mater. Interfaces.* **2016,** *8*, 2088-2096.

369. Sarkar, D.; Shukla, A.; Sarma, D. Substrate Integrated Nickel–Iron Ultrabattery with Extraordinarily Enhanced Performances. *ACS Energy Lett.* **2016,** *1*, 82-88.

370. Jiang, W.; Liang, F.; Wang, J.; Su, L.; Wu, Y.; Wang, L. Enhanced Electrochemical Performances of Feo X–Graphene Nanocomposites as Anode Materials for Alkaline Nickel–Iron Batteries. *RSC Adv.* **2014,** *4*, 15394-15399.

371. Hashempour, M.; Vicenzo, A.; Zhao, F.; Bestetti, M. Direct Growth of Mwcnts on 316 Stainless Steel by Chemical Vapor Deposition: Effect of Surface Nano-Features on Cnt Growth and Structure. *Carbon.* **2013,** *63*, 330-347.

372. Camilli, L.; Scarselli, M.; Del Gobbo, S.; Castrucci, P.; Nanni, F.; Gautron, E.; Lefrant, S.; De Crescenzi, M. The Synthesis and Characterization of Carbon Nanotubes Grown by Chemical Vapor Deposition Using a Stainless Steel Catalyst. *Carbon.* **2011,** *49*, 3307-3315.

373. Masarapu, C.; Wei, B. Direct Growth of Aligned Multiwalled Carbon Nanotubes on Treated Stainless Steel Substrates. *Langmuir.* **2007,** *23*, 9046-9049.

374. Wu, Y.; Qiao, P.; Chong, T.; Shen, Z. Carbon Nanowalls Grown by Microwave Plasma Enhanced Chemical Vapor Deposition. *Adv. Mater.* **2002,** *14*, 64-67.

375. Soliman, E. M.; Kandil, U. F.; Reda Taha, M. M. Investigation of Frp Lap Splice Using Epoxy Containing Carbon Nanotubes. *J. Compos. Constr.* **2014,** *19*, 04014045.

376. Garcia, E. J.; Wardle, B. L.; Hart, A. J.; Yamamoto, N. Fabrication and Multifunctional Properties of a Hybrid Laminate with Aligned Carbon Nanotubes Grown in Situ. *Compos. Sci. Technol.* **2008,** *68*, 2034-2041.

377. Garcia, E. J.; Wardle, B. L.; Hart, A. J. Joining Prepreg Composite Interfaces with Aligned Carbon Nanotubes. *Compos. Pt. A. Appl. Sci. Manuf.* **2008,** *39*, 1065-1070.

378. Blanco, J.; García, E. J.; Guzmán de Villoria, R.; Wardle, B. L. Limiting Mechanisms of Mode I Interlaminar Toughening of Composites Reinforced with Aligned Carbon Nanotubes. *J. Compos. Mater.* . **2009,** *43*, 825-841.

379. Wicks, S. S.; de Villoria, R. G.; Wardle, B. L. Interlaminar and Intralaminar Reinforcement of Composite Laminates with Aligned Carbon Nanotubes. *Compos. Sci. Technol.* **2010,** *70*, 20-28.

380. Garcia, E. J.; Hart, A. J.; Wardle, B. L.; Slocum, A. H.; Shim, D.-J. In *Aligned Carbon Nanotube Reinforcement of Graphite/Epoxy Ply Interfaces*, 16th International Conference on Composite Materials, Kioto, Japan, **2007**.

381. Deka, B. K.; Hazarika, A.; Kim, J.; Park, Y.-B.; Park, H. W. Multifunctional Cuo Nanowire Embodied Structural Supercapacitor Based on Woven Carbon Fiber/Ionic Liquid–Polyester Resin. *Composites Part A: Applied Science and Manufacturing.* **2016,** *87*, 256-262.

382. Lian, K. K.; Li, C.; Jung, R. H.; Thompson, L. C., Alkaline Gel Electrolyte for Electrochemical Cells. Google Patents: 1996.

383. Hall, D. S.; Lockwood, D. J.; Bock, C.; MacDougall, B. R. Nickel Hydroxides and Related Materials: A Review of Their Structures, Synthesis and Properties. *Proc. R. Soc. A.* **2015,** *471*, 20140792.

384. Henri, P. A.; Rommevaux-Jestin, C.; Lesongeur, F.; Mumford, A.; Emerson, D.; Godfroy, A.; Ménez, B. Structural Iron (Ii) of Basaltic Glass as an Energy Source for Zetaproteobacteria in an Abyssal Plain Environment, Off the Mid Atlantic Ridge. *Front. Microbiol.* **2016,** *6*, 1518.

385. Song, K.; Lee, Y.; Jo, M. R.; Nam, K. M.; Kang, Y.-M. Comprehensive Design of Carbon-Encapsulated Fe3o4 Nanocrystals and Their Lithium Storage Properties. *Nanotechnology.* **2012,** *23*, 505401.

386. Javaid, A.; Ho, K.; Bismarck, A.; Steinke, J.; Shaffer, M.; Greenhalgh, E. Improving the Multifunctional Behaviour of Structural Supercapacitors by Incorporating Chemically Activated Carbon Fibres and Mesoporous Silica Particles as Reinforcement. *J. Compos. Mater.* **2018**, 0021998318761216.

387. Cohn, A. P.; Muralidharan, N.; Carter, R.; Share, K.; Pint, C. L. Anode-Free Sodium Battery through in Situ Plating of Sodium Metal. *Nano Lett.* **2017,** *17*, 1296-1301.

388. Share, K.; Cohn, A. P.; Carter, R. E.; Pint, C. L. Mechanism of Potassium Ion Intercalation Staging in Few Layered Graphene from in Situ Raman Spectroscopy. *Nanoscale.* **2016,** *8*, 16435-16439.

389. Share, K.; Lewis, J.; Oakes, L.; Carter, R. E.; Cohn, A. P.; Pint, C. L. Tungsten Diselenide (Wse 2) as a High Capacity, Low Overpotential Conversion Electrode for Sodium Ion Batteries. *RSC Adv.* **2015,** *5*, 101262-101267.

390. Carter, R.; Oakes, L.; Muralidharan, N.; Cohn, A. P.; Douglas, A.; Pint, C. L. Polysulfide Anchoring Mechanism Revealed by Atomic Layer Deposition of V2o5 and Sulfur-Filled Carbon Nanotubes for Lithium–Sulfur Batteries. *ACS Appl. Mater. Interfaces.* **2017,** *9*, 7185-7192.

391. Carter, R.; Oakes, L.; Muralidharan, N.; Pint, C. L. Isothermal Sulfur Condensation into Carbon Scaffolds: Improved Loading, Performance, and Scalability for Lithium–Sulfur Battery Cathodes. *J. Phys. Chem. C.* **2017,** *121*, 7718-7727.

392. Carter, R.; Oakes, L.; Douglas, A.; Muralidharan, N.; Cohn, A. P.; Pint, C. L. A Sugar-Derived Room-Temperature Sodium Sulfur Battery with Long Term Cycling Stability. *Nano Lett.* **2017,** *17*, 1863-1869.

393. Oakes, L.; Carter, R.; Pint, C. L. Nanoscale Defect Engineering of Lithium–Sulfur Battery Composite Cathodes for Improved Performance. *Nanoscale.* **2016,** *8*, 19368-19375.

394. Carter, R.; Ejorh, D.; Share, K.; Cohn, A. P.; Douglas, A.; Muralidharan, N.; Tovar, T. M.; Pint, C. L. Surface Oxidized Mesoporous Carbons Derived from Porous Silicon as Dual Polysulfide Confinement and Anchoring Cathodes in Lithium Sulfur Batteries. *J. Power Sources.* **2016,** *330*, 70-77.

395. Douglas, A.; Carter, R.; Oakes, L.; Share, K.; Cohn, A. P.; Pint, C. L. Ultrafine Iron Pyrite (Fes2) Nanocrystals Improve Sodium–Sulfur and Lithium–Sulfur Conversion Reactions for Efficient Batteries. *ACS nano.* **2015,** *9*, 11156-11165.

396. Oakes, L.; Muralidharan, N.; Cohn, A. P.; Pint, C. L. Catalyst Morphology Matters for Lithium–Oxygen Battery Cathodes. *Nanotechnology.* **2016,** *27*, 495404.

397. Carter, R.; Oakes, L.; Cohn, A. P.; Holzgrafe, J.; Zarick, H. F.; Chatterjee, S.; Bardhan, R.; Pint, C. L. Solution Assembled Single-Walled Carbon Nanotube Foams: Superior Performance in Supercapacitors, Lithium-Ion, and Lithium–Air Batteries. *J. Phys. Chem. C.* **2014,** *118*, 20137-20151.

398. Carter, R.; Davis, B.; Oakes, L.; Maschmann, M. R.; Pint, C. L. A High Areal Capacity Lithium–Sulfur Battery Cathode Prepared by Site-Selective Vapor Infiltration of Hierarchical Carbon Nanotube Arrays. *Nanoscale.* **2017,** *9*, 15018-15026.

399. Davis, B. F.; Yan, X.; Muralidharan, N.; Oakes, L.; Pint, C. L.; Maschmann, M. R. Electrically Conductive Hierarchical Carbon Nanotube Networks with Tunable Mechanical Response. *ACS Appl. Mater. Interfaces.* **2016,** *8*, 28004-28011.

400. Avraham, E. S.; Westover, A. S.; Itzhak, A.; Shani, L.; Mor, V.; Girshevitz, O.; Pint, C. L.; Nessim, G. D. Patterned Growth of Carbon Nanotube Forests Using Cu and Cu/Ag Thin Film Reservoirs as Growth Inhibitors. *Carbon.* **2018**.

401. Li, M.; Carter, R.; Douglas, A.; Oakes, L.; Pint, C. L. Sulfur Vapor-Infiltrated 3d Carbon Nanotube Foam for Binder-Free High Areal Capacity Lithium–Sulfur Battery Composite Cathodes. *ACS Nano.* **2017,** *11*, 4877-4884.

402. Avraham, E. S.; Fleker, O.; Benisvy, L.; Oakes, L.; Pint, C. L.; Nessim, G. D. Inducing Porosity and Growing Carbon Nanofibers in Ferroin Perchlorate: An Example of Morphological Transitions in Coordination Complexes. *J. Solid State Chem.* **2017,** *253*, 21-28.

403. Douglas, A.; Carter, R. E.; Li, M.; Pint, C. L. Toward Small Diameter Carbon Nanotubes Synthesized from Captured Carbon Dioxide: Critical Role of Catalyst Coarsening. *ACS Appl. Mater. Interfaces.* **2018**.

404. Douglas, A.; Muralidharan, N.; Carter, R.; Pint, C. L. Sustainable Capture and Conversion of Carbon Dioxide into Valuable Multiwalled Carbon Nanotubes Using Metal Scrap Materials. *ACS Sus. Chem. Engg.* **2017,** *5*, 7104-7110.

405. Douglas, A.; Carter, R.; Muralidharan, N.; Oakes, L.; Pint, C. L. Iron Catalyzed Growth of Crystalline Multi-Walled Carbon Nanotubes from Ambient Carbon Dioxide Mediated by Molten Carbonates. *Carbon.* **2017,** *116*, 572-578.

406. Douglas, A.; Pint, C. L. Electrochemical Growth of Carbon Nanotubes and Graphene from Ambient Carbon Dioxide: Synergy with Conventional Gas-Phase Growth Mechanisms. *ECS J. Solid State Sci. Technol.* **2017,** *6*, M3084-M3089.

407. Li, M.; Carter, R.; Cohn, A. P.; Pint, C. L. Interconnected Foams of Helical Carbon Nanofibers Grown with Ultrahigh Yield for High Capacity Sodium Ion Battery Anodes. *Carbon.* **2016,** *107*, 109-115.

408. Licht, S.; Douglas, A.; Ren, J.; Carter, R.; Lefler, M.; Pint, C. L. Carbon Nanotubes Produced from Ambient Carbon Dioxide for Environmentally Sustainable Lithium-Ion and Sodium-Ion Battery Anodes. *ACS Cent. Sci.* **2016,** *2*, 162-168.

409. Westover, A. S.; Choi, J.; Cui, K.; Ishikawa, T.; Inoue, T.; Xiang, R.; Chiashi, S.; Kato, T.; Maruyama, S.; Pint, C. L. Load Dependent Frictional Response of Vertically Aligned Single-Walled Carbon Nanotube Films. *Scripta Mater.* **2016,** *125*, 63-67.

410. Share, K.; Westover, A.; Li, M.; Pint, C. L. Surface Engineering of Nanomaterials for Improved Energy Storage–a Review. *Chem. Eng. Sci.* **2016,** *154*, 3-19.